Abstract

NOJAVAN, SAEED. Damage Imaging Algorithms for Structural Health Monitoring using Electromagnetic Waves. (Under the direction of Dr. Fuh-Gwo Yuan.)

Reconstructing damage geometry with computationally efficient and effective algorithms is of primary importance in establishing a robust structural health monitoring system (SHMS). To this end, two linearized imaging algorithms, electromagnetic (EM) migration and Born imaging, are formulated for 3-D damage imaging of structures using EM waves. These algorithms are derived in both differential equation (DE) and integral equation (IE) formalisms in time-domain for inhomogeneous anisotropic and lossy structures.

When sensor data is collected in a common-source configuration (i.e., each set of sensor data is collected by individual actuator), the proposed imaging algorithms consist of three steps: (1) Back-propagation (migration) of the scattered field data derived from the measured sensor data; (2) Zero-lag cross-correlation of the back-propagated scattered field with the incident field in image area; and (3) Summation of partial images obtained from individual actuators. The back-propagation step can be carried out numerically based on either the DEs or the IEs associated with the back-propagated scattered field. In DE approach, the associated differential equations are discretized and solved by a finite difference time domain (FDTD) method. Although mathematically this approach is straightforward, it may be computationally intensive for 3-D cases. In IE approach, however, the Green's functions of the pristine structure are required. For general 3-D cases, numerical solutions of these Green's functions may be computationally intensive when analytical solutions are not available. Fortunately, the numerical solutions of the Green's functions, if needed, are carried

out only once prior to the monitoring stage. Having calculated the Green's functions, the back-propagation of the scattered field data is performed by integral (summation) operations during the monitoring stage.

To lower the computational cost of the zero-lag cross-correlation imaging condition in step (2), the incident field at each image point is approximated by a single-event function parameterized by a traveltime and an amplitude. It is shown that by applying similar approximations to the fields associated with the Green's functions of the pristine structure in the IE formalism of the algorithms, real-time damage imaging algorithms suitable for SHM application can be realized.

Another way of reducing the computational cost of the algorithms is to employ the poststack concept, typically used in geophysical exploration. Using this concept, the incident field in the image area is not needed in the imaging process at all but the sensor data should be collected in a zero-offset configuration (i.e., actuators and sensors are collocated).

To show the effectiveness of the DE and IE formalisms of the imaging algorithms, numerical simulations in 2-D transverse magnetic case for a reinforced concrete slab and a glass/epoxy composite plate with multiple damages are performed. In this simulated study, all sensor data, incident field, back-propagated (migrated) field, and the Green's functions of the pristine structure are generated *via* a FDTD method with second–order of accuracy in time and space.

It is concluded that the proposed imaging algorithms are capable of efficiently identifying the damages geometries, are robust against measurement noise, and in their IE formalism may be employed in a SHMS.

DAMAGE IMAGING ALGORITHMS FOR STRUCTURAL HEALTH MONITORING USING ELECTROMAGNETIC WAVES

by

SAEED NOJAVAN

A dissertation submitted to the Graduate Faculty of
North Carolina State University
in partial fulfillment of the
requirements for the Degree of
Doctor of Philosophy

MECHANICAL ENGINEERING

Raleigh

2006

Approved by:

Dr. Mohammad Noori

Dr. Kara Peters

Dr. Gianluca Lazzi

Dr. Fuh-Gwo Yuan
Chair of Advisory Committee

Dedication

To My Dear Wife Fatemeh

Biography

Saeed Nojavan was born on September 21, 1969 in Teharn, Iran. He is the son of Ali Akbar Nojavan and Mandegar Abbaszadeh and the brother of Majid, Hamid, Vahid, and Mohammad Nojavan. He began his academic career at Amir Kabir University of Technology (Polytechnic) in the fall of 1987 and completed his BS degree in Mechanical Engineering in summer 1992. He continued his education at University of Tehran in the fall of 1992 and completed his MS degree in Mechanical Engineering in summer 1995. He entered graduate school at North Carolina State University in the fall of 2002 in pursuit of a PhD degree in Mechanical Engineering.

Acknowledgements

I would like to thank Dr. Fuh-Gwo Yuan for suggesting the following work and serving as my graduate advisor over the past four years. I appreciate his support and guidance throughout the work.

I would also like to thank Dr. Mohammad Noori, Dr. Kara Peters, and Dr. Gianluca Lazzi for serving on my committee members and reading this dissertation.

Thanks also go to all the members in our research group specially Dr. Yun Jin, Mr. Lei Wang, Mr. Hussein Harb, Dr. S. Yang, Mr. Lei Liu, and Mr. Feng Zhang for their care and help. Special thanks go to Dr. Amir Homayoun Heidari for helping me with the migration theory.

Finally, I would like to thank my family and friends, specially my wife Fatemeh, for their encouragement and support to continue my education over the years.

This research was supported in part by the following grants: National Science Foundation Grant CMS-0301441, a fellowship from Goodrich Corporation, and a fellowship from North Carolina Space Grant Consortium.

Table of Contents

List of Figures.....vii
Introduction.....1
1. Fundamental Equations.....12
2. Forward Scattering of Electromagnetic Waves.....19
3. Inverse Scattering.....22
4. The Electromagnetic Migration Algorithm.....25
4.1. The First Approach.....26
4.2. The Second Approach (Lagrange Multipliers).....32
5. Born Imaging Algorithm.....39
5.1. Born Imaging Formulas.....39
5.2. The Relation between Adjoint Operators and Gradients.....47
6. Imaging Steps in Electromagnetic Migration and Born Imaging Algorithms.....50
7. Two-Dimensional Electromagnetic Field.....57
7.1. Born Imaging Formulas in TM Field.....58
7.2. Electromagnetic Migration Imaging Formulas in TM Field.....64
8. Numerical Results.....69
8.1. Isotropic Case.....71
8.1.1. Born Imaging (DE Formalism).....74
8.1.2. Born Imaging (DE Formalism; Poststack).....81
8.1.3. Born Imaging (IE Formalism).....86
8.1.4. EM Migration (DE Formalism).....93
8.1.5. EM Migration (DE Formalism; Poststack).....101
8.1.6. EM Migration (IE Formalism).....106
8.2. Anisotropic Case.....113
8.2.1. Born Imaging (DE Formalism).....116
8.2.2. Born Imaging (DE Formalism; Poststack).....121
8.2.3. Born Imaging (IE Formalism).....125
8.2.4. EM Migration (DE Formalism).....130

8.2.5. EM Migration (DE Formalism; Poststack) 136
8.2.6. EM Migration (IE Formalism) 140

9. Conclusions 145

References 149

Appendices 157

A. Dyadic Green's Functions in an Infinite Homogeneous Isotropic and Lossless Media 158

B. Reciprocity Theorems in Electromagnetic 159

C. The Fourier Transform Properties 163

List of Figures

3.1 The inverse medium problem: Finding scatterer EM properties using field measurement at sensor locations outside the scatterer 22

8.1.1 Cross section of a reinforced concrete slab with multiple damages 71

8.1.2 The time history of the excitation signal 71

8.1.3 The amplitude spectrum of the excitation signal 71

8.1.4 The *y*-component of the scattered electric field data, $E^{d}_{y;\,scat}$, excited from an actuator at $x = 50\,\text{mm}$ with sensor spacing of $\Delta_s = 6$ mm 72

8.1.5 The *x*-component of the scattered magnetic field data, $H^{d}_{x;\,scat}$, excited from an actuator at $x = 50\,\text{mm}$ with sensor spacing of $\Delta_s = 6$ mm 72

8.1.6 The *z*-component of the scattered magnetic field data, $H^{d}_{z;\,scat}$, excited from an actuator at $x = 50\,\text{mm}$ with sensor spacing of $\Delta_s = 6$ mm 73

8.1.1.1 Case (A); Permittivity image; Zero-lag cross-correlation imaging condition; 76

8.1.1.2 Case (A); Permittivity image; Excitation-time imaging condition (Max-energy arrival); 76

8.1.1.3 Case (A); Permittivity image; Modified excitation-time imaging condition (Max-energy arrival); . 76

8.1.1.4 Case (A); Permittivity image; Excitation-time imaging condition (First-arrival); 76

8.1.1.5 Case (A); Permittivity image; Modified excitation-time imaging condition (First-arrival); 76

8.1.1.6 Case (A); Permeability image; Zero-lag cross-correlation imaging condition; 76

8.1.1.7 Case (A); Permeability image; Excitation-time imaging condition (Max-energy arrival); 77

8.1.1.8 Case (A); Permeability image; Modified excitation-time imaging condition (Max-energy arrival); 77

8.1.1.9 Case (A); Permeability image; Excitation-time imaging condition (First-arrival); 77

8.1.1.10 Case (A); Permeability image; Modified excitation-time imaging condition (First-arrival); 77

8.1.1.11 Case (A); Conductivity image; Zero-lag cross-correlation imaging condition; 77

8.1.1.12 Case (A); Conductivity image; Excitation-time imaging condition (Max-energy arrival); 77

8.1.1.13 Case (A); Conductivity image; Modified excitation-time imaging condition (Max-energy arrival); 77

8.1.1.14 Case (A); Conductivity image; Excitation-time imaging condition (First-arrival); 77

8.1.1.15 Case (A); Conductivity image; Modified excitation-time imaging condition (First-arrival); 78

8.1.1.16 Case (B); Permittivity image; Modified excitation-time imaging condition (Max-energy arrival); . 78

8.1.1.17 Case (B); Permeability image; Modified excitation-time imaging condition (Max-energy arrival); 78

8.1.1.18 Case (B); Conductivity image; Modified excitation-time imaging condition (Max-energy arrival); 78

8.1.1.19 Case (C); Permittivity image; Modified excitation-time imaging condition (Max-energy arrival); . 78

8.1.1.20 Case (C); Permeability image; Modified excitation-time imaging condition (Max-energy arrival); 78

8.1.1.21 Case (C); Conductivity image; Modified excitation-time imaging condition (Max-energy arrival); 78

8.1.1.22 Case (D); Permittivity image; Zero-lag cross-correlation imaging condition; Noisy data SNR=5;.. 78

8.1.1.23 Case (D); Permittivity image; Modified excitation-time imaging condition (Max-energy arrival); Noisy data SNR=5;..... 79

8.1.1.24 Case (E); Permittivity image; Modified excitation-time imaging condition (Max-energy arrival); $\Delta_{s,a} = 1.5\lambda_{\min}$; 79

8.1.1.25 Case (F); Permittivity image; Modified excitation-time imaging condition (Max-energy arrival); $\Delta_{s,a} = 2\lambda_{\min}$; 79

8.1.1.26 Case (G); Permittivity image; Excitation-time imaging condition (Max-energy arrival); Half-space concrete;..... 79

8.1.1.27 Case (G); Permittivity image; Modified excitation-time imaging condition (Max-energy arrival); Half-space concrete; 79

8.1.1.28 Case (G); Permittivity image; Excitation-time imaging condition (First-arrival); Half-space concrete;..... 79

8.1.1.29 Case (G); Permittivity image; Modified excitation-time imaging condition (First-arrival); Half-space concrete;..... 79

8.1.1.30 Case (G); Permeability image; Modified excitation-time imaging condition (Max-energy arrival); Half-space concrete; 79

8.1.1.31 Case (G); Conductivity image; Modified excitation-time imaging condition (Max-energy arrival); Half-space concrete; 80

8.1.1.32 Case (H); Permittivity image; Excitation-time imaging condition (Max-energy arrival); Modified pristine structure;..... 80

8.1.1.33 Case (H); Permittivity image; Modified excitation-time imaging condition (Max-energy arrival); Modified pristine structure;..... 80

8.1.1.34 Case (H); Permittivity image; Excitation-time imaging condition (First-arrival); Modified pristine structure; 80

8.1.1.35 Case (H); Permittivity image; Modified excitation-time imaging condition (First-arrival); Modified pristine structure;..... 80

8.1.1.36 Case (H); Permeability image; Modified excitation-time imaging condition (Max-energy arrival); Modified pristine structure; 80

8.1.1.37 Case (H); Conductivity image; Modified excitation-time imaging condition (Max-energy arrival); Modified pristine structure; 80

8.1.1.38 Case (I); Permeability image; Modified excitation-time imaging condition (Max-energy arrival); Concrete slab without rebars; 80

8.1.2.1 Case (A); $E^{BP}_{y;scat}$ -image obtained by poststack Born imaging; 83

8.1.2.2 Case (A); $H^{BP}_{x;scat}$ -image obtained by poststack Born imaging; 83

8.1.2.3 Case (A); $H^{BP}_{z;scat}$ -image obtained by poststack Born imaging; 83

8.1.2.4 Case (B); $E^{BP}_{y;scat}$ -image obtained by poststack Born imaging; 83

8.1.2.5 Case (B); $H^{BP}_{x;scat}$ -image obtained by poststack Born imaging; 83

8.1.2.6 Case (B); $H^{BP}_{z;scat}$ -image obtained by poststack Born imaging; 83

8.1.2.7 Case (C); $E^{BP}_{y;scat}$ -image obtained by poststack Born imaging; 84

8.1.2.8 Case (C); $H^{BP}_{x;scat}$ -image obtained by poststack Born imaging; 84

8.1.2.9 Case (C); $H^{BP}_{z;scat}$ -image obtained by poststack Born imaging; 84

8.1.2.10 Case (D); $E^{BP}_{y;scat}$ -image obtained by poststack Born imaging; Noisy data SNR=5; 84

8.1.2.11 Case (E); $E^{BP}_{y;scat}$ -image obtained by poststack Born imaging; $\Delta = \lambda_{\min}$; 84

8.1.2.12 Case (F); $E^{BP}_{y;scat}$ -image obtained by poststack Born imaging; Half-space concrete; 84

8.1.2.13 Case (F); $H^{BP}_{x;scat}$ -image obtained by poststack Born imaging; Half-space concrete; 84

8.1.2.14 Case (F); $H^{BP}_{z;scat}$ -image obtained by poststack Born imaging; Half-space concrete; 84

8.1.2.15 Case (G); $E^{BP}_{y;scat}$ -image obtained by poststack Born imaging; Modified pristine structure; 85

8.1.2.16 Case (G); $H^{BP}_{x;scat}$ -image obtained by poststack Born imaging; Modified pristine structure; 85

8.1.2.17 Case (G); $H^{BP}_{z;scat}$ -image obtained by poststack Born imaging; Modified pristine structure; 85

8.1.2.18 Case (H); $E^{BP}_{y;scat}$ -image obtained by poststack Born imaging; Concrete slab without rebars; 85

8.1.3.1 Case (A); Permittivity image; Both $G_{yx;b}^{EM}$ and $\dot{E}_{y;inc}$ are approximated based on maximum-energy arrival criterion; Without amplitude; 88

8.1.3.2 Case (A); Permittivity image; Both $G_{yx;b}^{EM}$ and $\dot{E}_{y;inc}$ are approximated based on maximum-energy arrival criterion; With amplitude; 88

8.1.3.3 Case (A); Permittivity image; Both $G_{yx;b}^{EM}$ and $\dot{E}_{y;inc}$ are approximated based on first-arrival criterion; Without amplitude; 88

8.1.3.4 Case (A); Permittivity image; Both $G_{yx;b}^{EM}$ and $\dot{E}_{y;inc}$ are approximated based on first-arrival criterion; With amplitude; 88

8.1.3.5 Case (A); Permeability image; All $G_{xx;b}^{HM}$, $G_{zx;b}^{HM}$, $\dot{H}_{x;inc}$, and $\dot{H}_{z;inc}$ are approximated based on maximum-energy arrival criterion; With amplitude; 88

8.1.3.6 Case (A); Permeability image; All $G_{xx;b}^{HM}$, $G_{zx;b}^{HM}$, $\dot{H}_{x;inc}$, and $\dot{H}_{z;inc}$ are approximated based on first-arrival criterion; With amplitude; 88

8.1.3.7 Case (A); Conductivity image; Both $G_{yx;b}^{EM}$ and $E_{y;inc}$ are approximated based on maximum-energy arrival criterion; With amplitude; 89

8.1.3.8 Case (A); Conductivity image; Both $G_{yx;b}^{EM}$ and $E_{y;inc}$ are approximated based on first-arrival criterion; With amplitude; 89

8.1.3.9 Case (B); Permittivity image; Both $G_{yy;b}^{EJ}$ and $\dot{E}_{y;inc}$ are approximated based on maximum-energy arrival criterion; With amplitude; 89

8.1.3.10 Case (B); Permeability image; All $G_{xy;b}^{HJ}$, $G_{zy;b}^{HJ}$, $\dot{H}_{x;inc}$, and $\dot{H}_{z;inc}$ are approximated based on maximum-energy arrival criterion; With amplitude; 89

8.1.3.11 Case (B); Conductivity image; Both $G_{yy;b}^{EJ}$ and $E_{y;inc}$ are approximated based on maximum-energy arrival criterion; With amplitude; 89

8.1.3.12 Case (C); Permittivity image; Both $G_{yz;b}^{EM}$ and $\dot{E}_{y;inc}$ are approximated based on maximum-energy arrival criterion; With amplitude; 89

8.1.3.13 Case (C); Permeability image; All $G_{xz;b}^{HM}$, $G_{zz;b}^{HM}$, $\dot{H}_{x;inc}$, and $\dot{H}_{z;inc}$ are approximated based on maximum-energy arrival criterion; With amplitude; 90

8.1.3.14 Case (C); Conductivity image; Both $G_{yz;b}^{EM}$ and $E_{y;inc}$ are approximated based on maximum-energy arrival criterion; With amplitude; 90

8.1.3.15 Case (D); Permittivity image; Both $G_{yx;b}^{EM}$ and $\dot{E}_{y;inc}$ are approximated based on maximum-energy arrival criterion; With amplitude; Noisy data SNR=5; 90

8.1.3.16 Case (E); Permittivity image; Both $G_{yx;b}^{EM}$ and $\dot{E}_{y;inc}$ are approximated based on maximum-energy arrival criterion; With amplitude; $\Delta_{s,a} = 1.5\lambda_{\min}$; 90

8.1.3.17 Case (F); Permittivity image; Both $G^{EM}_{yx;b}$ and $\dot{E}_{y;inc}$ are approximated based on maximum-energy arrival criterion; With amplitude; $\Delta_{s,a} = 2\lambda_{\min}$;..... 90

8.1.3.18 Case (G); Permittivity image; Both $G^{EM}_{yx;b}$ and $\dot{E}_{y;inc}$ are approximated based on maximum-energy arrival criterion; Without amplitude; Half-space concrete; 90

8.1.3.19 Case (G); Permittivity image; Both $G^{EM}_{yx;b}$ and $\dot{E}_{y;inc}$ are approximated based on maximum-energy arrival criterion; With amplitude; Half-space concrete; 91

8.1.3.20 Case (G); Permittivity image; Both $G^{EM}_{yx;b}$ and $\dot{E}_{y;inc}$ are approximated based on first-arrival criterion; Without amplitude; Half-space concrete;..... 91

8.1.3.21 Case (G); Permittivity image; Both $G^{EM}_{yx;b}$ and $\dot{E}_{y;inc}$ are approximated based on first-arrival criterion; With amplitude; Half-space concrete;..... 91

8.1.3.22 Case (G); Permeability image; All $G^{HM}_{xx;b}$, $G^{HM}_{zx;b}$, $\dot{H}_{x;inc}$, and $\dot{H}_{z;inc}$ are approximated based on maximum-energy arrival criterion; With amplitude; Half-space concrete; 91

8.1.3.23 Case (G); Conductivity image; Both $G^{EM}_{yx;b}$ and $E_{y;inc}$ are approximated based on maximum-energy arrival criterion; With amplitude; Half-space concrete; 91

8.1.3.24 Case (H); Permittivity image; Both $G^{EM}_{yx;b}$ and $\dot{E}_{y;inc}$ are approximated based on maximum-energy arrival criterion; Without amplitude; Modified pristine structure;..... 91

8.1.3.25 Case (H); Permittivity image; Both $G^{EM}_{yx;b}$ and $\dot{E}_{y;inc}$ are approximated based on maximum-energy arrival criterion; With amplitude; Modified pristine structure; 92

8.1.3.26 Case (H); Permittivity image; Both $G^{EM}_{yx;b}$ and $\dot{E}_{y;inc}$ are approximated based on first-arrival criterion; Without amplitude; Modified pristine structure; 92

8.1.3.27 Case (H); Permittivity image; Both $G^{EM}_{yx;b}$ and $\dot{E}_{y;inc}$ are approximated based on first-arrival criterion; With amplitude; Modified pristine structure; 92

8.1.3.28 Case (H); Permeability image; All $G^{HM}_{xx;b}$, $G^{HM}_{zx;b}$, $\dot{H}_{x;inc}$, and $\dot{H}_{z;inc}$ are approximated based on maximum-energy arrival criterion; With amplitude; Modified pristine structure;..... 92

8.1.3.29 Case (H); Conductivity image; Both $G^{EM}_{yx;b}$ and $E_{y;inc}$ are approximated based on maximum-energy arrival criterion; With amplitude; Modified pristine structure; 92

8.1.3.30 Case (I); Permeability image; All $G^{HM}_{xx;b}$, $G^{HM}_{zx;b}$, $\dot{H}_{x;inc}$, and $\dot{H}_{z;inc}$ are approximated based on maximum-energy arrival criterion; With amplitude; Concrete slab without rebars;..... 92

8.1.4.1 Case (A); Permittivity image; Zero-lag cross-correlation imaging condition;..... 95

8.1.4.2 Case (A); Permittivity image; Excitation-time imaging condition (Max-energy arrival);..... 95

8.1.4.3 Case (A); Permittivity image; Modified excitation-time imaging condition (Max-energy arrival); . 95

8.1.4.4 Case (A); Permittivity image; Excitation-time imaging condition (First-arrival);..... 95

8.1.4.5 Case (A); Permittivity image; Modified excitation-time imaging condition (First-arrival); 96

8.1.4.6 Case (A); Permeability image; Zero-lag cross-correlation imaging condition; 96

8.1.4.7 Case (A); Permeability image; Excitation-time imaging condition (Max-energy arrival); 96

8.1.4.8 Case (A); Permeability image; Modified excitation-time imaging condition (Max-energy arrival); 96

8.1.4.9 Case (A); Permeability image; Excitation-time imaging condition (First-arrival);..... 96

8.1.4.10 Case (A); Permeability image; Modified excitation-time imaging condition (First-arrival); 96

8.1.4.11 Case (A); Conductivity image; Zero-lag cross-correlation imaging condition;..... 96

8.1.4.12 Case (A); Conductivity image; Excitation-time imaging condition (Max-energy arrival);..... 96

8.1.4.13 Case (A); Conductivity image; Modified excitation-time imaging condition (Max-energy arrival); 97

8.1.4.14 Case (A); Conductivity image; Excitation-time imaging condition (First-arrival); 97

8.1.4.15 Case (A); Conductivity image; Modified excitation-time imaging condition (First-arrival);..... 97

8.1.4.16 Case (B); Permittivity image; Modified excitation-time imaging condition (Max-energy arrival); Data treated as sources;..... 97

8.1.4.17 Case (B); Permeability image; Modified excitation-time imaging condition (Max-energy arrival); Data treated as sources;..... 97

8.1.4.18 Case (B); Conductivity image; Modified excitation-time imaging condition (Max-energy arrival); Data treated as sources;..... 97

8.1.4.19 Case (C); Permittivity image; Modified excitation-time imaging condition (Max-energy arrival); Only $E^d_{y;scat}$ as BC;..... 97

8.1.4.20 Case (C); Permeability image; Modified excitation-time imaging condition (Max-energy arrival); Only $E^d_{y;scat}$ as BC;..... 97

8.1.4.21 Case (C); Conductivity image; Modified excitation-time imaging condition (Max-energy arrival); Only $E^d_{y;scat}$ as BC;..... 98

8.1.4.22 Case (D); Permittivity image; Modified excitation-time imaging condition (Max-energy arrival); Only $H^d_{x;scat}$ as BC;..... 98

8.1.4.23 Case (D); Permeability image; Modified excitation-time imaging condition (Max-energy arrival); Only $H^d_{x;scat}$ as BC;..... 98

8.1.4.24 Case (D); Conductivity image; Modified excitation-time imaging condition (Max-energy arrival); Only $H^d_{x;scat}$ as BC;..... 98

8.1.4.25 Case (E); Conductivity image; Zero-lag cross-correlation imaging condition; Noisy data SNR=5;. 98

8.1.4.26 Case (E); Conductivity image; Modified excitation-time imaging condition (Max-energy arrival); Noisy data SNR=5;..... 98

8.1.4.27 Case (F); Conductivity image; Modified excitation-time imaging condition (Max-energy arrival); $\Delta_{s,a} = 1.5\lambda_{\min}$; 98

8.1.4.28 Case (G); Conductivity image; Modified excitation-time imaging condition (Max-energy arrival); $\Delta_{s,a} = 2\lambda_{\min}$; 98

8.1.4.29 Case (H); Permittivity image; Modified excitation-time imaging condition (Max-energy arrival); Half-space concrete; 99

8.1.4.30 Case (H); Permeability image; Modified excitation-time imaging condition (Max-energy arrival); Half-space concrete; 99

8.1.4.31 Case (H); Conductivity image; Excitation-time imaging condition (Max-energy arrival); Half-space concrete;..... 99

8.1.4.32 Case (H); Conductivity image; Modified excitation-time imaging condition (Max-energy arrival); Half-space concrete; 99

8.1.4.33 Case (H); Conductivity image; Excitation-time imaging condition (First-arrival); Half-space concrete;..... 99

8.1.4.34 Case (H); Conductivity image; Modified excitation-time imaging condition (First-arrival); Half-space concrete; 99

8.1.4.35 Case (I); Permittivity image; Modified excitation-time imaging condition (Max-energy arrival); Modified pristine structure;..... 99

8.1.4.36 Case (I); Permeability image; Modified excitation-time imaging condition (Max-energy arrival); Modified pristine structure;..... 99

8.1.4.37 Case (I); Conductivity image; Excitation-time imaging condition (Max-energy arrival); Modified pristine structure;.....100

8.1.4.38 Case (I); Conductivity image; Modified excitation-time imaging condition (Max-energy arrival); Modified pristine structure;.....100

8.1.4.39 Case (I); Conductivity image; Excitation-time imaging condition (First-arrival); Modified pristine structure; 100

8.1.4.40 Case (I); Conductivity image; Modified excitation-time imaging condition (First-arrival); Modified pristine structure;.....100

8.1.4.41 Case (J); Conductivity image; Modified excitation-time imaging condition (Max-energy arrival); Concrete slab without rebars; 100

8.1.5.1 Case (A); $E^{m}_{y;scat}$ -image obtained by poststack EM migration;.....103

8.1.5.2 Case (A); $H^m_{x;scat}$ -image obtained by poststack EM migration; 103

8.1.5.3 Case (A); $H^m_{z;scat}$ -image obtained by poststack EM migration; 103

8.1.5.4 Case (B); $E^m_{y;scat}$ -image obtained by poststack EM migration; Data treated as sources; 103

8.1.5.5 Case (B); $H^m_{x;scat}$ -image obtained by poststack EM migration; Data treated as sources;.....103

8.1.5.6 Case (B); $H^m_{z;scat}$ -image obtained by poststack EM migration; Data treated as sources;.....103

8.1.5.7 Case (C); $E^m_{y;scat}$ -image obtained by poststack EM migration; Only $E^d_{y;scat}$ as BC;.....104

8.1.5.8 Case (C); $H^m_{x;scat}$ -image obtained by poststack EM migration; Only $E^d_{y;scat}$ as BC; 104

8.1.5.9 Case (C); $H^m_{z;scat}$ -image obtained by poststack EM migration; Only $E^d_{y;scat}$ as BC; 104

8.1.5.10 Case (D); $E^m_{y;scat}$ -image obtained by poststack EM migration; Only $H^d_{x;scat}$ as BC; 104

8.1.5.11 Case (D); $H^m_{x;scat}$ -image obtained by poststack EM migration; Only $H^d_{x;scat}$ as BC;.....104

8.1.5.12 Case (D); $H^m_{z;scat}$ -image obtained by poststack EM migration; Only $H^d_{x;scat}$ as BC;.....104

8.1.5.13 Case (E); $H^m_{x;scat}$ -image obtained by poststack EM migration; Noisy data SNR=5; 104

8.1.5.14 Case (F); $H^m_{x;scat}$ -image obtained by poststack EM migration; $\Delta = \lambda_{\min}$; 104

8.1.5.15 Case (G); $E^m_{y;scat}$ -image obtained by poststack EM migration; Half-space concrete;.....105

8.1.5.16 Case (G); $H^m_{x;scat}$ -image obtained by poststack EM migration; Half-space concrete; 105

8.1.5.17 Case (G); $H^m_{z;scat}$ -image obtained by poststack EM migration; Half-space concrete; 105

8.1.5.18 Case (H); $E^m_{y;scat}$ -image obtained by poststack EM migration; Modified pristine structure; 105

8.1.5.19 Case (H); $H^m_{x;scat}$ -image obtained by poststack EM migration; Modified pristine structure;.....105

8.1.5.20 Case (H); $H^m_{z;scat}$ -image obtained by poststack EM migration; Modified pristine structure;.....105

8.1.5.21 Case (I); $H^m_{x;scat}$ -image obtained by poststack EM migration; Concrete slab without rebars; 105

8.1.6.1 Case (A); Permittivity image; All $G^{EM}_{yx;b}$, $G^{EJ}_{yy;b}$, and $\dot{E}_{y;inc}$ are approximated based on maximum-energy arrival criterion; Without amplitude; 108

8.1.6.2 Case (A); Permittivity image; All $G_{yx;b}^{EM}$, $G_{yy;b}^{EJ}$, and $\dot{E}_{y;inc}$ are approximated based on maximum-energy arrival criterion; With amplitude;.....108

8.1.6.3 Case (A); Permittivity image; All $G_{yx;b}^{EM}$, $G_{yy;b}^{EJ}$, and $\dot{E}_{y;inc}$ are approximated based on first-arrival criterion; Without amplitude;.....108

8.1.6.4 Case (A); Permittivity image; All $G_{yx;b}^{EM}$, $G_{yy;b}^{EJ}$, and $\dot{E}_{y;inc}$ are approximated based on first-arrival criterion; With amplitude;.....108

8.1.6.5 Case (A); Permeability image; All $G_{xy;b}^{HJ}$, $G_{zy;b}^{HJ}$, $G_{xx;b}^{HM}$, $G_{zx;b}^{HM}$, $\dot{H}_{x;inc}$, and $\dot{H}_{z;inc}$ are approximated based on maximum-energy arrival criterion; With amplitude;.....108

8.1.6.6 Case (A); Permeability image; All $G_{xy;b}^{HJ}$, $G_{zy;b}^{HJ}$, $G_{xx;b}^{HM}$, $G_{zx;b}^{HM}$, $\dot{H}_{x;inc}$, and $\dot{H}_{z;inc}$ are approximated based on first-arrival criterion; With amplitude;.....108

8.1.6.7 Case (A); Conductivity image; All $G_{yx;b}^{EM}$, $G_{yy;b}^{EJ}$, and $E_{y;inc}$ are approximated based on maximum-energy arrival criterion; With amplitude;.....109

8.1.6.8 Case (A); Conductivity image; All $G_{yx;b}^{EM}$, $G_{yy;b}^{EJ}$, and $E_{y;inc}$ are approximated based on first-arrival criterion; With amplitude;.....109

8.1.6.9 Case (B); Permittivity image; Both $G_{yx;b}^{EM}$ and $\dot{E}_{y;inc}$ are approximated based on maximum-energy arrival criterion; With amplitude; Only $E_{y;scat}^{d}$;.....109

8.1.6.10 Case (B); Permeability image; All $G_{xx;b}^{HM}$, $G_{zx;b}^{HM}$, $\dot{H}_{x;inc}$, and $\dot{H}_{z;inc}$ are approximated based on maximum-energy arrival criterion; With amplitude; Only $E_{y;scat}^{d}$;.....109

8.1.6.11 Case (B); Conductivity image; Both $G_{yx;b}^{EM}$ and $E_{y;inc}$ are approximated based on maximum-energy arrival criterion; With amplitude; Only $E_{y;scat}^{d}$;.....109

8.1.6.12 Case (C); Permittivity image; Both $G_{yy;b}^{EJ}$ and $\dot{E}_{y;inc}$ are approximated based on maximum-energy arrival criterion; With amplitude; Only $H_{x;scat}^{d}$;.....109

8.1.6.13 Case (C); Permeability image; All $G_{xy;b}^{HJ}$, $G_{zy;b}^{HJ}$, $\dot{H}_{x;inc}$, and $\dot{H}_{z;inc}$ are approximated based on maximum-energy arrival criterion; With amplitude; Only $H_{x;scat}^{d}$;.....110

8.1.6.14 Case (C); Conductivity image; Both $G_{yy;b}^{EJ}$ and $E_{y;inc}$ are approximated based on maximum-energy arrival criterion; With amplitude; Only $H_{x;scat}^{d}$;.....110

8.1.6.15 Case (D); Permittivity image; All $G_{yx;b}^{EM}$, $G_{yy;b}^{EJ}$, and $\dot{E}_{y;inc}$ are approximated based on maximum-energy arrival criterion; With amplitude; Noisy data SNR=5;.....110

8.1.6.16 Case (E); Permittivity image; All $G_{yx;b}^{EM}$, $G_{yy;b}^{EJ}$, and $\dot{E}_{y;inc}$ are approximated based on maximum-energy arrival criterion; With amplitude; $\Delta_{s,a} = 1.5\lambda_{\min}$;.....110

8.1.6.17 Case (F); Permittivity image; All $G^{EM}_{yx;b}$, $G^{EJ}_{yy;b}$, and $\dot{E}_{y;inc}$ are approximated based on maximum-energy arrival criterion; With amplitude; $\Delta_{s,a} = 2\lambda_{\min}$; 110

8.1.6.18 Case (G); Permittivity image; All $G^{EM}_{yx;b}$, $G^{EJ}_{yy;b}$, and $\dot{E}_{y;inc}$ are approximated based on maximum-energy arrival criterion; With amplitude; Half-space concrete; 110

8.1.6.19 Case (G); Permittivity image; All $G^{EM}_{yx;b}$, $G^{EJ}_{yy;b}$, and $\dot{E}_{y;inc}$ are approximated based on first-arrival criterion; With amplitude; Half-space concrete; 111

8.1.6.20 Case (G); Permeability image; All $G^{HJ}_{xy;b}$, $G^{HJ}_{zy;b}$, $G^{HM}_{xx;b}$, $G^{HM}_{zx;b}$, $\dot{H}_{x;inc}$, and $\dot{H}_{z;inc}$ are approximated based on maximum-energy arrival criterion; With amplitude; Half-space concrete; 111

8.1.6.21 Case (G); Conductivity image; All $G^{EM}_{yx;b}$, $G^{EJ}_{yy;b}$, and $E_{y;inc}$ are approximated based on maximum-energy arrival criterion; With amplitude; Half-space concrete; 111

8.1.6.22 Case (H); Permittivity image; All $G^{EM}_{yx;b}$, $G^{EJ}_{yy;b}$, and $\dot{E}_{y;inc}$ are approximated based on maximum-energy arrival criterion; With amplitude; Modified pristine structure; 111

8.1.6.23 Case (H); Permittivity image; All $G^{EM}_{yx;b}$, $G^{EJ}_{yy;b}$, and $\dot{E}_{y;inc}$ are approximated based on first-arrival criterion; With amplitude; Modified pristine structure; 111

8.1.6.24 Case (H); Permeability image; All $G^{HJ}_{xy;b}$, $G^{HJ}_{zy;b}$, $G^{HM}_{xx;b}$, $G^{HM}_{zx;b}$, $\dot{H}_{x;inc}$, and $\dot{H}_{z;inc}$ are approximated based on maximum-energy arrival criterion; With amplitude; Modified pristine structure; 111

8.1.6.25 Case (H); Conductivity image; All $G^{EM}_{yx;b}$, $G^{EJ}_{yy;b}$, and $E_{y;inc}$ are approximated based on maximum-energy arrival criterion; With amplitude; Modified pristine structure; 112

8.1.6.26 Case (I); Permittivity image; All $G^{EM}_{yx;b}$, $G^{EJ}_{yy;b}$, and $\dot{E}_{y;inc}$ are approximated based on maximum-energy arrival criterion; With amplitude; Concrete slab without rebars; 112

8.2.1 Cross section of a glass/epoxy composite plate with two delaminations 113

8.2.2 The time history of the excitation signal 113

8.2.3 The amplitude spectrum of the excitation signal 113

8.2.4 The *y*-component of the scattered electric field data, $E^{d}_{y;\,scat}$, excited from an actuator at $x = 25\text{mm}$ with sensor spacing of $\Delta_s = 2$ mm 114

8.2.5 The *x*-component of the scattered magnetic field data, $H^{d}_{x;\,scat}$, excited from an actuator at $x = 25\text{mm}$ with sensor spacing of $\Delta_s = 2$ mm 114

8.2.6 The *z*-component of the scattered magnetic field data, $H^{d}_{z;\,scat}$, excited from an actuator at $x = 25\text{mm}$ with sensor spacing of $\Delta_s = 2$ mm 115

8.2.1.1 Case (A); ε_{yy}-image; Zero-lag cross-correlation imaging condition; 118

8.2.1.2 Case (A); ε_{yy}-image; Excitation-time imaging condition (Max-energy arrival); 118

8.2.1.3 Case (A); ε_{yy}-image; Modified excitation-time imaging condition (Max-energy arrival); 118

8.2.1.4 Case (A); ε_{yy}-image; Excitation-time imaging condition (First-arrival);.....118

8.2.1.5 Case (A); ε_{yy}-image; Modified excitation-time imaging condition (First-arrival); 118

8.2.1.6 Case (A); μ_{xx}-image; Zero-lag cross-correlation imaging condition;.....118

8.2.1.7 Case (A); μ_{xx}-image; Modified excitation-time imaging condition (Max-energy arrival);.....118

8.2.1.8 Case (A); μ_{xx}-image; Modified excitation-time imaging condition (First-arrival);.....118

8.2.1.9 Case (A); μ_{zz}-image; Zero-lag cross-correlation imaging condition;.....118

8.2.1.10 Case (A); μ_{zz}-image; Modified excitation-time imaging condition (Max-energy arrival);.....118

8.2.1.11 Case (A); μ_{zz}-image; Modified excitation-time imaging condition (First-arrival);.....118

8.2.1.12 Case (A); σ_{yy}-image; Zero-lag cross-correlation imaging condition;.....118

8.2.1.13 Case (A); σ_{yy}-image; Modified excitation-time imaging condition (Max-energy arrival); 119

8.2.1.14 Case (A); σ_{yy}-image; Modified excitation-time imaging condition (First-arrival);.....119

8.2.1.15 Case (B); μ_{xx}-image; Modified excitation-time imaging condition (Max-energy arrival);.....119

8.2.1.16 Case (B); μ_{xx}-image; Modified excitation-time imaging condition (First-arrival);.....119

8.2.1.17 Case (C); μ_{xx}-image; Modified excitation-time imaging condition (Max-energy arrival);.....119

8.2.1.18 Case (C); μ_{xx}-image; Modified excitation-time imaging condition (First-arrival);.....119

8.2.1.19 Case (D); μ_{xx}-image; Modified excitation-time imaging condition (Max-energy arrival); Noisy data SNR=5; 119

8.2.1.20 Case (D); μ_{xx}-image; Modified excitation-time imaging condition (First-arrival); Noisy data SNR=5; 119

8.2.1.21 Case (E); μ_{xx}-image; Modified excitation-time imaging condition (Max-energy arrival); $\Delta_{s,a} = 2\lambda_{\min}$; 119

8.2.1.22 Case (E); μ_{xx}-image; Modified excitation-time imaging condition (First-arrival); $\Delta_{s,a} = 2\lambda_{\min}$; 119

8.2.1.23 Case (F); μ_{xx}-image; Modified excitation-time imaging condition (Max-energy arrival); $\Delta_{s,a} = 2.67\lambda_{\min}$; 119

8.2.1.24 Case (F); μ_{xx}-image; Modified excitation-time imaging condition (First-arrival); $\Delta_{s,a} = 2.67\lambda_{\min}$; .119

8.2.1.25 Case (G); μ_{xx}-image; Modified excitation-time imaging condition (Max-energy arrival); Longer data time span;....120

8.2.1.26 Case (G); μ_{xx}-image; Modified excitation-time imaging condition (First-arrival); Longer data time span;....120

8.2.1.27 Case (H); μ_{xx}-image; Modified excitation-time imaging condition (Max-energy arrival); Longer data time span; Modified pristine structure;....120

8.2.1.28 Case (H); μ_{xx}-image; Modified excitation-time imaging condition (First-arrival); Longer data time span; Modified pristine structure;....120

8.2.1.29 Case (I); μ_{xx}-image; Modified excitation-time imaging condition (Max-energy arrival); E_y^d; Modified pristine structure;....120

8.2.1.30 Case (I); μ_{xx}-image; Modified excitation-time imaging condition (First-arrival); E_y^d; Modified pristine structure;....120

8.2.2.1 Case (A); $E_{y;scat}^{BP}$-image obtained by poststack Born imaging;....123

8.2.2.2 Case (A); $H_{x;scat}^{BP}$-image obtained by poststack Born imaging;....123

8.2.2.3 Case (A); $H_{z;scat}^{BP}$-image obtained by poststack Born imaging;....123

8.2.2.4 Case (B); $E_{y;scat}^{BP}$-image obtained by poststack Born imaging; 123

8.2.2.5 Case (B); $H_{x;scat}^{BP}$-image obtained by poststack Born imaging;....123

8.2.2.6 Case (B); $H_{z;scat}^{BP}$-image obtained by poststack Born imaging;....123

8.2.2.7 Case (C); $E_{y;scat}^{BP}$-image obtained by poststack Born imaging; 123

8.2.2.8 Case (C); $H_{x;scat}^{BP}$-image obtained by poststack Born imaging;....123

8.2.2.9 Case (C); $H_{z;scat}^{BP}$-image obtained by poststack Born imaging;....123

8.2.2.10 Case (D); $H_{x;scat}^{BP}$-image obtained by poststack Born imaging; Noisy data SNR=5;....123

8.2.2.11 Case (E); $H_{x;scat}^{BP}$-image obtained by poststack Born imaging; $\Delta = \lambda_{\min}$;....123

8.2.2.12 Case (F); $H_{x;scat}^{BP}$ -image obtained by poststack Born imaging; $\Delta = 1.33\lambda_{\min}$; 123

8.2.2.13 Case (G); $H_{z;scat}^{BP}$ -image obtained by poststack Born imaging; Longer data time span;.....124

8.2.2.14 Case (H); $H_{z;scat}^{BP}$ -image obtained by poststack Born imaging; Longer data time span; Modified pristine structure;.....124

8.2.2.15 Case (I); $H_{z;scat}^{BP}$ -image obtained by poststack Born imaging; E_y^d ; Modified pristine structure;.....124

8.2.3.1 Case (A); ε_{yy} -image; Both $G_{yy;b}^{EJ}$ and $\dot{E}_{y;inc}$ are approximated based on maximum-energy arrival criterion; Without amplitude; 127

8.2.3.2 Case (A); ε_{yy} -image; Both $G_{yy;b}^{EJ}$ and $\dot{E}_{y;inc}$ are approximated based on maximum-energy arrival criterion; With amplitude;.....127

8.2.3.3 Case (A); ε_{yy} -image; Both $G_{yy;b}^{EJ}$ and $\dot{E}_{y;inc}$ are approximated based on first-arrival criterion; Without amplitude; 127

8.2.3.4 Case (A); ε_{yy} -image; Both $G_{yy;b}^{EJ}$ and $\dot{E}_{y;inc}$ are approximated based on first-arrival criterion; With amplitude; 127

8.2.3.5 Case (A); μ_{xx} -image; Both $G_{xy;b}^{HJ}$ and $\dot{H}_{x;inc}$ are approximated based on maximum-energy arrival criterion; With amplitude;.....127

8.2.3.6 Case (A); μ_{xx} -image; Both $G_{xy;b}^{HJ}$ and $\dot{H}_{x;inc}$ are approximated based on first-arrival criterion; With amplitude; 127

8.2.3.7 Case (A); μ_{zz} -image; Both $G_{zy;b}^{HJ}$ and $\dot{H}_{z;inc}$ are approximated based on maximum-energy arrival criterion; With amplitude;.....127

8.2.3.8 Case (A); μ_{zz} -image; Both $G_{zy;b}^{HJ}$ and $\dot{H}_{z;inc}$ are approximated based on first-arrival criterion; With amplitude; 127

8.2.3.9 Case (A); σ_{yy} -image; Both $G_{yy;b}^{EJ}$ and $E_{y;inc}$ are approximated based on maximum-energy arrival criterion; With amplitude;.....127

8.2.3.10 Case (A); σ_{yy} -image; Both $G_{yy;b}^{EJ}$ and $E_{y;inc}$ are approximated based on first-arrival criterion; With amplitude; 127

8.2.3.11 Case (B); μ_{xx} -image; Both $G_{xx;b}^{HM}$ and $\dot{H}_{x;inc}$ are approximated based on maximum-energy arrival criterion; With amplitude;.....127

8.2.3.12 Case (B); μ_{xx} -image; Both $G_{xx;b}^{HM}$ and $\dot{H}_{x;inc}$ are approximated based on first-arrival criterion; With amplitude; 127

8.2.3.13 Case (C); μ_{xx} -image; Both $G_{xx;b}^{HM}$ and $\dot{H}_{x;inc}$ are approximated based on maximum-energy arrival criterion; With amplitude;.....128

8.2.3.14 Case (C); μ_{xx}-image; Both $G^{HM}_{xx;b}$ and $\dot{H}_{x;inc}$ are approximated based on first-arrival criterion; With amplitude; 128

8.2.3.15 Case (D); μ_{xx}-image; Both $G^{HJ}_{xy;b}$ and $\dot{H}_{x;inc}$ are approximated based on maximum-energy arrival criterion; With amplitude; Noisy data SNR=5; 128

8.2.3.16 Case (D); μ_{xx}-image; Both $G^{HJ}_{xy;b}$ and $\dot{H}_{x;inc}$ are approximated based on first-arrival criterion; With amplitude; Noisy data SNR=5;.....128

8.2.3.17 Case (E); μ_{xx}-image; Both $G^{HJ}_{xy;b}$ and $\dot{H}_{x;inc}$ are approximated based on maximum-energy arrival criterion; With amplitude; $\Delta_{s,a} = 2\,\lambda_{\min}$; 128

8.2.3.18 Case (E); μ_{xx}-image; Both $G^{HJ}_{xy;b}$ and $\dot{H}_{x;inc}$ are approximated based on first-arrival criterion; With amplitude; $\Delta_{s,a} = 2\,\lambda_{\min}$; 128

8.2.3.19 Case (F); μ_{xx}-image; Both $G^{HJ}_{xy;b}$ and $\dot{H}_{x;inc}$ are approximated based on maximum-energy arrival criterion; With amplitude; $\Delta_{s,a} = 2.67\,\lambda_{\min}$;.....128

8.2.3.20 Case (F); μ_{xx}-image; Both $G^{HJ}_{xy;b}$ and $\dot{H}_{x;inc}$ are approximated based on first-arrival criterion; With amplitude; $\Delta_{s,a} = 2.67\,\lambda_{\min}$; 128

8.2.3.21 Case (G); μ_{xx}-image; Both $G^{HM}_{xx;b}$ and $\dot{H}_{x;inc}$ are approximated based on maximum-energy arrival criterion; With amplitude; Longer data time span; 128

8.2.3.22 Case (G); μ_{xx}-image; Both $G^{HM}_{xx;b}$ and $\dot{H}_{x;inc}$ are approximated based on first-arrival criterion; With amplitude; Longer data time span;.....128

8.2.3.23 Case (H); μ_{xx}-image; Both $G^{HM}_{xx;b}$ and $\dot{H}_{x;inc}$ are approximated based on maximum-energy arrival criterion; With amplitude; Longer data time span; Modified pristine structure;.....129

8.2.3.24 Case (H); μ_{xx}-image; Both $G^{HM}_{xx;b}$ and $\dot{H}_{x;inc}$ are approximated based on first-arrival criterion; With amplitude; Longer data time span; Modified pristine structure; 129

8.2.3.25 Case (I); μ_{xx}-image; Both $G^{HM}_{xx;b}$ and $\dot{H}_{x;inc}$ are approximated based on maximum-energy arrival criterion; With amplitude; E^d_y; Modified pristine structure; 129

8.2.3.26 Case (I); μ_{xx}-image; Both $G^{HM}_{xx;b}$ and $\dot{H}_{x;inc}$ are approximated based on first-arrival criterion; With amplitude; E^d_y; Modified pristine structure;.....129

8.2.4.1 Case (A); ε_{yy}-image; Zero-lag cross-correlation imaging condition; 132

8.2.4.2 Case (A); ε_{yy}-image; Excitation-time imaging condition (Max-energy arrival); 132

8.2.4.3 Case (A); ε_{yy}-image; Modified excitation-time imaging condition (Max-energy arrival);.....132

8.2.4.4 Case (A); ε_{yy}-image; Excitation-time imaging condition (First-arrival);.....132

8.2.4.5 Case (A); ε_{yy}-image; Modified excitation-time imaging condition (First-arrival); 132

8.2.4.6 Case (A); μ_{xx}-image; Zero-lag cross-correlation imaging condition;.....132

8.2.4.7 Case (A); μ_{xx}-image; Modified excitation-time imaging condition (Max-energy arrival);.....132

8.2.4.8 Case (A); μ_{xx}-image; Modified excitation-time imaging condition (First-arrival);.....132

8.2.4.9 Case (A); μ_{zz}-image; Zero-lag cross-correlation imaging condition;.....133

8.2.4.10 Case (A); μ_{zz}-image; Modified excitation-time imaging condition (Max-energy arrival);.....133

8.2.4.11 Case (A); μ_{zz}-image; Modified excitation-time imaging condition (First-arrival);.....133

8.2.4.12 Case (A); σ_{yy}-image; Zero-lag cross-correlation imaging condition;.....133

8.2.4.13 Case (A); σ_{yy}-image; Modified excitation-time imaging condition (Max-energy arrival); 133

8.2.4.14 Case (A); σ_{yy}-image; Modified excitation-time imaging condition (First-arrival);.....133

8.2.4.15 Case (B); μ_{xx}-image; Modified excitation-time imaging condition (Max-energy arrival); Data treated as sources;.....133

8.2.4.16 Case (B); μ_{xx}-image; Modified excitation-time imaging condition (First-arrival); Data treated as sources; 133

8.2.4.17 Case (B); μ_{zz}-image; Modified excitation-time imaging condition (Max-energy arrival); Data treated as sources;.....133

8.2.4.18 Case (B); μ_{zz}-image; Modified excitation-time imaging condition (First-arrival); Data treated as sources; 133

8.2.4.19 Case (C); μ_{xx}-image; Modified excitation-time imaging condition (Max-energy arrival); Only $E^d_{y;scat}$ as BC; 133

8.2.4.20 Case (C); μ_{xx}-image; Modified excitation-time imaging condition (First-arrival); Only $E^d_{y;scat}$ as BC; 133

8.2.4.21 Case (D); μ_{xx}-image; Modified excitation-time imaging condition (Max-energy arrival); Only $H^d_{x;scat}$ as BC;.....134

8.2.4.22 Case (D); μ_{xx}-image; Modified excitation-time imaging condition (First-arrival); Only $H^d_{x;scat}$ as BC; 134

8.2.4.23 Case (E); μ_{xx}-image; Modified excitation-time imaging condition (Max-energy arrival); Noisy data SNR=5; 134

8.2.4.24 Case (E); μ_{xx}-image; Modified excitation-time imaging condition (First-arrival); Noisy data SNR=5; 134

8.2.4.25 Case (F); μ_{xx}-image; Modified excitation-time imaging condition (Max-energy arrival); $\Delta_{s,a} = 2\,\lambda_{\min}$;....134

8.2.4.26 Case (F); μ_{xx}-image; Modified excitation-time imaging condition (First-arrival); $\Delta_{s,a} = 2\,\lambda_{\min}$;....134

8.2.4.27 Case (G); μ_{xx}-image; Modified excitation-time imaging condition (Max-energy arrival); $\Delta_{s,a} = 2.67\,\lambda_{\min}$;....134

8.2.4.28 Case (G); μ_{xx}-image; Modified excitation-time imaging condition (First-arrival); $\Delta_{s,a} = 2.67\,\lambda_{\min}$;....134

8.2.4.29 Case (H); μ_{xx}-image; Modified excitation-time imaging condition (Max-energy arrival); Longer data time span;....134

8.2.4.30 Case (H); μ_{xx}-image; Modified excitation-time imaging condition (First-arrival); Longer data time span;....134

8.2.4.31 Case (I); μ_{xx}-image; Modified excitation-time imaging condition (Max-energy arrival); Longer data time span; Modified pristine structure; 134

8.2.4.32 Case (I); μ_{xx}-image; Modified excitation-time imaging condition (First-arrival); Longer data time span; Modified pristine structure;....134

8.2.4.33 Case (J); μ_{xx}-image; Modified excitation-time imaging condition (Max-energy arrival); E_y^d and H_x^d; Modified pristine structure; 135

8.2.4.34 Case (J); μ_{xx}-image; Modified excitation-time imaging condition (First-arrival); E_y^d and H_x^d; Modified pristine structure;....135

8.2.5.1 Case (A); $E^m_{y;scat}$-image obtained by poststack EM migration;....138

8.2.5.2 Case (A); $H^m_{x;scat}$-image obtained by poststack EM migration; 138

8.2.5.3 Case (A); $H^m_{z;scat}$-image obtained by poststack EM migration; 138

8.2.5.4 Case (B); $E^m_{y;scat}$-image obtained by poststack EM migration; Data treated as sources; 138

8.2.5.5 Case (B); $H^m_{x;scat}$-image obtained by poststack EM migration; Data treated as sources;....138

8.2.5.6 Case (B); $H^m_{z;scat}$-image obtained by poststack EM migration; Data treated as sources;....138

8.2.5.7 Case (C); $E^{m}_{y;scat}$ -image obtained by poststack EM migration; Only $E^{d}_{y;scat}$ as BC's; 138

8.2.5.8 Case (C); $H^{m}_{x;scat}$ -image obtained by poststack EM migration; Only $E^{d}_{y;scat}$ as BC's;.....138

8.2.5.9 Case (C); $H^{m}_{z;scat}$ -image obtained by poststack EM migration; Only $E^{d}_{y;scat}$ as BC's;.....138

8.2.5.10 Case (D); $E^{m}_{y;scat}$ -image obtained by poststack EM migration; Only $H^{d}_{x;scat}$ as BC's; 138

8.2.5.11 Case (D); $H^{m}_{x;scat}$ -image obtained by poststack EM migration; Only $H^{d}_{x;scat}$ as BC's;.....139

8.2.5.12 Case (D); $H^{m}_{z;scat}$ -image obtained by poststack EM migration; Only $H^{d}_{x;scat}$ as BC's;.....139

8.2.5.13 Case (E); $H^{m}_{x;scat}$ -image obtained by poststack EM migration; Noisy data SNR=5; 139

8.2.5.14 Case (F); $H^{m}_{x;scat}$ -image obtained by poststack EM migration; $\Delta = \lambda_{\min}$; 139

8.2.5.15 Case (G); $H^{m}_{x;scat}$ -image obtained by poststack EM migration; $\Delta = 1.33\lambda_{\min}$;.....139

8.2.5.16 Case (H); $H^{m}_{x;scat}$ -image obtained by poststack EM migration; Longer data time span; 139

8.2.5.17 Case (I); $H^{m}_{x;scat}$ -image obtained by poststack EM migration; Longer data time span; Modified pristine structure;.....139

8.2.5.18 Case (J); $H^{m}_{x;scat}$ -image obtained by poststack EM migration; E^{d}_{y} and H^{d}_{x} ; Modified pristine structure; 139

8.2.6.1 Case (A); ε_{yy} -image; All $G^{EM}_{yx;b}$, $G^{EJ}_{yy;b}$, and $\dot{E}_{y;inc}$ are approximated based on maximum-energy arrival criterion; Without amplitude; 142

8.2.6.2 Case (A); ε_{yy} -image; All $G^{EM}_{yx;b}$, $G^{EJ}_{yy;b}$, and $\dot{E}_{y;inc}$ are approximated based on maximum-energy arrival criterion; With amplitude; 142

8.2.6.3 Case (A); ε_{yy} -image; All $G^{EM}_{yx;b}$, $G^{EJ}_{yy;b}$, and $\dot{E}_{y;inc}$ are approximated based on first-arrival criterion; Without amplitude; 142

8.2.6.4 Case (A); ε_{yy} -image; All $G^{EM}_{yx;b}$, $G^{EJ}_{yy;b}$, and $\dot{E}_{y;inc}$ are approximated based on first-arrival criterion; With amplitude; 142

8.2.6.5 Case (A); μ_{xx} -image; All $G^{HJ}_{xy;b}$, $G^{HM}_{xx;b}$, and $\dot{H}_{x;inc}$ are approximated based on maximum-energy arrival criterion; With amplitude; 142

8.2.6.6 Case (A); μ_{xx} -image; All $G^{HJ}_{xy;b}$, $G^{HM}_{xx;b}$, and $\dot{H}_{x;inc}$ are approximated based on first-arrival criterion; With amplitude; 142

8.2.6.7 Case (A); μ_{zz} -image; All $G^{HJ}_{zy;b}$, $G^{HM}_{zx;b}$, and $\dot{H}_{z;inc}$ are approximated based on maximum-energy arrival criterion; With amplitude; 142

8.2.6.8 Case (A); μ_{zz}-image; All $G^{HJ}_{zy;b}$, $G^{HM}_{zx;b}$, and $\dot{H}_{z;inc}$ are approximated based on first-arrival criterion; With amplitude;.....142

8.2.6.9 Case (A); σ_{yy}-image; All $G^{EM}_{yx;b}$, $G^{EJ}_{yy;b}$, and $E_{y;inc}$ are approximated based on maximum-energy arrival criterion; With amplitude;.....142

8.2.6.10 Case (A); σ_{yy}-image; All $G^{EM}_{yx;b}$, $G^{EJ}_{yy;b}$, and $E_{y;inc}$ are approximated based on first-arrival criterion; With amplitude;.....142

8.2.6.11 Case (B); μ_{xx}-image; Both $G^{HM}_{xx;b}$ and $\dot{H}_{x;inc}$ are approximated based on maximum-energy arrival criterion; With amplitude; Only $E^{d}_{y;scat}$;.....143

8.2.6.12 Case (B); μ_{xx}-image; Both $G^{HM}_{xx;b}$ and $\dot{H}_{x;inc}$ are approximated based on first-arrival criterion; With amplitude; Only $E^{d}_{y;scat}$;.....143

8.2.6.13 Case (C); μ_{xx}-image; Both $G^{HJ}_{xy;b}$ and $\dot{H}_{x;inc}$ are approximated based on maximum-energy arrival criterion; With amplitude; Only $H^{d}_{x;scat}$;.....143

8.2.6.14 Case (C); μ_{xx}-image; Both $G^{HJ}_{xy;b}$ and $\dot{H}_{x;inc}$ are approximated based on first-arrival criterion; With amplitude; Only $H^{d}_{x;scat}$;.....143

8.2.6.15 Case (D); μ_{xx}-image; All $G^{HJ}_{xy;b}$, $G^{HM}_{xx;b}$, and $\dot{H}_{x;inc}$ are approximated based on maximum-energy arrival criterion; With amplitude; Noisy data SNR=5;.....143

8.2.6.16 Case (D); μ_{xx}-image; All $G^{HJ}_{xy;b}$, $G^{HM}_{xx;b}$, and $\dot{H}_{x;inc}$ are approximated based on first-arrival criterion; With amplitude; Noisy data SNR=5;.....143

8.2.6.17 Case (E); μ_{xx}-image; All $G^{HJ}_{xy;b}$, $G^{HM}_{xx;b}$, and $\dot{H}_{x;inc}$ are approximated based on maximum-energy arrival criterion; With amplitude; $\Delta_{s,a} = 2\,\lambda_{\min}$;.....143

8.2.6.18 Case (E); μ_{xx}-image; All $G^{HJ}_{xy;b}$, $G^{HM}_{xx;b}$, and $\dot{H}_{x;inc}$ are approximated based on first-arrival criterion; With amplitude; $\Delta_{s,a} = 2\,\lambda_{\min}$;.....143

8.2.6.19 Case (F); μ_{xx}-image; All $G^{HJ}_{xy;b}$, $G^{HM}_{xx;b}$, and $\dot{H}_{x;inc}$ are approximated based on maximum-energy arrival criterion; With amplitude; $\Delta_{s,a} = 2.67\,\lambda_{\min}$;.....143

8.2.6.20 Case (F); μ_{xx}-image; All $G^{HJ}_{xy;b}$, $G^{HM}_{xx;b}$, and $\dot{H}_{x;inc}$ are approximated based on first-arrival criterion; With amplitude; $\Delta_{s,a} = 2.67\,\lambda_{\min}$;.....143

8.2.6.21 Case (G); μ_{xx}-image; All $G^{HJ}_{xy;b}$, $G^{HM}_{xx;b}$, and $\dot{H}_{x;inc}$ are approximated based on maximum-energy arrival criterion; With amplitude; Longer data time span;.....144

8.2.6.22 Case (G); μ_{xx}-image; All $G^{HJ}_{xy;b}$, $G^{HM}_{xx;b}$, and $\dot{H}_{x;inc}$ are approximated based on first-arrival criterion; With amplitude; Longer data time span;.....144

8.2.6.23 Case (H); μ_{xx}-image; All $G_{xy;b}^{HJ}$, $G_{xx;b}^{HM}$, and $\dot{H}_{x;inc}$ are approximated based on maximum-energy arrival criterion; With amplitude; Longer data time span; Modified pristine structure;.....144

8.2.6.24 Case (H); μ_{xx}-image; All $G_{xy;b}^{HJ}$, $G_{xx;b}^{HM}$, and $\dot{H}_{x;inc}$ are approximated based on first-arrival criterion; With amplitude; Longer data time span; Modified pristine structure; 144

8.2.6.25 Case (I); μ_{xx}-image; All $G_{xy;b}^{HJ}$, $G_{xx;b}^{HM}$, and $\dot{H}_{x;inc}$ are approximated based on maximum-energy arrival criterion; With amplitude; E_y^d and H_x^d; Modified pristine structure;.....144

8.2.6.26 Case (I); μ_{xx}-image; All $G_{xy;b}^{HJ}$, $G_{xx;b}^{HM}$, and $\dot{H}_{x;inc}$ are approximated based on first-arrival criterion; With amplitude; E_y^d and H_x^d; Modified pristine structure; 144

Introduction

The integrity of structures such as aircrafts, bridges, and dams needs to be monitored to avoid unexpected failures. In order to ensure both safety and functionality of these structures and prevent their failures, it is crucial to continuously monitor their condition and detect the presence, the location, and the extent of damages as they occur. Proper corrective actions can then be taken to temporarily mitigate the effects of such damages until structures can be repaired.

Periodic inspections or scheduled maintenance using conventional nondestructive evaluation/inspection (NDE/NDI) techniques require extensive labor, cause downtime, and are expensive. Most inspection techniques such as conventional ultrasonic or eddy currents need a transducer to be scanned point-by-point over the structure under inspection which is a time-consuming process. Moreover, for structural components that are hard to inspect, disassembly of the structure may be necessary (Krautkramer and Krautkramer, 1990 and Bray and McBride, 1992).

The essence of structural health monitoring (SHM) technology is to develop autonomous built-in systems for the continuous (or on-demand) monitoring, inspection, and damage detection of structures with minimum labor involvement (Chang, 1997). The potential benefits from a structural health monitoring system (SHMS) are enormous such as real-time monitoring and reporting, saving in maintenance cost, reducing labor, downtime and human error, and improving safety and reliability. Typically, such a built-in diagnostic system, in addition to the structures to be monitored, would include two major components: a built-in network of sensors for collecting sensor data and damage identification software for interpretation of the sensor data in terms of the physical condition of the structures. The diagnostic systems available for SHM can be broadly classified based on sensor functionality: passive sensing system without known inputs (sensors only) and active sensing system with known inputs (both sensors and actuators). A passive system uses sensors such as MEMS, fiber optics, strain gages, piezoelectrics, and accelerometers to continuously “listen” for characteristic signals from the structure due to external impact events, damage evolution, the change in environmental conditions in terms of loads, temperature, chemistry,

and etc. The most significant passive sensing systems are acoustic emission, strain/loads monitoring, and frequency response methods. Along with the sensors, an active system is also equipped with actuators to generate selected diagnostic (excitation) signals to interrogate the "health" status of the structures. In general, a passive system is used to monitor the condition and/or detect the damages of the structures; while an active system is targeted to identify the location and the nature of the damages of individual components of the structures.

SHM systems can also be broadly classified into two categories: (i) global methods that infer or assess the state of a structure from its overall modal response; and (ii) local methods that monitor the material degradation (property changes, flaws, etc.) at critical areas of the structure (Johnson *et al.*, 2004). The global methods are attractive primarily because they only need fewer sensors, thus cost effective, but their sensitivity to the damage is low. While the local methods are more sensitive to localized damages and can provide more quantitative information. It should be pointed out that the so-called vibration-based SHM systems fall into the global SHM systems. A local SHMS using actuators and sensors for active sensing is studied in this dissertation.

Generally, the excitation signal (wave) in an active SHMS can be mechanical or non-mechanical. Mechanical signals, such as acoustic and ultrasonic (frequency > 20 kHz), are those in which a mechanical medium (i.e., solid, fluid, or gas) is required for wave propagation. In contrast, non-mechanical signals, such as electromagnetic (EM), can propagate in any medium including vacuum, thereby enabling non-contact diagnosis. It is worth mentioning that radio waves, microwaves, infrared light, visible light, ultraviolet light, X-rays, and γ-rays reflect different regions of the EM spectrum. However, in this study, "EM waves" will imply the microwave region of the EM spectrum, generally between a few hundred MHz and a few hundred GHz (Bahr, 1995). It should be noted that various types of excitation signals with different waveforms may provide different degrees of sensitivities to a specific type of damage in a structure. This is because the sensor response from a specified excitation signal generally depends on the interaction between the sensor/actuator and the host structure, the material properties of the structure through which the signal propagates, and the damage mechanisms.

Regarding the sensitivity of mechanical and non-mechanical waves in detecting the damages, Lemistre and Balageas (2004) showed that low-frequency electromagnetic waves (~ 700 kHz) were more sensitive to damages generated by aggressions such as burning, lightning, and liquid ingress in graphite/epoxy composites where the electrical properties show a large contrast in the damage regions; ultrasonic waves (~ 400 kHz) more sensitive to delaminations due to impact. Büyüköztürk (1998) concluded that imaging methods using microwaves were effective in locating and imaging rebars, cracks, and voids in concrete structures. However, microwaves experience high attenuation in moisture, and total reflection from metals which makes it difficult to image areas beneath closely spaced rebars. In contrast, ultrasonic waves are not affected by the presence of reinforcements and moisture, but they suffer high attenuation for the size of inhomogeneities comparable to the excitation wavelength due to wave scattering (Iyer *et al*., 2005). Zoghi (2000) and Liu and Bethesda (1998) also showed that the ultrasonic wave might not be a good option for NDE of thick, multilayered composite structures specially when composites were made of porous, coarse grained, low-permittivity or low-loss dielectric materials such as glass/epoxy composites, commonly used for ship-hall and masts in marine environments. The high attenuation of ultrasonic signals in such materials dictates the application of relatively low excitation frequency in order to obtain the required penetration depth, thereby reducing image resolution. On the contrary, EM waves can penetrate deep inside these materials and interact with their inner structure without suffering from high attenuation. A reverse situation occurs with conductive materials (e.g., metals) or non-perfectly conductive materials (e.g., graphite/epoxy composites) where the high attenuation of EM waves forces the use of relatively low excitation frequency, leading to a poor depth resolution of the image.

Having considered the above arguments, to ensure the identification of all types of damages in a structure, different types of excitation signals (i.e. mechanical and non-mechanical) should be employed for monitoring the structure (Lemistre and Balageas, 2004). While mechanical waves have been widely used in SHMS, the usage of EM waves has been very limited. In order to show the salient features of EM waves in providing high-resolution image of damages specially in dielectric structures, complement to the mechanical waves, the application of EM waves will be investigated in this study.

The damage characterization plays a major role in quantifying the damage in SHMS and can be regarded as the brain of the system. Mathematically speaking, determination of the physical condition of a structure based on sensor data is an inverse problem. Typically, such inverse problem is both *nonlinear* and *ill-posed*. By ill-posedness, in the sense of Hadamard (Hadamard, 1923), it is meant that one of the following conditions is violated: the existence of the solution; the uniqueness of the solution; or the continuous dependence of the solution on the data (stability condition). The uniqueness condition is generally violated because complete data collection from limited number of sensors is not practically feasible in SHM. In addition, the instability refers to the sensitivity of the solution to noise and measurement errors (Haykin, 1999). Regularization techniques are usually used to handle the ill-posedness of inverse problems.

In terms of the type of the model being inverted to determine the physical conditions of the structure, an inverse scattering problem is often classified into *inverse medium problem* and *inverse obstacle problem*. In inverse medium problem, one attempts to reconstruct the material properties of a scatterer (damage) inside a host structure. On the other hand, in inverse obstacle problem, the goal is to merely reconstruct the shape (geometry) of the scatterer: reconstruction of the material properties is of secondary importance.

The methodologies available for solving inverse scattering problems can be categorized roughly into three different classes: I) *Nonlinear inversion methods*; II) *Linearized inversion methods*; III) *Linearized imaging methods*.

I) Nonlinear inversion methods

A rational way to solve the nonlinear inverse problem is *via* nonlinear inversion methods. These methods attempt to construct a full solution of the inverse problem by sequentially updating a model that can simulate the real structure response. *Born iterative* method (Chaturvedi and Plumb, 1995), *distorted-Born iterative* method (Weedon *et al.*, 2000), *local shape method* (Weedon *et al.*, 2000), *dual-space method* (Colton and Monk, 1994), *gradient-based* methods (Rekanos and Räisänen, 2003, Takenaka *et al.*, 2003, Belkebir *et al.*, 1997, and Tarokh *et al.*, 2004), *contrast source method* (van den Berg and Kleinman, 1997 and Abubakar and van den Berg, 2002), *level-set method* (Ramananjaona *et*

al., 2001), and *genetic algorithms* (Chien *et al*., 2005) are different *iterative* nonlinear inversion methods that have been investigated. These methods are the most accurate methods for solving inverse problems and tolerate irregular and coarse data collection as well. However, they are computationally very intensive and cannot be employed practically in a SHMS. In addition, slow convergence rate and/or convergence to a local minima are some of the important issues that should be carefully considered.

It is worth mentioning that the *linear sampling method* (Colton *et al*., 2003) and its modifications such as *factorization method* (Kirsch, 2004) for shape reconstruction, do not require any iterations in spite of belonging to the nonlinear inversion methods. These methods are computationally efficient, but they have been shown to be very sensitive to incomplete and noisy data (Ramm and Gutman, 2005).

Other nonlinear inversion methods employing *artificial neural network* (Rekanos, 2002) and *support vector machine* (Bermani *et al.*, 2004) concepts have been explored. These methods which require a large amount of training data are computationally efficient for SHM. At present time, their applications have been limited to very simple damage geometries.

Due to the impracticability of employing the nonlinear inversion methods in SHMS, linearized inversion and imaging methods are discussed separately below.

II) Linearized inversion methods

In linearized inversion methods, an approximation is made that transforms the full nonlinear inverse scattering problem to a more tractable linear problem. Commonly used approximations are the *Physical Optics* (*PO*) or *Kirchhoff* approximation typically for impenetrable (perfect conductor) scatterers, and the weak scatterer approximations called *Born* and *Rytov* approximations for penetrable (dielectric) scatterers (Büyüköztürk, 1998). While the PO-based linearized inversion methods reconstruct the shape of the scatterer, the methods based on the Born or Rytov approximation can estimate the material properties of the scatterer. It should be pointed out that the linearized inversion methods still remain *ill-posed*, thus an appropriate regularization technique is usually required.

In the EM PO-based method, it is assumed that the total tangential (to the surface) magnetic field is twice the incident tangential magnetic field on the illuminated side of a perfect conductor scatterer and zero on the shadow side (Bojarski, 1982). This approximation yields valid results only for the scatterers that are large compared to the excitation wavelength (i.e., in a high-frequency range) and have convex surfaces (Langenberg, 1989). When a far-field approximation is included in the PO-based inversion methods, the method is called Physical Optics Far-Field Inverse Scattering (POFFIS). Langenberg *et al*. (1997) applied a time-domain EM version of POFFIS to locate metal ducts in reinforced concrete structures. However, the formulation was limited to homogeneous isotropic and lossless structures. Other examples of the PO-based shape reconstruction for perfect conductor and dielectric scatterers embedded in a homogeneous isotropic and lossless structure can be found in Soldovieri *et al*. (2005) and Liseno and Pierri (2004), respectively.

In Born approximation (or distorted Born approximation for inhomogeneous structures), which is the very commonly used weak scatterer approximation, the scattered field inside the scatterer is neglected. Therefore, the linearized inversion methods based on Born approximation can only estimate the material properties of the weak scatterers: when the material properties of the scatterer and the host structure are close and the size of the scatterer is small compared to the excitation wavelength (i.e., in a relatively low-frequency range) (e.g., Leone *et al.*, 1999 and Slaney *et al.*, 1984).

In some special cases, for example, a half-space homogeneous isotropic structure, an *explicit* inversion of the linearized equations can be constructed often with Fourier or related integral transforms. Using fast Fourier transforms in the implementation, this method, so-called *diffraction tomography* (DT), is computationally efficient and quite tolerant to noise and measurement errors (Cui and Chew, 2002). However, most DT algorithms place severe constraints on the sensor configurations, such as the requirement that sensors be uniformly separated by a maximum of one-half excitation wavelength (Kak and Slaney, 1988 and Weedon *et al.*, 2000). Deming and Devaney (1997) mentioned that DT was adequate for quantitatively reconstructing scatterers with roughly 20% contrast, when the size of the scatterer was on the order of an excitation wavelength. In general, as the scatterer size decreases the allowable contrast increases for maintaining similar quality of the

reconstruction. It has been further shown that for strong scatterers, DT can still be used for identifying the location and size of the scatterer (Cui and Chew, 2002). Wang and Oristaglio (2000) developed an *explicit* linearized inversion method utilizing the generalized Radon transform for inhomogeneous isotropic structures. They used geometrical optics (ray theory) approximation for the Green's functions of host structure and far-field approximation in addition to the Born approximation. Unfortunately, the imaging results were not satisfactory.

It is worth mentioning that when the scatterer size is much greater than the excitation wavelength (i.e., in a very high-frequency range), *Computerized Tomography* (CT) method, which is based on geometrical model of radiation propagation, can be employed, e.g., X-ray and ultrasonic CT. However, when the scatterer size is comparable or smaller than the excitation wavelength, diffraction effect becomes significant and ray theory (geometric propagation) based concepts should not be used; instead one must resort directly to wave propagation and diffraction-based phenomena (Kak and Slaney, 1988).

An alternative to the Fourier algorithms of DT is to discretize the linearized integral equations and solve the set of linear algebraic equations numerically, e.g., using a regularized least-squares method. For instance, Barkeshli *et al.* (1992) applied method of moments (MOM) to discretize the linearized integral equations, solved the set of algebraic linear equations by a conjugate gradient algorithm, and presented 3-D images of some flaws in a one-layer graphite/epoxy composite slab. However, this approach, which requires the Green's functions of the host structure, is not computationally efficient due to the iterative process involved in the solution of the linear algebraic equations. Recently, new linearized inversion techniques based on some modifications on the Born approximation such as *extended Born approximation* (Liu *et al.*, 2002), *modified extended Born approximation* (Tseng *et al.*, 2003), *quasi-analytical approximation* (Zhdanov and Hursan, 2000), *localized quasi-linear approximation* (Zhdanov and Tartaras, 2002), and *modified quasi-linear approximation* (Zhou and Liu, 2000), have been reported. Although these methods are more accurate than the Born approximation-based methods in terms of material properties estimation, they are more computationally intensive.

Although the determination of damaged material properties using the above methods is desirable, identifying the shape of damages with computationally efficient algorithms is the

primary and minimum practical goal of a SHMS. As such, linearized imaging methods should be employed.

III) Linearized imaging methods

Linearized imaging methods can only provide the geometries of damages in a structure, sufficient for SHM application. A very important advantage of these methods is that unlike linearized inversion methods, they are well-posed. *Holographic imaging methods*, *synthetic aperture focusing techniques* (*SAFT*), *migration algorithms*, and *time-reversal* (*TR*) *techniques* mentioned in the literature all belong to this category of linearized imaging methods.

Langenberg *et al.* (1986) showed that the images obtained from both conventional and generalized holography are poor solutions to the inverse scattering problem. Kim *et al.* (2004) adopted a holographic technique to identify different damages in concrete slabs. Guo *et al.* (1998) also developed a near-field holographic algorithm to locate highly conducting small buried objects such as mines. However, both approaches were limited to homogeneous isotropic structures.

Johansson and Mast (1994) employed a SAFT algorithm in time-domain to construct 3-D images of different flaws and rebars in a concrete slab. Although the method was capable of handling layered structures, the polarization (vector) characteristic of EM waves was not utilized and also the quality of the resulting images was not satisfactory. Fear *et al.* (2002) presented a *confocal microwave imaging technique* for breast cancer detection which is conceptually similar to time-domain SAFT. Marklein *et al.* (2002) also mentioned that SAFT might be extended to EM vector fields and inhomogeneous anisotropic structures.

Migration algorithms, widely used in seismic prospecting and geophysical exploration, have also been used in EM applications such as ground penetration radar (GPR) and electromagnetic induction (EMI). In GPR, used for imaging shallow scatterers (i.e., scatterers close to the ground surface), displacement currents are dominant due to high-frequency of EM field, so the field propagates into the structure, whereas in EMI, used for imaging deep scatterers, conduction currents are dominant due to low-frequency of the EM field, therefore, the field diffuses into the structure. Generally, migration algorithms are

classified into two groups (e.g., Gray, 1999): *poststack migration* (all the data are stacked into a greatly reduced data volume to simulate an ideal zero-offset data before migration) and *prestack migration* (all the data are migrated before the images are stacked to form the final image). Prestack migration is computationally more intensive than poststack migration but provides high fidelity of the image, i.e., image with better resolution and higher signal-to-noise ratio. Migration algorithms can also be performed in different domains such as time-space, frequency-space, and frequency-wavenumber (*f-k*) domains. *Kirchhoff migration* (KM), *f-k migration*, *phase-shift migration*, *one-way finite difference migration*, and *Reverse-time migration* (RTM) are some common types of migration algorithms. Although migration algorithms are well established in acoustic and elastic cases and recently in SHM of plates (e.g., Lin and Yuan, 2005 and Wang and Yuan, 2005), they are not yet fully explored in EM case.

Regarding time-reversal (TR) techniques, they follow the same principles as migration algorithms. Kosmos and Rappaport (2005) simulated the TR technique for breast cancer detection considering a 2-D lossy inhomogeneous breast model and using a minimum entropy criterion for imaging time. Yavuz and Teixeira (2005) also investigated the super-resolution characteristic of the TR technique in a continuous random lossless structure. The technique focused back the received signals generated by a point source and collected by a linear array to the original source position.

In what follows, major studies on different EM migration algorithms are reviewed. The EM migration based on the Maxwell's equations was originally developed by Zhdanov (1988). Zhdanov *et al.* (1996) presented a 2-D one-way finite difference migration in frequency-space domain for EMI applications which was modified later by Peng *et al.* (2001). Zhdanov and Portniaguine (1997) developed time-domain EM migration in both integral equation and differential equation forms for EMI application corresponding to KM and RTM, respectively. Feng and Sato (2004) applied a prestack time-domain KM for landmine detection. However, their method was based on scalar wave equation assumption and inhomogeneity of the host structure was partially taken into account. Zhdanov and Li (1997) and (1998) applied a 2-D prestack RTM for EMI applications. Also, Sanada and Ashida (1998) employed a 2-D poststack RTM for GPR application, but the synthetic zero-

offset data was based on incorrect exploding reflector model. Later, Leuschen and Plumb (2001), introduced a 3-D matched filter-based RTM for GPR application in both poststack and prestack forms. Recently, Di and Wang (2004) used finite element method instead of finite difference in a 2-D RTM for GPR application. Regarding to the *f-k* migration, Büyüköztürk *et al.* (2003) adopted such a method for NDE of fiber-reinforced-plastic-confined concrete using wide-band microwaves, but the method was based on scalar wave equation assumption. Xu *et al*. (2003) introduced an optimized version of *f-k* migration for GPR application that took into account the roughness of air-ground interface and the attenuation of the ground. However, the method was not computationally efficient and it was based on scalar wave equation assumption as well. The method proposed by van der Kruk *et al.* (2003), a 3-D imaging algorithm in a (*f-k*) domain for GPR application, took into account the vectorial characteristics of the EM waves but was limited to half-space homogeneous isotropic structures. It should be mentioned that in all these studies, the case of the anisotropic structures has not been studied.

In this dissertation, the EM migration developed by Zhdanov for geophysical exploration in inhomogeneous isotropic structures is extended to anisotropic structures and used as a damage imaging algorithm for a SHMS.

It has been identified that the standard prestack migration operator can be regarded as the adjoint of the linear forward modeling operator (Claerbout, 1992). Based on this analogy, the adjoint operators for general transient EM fields in an inhomogeneous anisotropic structure are derived, and *Born imaging algorithm* as the second proposed linearized imaging technique is introduced.

In this study, first the two proposed linearized imaging algorithms, EM migration and Born imaging, are formulated in both differential equation (DE) and integral equation (IE) formalisms in time-domain for 3-D damage imaging of inhomogeneous anisotropic and lossy structures. Then, it is shown that by applying proper approximations in the IE formalism of these algorithms, real-time damage imaging algorithms suitable for SHM application can be realized.

This dissertation is divided into several chapters as follows: Chapter 1 begins with the Maxwell's equations, their solutions in terms of dyadic Green's functions and their adjoints. Also, some properties of ordinary and adjoint dyadic Green's functions such as reciprocity relations and time-translation properties are reviewed. To prepare for the modeling the inverse scattering problem, a forward scattering problem of EM waves when a scatterer is embedded in a host structure is described in Chapter 2. In Chapter 3, the inverse scattering problem in its IE formalism is presented. The first proposed imaging algorithm, the EM migration, is formulated in Chapter 4 for general transient EM fields in an anisotropic inhomogeneous structure using two approaches. In Chapter 5, the second proposed imaging algorithm, the Born imaging, is introduced and then its relationship with gradient-based inversion methods is discussed. Imaging steps of the DE and IE formalisms of the algorithms, various approximations with the aim of reducing the computational cost of these algorithms, and advantages and shortcomings of the DE and IE approaches for SHM application are discussed in detail in Chapter 6. In Chapter 7, the imaging algorithms are specialized for 2-D transverse magnetic (TM) waves. The effectiveness of the algorithms for 2-D damage imaging of a reinforced concrete slab and a glass/epoxy composite plate with multiple damages is demonstrated in Chapter 8.

In this simulated study, a finite difference time-domain method has been used to generate all sensor data, incident field, the fields associated with the Green's functions of the pristine structure, and back-propagated (migrated) scattered field.

1. Fundamental Equations

This chapter briefly describes the fundamental equations: Maxwell's equations, their fundamental solutions in terms of dyadic Green's functions, their adjoints, and reciprocity relations. Some of the details can be found in Felsen and Marcuvitz (1994).

The Maxwell's equations in the differential representation, including both external electric and magnetic current sources, are expressed by (Balanis, 1989):

$$\nabla \times \boldsymbol{E} = -\frac{\partial \boldsymbol{B}}{\partial t} - \boldsymbol{M} \tag{1.1}$$

$$\nabla \times \boldsymbol{H} = \boldsymbol{J}_C + \frac{\partial \boldsymbol{D}}{\partial t} + \boldsymbol{J} \tag{1.2}$$

$$\nabla \cdot \boldsymbol{B} = \rho_i^H \tag{1.3}$$

$$\nabla \cdot \boldsymbol{D} = \rho_i^E + \rho_C^E = \rho^E \tag{1.4}$$

where

$\boldsymbol{E}$ ≡ electric field intensity (Volts/meter)
$\boldsymbol{H}$ ≡ magnetic field intensity (Amperes/meter)
$\boldsymbol{D}$ ≡ electric flux density or electric displacement (Coulombs/meter^2)
$\boldsymbol{B}$ ≡ magnetic flux density (Webers/meter^2)
$\boldsymbol{M}$ ≡ prescribed (source) magnetic current density (Volts/meter^2)
$\boldsymbol{J}_C$ ≡ conduction electric current density (Amperes/meter^2)
$\boldsymbol{J}$ ≡ prescribed (source) electric current density (Amperes/meter^2)
ρ^E ≡ total electric charge density (Coulombs/meter^3)
ρ_i^E ≡ prescribed electric charge density (Coulombs/meter^3)
ρ_C^E ≡ conduction electric charge density (Coulombs/meter^3)
ρ_i^H ≡ prescribed magnetic charge density (Webers/meter^3)

In addition, the continuity equations governing the conservation law of charges are:

$$\nabla \cdot \boldsymbol{J} = -\frac{\partial \rho_i^E}{\partial t} \tag{1.5}$$

$$\nabla \cdot \boldsymbol{J}_C = -\frac{\partial \rho_C^E}{\partial t} \tag{1.6}$$

$$\nabla \cdot \boldsymbol{M} = -\frac{\partial \rho_i^H}{\partial t} \tag{1.7}$$

For a time-varying EM field, Eq. (1.3) and (1.4) can be derived from Eq. (1.1), (1.2) *via* the continuity equations (1.5) – (1.7). For example, taking the divergence of (1.1) and using the continuity equation (1.7) lead to Eq. (1.3). Since only two of the four Maxwell's equations are independent in electrodynamics, Eq. (1.1) and (1.2) are sufficient to work with. However, there are five vector unknowns, $\boldsymbol{E}, \boldsymbol{H}, \boldsymbol{B}, \boldsymbol{D}$ and $\boldsymbol{J}_C$, with only two vector equations, Eq. (1.1) and (1.2). For a linear, time-invariant, instantaneously reacting, inhomogeneous anisotropic medium, the constitutive relations are:

$$\begin{aligned} \boldsymbol{D}(\boldsymbol{r},t) &= \boldsymbol{\varepsilon}(\boldsymbol{r}) \cdot \boldsymbol{E}(\boldsymbol{r},t) \\ \boldsymbol{B}(\boldsymbol{r},t) &= \boldsymbol{\mu}(\boldsymbol{r}) \cdot \boldsymbol{H}(\boldsymbol{r},t) \\ \boldsymbol{J}_C(\boldsymbol{r},t) &= \boldsymbol{\sigma}(\boldsymbol{r}) \cdot \boldsymbol{E}(\boldsymbol{r},t) \end{aligned} \tag{1.8}$$

where $\boldsymbol{\sigma}(\boldsymbol{r})$, $\boldsymbol{\varepsilon}(\boldsymbol{r})$, and $\boldsymbol{\mu}(\boldsymbol{r})$ are conductivity, permittivity, and permeability tensors, respectively. Then, Eq. (1.1) and (1.2) using Eq. (1.8) become:

$$\begin{cases} \nabla \times \boldsymbol{E}(\boldsymbol{r},t) = -\boldsymbol{\mu}(\boldsymbol{r}) \cdot \dot{\boldsymbol{H}}(\boldsymbol{r},t) - \boldsymbol{M}(\boldsymbol{r},t) \\ \nabla \times \boldsymbol{H}(\boldsymbol{r},t) = \boldsymbol{\sigma}(\boldsymbol{r}) \cdot \boldsymbol{E}(\boldsymbol{r},t) + \boldsymbol{\varepsilon}(\boldsymbol{r}) \cdot \dot{\boldsymbol{E}}(\boldsymbol{r},t) + \boldsymbol{J}(\boldsymbol{r},t) \end{cases} \tag{1.9}$$

where the dot denotes partial derivative with respect to time.

For uniqueness of the fields $\boldsymbol{E}$ and $\boldsymbol{H}$, it is required that the excitations $\boldsymbol{J}$ and $\boldsymbol{M}$ vanish for $t < t_1$ and the fields satisfy the initial (causality) condition, i.e., $\boldsymbol{E} = 0 = \boldsymbol{H}$ for $t \le t_1$, and the appropriate boundary conditions.

In the following, the derived relations will be based on Eq. (1.9).

One way to represent the response of a linear system such as Eq. (1.9) to arbitrary sources is using the point source response or Green's function approach. Regarding to Eq. (1.9), four different dyadic Green's functions need to be introduced. Note that a dyad is the juxtaposition of two vectors $\mathbf{D} = \boldsymbol{AB}$ defined by $\mathbf{D} \cdot \boldsymbol{C} = \boldsymbol{A}(\boldsymbol{B} \cdot \boldsymbol{C})$ and $\boldsymbol{C} \cdot \mathbf{D} = (\boldsymbol{C} \cdot \boldsymbol{A})\boldsymbol{B}$, where $\mathbf{D}$ is a dyad and $\boldsymbol{A}$, $\boldsymbol{B}$, and $\boldsymbol{C}$ are vectors. In fact, a dyadic Green's function is a dyad that relates a vector electric or magnetic field to a vector current source. Therefore, the

corresponding dyadic Green's functions assume the following forms (Oristaglio and Blok, 1994):

$$\begin{cases} \nabla \times \mathbf{G}^{EJ}(\boldsymbol{r},t;\boldsymbol{r}',t') = -\boldsymbol{\mu} \cdot \dfrac{\partial \mathbf{G}^{HJ}(\boldsymbol{r},t;\boldsymbol{r}',t')}{\partial t} \\ \nabla \times \mathbf{G}^{HJ}(\boldsymbol{r},t;\boldsymbol{r}',t') = \boldsymbol{\sigma} \cdot \mathbf{G}^{EJ}(\boldsymbol{r},t;\boldsymbol{r}',t') + \boldsymbol{\varepsilon} \cdot \dfrac{\partial \mathbf{G}^{EJ}(\boldsymbol{r},t;\boldsymbol{r}',t')}{\partial t} + \delta(\boldsymbol{r}-\boldsymbol{r}')\,\delta(t-t')\,\mathbf{I} \end{cases} \tag{1.10}$$

$$\begin{cases} \nabla \times \mathbf{G}^{EM}(\boldsymbol{r},t;\boldsymbol{r}',t') = -\boldsymbol{\mu} \cdot \dfrac{\partial \mathbf{G}^{HM}(\boldsymbol{r},t;\boldsymbol{r}',t')}{\partial t} - \delta(\boldsymbol{r}-\boldsymbol{r}')\,\delta(t-t')\,\mathbf{I} \\ \nabla \times \mathbf{G}^{HM}(\boldsymbol{r},t;\boldsymbol{r}',t') = \boldsymbol{\sigma} \cdot \mathbf{G}^{EM}(\boldsymbol{r},t;\boldsymbol{r}',t') + \boldsymbol{\varepsilon} \cdot \dfrac{\partial \mathbf{G}^{EM}(\boldsymbol{r},t;\boldsymbol{r}',t')}{\partial t} \end{cases} \tag{1.11}$$

where $\mathbf{G}^{EJ}$ and $\mathbf{G}^{HJ}$ are the electric and magnetic dyadic Green's functions due to a point electric current, and $\mathbf{G}^{EM}$ and $\mathbf{G}^{HM}$ are the electric and magnetic dyads due to a point magnetic source located at $\boldsymbol{r} = \boldsymbol{r}'$ and excited at $t = t'$, respectively. For the sake of clarity, for example, $G_{xy}^{EJ}(\boldsymbol{r},t;\boldsymbol{r}',t')$ denotes the *x*-component of the electric field at point $\boldsymbol{r}$ and time *t* generated by an impulsive point electric current dipole in *y*-direction, located at $\boldsymbol{r} = \boldsymbol{r}'$, and excited at $t = t'$.

All these dyadic Green's functions satisfy the initial (causality) conditions:

$$\mathbf{G}(\boldsymbol{r},t;\boldsymbol{r}',t') = 0 \qquad\qquad t \le t' \tag{1.12}$$

and the appropriate boundary conditions. Based on superposition principle, the electromagnetic field can be expressed in terms of dyadic Green's functions as:

$$\begin{aligned} \boldsymbol{E}(\boldsymbol{r},t) &= \int_{V_J}\int_{t_1}^{t} \mathbf{G}^{EJ}(\boldsymbol{r},t;\boldsymbol{r}',t') \cdot \boldsymbol{J}(\boldsymbol{r}',t')\,dt'dV' + \int_{V_M}\int_{t_1}^{t} \mathbf{G}^{EM}(\boldsymbol{r},t;\boldsymbol{r}',t') \cdot \boldsymbol{M}(\boldsymbol{r}',t')\,dt'dV' \\ \boldsymbol{H}(\boldsymbol{r},t) &= \int_{V_J}\int_{t_1}^{t} \mathbf{G}^{HJ}(\boldsymbol{r},t;\boldsymbol{r}',t') \cdot \boldsymbol{J}(\boldsymbol{r}',t')\,dt'dV' + \int_{V_M}\int_{t_1}^{t} \mathbf{G}^{HM}(\boldsymbol{r},t;\boldsymbol{r}',t') \cdot \boldsymbol{M}(\boldsymbol{r}',t')\,dt'dV' \end{aligned} \tag{1.13}$$

where V_J and V_M are the finite volumes occupied by $\boldsymbol{J}$ and $\boldsymbol{M}$, respectively. The dyadic Green's functions formulas for an infinite homogeneous isotropic medium are given in Appendix A.

In the case of a *reciprocal medium*, i.e., $\boldsymbol{\sigma} = \boldsymbol{\sigma}^T$, $\boldsymbol{\varepsilon} = \boldsymbol{\varepsilon}^T$, and $\boldsymbol{\mu} = \boldsymbol{\mu}^T$, based on *reciprocity theorem* of the convolution type in an infinite medium, the following symmetry properties of dyadic Green's functions hold (De Hoop, 1995):

$$\begin{cases} \mathbf{G}^{EJ}(\boldsymbol{r},t;\boldsymbol{r}',t') = +\mathbf{G}^{EJ^T}(\boldsymbol{r}',-t';\boldsymbol{r},-t) \\ \mathbf{G}^{EM}(\boldsymbol{r},t;\boldsymbol{r}',t') = -\mathbf{G}^{HJ^T}(\boldsymbol{r}',-t';\boldsymbol{r},-t) \\ \mathbf{G}^{HJ}(\boldsymbol{r},t;\boldsymbol{r}',t') = -\mathbf{G}^{EM^T}(\boldsymbol{r}',-t';\boldsymbol{r},-t) \\ \mathbf{G}^{HM}(\boldsymbol{r},t;\boldsymbol{r}',t') = +\mathbf{G}^{HM^T}(\boldsymbol{r}',-t';\boldsymbol{r},-t) \end{cases} \tag{1.14}$$

where superscript "*T*" denotes transpose operation.

Another useful property of dyadic Green's functions is *time translation property* for a time-invariant (stationary) domain (Heberman, 1987):

$$\mathbf{G}(\boldsymbol{r},t;\boldsymbol{r}',t') = \mathbf{G}(\boldsymbol{r},t-t';\boldsymbol{r}',0) \tag{1.15}$$

In the following, the above equations can be derived in the frequency domain as well. The Fourier transform definition and its properties are given in Appendix C. Using the time derivative property (C.3), Eq. (1.9) transforms into

$$\begin{cases} \nabla \times \boldsymbol{E} = j\omega\boldsymbol{\mu}\cdot\boldsymbol{H} - \boldsymbol{M} \\ \nabla \times \boldsymbol{H} = -j\omega\boldsymbol{\varepsilon}_c\cdot\boldsymbol{E} + \boldsymbol{J} \end{cases} \tag{1.16}$$

where $\boldsymbol{\varepsilon}_c$, complex permittivity tensor, is define as:

$$\boldsymbol{\varepsilon}_c = \boldsymbol{\varepsilon} + j\frac{1}{\omega}\boldsymbol{\sigma} \tag{1.17}$$

The frequency counterpart of Eq. (1.10) and (1.11), based on time translation property (1.15), relation (C.13), and the shifting property (C.4), are:

$$\begin{cases} \nabla \times \mathbf{G}^{EJ} = j\omega\boldsymbol{\mu}\cdot\mathbf{G}^{HJ} \\ \nabla \times \mathbf{G}^{HJ} = -j\omega\boldsymbol{\varepsilon}_c\cdot\mathbf{G}^{EJ} + \delta(\boldsymbol{r}-\boldsymbol{r}')\,\mathbf{I} \end{cases} \tag{1.18}$$

$$\begin{cases} \nabla \times \mathbf{G}^{EM} = j\omega\boldsymbol{\mu}\cdot\mathbf{G}^{HM} - \delta(\boldsymbol{r}-\boldsymbol{r}')\,\mathbf{I} \\ \nabla \times \mathbf{G}^{HM} = -j\omega\boldsymbol{\varepsilon}_c\cdot\mathbf{G}^{EM} \end{cases} \tag{1.19}$$

Using the time translation property (1.15) and the convolution theorem (C.7), the relations (1.13) transform into the following relations

$$\begin{aligned}\boldsymbol{E}(\boldsymbol{r},\omega) &= \int_{V_J} \mathbf{G}^{EJ}(\boldsymbol{r};\boldsymbol{r}'\,|\,\omega)\cdot\boldsymbol{J}(\boldsymbol{r}',\omega)\,dV' + \int_{V_M} \mathbf{G}^{EM}(\boldsymbol{r};\boldsymbol{r}'\,|\,\omega)\cdot\boldsymbol{M}(\boldsymbol{r}',\omega)\,dV' \\ \boldsymbol{H}(\boldsymbol{r},\omega) &= \int_{V_J} \mathbf{G}^{HJ}(\boldsymbol{r};\boldsymbol{r}'\,|\,\omega)\cdot\boldsymbol{J}(\boldsymbol{r}',\omega)\,dV' + \int_{V_M} \mathbf{G}^{HM}(\boldsymbol{r};\boldsymbol{r}'\,|\,\omega)\cdot\boldsymbol{M}(\boldsymbol{r}',\omega)\,dV'\end{aligned} \tag{1.20}$$

Also, the symmetry properties (1.14), using the time translation property (1.15) and the shifting property (C.4), become:

$$\begin{cases}\mathbf{G}^{EJ}(\boldsymbol{r};\boldsymbol{r}'\,|\,\omega) &= +\mathbf{G}^{EJ^T}(\boldsymbol{r}';\boldsymbol{r}\;\,|\,\omega) \\ \mathbf{G}^{EM}(\boldsymbol{r};\boldsymbol{r}'\,|\,\omega) &= -\mathbf{G}^{HJ^T}(\boldsymbol{r}';\boldsymbol{r}\,|\,\omega) \\ \mathbf{G}^{HJ}(\boldsymbol{r};\boldsymbol{r}'\,|\,\omega) &= -\mathbf{G}^{EM^T}(\boldsymbol{r}';\boldsymbol{r}\,|\,\omega) \\ \mathbf{G}^{HM}(\boldsymbol{r};\boldsymbol{r}'\,|\,\omega) &= +\mathbf{G}^{HM^T}(\boldsymbol{r}';\boldsymbol{r}\,|\,\omega)\end{cases} \tag{1.21}$$

Adjoint EM fields play an important role in inverse scattering problem. Following the definition of Felsen and Marcuvitz (1994), the equations for adjoint electric and magnetic fields $\hat{\boldsymbol{E}}(\boldsymbol{r},t)$ and $\hat{\boldsymbol{H}}(\boldsymbol{r},t)$ can be obtained from the ordinary field equations (1.9) by transposing the EM property tensors and temporal and spatial reflection transformation $\partial/\partial t \to -\partial/\partial t$ and $\nabla \to -\nabla$. One thus obtains:

$$\begin{cases}-\nabla\times\hat{\boldsymbol{E}} = \boldsymbol{\mu}^T\cdot\dot{\hat{\boldsymbol{H}}} - \hat{\boldsymbol{M}} \\ -\nabla\times\hat{\boldsymbol{H}} = \boldsymbol{\sigma}^T\cdot\hat{\boldsymbol{E}} - \boldsymbol{\varepsilon}^T\cdot\dot{\hat{\boldsymbol{E}}} + \hat{\boldsymbol{J}}\end{cases} \tag{1.22}$$

which are subject to reflected initial condition $\hat{\boldsymbol{E}} = 0 = \hat{\boldsymbol{H}}$ for $t \geq t_2$ corresponding to excitations $\hat{\boldsymbol{J}}$ and $\hat{\boldsymbol{M}}$ that vanish for $t > t_2$ and appropriate reflected boundary conditions. The corresponding adjoint dyadic Green's functions satisfy the following equations:

$$\begin{cases}-\nabla\times\hat{\mathbf{G}}^{EJ}(\boldsymbol{r},t;\boldsymbol{r}',t') = \boldsymbol{\mu}^T\cdot\dfrac{\partial\hat{\mathbf{G}}^{HJ}(\boldsymbol{r},t;\boldsymbol{r}',t')}{\partial t} \\ -\nabla\times\hat{\mathbf{G}}^{HJ}(\boldsymbol{r},t;\boldsymbol{r}',t') = \boldsymbol{\sigma}^T\cdot\hat{\mathbf{G}}^{EJ}(\boldsymbol{r},t;\boldsymbol{r}',t') - \boldsymbol{\varepsilon}^T\cdot\dfrac{\partial\hat{\mathbf{G}}^{EJ}(\boldsymbol{r},t;\boldsymbol{r}',t')}{\partial t} + \delta(\boldsymbol{r}-\boldsymbol{r}')\,\delta(t-t')\,\mathbf{I}\end{cases} \tag{1.23}$$

$$\begin{cases} -\nabla\times\hat{\mathbf{G}}^{EM}(\boldsymbol{r},t;\boldsymbol{r}',t') = \boldsymbol{\mu}^{T}\cdot\dfrac{\partial\hat{\mathbf{G}}^{HM}(\boldsymbol{r},t;\boldsymbol{r}',t')}{\partial t} - \delta(\boldsymbol{r}-\boldsymbol{r}')\,\delta(t-t')\,\mathbf{I} \\ -\nabla\times\hat{\mathbf{G}}^{HM}(\boldsymbol{r},t;\boldsymbol{r}',t') = \boldsymbol{\sigma}^{T}\cdot\hat{\mathbf{G}}^{EM}(\boldsymbol{r},t;\boldsymbol{r}',t') - \boldsymbol{\varepsilon}^{T}\cdot\dfrac{\partial\hat{\mathbf{G}}^{EM}(\boldsymbol{r},t;\boldsymbol{r}',t')}{\partial t} \end{cases} \tag{1.24}$$

These adjoint Green's functions are anti-causal

$$\hat{\mathbf{G}}(\boldsymbol{r},t;\boldsymbol{r}',t') = 0 \qquad\qquad t \geq t' \tag{1.25}$$

and satisfy the appropriate reflected boundary conditions. Note that the time translation property still holds,

$$\hat{\mathbf{G}}(\boldsymbol{r},t;\boldsymbol{r}',t') = \hat{\mathbf{G}}(\boldsymbol{r},t-t';\boldsymbol{r}',0) \tag{1.26}$$

Linearity of the adjoint equations (1.22) indicates that the adjoint fields are representable in a form similar to those in Eq. (1.13):

$$\begin{aligned} \hat{\boldsymbol{E}}(\boldsymbol{r},t) &= \int_{V_{\hat{J}}}\int_{t_2}^{t}\hat{\mathbf{G}}^{EJ}(\boldsymbol{r},t;\boldsymbol{r}',t')\cdot\hat{\boldsymbol{J}}(\boldsymbol{r}',t')\,dt'dV' + \int_{V_{\hat{M}}}\int_{t_2}^{t}\hat{\mathbf{G}}^{EM}(\boldsymbol{r},t;\boldsymbol{r}',t')\cdot\hat{\boldsymbol{M}}(\boldsymbol{r}',t')\,dt'dV' \\ \hat{\boldsymbol{H}}(\boldsymbol{r},t) &= \int_{V_{\hat{J}}}\int_{t_2}^{t}\hat{\mathbf{G}}^{HJ}(\boldsymbol{r},t;\boldsymbol{r}',t')\cdot\hat{\boldsymbol{J}}(\boldsymbol{r}',t')\,dt'dV' + \int_{V_{\hat{M}}}\int_{t_2}^{t}\hat{\mathbf{G}}^{HM}(\boldsymbol{r},t;\boldsymbol{r}',t')\cdot\hat{\boldsymbol{M}}(\boldsymbol{r}',t')\,dt'dV' \end{aligned} \tag{1.27}$$

where $V_{\hat{J}}$ and $V_{\hat{M}}$ are the finite volumes occupied by $\hat{\boldsymbol{J}}$ and $\hat{\boldsymbol{M}}$, respectively. Note that in the above relations: $t \leq t' \leq t_2$. In addition, adjoint dyadic Green's functions have the following relationships with dyadic Green' functions (derivation in Appendix B):

$$\begin{cases} \hat{\mathbf{G}}^{EJ}(\boldsymbol{r},t;\boldsymbol{r}',t') = \mathbf{G}^{EJ^{T}}(\boldsymbol{r}',t';\boldsymbol{r},t) \\ \hat{\mathbf{G}}^{EM}(\boldsymbol{r},t;\boldsymbol{r}',t') = \mathbf{G}^{HJ^{T}}(\boldsymbol{r}',t';\boldsymbol{r},t) \\ \hat{\mathbf{G}}^{HJ}(\boldsymbol{r},t;\boldsymbol{r}',t') = \mathbf{G}^{EM^{T}}(\boldsymbol{r}',t';\boldsymbol{r},t) \\ \hat{\mathbf{G}}^{HM}(\boldsymbol{r},t;\boldsymbol{r}',t') = \mathbf{G}^{HM^{T}}(\boldsymbol{r}',t';\boldsymbol{r},t) \end{cases} \tag{1.28}$$

Considering the relations (1.14), valid for a reciprocal medium, the above relations can also be expressed as:

$$\begin{cases} \hat{\mathbf{G}}^{EJ}(\boldsymbol{r},t;\boldsymbol{r}',t') &= +\mathbf{G}^{EJ}(\boldsymbol{r},-t;\boldsymbol{r}',-t') \\ \hat{\mathbf{G}}^{EM}(\boldsymbol{r},t;\boldsymbol{r}',t') &= -\mathbf{G}^{EM}(\boldsymbol{r},-t;\boldsymbol{r}',-t') \\ \hat{\mathbf{G}}^{HJ}(\boldsymbol{r},t;\boldsymbol{r}',t') &= -\mathbf{G}^{HJ}(\boldsymbol{r},-t;\boldsymbol{r}',-t') \\ \hat{\mathbf{G}}^{HM}(\boldsymbol{r},t;\boldsymbol{r}',t') &= +\mathbf{G}^{HM}(\boldsymbol{r},-t;\boldsymbol{r}',-t') \end{cases} \tag{1.29}$$

Using time translation properties (1.15) and (1.26), the shifting property (C.4) and the conjugate property (C.5), the above relations in frequency domain take the following forms:

$$\begin{cases} \hat{\mathbf{G}}^{EJ}(\boldsymbol{r};\boldsymbol{r}'|\,\omega) &= +\mathbf{G}^{EJ^*}(\boldsymbol{r};\boldsymbol{r}'|\,\omega) \\ \hat{\mathbf{G}}^{EM}(\boldsymbol{r};\boldsymbol{r}'|\,\omega) &= -\mathbf{G}^{EM^*}(\boldsymbol{r};\boldsymbol{r}'|\,\omega) \\ \hat{\mathbf{G}}^{HJ}(\boldsymbol{r};\boldsymbol{r}'|\,\omega) &= -\mathbf{G}^{HJ^*}(\boldsymbol{r};\boldsymbol{r}'|\,\omega) \\ \hat{\mathbf{G}}^{HM}(\boldsymbol{r};\boldsymbol{r}'|\,\omega) &= +\mathbf{G}^{HM^*}(\boldsymbol{r};\boldsymbol{r}'|\,\omega) \end{cases} \tag{1.30}$$

2. Forward Scattering of Electromagnetic Waves

In this chapter, the forward (direct) scattering problem of a finite scatterer (damage), occupying the volume V_{scat}, embedded in a host structure (background medium) and excited by finite electric and/or magnetic current sources at $t_1 = 0$ is investigated in both differential equation and integral equation formalisms. In this case, the Maxwell's equations are:

$$\begin{cases} \nabla \times \boldsymbol{E} = -\boldsymbol{\mu} \cdot \dot{\boldsymbol{H}} - \boldsymbol{M} \\ \nabla \times \boldsymbol{H} = \boldsymbol{\sigma} \cdot \boldsymbol{E} + \boldsymbol{\varepsilon} \cdot \dot{\boldsymbol{E}} + \boldsymbol{J} \end{cases} \tag{2.1}$$

where

$$\boldsymbol{\mu}, \boldsymbol{\sigma}, \boldsymbol{\varepsilon} = \begin{cases} \boldsymbol{\mu}(\boldsymbol{r}), \boldsymbol{\sigma}(\boldsymbol{r}), \boldsymbol{\varepsilon}(\boldsymbol{r}) & \boldsymbol{r} \subset V_{scat} \\ \boldsymbol{\mu}_b(\boldsymbol{r}), \boldsymbol{\sigma}_b(\boldsymbol{r}), \boldsymbol{\varepsilon}_b(\boldsymbol{r}) & \boldsymbol{r} \not\subset V_{scat} \end{cases} \tag{2.2}$$

and subscript "*b*" implies background. Now, the total field is decomposed into incident and scattered fields, i.e.,

$$\begin{aligned} \boldsymbol{E} &= \boldsymbol{E}_{inc} + \boldsymbol{E}_{scat} \\ \boldsymbol{H} &= \boldsymbol{H}_{inc} + \boldsymbol{H}_{scat} \end{aligned} \tag{2.3}$$

where the subscripts "*inc*" and "*scat* " denote incident and scattered fields, respectively.

The incident field is defined as the field due to the sources $\boldsymbol{J}$ and/or $\boldsymbol{M}$ in the absence of the scatterer; therefore, it satisfies Eq. (2.1) in the host structure,

$$\begin{cases} \nabla \times \boldsymbol{E}_{inc} = -\boldsymbol{\mu}_b \cdot \dot{\boldsymbol{H}}_{inc} - \boldsymbol{M} \\ \nabla \times \boldsymbol{H}_{inc} = \boldsymbol{\sigma}_b \cdot \boldsymbol{E}_{inc} + \boldsymbol{\varepsilon}_b \cdot \dot{\boldsymbol{E}}_{inc} + \boldsymbol{J} \end{cases} \tag{2.4}$$

The equations for the scattered field can be derived using Eq. (2.1) to (2.4) as:

$$\begin{cases} \nabla \times \boldsymbol{E}_{scat} = -\boldsymbol{\mu}_b \cdot \dot{\boldsymbol{H}}_{scat} - \left[\Delta\boldsymbol{\mu} \cdot \dot{\boldsymbol{H}} \right] \\ \nabla \times \boldsymbol{H}_{scat} = \boldsymbol{\sigma}_b \cdot \boldsymbol{E}_{scat} + \boldsymbol{\varepsilon}_b \cdot \dot{\boldsymbol{E}}_{scat} + \left[\Delta\boldsymbol{\sigma} \cdot \boldsymbol{E} + \Delta\boldsymbol{\varepsilon} \cdot \dot{\boldsymbol{E}} \right] \end{cases} \tag{2.5}$$

where *contrast EM properties* are defined as:

$$\begin{aligned}
\Delta\boldsymbol{\mu} &= \boldsymbol{\mu} - \boldsymbol{\mu}_b \\
\Delta\boldsymbol{\varepsilon} &= \boldsymbol{\varepsilon} - \boldsymbol{\varepsilon}_b \\
\Delta\boldsymbol{\sigma} &= \boldsymbol{\sigma} - \boldsymbol{\sigma}_b
\end{aligned} \tag{2.6}$$

Note that, one can consider $\Delta\boldsymbol{\mu}\cdot\dot{\boldsymbol{H}}$ and $\Delta\boldsymbol{\sigma}\cdot\boldsymbol{E}+\Delta\boldsymbol{\varepsilon}\cdot\dot{\boldsymbol{E}}$ as effective magnetic and electric volume currents, respectively, induced by the total magnetic and electric fields inside the scatterer. In fact, the scattered field is generated due to these effective induced currents inside the scatterer. These effective currents are called *scattering currents* or *contrast sources* (Oristaglio and Blok, 1994).

In view of the relations (1.9) and (1.13), the incident and scattered fields in Eq. (2.4) and (2.5) can be expressed in terms of the Green's functions of the host structure,

$$\begin{aligned}
\boldsymbol{E}_{inc}(\boldsymbol{r},t) &= \int_0^t\int_{V_J} \mathbf{G}_b^{EJ}(\boldsymbol{r},t;\boldsymbol{r}',t')\cdot\boldsymbol{J}(\boldsymbol{r}',t')\,dV'dt' + \int_0^t\int_{V_M} \mathbf{G}_b^{EM}(\boldsymbol{r},t;\boldsymbol{r}',t')\cdot\boldsymbol{M}(\boldsymbol{r}',t')\,dV'dt' \\
\boldsymbol{H}_{inc}(\boldsymbol{r},t) &= \int_0^t\int_{V_J} \mathbf{G}_b^{HJ}(\boldsymbol{r},t;\boldsymbol{r}',t')\cdot\boldsymbol{J}(\boldsymbol{r}',t')\,dV'dt' + \int_0^t\int_{V_M} \mathbf{G}_b^{HM}(\boldsymbol{r},t;\boldsymbol{r}',t')\cdot\boldsymbol{M}(\boldsymbol{r}',t')\,dV'dt'
\end{aligned} \tag{2.7}$$

$$\begin{aligned}
\boldsymbol{E}_{scat}(\boldsymbol{r},t) &= \int_0^t\int_{V_{scat}} \mathbf{G}_b^{EJ}(\boldsymbol{r},t;\boldsymbol{r}',t')\cdot\left[\Delta\boldsymbol{\sigma}(\boldsymbol{r}')\cdot\boldsymbol{E}(\boldsymbol{r}',t')+\Delta\boldsymbol{\varepsilon}(\boldsymbol{r}')\cdot\dot{\boldsymbol{E}}(\boldsymbol{r}',t')\right]dV'dt' + \\
&\qquad \int_0^t\int_{V_{scat}} \mathbf{G}_b^{EM}(\boldsymbol{r},t;\boldsymbol{r}',t')\cdot\left[\Delta\boldsymbol{\mu}(\boldsymbol{r}')\cdot\dot{\boldsymbol{H}}(\boldsymbol{r}',t')\right]dV'dt' \\
\boldsymbol{H}_{scat}(\boldsymbol{r},t) &= \int_0^t\int_{V_{scat}} \mathbf{G}_b^{HJ}(\boldsymbol{r},t;\boldsymbol{r}',t')\cdot\left[\Delta\boldsymbol{\sigma}(\boldsymbol{r}')\cdot\boldsymbol{E}(\boldsymbol{r}',t')+\Delta\boldsymbol{\varepsilon}(\boldsymbol{r}')\cdot\dot{\boldsymbol{E}}(\boldsymbol{r}',t')\right]dV'dt' + \\
&\qquad \int_0^t\int_{V_{scat}} \mathbf{G}_b^{HM}(\boldsymbol{r},t;\boldsymbol{r}',t')\cdot\left[\Delta\boldsymbol{\mu}(\boldsymbol{r}')\cdot\dot{\boldsymbol{H}}(\boldsymbol{r}',t')\right]dV'dt'
\end{aligned} \tag{2.8}$$

Using the relations (C.3), (C.7), and (1.15), Eq. (2.7) and (2.8) can be easily transformed into the frequency domain as:

$$\begin{aligned}
\boldsymbol{E}_{inc}(\boldsymbol{r},\omega) &= \int_{V_J} \mathbf{G}_b^{EJ}(\boldsymbol{r};\boldsymbol{r}'\,|\,\omega)\cdot\boldsymbol{J}(\boldsymbol{r}',\omega)\,dV' + \int_{V_M} \mathbf{G}_b^{EM}(\boldsymbol{r};\boldsymbol{r}'\,|\,\omega)\cdot\boldsymbol{M}(\boldsymbol{r}',\omega)\,dV' \\
\boldsymbol{H}_{inc}(\boldsymbol{r},\omega) &= \int_{V_J} \mathbf{G}_b^{HJ}(\boldsymbol{r};\boldsymbol{r}'\,|\,\omega)\cdot\boldsymbol{J}(\boldsymbol{r}',\omega)\,dV' + \int_{V_M} \mathbf{G}_b^{HM}(\boldsymbol{r};\boldsymbol{r}'\,|\,\omega)\cdot\boldsymbol{M}(\boldsymbol{r}',\omega)\,dV'
\end{aligned} \tag{2.9}$$

$$
\begin{aligned}
\boldsymbol{E}_{scat}(\boldsymbol{r},\omega) &= \int_{V_{scat}} \mathbf{G}_b^{EJ}\ (\boldsymbol{r};\boldsymbol{r}'\mid\omega)\cdot\left[-\,j\omega\Delta\boldsymbol{\varepsilon}_c(\boldsymbol{r}')\cdot\boldsymbol{E}(\boldsymbol{r}',\omega)\right]dV' + \\
&\quad \int_{V_{scat}} \mathbf{G}_b^{EM}\ (\boldsymbol{r};\boldsymbol{r}'\mid\omega)\cdot\left[-\,j\omega\Delta\boldsymbol{\mu}(\boldsymbol{r}')\cdot\boldsymbol{H}(\boldsymbol{r}',\omega)\right]dV' \\
\boldsymbol{H}_{scat}(\boldsymbol{r},\omega) &= \int_{V_{scat}} \mathbf{G}_b^{HJ}\ (\boldsymbol{r};\boldsymbol{r}'\mid\omega)\cdot\left[-\,j\omega\Delta\boldsymbol{\varepsilon}_c(\boldsymbol{r}')\cdot\boldsymbol{E}(\boldsymbol{r}',\omega)\right]dV' + \\
&\quad \int_{V_{scat}} \mathbf{G}_b^{HM}\ (\boldsymbol{r};\boldsymbol{r}'\mid\omega)\cdot\left[-\,j\omega\Delta\boldsymbol{\mu}(\boldsymbol{r}')\cdot\boldsymbol{H}(\boldsymbol{r}',\omega)\right]dV'
\end{aligned}
\tag{2.10}
$$

where

$$
\Delta\boldsymbol{\varepsilon}_c = \Delta\boldsymbol{\varepsilon} + j\frac{1}{\omega}\Delta\boldsymbol{\sigma} \tag{2.11}
$$

3. Inverse Scattering

In inverse scattering (medium) problems, one attempts to quantify the material properties of the scatterer (damage) from the scattered field measurement outside the scatterer. The measurement may be set up on a closed surface around the scatterer or on a planar surface outside the scatterer. Figure 3.1 shows a cross-section of a scatterer inside a known host structure (background medium), an actuator, and some sensors located on a planar observation surface for scattered field measurement. It should be noted that the inverse scattering problem can be formulated both in differential equation and integral equation (IE) formalisms. Here, the IE formulation is presented.

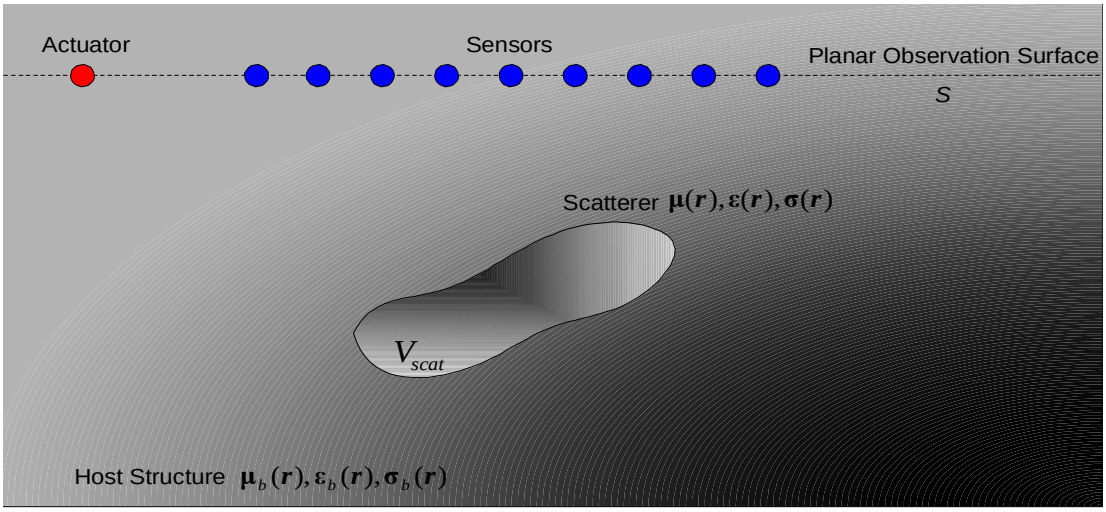

Figure 3.1. The inverse medium problem: Finding scatterer EM properties using field measurement at sensor locations outside the scatterer

For the case considered in the previous chapter, when total electric and/or magnetic fields are measured on a planar observation surface *S* outside the scatterer region, the IE formulation of the inverse medium problem can be set up using Eq. (2.8) as (Oristaglio and Blok, 1994):

Given $\boldsymbol{E}^d(\boldsymbol{r},t)$ and/or $\boldsymbol{H}^d(\boldsymbol{r},t)$ (the measured total electric and/or magnetic fields at sensor locations on the observation surface *S*), $\boldsymbol{E}_{inc}$, $\boldsymbol{H}_{inc}$, and the Green's functions of the host structure, the contrast EM properties $\Delta\boldsymbol{\sigma}(\boldsymbol{r})$, $\Delta\boldsymbol{\varepsilon}(\boldsymbol{r})$, and $\Delta\boldsymbol{\mu}(\boldsymbol{r})$ should be recovered from *data equations*,

$$\boldsymbol{E}^{d}(\boldsymbol{r},t)=\boldsymbol{E}_{inc}(\boldsymbol{r},t)+\int_0^t\int_{V_{scat}}\mathbf{G}_b^{EJ}(\boldsymbol{r},t;\boldsymbol{r}',t')\cdot\left[\Delta\boldsymbol{\sigma}(\boldsymbol{r}')\cdot\boldsymbol{E}(\boldsymbol{r}',t')+\Delta\boldsymbol{\varepsilon}(\boldsymbol{r}')\cdot\dot{\boldsymbol{E}}(\boldsymbol{r}',t')\right]dV'dt'+$$
$$\int_0^t\int_{V_{scat}}\mathbf{G}_b^{EM}(\boldsymbol{r},t;\boldsymbol{r}',t')\cdot\left[\Delta\boldsymbol{\mu}(\boldsymbol{r}')\cdot\dot{\boldsymbol{H}}(\boldsymbol{r}',t')\right]dV'dt'$$
$$\boldsymbol{H}^{d}(\boldsymbol{r},t)=\boldsymbol{H}_{inc}(\boldsymbol{r},t)+\int_0^t\int_{V_{scat}}\mathbf{G}_b^{HJ}(\boldsymbol{r},t;\boldsymbol{r}',t')\cdot\left[\Delta\boldsymbol{\sigma}(\boldsymbol{r}')\cdot\boldsymbol{E}(\boldsymbol{r}',t')+\Delta\boldsymbol{\varepsilon}(\boldsymbol{r}')\cdot\dot{\boldsymbol{E}}(\boldsymbol{r}',t')\right]dV'dt'+ \quad (3.1)$$
$$\int_0^t\int_{V_{scat}}\mathbf{G}_b^{HM}(\boldsymbol{r},t;\boldsymbol{r}',t')\cdot\left[\Delta\boldsymbol{\mu}(\boldsymbol{r}')\cdot\dot{\boldsymbol{H}}(\boldsymbol{r}',t')\right]dV'dt'$$
where : $\boldsymbol{r}'\in V_{scat}$ and $\boldsymbol{r}\in S$

The data equations provide an integral relation between the measured field (data) and the unknowns ($\Delta\boldsymbol{\sigma}(\boldsymbol{r})$, $\Delta\boldsymbol{\varepsilon}(\boldsymbol{r})$, and $\Delta\boldsymbol{\mu}(\boldsymbol{r})$). It is not yet, however, a complete formulation of the inverse medium problem because there is another unknown under the integrals: the total electric field and time derivative of electric and magnetic fields inside the scatterer region V_{scat}. Clearly, other equations are required to specify $\boldsymbol{E}$ and $\boldsymbol{H}$. The other equations, so called *domain equations*, are the same integral equations, but written with $\boldsymbol{r}\in V_{scat}$,

$$\boldsymbol{E}(\boldsymbol{r},t)=\boldsymbol{E}_{inc}(\boldsymbol{r},t)+\int_0^t\int_{V_{scat}}\mathbf{G}_b^{EJ}(\boldsymbol{r},t;\boldsymbol{r}',t')\cdot\left[\Delta\boldsymbol{\sigma}(\boldsymbol{r}')\cdot\boldsymbol{E}(\boldsymbol{r}',t')+\Delta\boldsymbol{\varepsilon}(\boldsymbol{r}')\cdot\dot{\boldsymbol{E}}(\boldsymbol{r}',t')\right]dV'dt'+$$
$$\int_0^t\int_{V_{scat}}\mathbf{G}_b^{EM}(\boldsymbol{r},t;\boldsymbol{r}',t')\cdot\left[\Delta\boldsymbol{\mu}(\boldsymbol{r}')\cdot\dot{\boldsymbol{H}}(\boldsymbol{r}',t')\right]dV'dt'$$
$$\boldsymbol{H}(\boldsymbol{r},t)=\boldsymbol{H}_{inc}(\boldsymbol{r},t)+\int_0^t\int_{V_{scat}}\mathbf{G}_b^{HJ}(\boldsymbol{r},t;\boldsymbol{r}',t')\cdot\left[\Delta\boldsymbol{\sigma}(\boldsymbol{r}')\cdot\boldsymbol{E}(\boldsymbol{r}',t')+\Delta\boldsymbol{\varepsilon}(\boldsymbol{r}')\cdot\dot{\boldsymbol{E}}(\boldsymbol{r}',t')\right]dV'dt'+ \quad (3.2)$$
$$\int_0^t\int_{V_{scat}}\mathbf{G}_b^{HM}(\boldsymbol{r},t;\boldsymbol{r}',t')\cdot\left[\Delta\boldsymbol{\mu}(\boldsymbol{r}')\cdot\dot{\boldsymbol{H}}(\boldsymbol{r}',t')\right]dV'dt'$$
where : $\boldsymbol{r}',\boldsymbol{r}\in V_{scat}$

Thus, in the IE formalism, the inverse medium problem is formulated as a coupled set of integral equations (3.1) and (3.2) for the unknown quantities: (1) $\Delta\boldsymbol{\sigma}(\boldsymbol{r})$, $\Delta\boldsymbol{\varepsilon}(\boldsymbol{r})$, and $\Delta\boldsymbol{\mu}(\boldsymbol{r})$, the *contrast EM properties*; (2) The total electric field and time derivative of electric and magnetic fields inside the scatterer.

The coupling between two equations is nonlinear due to the multiplication of the unknowns which occurs in both data and domain equations. In other words, this inverse problem is nonlinear in contrast properties because the total field inside the scatterer, which multiplies the contrast properties, also is a function of the contrast properties. Notice how, for instance, the total electric field inside the scatterer in data equation (3.1) depends on the

contrast EM properties through domain equation (3.2). This is called *multiple scattering effect* (e.g., Chew, 1995).

Unfortunately, this nonlinear inverse problem is ill-posed as well. By ill-posedness, in the sense of Hadamard (Hadamard, 1923), it is meant that one of the following conditions is violated: the existence of the solution; the uniqueness of the solution; or the continuous dependence of the solution on the data (stability condition). The uniqueness condition is generally violated because complete data collection from limited number of sensors is not practically feasible in SHM. In addition, the instability refers to the sensitivity of the solution to noise and measurement errors (Haykin, 1999). Regularization techniques are usually used to handle the ill-posedness of inverse problem.

4. The Electromagnetic Migration Algorithm

The basic principles of electromagnetic (EM) migration were first formulated by Zhdanov (1988) for the case of diffusive EM field in geophysical exploration. He introduced time-domain EM migration as the solution of the boundary value problem in a semi-infinite space (the earth) for the adjoint Maxwell's equations, in which the boundary values of the migrated field on the observation surface are determined by the measured EM field. Zhdanov and Portniaguine (1997) showed that this EM migration could be associated with the inverse problem solution: First, they introduced the *EM energy flow of the residual field*, the difference between the measured EM field and the calculated (simulated) EM field for a given model, through the observation surface as a functional of the conductivity distribution in the model. Then, it was shown the EM migration can be considered as the first iteration in the general EM inversion procedure, based on the minimization of the residual field energy flow through the observation surface. They called their iterative method, the *iterative EM migration*. The extension of this algorithm for the case of general transient EM field, where both conductivity and permittivity images are obtained, was made by Zhdanov (2001).

In this study, the time-domain EM migration algorithm for inhomogeneous isotropic structures is extended to inhomogeneous anisotropic case. Moreover, permeability images are constructed in addition to the conductivity and permittivity ones. To derive the imaging formulas, two approaches based on the minimization of the residual field energy flow through the observation surface are presented. In the second approach, the constraint of fulfillment of the Maxwell's equations by the calculated EM field is explicitly considered in the minimization problem using Lagrange multipliers. Although both approaches provide identical imaging results for reciprocal host structures, the second approach is mathematically more elegant.

4.1. The First Approach

Consider multiple scatterers (damages) embedded in a host structure (background medium) with known EM properties $\boldsymbol{\sigma}_b(\boldsymbol{r})$, $\boldsymbol{\varepsilon}_b(\boldsymbol{r})$, and $\boldsymbol{\mu}_b(\boldsymbol{r})$. All scatterers are assumed to be enclosed by the scatterer region or domain of investigation *D*. The scatterers are illuminated by incident EM waves, which are generated by actuators (sources) placed at *M* distinct positions $\boldsymbol{s}_j \in \{\boldsymbol{s}_1,\ldots,\boldsymbol{s}_M\}$ outside *D*. For each incidence, the total transient EM field is measured over an observation surface *S* outside *D* and for the time interval $[0\,,T]$. It is also assumed that the sources and all fields are zero before $t=0$.

When the goal is to estimate the spatial distribution of the EM properties inside the domain *D* using the set of measurements, inversion methods should be employed. Gradient-based inversion methods are very common for solving nonlinear inverse scattering problems. In these methods, first, a nonlinear cost (objective) functional is constructed (e.g., data error (misfit) functional, which is the norm of the difference between the measured field and the calculated field obtained from a model on the observation surface). Then, the cost functional is minimized in order to obtain the best estimation of EM properties inside *D*. The minimization is carried out by sequentially updating the model by steps along the gradient directions.

To construct the cost functional in the EM migration, a total instantaneous power flow of the residual field through the observation surface is defined for each experiment as:

$$p_j(t) = \int_S \left(\Delta\boldsymbol{E}_j \times \Delta\boldsymbol{H}_j\right)\cdot \boldsymbol{n}\, dS \tag{4.1.1}$$

where $\boldsymbol{n}$ is a unit normal vector pointing outward of S (pointing away the scatterer region) and the data residuals are given by

$$\begin{aligned} \Delta\boldsymbol{E}_j(\boldsymbol{r},t) &= \boldsymbol{E}_j^d(\boldsymbol{r},t) - \boldsymbol{E}_j(\boldsymbol{r},t) \\ \Delta\boldsymbol{H}_j(\boldsymbol{r},t) &= \boldsymbol{H}_j^d(\boldsymbol{r},t) - \boldsymbol{H}_j(\boldsymbol{r},t) \end{aligned} \tag{4.1.2}$$

where $\boldsymbol{E}_j^d(\boldsymbol{r},t)$ and $\boldsymbol{H}_j^d(\boldsymbol{r},t)$ are the measured EM field, and $\boldsymbol{E}_j(\boldsymbol{r},t)$ and $\boldsymbol{H}_j(\boldsymbol{r},t)$ are the calculated EM field for a given model.

It has been shown (Zhdanov, 2002) that the power flow of the residual field is non-negative, i.e., $p_j(t) \geq 0$. Note that there are no external EM sources inside the region surrounded by the observation surface *S* (the scatterer region). Based on the non-negativeness property of the power flow, the following cost functional is introduced:

$$P(\boldsymbol{\sigma}, \boldsymbol{\varepsilon}, \boldsymbol{\mu}) = \sum_{j=1}^{M} \int_0^T \int_S \left(\Delta \boldsymbol{E}_j \times \Delta \boldsymbol{H}_j \right) \cdot \boldsymbol{n} \, dS \, dt \tag{4.1.3}$$

The dependence of the functional *P* on the *model parameters* ($\boldsymbol{\sigma}$, $\boldsymbol{\varepsilon}$, and $\boldsymbol{\mu}$) arises from the implicit dependence of the calculated fields $\boldsymbol{E}_j(\boldsymbol{r},t)$ and $\boldsymbol{H}_j(\boldsymbol{r},t)$ on these parameters.

In a steepest descent method, the simplest gradient method, the minimization of *P* is carried out by updating the model by steps along the gradient directions. Let $\boldsymbol{\sigma}^{(n)}$, $\boldsymbol{\varepsilon}^{(n)}$, and $\boldsymbol{\mu}^{(n)}$ be the conductivity, permittivity, and permeability of the model at the n^{th} iteration and let $\boldsymbol{\gamma}_\sigma^{(n)}$, $\boldsymbol{\gamma}_\varepsilon^{(n)}$, and $\boldsymbol{\gamma}_\mu^{(n)}$ be the gradients of *P* with respect to $\boldsymbol{\sigma}^{(n)}$, $\boldsymbol{\varepsilon}^{(n)}$, and $\boldsymbol{\mu}^{(n)}$. Then,

$$\begin{aligned}
\boldsymbol{\sigma}^{(n+1)} &= \boldsymbol{\sigma}^{(n)} - \alpha_\sigma^{(n)} \, \boldsymbol{\gamma}_\sigma^{(n)} \\
\boldsymbol{\varepsilon}^{(n+1)} &= \boldsymbol{\varepsilon}^{(n)} - \alpha_\varepsilon^{(n)} \, \boldsymbol{\gamma}_\varepsilon^{(n)} \\
\boldsymbol{\mu}^{(n+1)} &= \boldsymbol{\mu}^{(n)} - \alpha_\mu^{(n)} \, \boldsymbol{\gamma}_\mu^{(n)}
\end{aligned} \tag{4.1.4}$$

where $\alpha_\sigma^{(n)}$, $\alpha_\varepsilon^{(n)}$, and $\alpha_\mu^{(n)}$ are positive step lengths and their optimal values at each iteration are usually obtained using a line-search method. For continuous models, the gradients are actually *Frechet derivatives* of *P*, i.e.,

$$\boldsymbol{\gamma}_\sigma = \frac{\partial P}{\partial \boldsymbol{\sigma}} \tag{4.1.5}$$

$$\boldsymbol{\gamma}_\varepsilon = \frac{\partial P}{\partial \boldsymbol{\varepsilon}} \tag{4.1.6}$$

$$\boldsymbol{\gamma}_\mu = \frac{\partial P}{\partial \boldsymbol{\mu}} \tag{4.1.7}$$

These are linear functionals such that for small perturbations $\delta\boldsymbol{\sigma}(\boldsymbol{r}'), \delta\boldsymbol{\varepsilon}(\boldsymbol{r}'), \text{and } \delta\boldsymbol{\mu}(\boldsymbol{r}')$ about the current model,

$$\begin{aligned}\delta P &= P(\boldsymbol{\sigma}+\delta\boldsymbol{\sigma},\boldsymbol{\varepsilon}+\delta\boldsymbol{\varepsilon},\boldsymbol{\mu}+\delta\boldsymbol{\mu}) - P(\boldsymbol{\sigma},\boldsymbol{\varepsilon},\boldsymbol{\mu}) \\ &= <\boldsymbol{\gamma}_\sigma,\delta\boldsymbol{\sigma}>_{H_M} + <\boldsymbol{\gamma}_\varepsilon,\delta\boldsymbol{\varepsilon}>_{H_M} + <\boldsymbol{\gamma}_\mu,\delta\boldsymbol{\mu}>_{H_M} + \\ &\quad \text{terms of the order}\left\{ \|\delta\boldsymbol{\sigma}\|^2_{H_M}, \|\delta\boldsymbol{\varepsilon}\|^2_{H_M}, \|\delta\boldsymbol{\mu}\|^2_{H_M} \right\}\end{aligned} \tag{4.1.8}$$

where $<\cdot,\cdot>_{H_M}$ and $\|\cdot\|_{H_M}$ indicate dot product and norm on the Hilbert space of models, respectively, with the following definitions:

$$<\delta\mathbf{m}_1,\delta\mathbf{m}_2>_{H_M} = \int_D \delta\mathbf{m}_1(\boldsymbol{r}) : \delta\mathbf{m}_2^T(\boldsymbol{r})\,dV \qquad \forall\,\delta\mathbf{m}_1,\delta\mathbf{m}_2 \in H_M \tag{4.1.9}$$

$$\|\delta\mathbf{m}\|^2_{H_M} = <\delta\mathbf{m},\delta\mathbf{m}>_{H_M} \tag{4.1.10}$$

where D is the domain over which the model is allowed to vary (scatterer region) and $\delta\mathbf{m}$ stands for $\delta\boldsymbol{\sigma}$, $\delta\boldsymbol{\varepsilon}$, or $\delta\boldsymbol{\mu}$.

It should be noted that the most important step in an iterative gradient-based method is to calculate the gradients of the functional with respect to the model parameters at each iteration. In view of relation (4.1.8) and definitions (4.1.9) and (4.1.10), the first variation of P is:

$$\begin{aligned}\delta^{(1)}P &= <\boldsymbol{\gamma}_\sigma,\delta\boldsymbol{\sigma}>_{H_M} + <\boldsymbol{\gamma}_\varepsilon,\delta\boldsymbol{\varepsilon}>_{H_M} + <\boldsymbol{\gamma}_\mu,\delta\boldsymbol{\mu}>_{H_M} \\ &= \int_D \boldsymbol{\gamma}_\sigma(\boldsymbol{r}') : \delta\boldsymbol{\sigma}^T(\boldsymbol{r}')\,dV' + \int_D \boldsymbol{\gamma}_\varepsilon(\boldsymbol{r}') : \delta\boldsymbol{\varepsilon}^T(\boldsymbol{r}')\,dV' + \int_D \boldsymbol{\gamma}_\mu(\boldsymbol{r}') : \delta\boldsymbol{\mu}^T(\boldsymbol{r}')\,dV'\end{aligned} \tag{4.1.11}$$

The first variation of P using Eq. (4.1.3) together with Eq. (4.1.2) can also be obtained as

$$\delta^{(1)}P = -\sum_{j=1}^{M}\int_0^T\int_S \left(\Delta\boldsymbol{E}_j \times \delta\boldsymbol{H}_j - \Delta\boldsymbol{H}_j \times \delta\boldsymbol{E}_j\right)\cdot\boldsymbol{n}\,dS\,dt \tag{4.1.12}$$

where $\delta\boldsymbol{E}_j(\boldsymbol{r},t)$ and $\delta\boldsymbol{H}_j(\boldsymbol{r},t)$ are the change in the calculated data when the model parameters are changed. The first variation of the Maxwell's equations (1.9) with respect to the model parameters is

$$\begin{cases}\nabla\times\delta\boldsymbol{E}_j = -\boldsymbol{\mu}\cdot\delta\dot{\boldsymbol{H}}_j - \left[\delta\boldsymbol{\mu}\cdot\dot{\boldsymbol{H}}_j\right] \\ \nabla\times\delta\boldsymbol{H}_j = \boldsymbol{\sigma}\cdot\delta\boldsymbol{E}_j + \boldsymbol{\varepsilon}\cdot\delta\dot{\boldsymbol{E}}_j + \left[\delta\boldsymbol{\sigma}\cdot\boldsymbol{E}_j + \delta\boldsymbol{\varepsilon}\cdot\dot{\boldsymbol{E}}_j\right]\end{cases} \tag{4.1.13}$$

The terms in the brackets can be considered as effective current sources for the perturbed field. Using Eq. (1.13), these perturbed electric and magnetic fields can be written in terms of dyadic Green's functions as:

$$\delta \boldsymbol{E}_j(\boldsymbol{r},t) = \int_0^t \int_D \mathbf{G}^{EJ}(\boldsymbol{r},t;\boldsymbol{r}',t') \cdot \left[\delta\boldsymbol{\sigma}(\boldsymbol{r}') \cdot \boldsymbol{E}_j(\boldsymbol{r}',t') + \delta\boldsymbol{\varepsilon}(\boldsymbol{r}') \cdot \dot{\boldsymbol{E}}_j(\boldsymbol{r}',t')\right] dV'dt' + \int_0^t \int_D \mathbf{G}^{EM}(\boldsymbol{r},t;\boldsymbol{r}',t') \cdot \left[\delta\boldsymbol{\mu}(\boldsymbol{r}') \cdot \dot{\boldsymbol{H}}_j(\boldsymbol{r}',t')\right] dV'dt' \tag{4.1.14}$$

$$\delta \boldsymbol{H}_j(\boldsymbol{r},t) = \int_0^t \int_D \mathbf{G}^{HJ}(\boldsymbol{r},t;\boldsymbol{r}',t') \cdot \left[\delta\boldsymbol{\sigma}(\boldsymbol{r}') \cdot \boldsymbol{E}_j(\boldsymbol{r}',t') + \delta\boldsymbol{\varepsilon}(\boldsymbol{r}') \cdot \dot{\boldsymbol{E}}_j(\boldsymbol{r}',t')\right] dV'dt' + \int_0^t \int_D \mathbf{G}^{HM}(\boldsymbol{r},t;\boldsymbol{r}',t') \cdot \left[\delta\boldsymbol{\mu}(\boldsymbol{r}') \cdot \dot{\boldsymbol{H}}_j(\boldsymbol{r}',t')\right] dV'dt' \tag{4.1.15}$$

Substituting Eq. (4.1.14) and (4.1.15) into (4.1.12), using relation (4.1.11), interchanging the time integrals, and then using relations (1.28), the gradients of *P* are obtained as

$$\boldsymbol{\gamma}_\sigma(\boldsymbol{r}') = \frac{\partial P}{\partial \boldsymbol{\sigma}} = \sum_{j=1}^{M} \int_0^T \boldsymbol{E}^{m}_{\Delta;j}(\boldsymbol{r}',t') \; \boldsymbol{E}_j(\boldsymbol{r}',t') \; dt' \tag{4.1.16}$$

$$\boldsymbol{\gamma}_\varepsilon(\boldsymbol{r}') = \frac{\partial P}{\partial \boldsymbol{\varepsilon}} = \sum_{j=1}^{M} \int_0^T \boldsymbol{E}^{m}_{\Delta;j}(\boldsymbol{r}',t') \; \dot{\boldsymbol{E}}_j(\boldsymbol{r}',t') \; dt' \tag{4.1.17}$$

$$\boldsymbol{\gamma}_\mu(\boldsymbol{r}') = \frac{\partial P}{\partial \boldsymbol{\mu}} = \sum_{j=1}^{M} \int_0^T \boldsymbol{H}^{m}_{\Delta;j}(\boldsymbol{r}',t') \; \dot{\boldsymbol{H}}_j(\boldsymbol{r}',t') \; dt' \tag{4.1.18}$$

where

$$\begin{aligned} \boldsymbol{E}^{m}_{\Delta;j}(\boldsymbol{r}',t') &= \int_S \int_T^{t'} \left\{ \hat{\mathbf{G}}^{EJ}(\boldsymbol{r}',t';\boldsymbol{r},t) \cdot \left[-\boldsymbol{n} \times \Delta\boldsymbol{H}_j(\boldsymbol{r},t)\right] + \hat{\mathbf{G}}^{EM}(\boldsymbol{r}',t';\boldsymbol{r},t) \cdot \left[\boldsymbol{n} \times \Delta\boldsymbol{E}_j(\boldsymbol{r},t)\right] \right\} dt \, dS \\ \boldsymbol{H}^{m}_{\Delta;j}(\boldsymbol{r}',t') &= \int_S \int_T^{t'} \left\{ \hat{\mathbf{G}}^{HJ}(\boldsymbol{r}',t';\boldsymbol{r},t) \cdot \left[-\boldsymbol{n} \times \Delta\boldsymbol{H}_j(\boldsymbol{r},t)\right] + \hat{\mathbf{G}}^{HM}(\boldsymbol{r}',t';\boldsymbol{r},t) \cdot \left[\boldsymbol{n} \times \Delta\boldsymbol{E}_j(\boldsymbol{r},t)\right] \right\} dt \, dS \end{aligned} \tag{4.1.19}$$

Using the host structure as the initial guess for the model in the first iteration, the following changes should be applied:

$$(\boldsymbol{\sigma},\boldsymbol{\varepsilon},\boldsymbol{\mu}) \to (\boldsymbol{\sigma}_b,\boldsymbol{\varepsilon}_b,\boldsymbol{\mu}_b) \;\; \Rightarrow \;\; \begin{cases} \boldsymbol{E}_j \to \boldsymbol{E}_{inc;j} \\ \boldsymbol{H}_j \to \boldsymbol{H}_{inc;j} \end{cases} ; \; \begin{cases} \Delta\boldsymbol{E}_j \to \boldsymbol{E}^d_j - \boldsymbol{E}_{inc;j} = \boldsymbol{E}^d_{scat;j} \\ \Delta\boldsymbol{H}_j \to \boldsymbol{H}^d_j - \boldsymbol{H}_{inc;j} = \boldsymbol{H}^d_{scat;j} \end{cases} ; \; \hat{\mathbf{G}} \to \hat{\mathbf{G}}_b \tag{4.1.20}$$

Then, Eq. (4.1.19) for the *migrated residual field* are changed into the following equations for the *migrated scattered field*:

$$\boldsymbol{E}^{m}_{scat;j}(\boldsymbol{r}',t') = \int_S \int_T^{t'} \left\{ \hat{\mathbf{G}}^{EJ}_b(\boldsymbol{r}',t';\boldsymbol{r},t) \cdot \left[-\boldsymbol{n}\times\boldsymbol{H}^{d}_{scat;j}(\boldsymbol{r},t) \right] + \hat{\mathbf{G}}^{EM}_b(\boldsymbol{r}',t';\boldsymbol{r},t) \cdot \left[\boldsymbol{n}\times\boldsymbol{E}^{d}_{scat;j}(\boldsymbol{r},t) \right] \right\} dt\, dS$$

$$\boldsymbol{H}^{m}_{scat;j}(\boldsymbol{r}',t') = \int_S \int_T^{t'} \left\{ \hat{\mathbf{G}}^{HJ}_b(\boldsymbol{r}',t';\boldsymbol{r},t) \cdot \left[-\boldsymbol{n}\times\boldsymbol{H}^{d}_{scat;j}(\boldsymbol{r},t) \right] + \hat{\mathbf{G}}^{HM}_b(\boldsymbol{r}',t';\boldsymbol{r},t) \cdot \left[\boldsymbol{n}\times\boldsymbol{E}^{d}_{scat;j}(\boldsymbol{r},t) \right] \right\} dt\, dS$$

(4.1.21)

In this case, the negative gradients of P with respect to the model parameters in Eq. (4.1.16) to (4.1.18) are defined as *apparent contrast properties*, i.e.,

$$\Delta\hat{\boldsymbol{\sigma}}(\boldsymbol{r}') = -\sum_{j=1}^{M} \int_0^T \boldsymbol{E}^{m}_{scat;j}(\boldsymbol{r}',t')\ \boldsymbol{E}_{inc;j}(\boldsymbol{r}',t')\ dt' \tag{4.1.22}$$

$$\Delta\hat{\boldsymbol{\varepsilon}}(\boldsymbol{r}') = -\sum_{j=1}^{M} \int_0^T \boldsymbol{E}^{m}_{scat;j}(\boldsymbol{r}',t')\ \dot{\boldsymbol{E}}_{inc;j}(\boldsymbol{r}',t')\ dt' \tag{4.1.23}$$

$$\Delta\hat{\boldsymbol{\mu}}(\boldsymbol{r}') = -\sum_{j=1}^{M} \int_0^T \boldsymbol{H}^{m}_{scat;j}(\boldsymbol{r}',t')\ \dot{\boldsymbol{H}}_{inc;j}(\boldsymbol{r}',t')\ dt' \tag{4.1.24}$$

Note that the apparent contrast properties are not approximations of the contrast EM properties. In fact, the physical dimensions of the apparent contrasts are completely different from those of the contrast EM properties. The images constructed from the above relations are called the *conductivity, permittivity, and permeability images*, respectively.

In view of Eq. (1.27), it can be observed that the integral equations (4.1.21) with $T \geq t \geq t'$ has the appropriate form for propagation with the adjoint Green's functions. For instance, $\hat{\mathbf{G}}^{EM}_b(\boldsymbol{r}',t';\boldsymbol{r},t)$ ($\hat{\mathbf{G}}^{EJ}_b(\boldsymbol{r}',t';\boldsymbol{r},t)$) gives the electric field at $\boldsymbol{r}'$ and time t' caused by a magnetic (electric) current source, here $\boldsymbol{n}\times\boldsymbol{E}^{d}_{scat;j}(\boldsymbol{r},t)$ ($-\boldsymbol{n}\times\boldsymbol{H}^{d}_{scat;j}(\boldsymbol{r},t)$), radiating at $\boldsymbol{r}$ at a later time t. Note that ordinary scattered fields, governed by the Maxwell's equations, propagate from scatterers to observation surface, whereas migrated scattered fields, governed by the adjoint Maxwell's equations, propagate from the observation surface to their original place, the scatterers. Mathematically, the imaging formulas (4.1.22) to (4.1.24) represent negative zero-lag cross-correlation of the migrated scattered field with the incident field.

In practice, the measurement is performed at discrete locations $\boldsymbol{r}_i \in \{\boldsymbol{r}_1, \ldots, \boldsymbol{r}_N\}$ on a planar observation surface. Then, Eq. (4.1.21) can be written as

$$\boldsymbol{E}^{m}_{scat;j}(\boldsymbol{r}',t') = \sum_{i=1}^{N} \int_{T}^{t'} \left\{ \hat{\mathbf{G}}_b^{EJ}(\boldsymbol{r}',t';\boldsymbol{r}_i,t) \cdot \left[-\boldsymbol{n} \times \boldsymbol{H}^{d}_{scat;j}(\boldsymbol{r}_i,t) \right] + \hat{\mathbf{G}}_b^{EM}(\boldsymbol{r}',t';\boldsymbol{r}_i,t) \cdot \left[\boldsymbol{n} \times \boldsymbol{E}^{d}_{scat;j}(\boldsymbol{r}_i,t) \right] \right\} dt$$

$$\boldsymbol{H}^{m}_{scat;j}(\boldsymbol{r}',t') = \sum_{i=1}^{N} \int_{T}^{t'} \left\{ \hat{\mathbf{G}}_b^{HJ}(\boldsymbol{r}',t';\boldsymbol{r}_i,t) \cdot \left[-\boldsymbol{n} \times \boldsymbol{H}^{d}_{scat;j}(\boldsymbol{r}_i,t) \right] + \hat{\mathbf{G}}_b^{HM}(\boldsymbol{r}',t';\boldsymbol{r}_i,t) \cdot \left[\boldsymbol{n} \times \boldsymbol{E}^{d}_{scat;j}(\boldsymbol{r}_i,t) \right] \right\} dt \tag{4.1.25}$$

Note that the above equations actually represent the integral equation formalism of the migrated scattered field. Considering Eq. (1.27) and the adjoint field equations (1.22), it can be inferred that the migrated scattered field satisfies equations adjoint to Maxwell's equations and that the source terms for these adjoint equations are $\boldsymbol{n} \times \boldsymbol{E}^{d}_{scat;j}(\boldsymbol{r}_i,t)$ and $-\boldsymbol{n} \times \boldsymbol{H}^{d}_{scat;j}(\boldsymbol{r}_i,t)$ at all the sensor locations radiating as magnetic and electric current sources in reverse time, respectively. Therefore, the differential equation formalism of the migrated scattered field is given by:

$$\begin{cases} -\nabla \times \boldsymbol{E}^{m}_{scat;j}(\boldsymbol{r},t) = \boldsymbol{\mu}_b^{T} \cdot \dot{\boldsymbol{H}}^{m}_{scat;j}(\boldsymbol{r},t) - \sum_{i=1}^{N} \left[\boldsymbol{n} \times \boldsymbol{E}^{d}_{scat;j}(\boldsymbol{r}_i,t) \right] \delta(\boldsymbol{r} - \boldsymbol{r}_i) \\ -\nabla \times \boldsymbol{H}^{m}_{scat;j}(\boldsymbol{r},t) = \boldsymbol{\sigma}_b^{T} \cdot \boldsymbol{E}^{m}_{scat;j}(\boldsymbol{r},t) - \boldsymbol{\varepsilon}_b^{T} \cdot \dot{\boldsymbol{E}}^{m}_{scat;j}(\boldsymbol{r},t) + \sum_{i=1}^{N} \left[-\boldsymbol{n} \times \boldsymbol{H}^{d}_{scat;j}(\boldsymbol{r}_i,t) \right] \delta(\boldsymbol{r} - \boldsymbol{r}_i) \end{cases} \tag{4.1.26}$$

where : $t = T \cdots 0$

Unlike Eq. (4.1.26) in which the sensor data are treated as sources, Zhdanov defined the migrated scattered field as the solution of the boundary value problem for the homogeneous adjoint Maxwell's equations, in which the time-dependent boundary values of the migrated field on the observation surface are determined by the scattered field data; i.e.,

$$\begin{cases} -\nabla \times \boldsymbol{E}^{m}_{scat;j}(\boldsymbol{r},t) = \boldsymbol{\mu}_b^{T} \cdot \dot{\boldsymbol{H}}^{m}_{scat;j}(\boldsymbol{r},t) \\ -\nabla \times \boldsymbol{H}^{m}_{scat;j}(\boldsymbol{r},t) = \boldsymbol{\sigma}_b^{T} \cdot \boldsymbol{E}^{m}_{scat;j}(\boldsymbol{r},t) - \boldsymbol{\varepsilon}_b^{T} \cdot \dot{\boldsymbol{E}}^{m}_{scat;j}(\boldsymbol{r},t) \end{cases} \tag{4.1.27a}$$

$$\text{BC's} : \begin{cases} \boldsymbol{n} \times \boldsymbol{E}^{m}_{scat;j}(\boldsymbol{r}_i,t) = \boldsymbol{n} \times \boldsymbol{E}^{d}_{scat;j}(\boldsymbol{r}_i,t) \\ \boldsymbol{n} \times \boldsymbol{H}^{m}_{scat;j}(\boldsymbol{r}_i,t) = \boldsymbol{n} \times \boldsymbol{H}^{d}_{scat;j}(\boldsymbol{r}_i,t) \end{cases} \quad \boldsymbol{r}_i \in \{\boldsymbol{r}_1, \ldots, \boldsymbol{r}_N\}; \quad t = T \cdots 0 \tag{4.1.27b}$$

Using relations (1.29) for a reciprocal host structure and simple change of variables in Eq. (4.1.25), the *time-reversed migrated scattered field* can be expressed in terms of ordinary Green's functions of the host structure as:

$$\widetilde{\boldsymbol{E}}^{\,m}_{scat;\,j}(\boldsymbol{r}',t') = +\sum_{i=1}^{N}\int_0^{t'}\Big\{\mathbf{G}_b^{EJ}(\boldsymbol{r}',t';\boldsymbol{r}_i,t)\cdot\big[\boldsymbol{n}\times\widetilde{\boldsymbol{H}}^{\,d}_{scat;\,j}(\boldsymbol{r}_i,t)\big]+\mathbf{G}_b^{EM}(\boldsymbol{r}',t';\boldsymbol{r}_i,t)\cdot\big[\boldsymbol{n}\times\widetilde{\boldsymbol{E}}^{\,d}_{scat;\,j}(\boldsymbol{r}_i,t)\big]\Big\}\,dt$$

$$\widetilde{\boldsymbol{H}}^{\,m}_{scat;\,j}(\boldsymbol{r}',t') = -\sum_{i=1}^{N}\int_0^{t'}\Big\{\mathbf{G}_b^{HJ}(\boldsymbol{r}',t';\boldsymbol{r}_i,t)\cdot\big[\boldsymbol{n}\times\widetilde{\boldsymbol{H}}^{\,d}_{scat;\,j}(\boldsymbol{r}_i,t)\big]+\mathbf{G}_b^{HM}(\boldsymbol{r}',t';\boldsymbol{r}_i,t)\cdot\big[\boldsymbol{n}\times\widetilde{\boldsymbol{E}}^{\,d}_{scat;\,j}(\boldsymbol{r}_i,t)\big]\Big\}\,dt \tag{4.1.28}$$

where the time-reversed of an arbitrary function is defined as:

$$\widetilde{f}(\boldsymbol{r},t) = f(\boldsymbol{r},T-t) \tag{4.1.29}$$

4.2. The Second Approach (Lagrange Multipliers)

Consider multiple scatterers (damages) embedded in a host structure (background medium) with known EM properties $\boldsymbol{\sigma}_b(\boldsymbol{r})$, $\boldsymbol{\varepsilon}_b(\boldsymbol{r})$, and $\boldsymbol{\mu}_b(\boldsymbol{r})$. All scatterers are assumed to be enclosed by the scatterer region or domain of investigation *D*. The scatterers are illuminated by incident EM waves, which are generated by actuators (sources) placed at *M* distinct positions $\boldsymbol{s}_j \in \{\boldsymbol{s}_1,\ldots,\boldsymbol{s}_M\}$ outside *D*. For each incidence, the total transient EM field is measured over an observation surface *S* outside *D* and for the time interval $[0\,,T]$. It is also assumed that the sources and all fields are zero before $t=0$. The objective is to estimate the spatial distribution of the EM properties inside the domain *D* using the set of measurements.

Gradient-based inversion methods are very common for solving nonlinear inverse scattering problems. In these methods, first, a nonlinear cost (objective) functional is constructed (e.g., data error (misfit) functional, which is the norm of the difference between the measured field and the calculated field obtained from a model on the observation surface). Then, the cost functional is minimized in order to obtain the best estimation of EM

properties inside *D*. The minimization is carried out by sequentially updating the model by steps along the gradient directions.

To construct the cost functional in the EM migration, a total instantaneous power flow of the residual field through the observation surface is defined for each experiment as:

$$p_j(t) = \int_S \left(\Delta \boldsymbol{E}_j \times \Delta \boldsymbol{H}_j \right) \cdot \boldsymbol{n} \, dS \tag{4.2.1}$$

where $\boldsymbol{n}$ is a unit normal vector pointing outward of S (pointing away the scatterer region) and the data residuals are given by

$$\begin{aligned} \Delta \boldsymbol{E}_j(\boldsymbol{r},t) &= \boldsymbol{E}_j^d(\boldsymbol{r},t) - \boldsymbol{E}_j(\boldsymbol{r},t) \\ \Delta \boldsymbol{H}_j(\boldsymbol{r},t) &= \boldsymbol{H}_j^d(\boldsymbol{r},t) - \boldsymbol{H}_j(\boldsymbol{r},t) \end{aligned} \tag{4.2.2}$$

where $\boldsymbol{E}_j^d(\boldsymbol{r},t)$ and $\boldsymbol{H}_j^d(\boldsymbol{r},t)$ are the measured EM field, and $\boldsymbol{E}_j(\boldsymbol{r},t)$ and $\boldsymbol{H}_j(\boldsymbol{r},t)$ are the calculated EM field for a given model.

It has been shown (Zhdanov, 2002) that the power flow of the residual field is non-negative, i.e., $p_j(t) \geq 0$. Note that there are no external EM sources inside the region surrounded by the observation surface *S* (the scatterer region). Based on the non-negativeness property of the power flow, the following cost functional is introduced:

$$P(\boldsymbol{\sigma}, \boldsymbol{\varepsilon}, \boldsymbol{\mu}) = \sum_{j=1}^{M} \int_0^T \int_S \left(\Delta \boldsymbol{E}_j \times \Delta \boldsymbol{H}_j \right) \cdot \boldsymbol{n} \, dS \, dt \tag{4.2.3}$$

The dependence of the functional *P* on the *model parameters* ($\boldsymbol{\sigma}$, $\boldsymbol{\varepsilon}$, and $\boldsymbol{\mu}$) arises from the implicit dependence of the calculated field $\boldsymbol{E}_j(\boldsymbol{r},t)$ and $\boldsymbol{H}_j(\boldsymbol{r},t)$ on these parameters. Now, the constraint of fulfillment of the Maxwell's equations (1.9) is introduced to *P* by using Lagrange vector-multipliers $\boldsymbol{E}^{adj}$ and $\boldsymbol{H}^{adj}$. This leads to the augmented cost functional (Rekanos and Räisänen, 2003):

$$F(\boldsymbol{\sigma},\boldsymbol{\varepsilon},\boldsymbol{\mu},\boldsymbol{E},\boldsymbol{H},\boldsymbol{E}^{adj},\boldsymbol{H}^{adj}) = \sum_{j=1}^{M}\int_0^T\int_S \left(\Delta\boldsymbol{E}_j \times \Delta\boldsymbol{H}_j\right)\cdot\boldsymbol{n}\,dS\,dt + \sum_{j=1}^{M}\int_0^T\int_V \left[\boldsymbol{E}_j^{adj}\cdot\left(\nabla\times\boldsymbol{H}_j - \boldsymbol{\sigma}\cdot\boldsymbol{E}_j - \boldsymbol{\varepsilon}\cdot\dot{\boldsymbol{E}}_j - \boldsymbol{J}_j\right) + \boldsymbol{H}_j^{adj}\cdot\left(\nabla\times\boldsymbol{E}_j + \boldsymbol{\mu}\cdot\dot{\boldsymbol{H}}_j + \boldsymbol{M}_j\right)\right] dV\,dt \tag{4.2.4}$$

where V is the total space of field computation. The necessary condition for the minimization of F is that its first variation is equal to zero, i.e., $\delta^{(1)}F = 0$,

$$\begin{aligned}\delta^{(1)}F = &\sum_{j=1}^{M}\int_0^T\int_S \left(-\delta\boldsymbol{E}_j\times\Delta\boldsymbol{H}_j + \Delta\boldsymbol{E}_j\times-\delta\boldsymbol{H}_j\right)\cdot\boldsymbol{n}\,dS\,dt + \\ &\sum_{j=1}^{M}\int_0^T\int_V \left[\delta\boldsymbol{E}_j^{adj}\cdot\left(\nabla\times\boldsymbol{H}_j - \boldsymbol{\sigma}\cdot\boldsymbol{E}_j - \boldsymbol{\varepsilon}\cdot\dot{\boldsymbol{E}}_j - \boldsymbol{J}_j\right) + \right. \\ &\left.\delta\boldsymbol{H}_j^{adj}\cdot\left(\nabla\times\boldsymbol{E}_j + \boldsymbol{\mu}\cdot\dot{\boldsymbol{H}}_j + \boldsymbol{M}_j\right)\right] dV\,dt + \\ &\sum_{j=1}^{M}\int_0^T\int_V \left[\boldsymbol{E}_j^{adj}\cdot\left(\nabla\times\delta\boldsymbol{H}_j - \delta\boldsymbol{\sigma}\cdot\boldsymbol{E}_j - \boldsymbol{\sigma}\cdot\delta\boldsymbol{E}_j - \delta\boldsymbol{\varepsilon}\cdot\dot{\boldsymbol{E}}_j - \boldsymbol{\varepsilon}\cdot\delta\dot{\boldsymbol{E}}_j\right) + \right. \\ &\left.\boldsymbol{H}_j^{adj}\cdot\left(\nabla\times\delta\boldsymbol{E}_j + \delta\boldsymbol{\mu}\cdot\dot{\boldsymbol{H}}_j + \boldsymbol{\mu}\cdot\delta\dot{\boldsymbol{H}}_j\right)\right] dV\,dt = 0\end{aligned} \tag{4.2.5}$$

In practice, the measurement is performed at discrete locations $\boldsymbol{r}_i \in \{\boldsymbol{r}_1,\ldots,\boldsymbol{r}_N\}$ on a planar observation surface S. Using the divergence (Gauss') theorem, integration by parts, and the following identities for vectors $\boldsymbol{A}$, $\boldsymbol{B}$, and $\boldsymbol{C}$ and second-order tensor $\mathbf{D}$:

$$\begin{aligned}&\nabla\cdot(\boldsymbol{A}\times\boldsymbol{B}) = \boldsymbol{B}\cdot\nabla\times\boldsymbol{A} - \boldsymbol{A}\cdot\nabla\times\boldsymbol{B}\\ &\boldsymbol{A}\cdot(\boldsymbol{B}\times\boldsymbol{C}) = \boldsymbol{B}\cdot(\boldsymbol{C}\times\boldsymbol{A}) = \boldsymbol{C}\cdot(\boldsymbol{A}\times\boldsymbol{B})\\ &\boldsymbol{A}\cdot(\mathbf{D}\cdot\boldsymbol{B}) = \boldsymbol{B}\cdot(\mathbf{D}^T\cdot\boldsymbol{A}) = \boldsymbol{A}\boldsymbol{B}:\mathbf{D}^T,\end{aligned} \tag{4.2.6}$$

the first variation of F is reduced to

$$
\begin{aligned}
\delta^{(1)}F = &\sum_{j=1}^{M}\int_0^T\int_V \Big[\delta \boldsymbol{E}_j^{adj}\cdot\left(\nabla\times\boldsymbol{H}_j-\boldsymbol{\sigma}\cdot\boldsymbol{E}_j-\boldsymbol{\varepsilon}\cdot\dot{\boldsymbol{E}}_j-\boldsymbol{J}_j\right)+\\
&\qquad \delta \boldsymbol{H}_j^{adj}\cdot\left(\nabla\times\boldsymbol{E}_j+\boldsymbol{\mu}\cdot\dot{\boldsymbol{H}}_j+\boldsymbol{M}_j\right)\Big]dV\,dt+\\
&\sum_{j=1}^{M}\int_0^T\int_V\Bigg[\delta\boldsymbol{H}_j\cdot\left(\nabla\times\boldsymbol{E}_j^{adj}-\boldsymbol{\mu}^T\cdot\dot{\boldsymbol{H}}_j^{adj}-\sum_{i=1}^{N}\left(\boldsymbol{n}\times\Delta\boldsymbol{E}_j\right)\delta(\boldsymbol{r}-\boldsymbol{r}_i)\right)+\\
&\qquad \delta\boldsymbol{E}_j\cdot\left(\nabla\times\boldsymbol{H}_j^{adj}-\boldsymbol{\sigma}^T\cdot\boldsymbol{E}_j^{adj}+\boldsymbol{\varepsilon}^T\cdot\dot{\boldsymbol{E}}_j^{adj}+\sum_{i=1}^{N}\left(\boldsymbol{n}\times\Delta\boldsymbol{H}_j\right)\delta(\boldsymbol{r}-\boldsymbol{r}_i)\right)\Bigg]dV\,dt+\\
&\int_D\Bigg[\left(-\sum_{j=1}^{M}\int_0^T\boldsymbol{E}_j^{adj}\boldsymbol{E}_j\,dt\right):\delta\boldsymbol{\sigma}^T+\left(-\sum_{j=1}^{M}\int_0^T\boldsymbol{E}_j^{adj}\dot{\boldsymbol{E}}_j\,dt\right):\delta\boldsymbol{\varepsilon}^T+\left(\sum_{j=1}^{M}\int_0^T\boldsymbol{H}_j^{adj}\dot{\boldsymbol{H}}_j\,dt\right):\delta\boldsymbol{\mu}^T\Bigg]\,dV+\\
&\sum_{j=1}^{M}\int_V\left[\boldsymbol{H}_j^{adj}\cdot\left(\boldsymbol{\mu}\cdot\delta\boldsymbol{H}_j\right)-\boldsymbol{E}_j^{adj}\cdot\left(\boldsymbol{\varepsilon}\cdot\delta\boldsymbol{E}_j\right)\right]_0^T dV-\\
&\sum_{j=1}^{M}\int_0^T\int_{\partial V}\left(\boldsymbol{E}_j^{adj}\times\delta\boldsymbol{H}_j+\boldsymbol{H}_j^{adj}\times\delta\boldsymbol{E}_j\right)\cdot\boldsymbol{n}_V\,dS\,dt=0
\end{aligned}
\tag{4.2.7}
$$

where ∂V and $\boldsymbol{n}_V$ are the surface boundary of the volume V and the outward unit vector normal to the surface ∂V, respectively.

The stationary condition (4.2.7) requires that the Lagrange multipliers $\boldsymbol{E}_j^{adj}$ and $\boldsymbol{H}_j^{adj}$, which can also be recognized as the *adjoint field*, should satisfy the following equations (coefficient terms of $\delta\boldsymbol{H}_j$ and $\delta\boldsymbol{E}_j$):

$$
\begin{cases}
\nabla\times\boldsymbol{E}_j^{adj}=\boldsymbol{\mu}^T\cdot\dot{\boldsymbol{H}}_j^{adj}-\sum_{i=1}^{N}\left[-\boldsymbol{n}\times\Delta\boldsymbol{E}_j\right]\delta(\boldsymbol{r}-\boldsymbol{r}_i)\\
\nabla\times\boldsymbol{H}_j^{adj}=\boldsymbol{\sigma}^T\cdot\boldsymbol{E}_j^{adj}-\boldsymbol{\varepsilon}^T\cdot\dot{\boldsymbol{E}}_j^{adj}+\sum_{i=1}^{N}\left[-\boldsymbol{n}\times\Delta\boldsymbol{H}_j\right]\delta(\boldsymbol{r}-\boldsymbol{r}_i)
\end{cases}
\tag{4.2.8}
$$

The corresponding initial and boundary conditions of the above equations can be obtained from condition (4.2.7). For example, when the EM field has zero initial condition and satisfies the *Sommerfeld radiation condition*, i.e.,

$$
\boldsymbol{E}_j(\boldsymbol{r},t=0)=\boldsymbol{H}_j(\boldsymbol{r},t=0)=0 \tag{4.2.9}
$$

$$\lim_{r\to\infty} r[\nabla\times\boldsymbol{E}_j + c_0^{-1}\boldsymbol{n}_V\times\dot{\boldsymbol{E}}_j] = 0$$
$$\lim_{r\to\infty} r[\nabla\times\boldsymbol{H}_j + c_0^{-1}\boldsymbol{n}_V\times\dot{\boldsymbol{H}}_j] = 0 \qquad (4.2.10)$$

where $r = |\boldsymbol{r}|$ and c_0 is the EM speed in vacuum, the initial and boundary conditions for $\boldsymbol{E}_j^{adj}$ and $\boldsymbol{H}_j^{adj}$ are derived as:

$$\boldsymbol{E}_j^{adj}(\boldsymbol{r}, t=T) = \boldsymbol{H}_j^{adj}(\boldsymbol{r}, t=T) = 0 \qquad (4.2.11)$$

$$\lim_{r\to\infty} r[\nabla\times\boldsymbol{E}_j^{adj} - c_0^{-1}\boldsymbol{n}_V\times\dot{\boldsymbol{E}}_j^{adj}] = 0$$
$$\lim_{r\to\infty} r[\nabla\times\boldsymbol{H}_j^{adj} - c_0^{-1}\boldsymbol{n}_V\times\dot{\boldsymbol{H}}_j^{adj}] = 0 \qquad (4.2.12)$$

From Eq. (4.2.8) and the initial and boundary conditions (4.2.11) and (4.2.12), it is concluded that the adjoint field is generated by sources located at the positions of measurements. Actually, these sources are the discrepancies between the measured and calculated fields. Furthermore, it is observed that the adjoint field propagates backward in time, starting at $t = T$.

The gradients (Frechet derivatives) of the functional *F* with respect to the model parameters inside *D* are obtained from those terms of relation (4.2.7) that include the first variations of the parameters. In particular, the gradients are given by

$$\frac{\partial F}{\partial \boldsymbol{\sigma}} = -\sum_{j=1}^{M}\int_0^T \boldsymbol{E}_j^{adj}\boldsymbol{E}_j\, dt \qquad (4.2.13)$$

$$\frac{\partial F}{\partial \boldsymbol{\varepsilon}} = -\sum_{j=1}^{M}\int_0^T \boldsymbol{E}_j^{adj}\dot{\boldsymbol{E}}_j\, dt \qquad (4.2.14)$$

$$\frac{\partial F}{\partial \boldsymbol{\mu}} = +\sum_{j=1}^{M}\int_0^T \boldsymbol{H}_j^{adj}\dot{\boldsymbol{H}}_j\, dt \qquad (4.2.15)$$

The above gradients can be utilized in any iterative gradient-based inversion algorithm used for estimating the EM properties.

In the EM migration algorithm, the negative gradients are defined as the imaging formulas provided that the model is the host structure. Thus, the following changes should be applied:

$$(\boldsymbol{\sigma},\boldsymbol{\varepsilon},\boldsymbol{\mu}) \to (\boldsymbol{\sigma}_b,\boldsymbol{\varepsilon}_b,\boldsymbol{\mu}_b) \quad \Rightarrow \quad \begin{cases} \boldsymbol{E}_j \to \boldsymbol{E}_{inc;j} \\ \boldsymbol{H}_j \to \boldsymbol{H}_{inc;j} \end{cases}; \quad \begin{cases} \Delta\boldsymbol{E}_j \to \boldsymbol{E}_j^d - \boldsymbol{E}_{inc;j} = \boldsymbol{E}_{scat;j}^d \\ \Delta\boldsymbol{H}_j \to \boldsymbol{H}_j^d - \boldsymbol{H}_{inc;j} = \boldsymbol{H}_{scat;j}^d \end{cases} \tag{4.2.16}$$

Considering the above changes on the gradients (4.2.13) to (4.2.15), the conductivity, permittivity and permeability imaging formulas are obtained as:

$$\Delta\hat{\boldsymbol{\sigma}}(\boldsymbol{r}) = +\sum_{j=1}^{M}\int_0^T \boldsymbol{E}_j^{adj}(\boldsymbol{r},t)\,\boldsymbol{E}_{inc;j}(\boldsymbol{r},t)\,dt \tag{4.2.17}$$

$$\Delta\hat{\boldsymbol{\varepsilon}}(\boldsymbol{r}) = +\sum_{j=1}^{M}\int_0^T \boldsymbol{E}_j^{adj}(\boldsymbol{r},t)\,\dot{\boldsymbol{E}}_{inc;j}(\boldsymbol{r},t)\,dt \tag{4.2.18}$$

$$\Delta\hat{\boldsymbol{\mu}}(\boldsymbol{r}) = -\sum_{j=1}^{M}\int_0^T \boldsymbol{H}_j^{adj}(\boldsymbol{r},t)\,\dot{\boldsymbol{H}}_{inc;j}(\boldsymbol{r},t)\,dt \tag{4.2.19}$$

Applying the changes (4.2.16) on the adjoint equations (4.2.8), leads to the following equations for calculating the adjoint field used in EM migration imaging formulas (4.2.17) to (4.2.19),

$$\begin{cases} \nabla\times\boldsymbol{E}_j^{adj} = \boldsymbol{\mu}_b^T\cdot\dot{\boldsymbol{H}}_j^{adj} - \sum_{i=1}^{N}\left[-\boldsymbol{n}\times\boldsymbol{E}_{scat;j}^d\right]\delta(\boldsymbol{r}-\boldsymbol{r}_i) \\ \nabla\times\boldsymbol{H}_j^{adj} = \boldsymbol{\sigma}_b^T\cdot\boldsymbol{E}_j^{adj} - \boldsymbol{\varepsilon}_b^T\cdot\dot{\boldsymbol{E}}_j^{adj} + \sum_{i=1}^{N}\left[-\boldsymbol{n}\times\boldsymbol{H}_{scat;j}^d\right]\delta(\boldsymbol{r}-\boldsymbol{r}_i) \end{cases} \tag{4.2.20}$$

By applying the time transformation $t = T - t$, equations (4.2.20) and the associated initial and boundary conditions (4.2.11) and (4.2.12) are transformed into:

$$\begin{cases} \nabla\times\tilde{\boldsymbol{E}}_j^{adj} = -\boldsymbol{\mu}_b^T\cdot\ddot{\tilde{\boldsymbol{H}}}_j^{adj} - \sum_{i=1}^{N}\left[-\boldsymbol{n}\times\tilde{\boldsymbol{E}}_{scat;j}^d\right]\delta(\boldsymbol{r}-\boldsymbol{r}_i) \\ \nabla\times\tilde{\boldsymbol{H}}_j^{adj} = \boldsymbol{\sigma}_b^T\cdot\tilde{\boldsymbol{E}}_j^{adj} + \boldsymbol{\varepsilon}_b^T\cdot\dot{\tilde{\boldsymbol{E}}}_j^{adj} + \sum_{i=1}^{N}\left[-\boldsymbol{n}\times\tilde{\boldsymbol{H}}_{scat;j}^d\right]\delta(\boldsymbol{r}-\boldsymbol{r}_i) \end{cases} \tag{4.2.21}$$

$$\tilde{\boldsymbol{E}}_j^{adj}(\boldsymbol{r},t=0) = \tilde{\boldsymbol{H}}_j^{adj}(\boldsymbol{r},t=0) = 0 \tag{4.2.22}$$

$$\lim_{r\to\infty} r[\nabla\times\tilde{\tilde{\boldsymbol{E}}}_j^{adj} + c_0^{-1}\boldsymbol{n}_V\times\dot{\tilde{\tilde{\boldsymbol{E}}}}_j^{adj}] = 0$$
$$\lim_{r\to\infty} r[\nabla\times\tilde{\tilde{\boldsymbol{H}}}_j^{adj} + c_0^{-1}\boldsymbol{n}_V\times\dot{\tilde{\tilde{\boldsymbol{H}}}}_j^{adj}] = 0 \qquad (4.2.23)$$

where the time-reversed of an arbitrary function is defined in (4.1.29).

Therefore, the *time-reversed adjoint field* satisfies ordinary Maxwell's equations in a medium with the EM properties transposed to those of the host structure, has zero initial condition at $t = 0$, satisfies Sommerfeld radiation condition and propagates forward in time.

In the case of reciprocal host structures, $\boldsymbol{\sigma}_b = \boldsymbol{\sigma}_b^T, \boldsymbol{\varepsilon}_b = \boldsymbol{\varepsilon}_b^T, \boldsymbol{\mu}_b = \boldsymbol{\mu}_b^T$, the time-reversed adjoint field satisfies ordinary Maxwell's equations in the host structure with the $-\boldsymbol{n}\times\tilde{\boldsymbol{H}}_{scat;j}^{d}$ and $-\boldsymbol{n}\times\tilde{\boldsymbol{E}}_{scat;j}^{d}$ as electric and magnetic current sources located at sensor positions. Then, the time-reversed adjoint field can be expressed in terms of ordinary Green's functions of the host structure as:

$$\tilde{\boldsymbol{E}}_j^{adj}(\boldsymbol{r},t) = \sum_{i=1}^{N}\int_0^t \left\{\mathbf{G}_b^{EJ}(\boldsymbol{r},t;\boldsymbol{r}_i,t')\cdot\left[-\boldsymbol{n}\times\tilde{\boldsymbol{H}}_{scat;j}^{d}(\boldsymbol{r}_i,t')\right] + \mathbf{G}_b^{EM}(\boldsymbol{r},t;\boldsymbol{r}_i,t')\cdot\left[-\boldsymbol{n}\times\tilde{\boldsymbol{E}}_{scat;j}^{d}(\boldsymbol{r}_i,t')\right]\right\}dt'$$
$$\tilde{\boldsymbol{H}}_j^{adj}(\boldsymbol{r},t) = \sum_{i=1}^{N}\int_0^t \left\{\mathbf{G}_b^{HJ}(\boldsymbol{r},t;\boldsymbol{r}_i,t')\cdot\left[-\boldsymbol{n}\times\tilde{\boldsymbol{H}}_{scat;j}^{d}(\boldsymbol{r}_i,t')\right] + \mathbf{G}_b^{HM}(\boldsymbol{r},t;\boldsymbol{r}_i,t')\cdot\left[-\boldsymbol{n}\times\tilde{\boldsymbol{E}}_{scat;j}^{d}(\boldsymbol{r}_i,t')\right]\right\}dt' \qquad (4.2.24)$$

Comparing Eq. (4.1.22) to (4.1.24) and (4.1.28) with Eq. (4.2.17) to (4.2.19) and (4.2.24), it is concluded that the two approaches are equivalent.

5. Born Imaging Algorithm

It has been identified that the standard prestack migration operator can be regarded as the adjoint of the linear forward modeling operator (Claerbout, 1992). Based on this analogy, in the first section of this chapter, the adjoint operators for general transient EM fields in an inhomogeneous anisotropic structure are derived. These adjoint operators form our second proposed linearized imaging algorithm: *Born imaging algorithm*. At the second section of the chapter, the relation between the adjoint operators and the gradients (Frechet derivatives or sensitivities) of an error functional with respect to model parameters typically used in iterations of gradient-based inversion methods is discussed.

5.1. Born Imaging Formulas

The first step for developing the Born imaging algorithm is to linearize the nonlinear inverse medium problem by applying the Born approximation. In Born approximation, the total field inside the scatterer (damage) in Eq. (3.1) is approximated by the incident field, i.e.,

$$\begin{aligned}\boldsymbol{E}_{scat}^{d}(\boldsymbol{r},t) \cong & \int_0^t \int_{V_{scat}} \mathbf{G}_b^{EJ}(\boldsymbol{r},t;\boldsymbol{r}',t') \cdot \left[\Delta\boldsymbol{\sigma}(\boldsymbol{r}') \cdot \boldsymbol{E}_{inc}(\boldsymbol{r}',t') + \Delta\boldsymbol{\varepsilon}(\boldsymbol{r}') \cdot \dot{\boldsymbol{E}}_{inc}(\boldsymbol{r}',t')\right] dV'dt' + \\ & \int_0^t \int_{V_{scat}} \mathbf{G}_b^{EM}(\boldsymbol{r},t;\boldsymbol{r}',t') \cdot \left[\Delta\boldsymbol{\mu}(\boldsymbol{r}') \cdot \dot{\boldsymbol{H}}_{inc}(\boldsymbol{r}',t')\right] dV'dt'\end{aligned} \tag{5.1.1a}$$

$$\begin{aligned}\boldsymbol{H}_{scat}^{d}(\boldsymbol{r},t) \cong & \int_0^t \int_{V_{scat}} \mathbf{G}_b^{HJ}(\boldsymbol{r},t;\boldsymbol{r}',t') \cdot \left[\Delta\boldsymbol{\sigma}(\boldsymbol{r}') \cdot \boldsymbol{E}_{inc}(\boldsymbol{r}',t') + \Delta\boldsymbol{\varepsilon}(\boldsymbol{r}') \cdot \dot{\boldsymbol{E}}_{inc}(\boldsymbol{r}',t')\right] dV'dt' + \\ & \int_0^t \int_{V_{scat}} \mathbf{G}_b^{HM}(\boldsymbol{r},t;\boldsymbol{r}',t') \cdot \left[\Delta\boldsymbol{\mu}(\boldsymbol{r}') \cdot \dot{\boldsymbol{H}}_{inc}(\boldsymbol{r}',t')\right] dV'dt'\end{aligned} \tag{5.1.1b}$$

where the scattered electric and magnetic fields data are:

$$\boldsymbol{E}_{scat}^{d}(\boldsymbol{r},t) = \boldsymbol{E}^{d}(\boldsymbol{r},t) - \boldsymbol{E}_{inc}(\boldsymbol{r},t) \tag{5.1.2a}$$

$$\boldsymbol{H}_{scat}^{d}(\boldsymbol{r},t) = \boldsymbol{H}^{d}(\boldsymbol{r},t) - \boldsymbol{H}_{inc}(\boldsymbol{r},t) \tag{5.1.2b}$$

This approximation transforms the inherently nonlinear inverse problem into a linear one, because only $\Delta\boldsymbol{\sigma}(\boldsymbol{r})$, $\Delta\boldsymbol{\varepsilon}(\boldsymbol{r})$, and $\Delta\boldsymbol{\mu}(\boldsymbol{r})$ are unknowns in the above integral equations.

In other words, the scattered field data linearly depends on the contrast EM properties. However, the inverse problem of solving $\Delta\boldsymbol{\sigma}(\boldsymbol{r})$, $\Delta\boldsymbol{\varepsilon}(\boldsymbol{r})$, and $\Delta\boldsymbol{\mu}(\boldsymbol{r})$ still remains ill-posed. It is worth noting that the data collected by sensors on an observation surface is actually the total electric and magnetic field ($\boldsymbol{E}^d$ and $\boldsymbol{H}^d$). One can simply obtain the scattered field data from $\boldsymbol{E}^d_{scat} = \boldsymbol{E}^d - \boldsymbol{E}_{inc}$ and $\boldsymbol{H}^d_{scat} = \boldsymbol{H}^d - \boldsymbol{H}_{inc}$ by knowing the incident field on the observation surface.

It should be pointed out that as in the diffraction tomographic method (e.g., Cui and Chew, 2002) the linearized imaging formulas are derived in three steps. In each step, only one of the contrast EM properties is kept as the unknown and the other two are assumed to be zero.

Let's first consider the case when $\Delta\boldsymbol{\sigma}(\boldsymbol{r})$ and $\Delta\boldsymbol{\mu}(\boldsymbol{r})$ are zero. Then, Eq. (5.1.1) reduce to:

$$\boldsymbol{E}^d_{scat}(\boldsymbol{r},t) \cong \boldsymbol{L}^{E,\varepsilon}_b[\Delta\boldsymbol{\varepsilon}] = \int_0^t \int_{V_{scat}} \mathbf{G}^{EJ}_b(\boldsymbol{r},t;\boldsymbol{r}',t') \cdot \left[\Delta\boldsymbol{\varepsilon}(\boldsymbol{r}') \cdot \dot{\boldsymbol{E}}_{inc}(\boldsymbol{r}',t')\right] dV'dt' \tag{5.1.3a}$$

$$\boldsymbol{H}^d_{scat}(\boldsymbol{r},t) \cong \boldsymbol{L}^{H,\varepsilon}_b[\Delta\boldsymbol{\varepsilon}] = \int_0^t \int_{V_{scat}} \mathbf{G}^{HJ}_b(\boldsymbol{r},t;\boldsymbol{r}',t') \cdot \left[\Delta\boldsymbol{\varepsilon}(\boldsymbol{r}') \cdot \dot{\boldsymbol{E}}_{inc}(\boldsymbol{r}',t')\right] dV'dt' \tag{5.1.3b}$$

where $\boldsymbol{L}^{E,\varepsilon}_b$ and $\boldsymbol{L}^{H,\varepsilon}_b$ are the linear modeling operators.

Generally speaking, to obtain the contrast permittivity $\Delta\boldsymbol{\varepsilon}$ from the measurements $\boldsymbol{E}^d_{scat}$ or $\boldsymbol{H}^d_{scat}$, the inverse of the linear modeling operators $\boldsymbol{L}^{E,\varepsilon}_b$ or $\boldsymbol{L}^{H,\varepsilon}_b$ are required. However, in Born imaging algorithm, these inverse operators are approximated with adjoint operators. Then, depending on which measured field, electric or magnetic, is being used, two imaging formulas can be written as follows:

$$\Delta\hat{\boldsymbol{\varepsilon}}_E(\boldsymbol{r}') = \hat{\boldsymbol{L}}^{E,\varepsilon}_b[\boldsymbol{E}^d_{scat}] \tag{5.1.4a}$$

$$\Delta\hat{\boldsymbol{\varepsilon}}_H(\boldsymbol{r}') = \hat{\boldsymbol{L}}^{H,\varepsilon}_b[\boldsymbol{H}^d_{scat}] \tag{5.1.4b}$$

where $\hat{\boldsymbol{L}}^{E,\varepsilon}_b$ and $\hat{\boldsymbol{L}}^{H,\varepsilon}_b$ are the *adjoint* (*imaging*) *operators* of $\boldsymbol{L}^{E,\varepsilon}_b$ and $\boldsymbol{L}^{H,\varepsilon}_b$, respectively, and $\Delta\hat{\boldsymbol{\varepsilon}}$ is the *apparent contrast permittivity*. Note that the apparent contrast permittivity is not an

approximation of the contrast permittivity due to the substitution of the linear inverse operator with the adjoint operator.

The adjoint operators can be derived using functional analysis theory (e.g., Zhdanov, 2002). To do so, a Hilbert space H_D of data (scattered field on the observation surface S) is defined with the following inner products:

$$< \boldsymbol{d}_1, \boldsymbol{d}_2 >_{H_D} = \int_0^T \int_S \boldsymbol{d}_1(\boldsymbol{r},t) \cdot \boldsymbol{d}_2(\boldsymbol{r},t) dS dt \qquad \forall \boldsymbol{d}_1, \boldsymbol{d}_2 \in H_D \tag{5.1.5}$$

where "T" is the maximum time of measurement.

Then, a Hilbert space H_M of contrast permittivity is introduced with the following inner products:

$$< \Delta\boldsymbol{\varepsilon}_1, \Delta\boldsymbol{\varepsilon}_2 >_{H_M} = \int_D \Delta\boldsymbol{\varepsilon}_1(\boldsymbol{r}') : \Delta\boldsymbol{\varepsilon}_2^T(\boldsymbol{r}') dV' \qquad \forall \Delta\boldsymbol{\varepsilon}_1, \Delta\boldsymbol{\varepsilon}_2 \in H_M \tag{5.1.6}$$

where " : " indicates double dot product of tensors and D is the scatterer region.

The above definitions can be expressed in component form,

$$< \boldsymbol{d}_1, \boldsymbol{d}_2 >_{H_D} = \int_0^T \int_S d_{1i}(\boldsymbol{r},t)\, d_{2i}(\boldsymbol{r},t) dS dt \qquad i = 1,2,3 \tag{5.1.7}$$

$$< \Delta\boldsymbol{\varepsilon}_1, \Delta\boldsymbol{\varepsilon}_2 >_{H_M} = \int_D \Delta\varepsilon_{1\,jk}(\boldsymbol{r}') \Delta\varepsilon_{2\,jk}(\boldsymbol{r}') dV' \qquad j,k = 1,2,3 \tag{5.1.8}$$

The mathematical relationships among the operators and their adjoints are:

$$< \boldsymbol{L}_b^{E,\varepsilon}[\Delta\boldsymbol{\varepsilon}], \boldsymbol{d} >_{H_D} = < \Delta\boldsymbol{\varepsilon}, \hat{\boldsymbol{L}}_b^{E,\varepsilon}[\boldsymbol{d}] >_{H_M} \qquad \forall \boldsymbol{d} \in H_D \text{ and } \forall \Delta\boldsymbol{\varepsilon} \in H_M \tag{5.1.9a}$$

$$< \boldsymbol{L}_b^{H,\varepsilon}[\Delta\boldsymbol{\varepsilon}], \boldsymbol{d} >_{H_D} = < \Delta\boldsymbol{\varepsilon}, \hat{\boldsymbol{L}}_b^{H,\varepsilon}[\boldsymbol{d}] >_{H_M} \qquad \forall \boldsymbol{d} \in H_D \text{ and } \forall \Delta\boldsymbol{\varepsilon} \in H_M \tag{5.1.9b}$$

Using the definitions (5.1.5) and (5.1.7) of inner products and expression (5.1.3a), the left hand side of Eq. (5.1.9a) can be written as:

$$
\begin{aligned}
< \boldsymbol{L}_b^{E,\varepsilon}\,[\Delta\boldsymbol{\varepsilon}], \boldsymbol{d} >_{H_D} &= \int_0^T \int_S \boldsymbol{L}_b^{E,\varepsilon}\,[\Delta\boldsymbol{\varepsilon}] \cdot \boldsymbol{d}(\boldsymbol{r},t) dSdt \\
&= \int_0^T \int_S \left[\int_0^t \int_D \mathbf{G}_b^{EJ}(\boldsymbol{r},t;\boldsymbol{r}',t') \cdot \Delta\boldsymbol{\varepsilon}(\boldsymbol{r}') \cdot \dot{\boldsymbol{E}}_{inc}(\boldsymbol{r}',t')\, dV'dt' \right] \cdot \boldsymbol{d}(\boldsymbol{r},t) dSdt \\
&= \int_0^T \int_S \left[\int_0^t \int_D G_b^{EJ}{}_{ij}(\boldsymbol{r},t;\boldsymbol{r}',t')\, \Delta\varepsilon_{jk}(\boldsymbol{r}')\, \dot{E}_{inc\,k}(\boldsymbol{r}',t')\, dV'dt' \right] d_i(\boldsymbol{r},t) dSdt \\
&= \int_D \Delta\varepsilon_{jk}(\boldsymbol{r}') \left\{ \int_0^T \left[\int_{t'}^T \int_S d_i(\boldsymbol{r},t)\, G_b^{EJ}{}_{ij}(\boldsymbol{r},t;\boldsymbol{r}',t') dSdt \right] \dot{E}_{inc\,k}(\boldsymbol{r}',t')\, dt' \right\} dV'
\end{aligned}
\tag{5.1.10}
$$

Therefore, based on Eq. (5.1.9a) and the definitions (5.1.6) and (5.1.8), the desired adjoint operator $\hat{\boldsymbol{L}}_b^{E,\varepsilon}$ is found to be:

$$
\begin{aligned}
\hat{\boldsymbol{L}}_b^{E,\varepsilon}\,[\boldsymbol{d}] &= \int_0^T \left[\int_{t'}^T \int_S d_i(\boldsymbol{r},t)\, G_b^{EJ}{}_{ij}(\boldsymbol{r},t;\boldsymbol{r}',t') dSdt \right] \dot{E}_{inc\,k}(\boldsymbol{r}',t')\, dt' \\
&= \int_0^T \left[\int_{t'}^T \int_S \boldsymbol{d}(\boldsymbol{r},t) \cdot \mathbf{G}_b^{EJ}(\boldsymbol{r},t;\boldsymbol{r}',t') dSdt \right] \dot{\boldsymbol{E}}_{inc}(\boldsymbol{r}',t')\, dt'
\end{aligned}
\tag{5.1.11a}
$$

Similarly, the other adjoint operator can be obtained as

$$
\hat{\boldsymbol{L}}_b^{H,\varepsilon}\,[\boldsymbol{d}] = \int_0^T \left[\int_{t'}^T \int_S \boldsymbol{d}(\boldsymbol{r},t) \cdot \mathbf{G}_b^{HJ}(\boldsymbol{r},t;\boldsymbol{r}',t') dSdt \right] \dot{\boldsymbol{E}}_{inc}(\boldsymbol{r}',t')\, dt' \tag{5.1.11b}
$$

Using the derived adjoint operators, the imaging formulas (5.1.4) become:

$$
\Delta\hat{\boldsymbol{\varepsilon}}_E(\boldsymbol{r}') = \int_0^T \left[\int_{t'}^T \int_S \boldsymbol{E}_{scat}^{d}(\boldsymbol{r},t) \cdot \mathbf{G}_b^{EJ}(\boldsymbol{r},t;\boldsymbol{r}',t') dSdt \right] \dot{\boldsymbol{E}}_{inc}(\boldsymbol{r}',t')\, dt' \tag{5.1.12a}
$$

$$
\Delta\hat{\boldsymbol{\varepsilon}}_H(\boldsymbol{r}') = \int_0^T \left[\int_{t'}^T \int_S \boldsymbol{H}_{scat}^{d}(\boldsymbol{r},t) \cdot \mathbf{G}_b^{HJ}(\boldsymbol{r},t;\boldsymbol{r}',t') dSdt \right] \dot{\boldsymbol{E}}_{inc}(\boldsymbol{r}',t')\, dt' \tag{5.1.12b}
$$

or

$$
\Delta\hat{\boldsymbol{\varepsilon}}_E(\boldsymbol{r}') = \int_0^T \left[\int_{t'}^T \int_S \mathbf{G}_b^{EJ^T}(\boldsymbol{r},t;\boldsymbol{r}',t') \cdot \boldsymbol{E}_{scat}^{d}(\boldsymbol{r},t)\, dSdt \right] \dot{\boldsymbol{E}}_{inc}(\boldsymbol{r}',t')\, dt' \tag{5.1.13a}
$$

$$
\Delta\hat{\boldsymbol{\varepsilon}}_H(\boldsymbol{r}') = \int_0^T \left[\int_{t'}^T \int_S \mathbf{G}_b^{HJ^T}(\boldsymbol{r},t;\boldsymbol{r}',t') \cdot \boldsymbol{H}_{scat}^{d}(\boldsymbol{r},t)\, dSdt \right] \dot{\boldsymbol{E}}_{inc}(\boldsymbol{r}',t')\, dt' \tag{5.1.13b}
$$

Using the relations of dyadic Green's functions and their adjoints in Eq. (1.28), the imaging formulas can also be expressed as:

$$\Delta\hat{\boldsymbol{\varepsilon}}_E(\boldsymbol{r}') = \int_0^T \left[\int_{t'}^T \int_S \hat{\mathbf{G}}_b^{EJ}(\boldsymbol{r}',t';\boldsymbol{r},t) \cdot \boldsymbol{E}_{scat}^d(\boldsymbol{r},t)\, dSdt \right] \dot{\boldsymbol{E}}_{inc}(\boldsymbol{r}',t')\, dt' \tag{5.1.14a}$$

$$\Delta\hat{\boldsymbol{\varepsilon}}_H(\boldsymbol{r}') = \int_0^T \left[\int_{t'}^T \int_S \hat{\mathbf{G}}_b^{EM}(\boldsymbol{r}',t';\boldsymbol{r},t) \cdot \boldsymbol{H}_{scat}^d(\boldsymbol{r},t)\, dSdt \right] \dot{\boldsymbol{E}}_{inc}(\boldsymbol{r}',t')\, dt' \tag{5.1.14b}$$

or

$$\Delta\hat{\boldsymbol{\varepsilon}}_E(\boldsymbol{r}') = -\int_0^T \boldsymbol{E}_{Escat}^{BP}(\boldsymbol{r}',t')\, \dot{\boldsymbol{E}}_{inc}(\boldsymbol{r}',t')\, dt' \tag{5.1.15a}$$

$$\Delta\hat{\boldsymbol{\varepsilon}}_H(\boldsymbol{r}') = -\int_0^T \boldsymbol{E}_{Hscat}^{BP}(\boldsymbol{r}',t')\, \dot{\boldsymbol{E}}_{inc}(\boldsymbol{r}',t')\, dt' \tag{5.1.15b}$$

where

$$\boldsymbol{E}_{Escat}^{BP}(\boldsymbol{r}',t') = \int_T^{t'} \int_S \hat{\mathbf{G}}_b^{EJ}(\boldsymbol{r}',t';\boldsymbol{r},t) \cdot \boldsymbol{E}_{scat}^d(\boldsymbol{r},t)\, dSdt \tag{5.1.16a}$$

$$\boldsymbol{E}_{Hscat}^{BP}(\boldsymbol{r}',t') = \int_T^{t'} \int_S \hat{\mathbf{G}}_b^{EM}(\boldsymbol{r}',t';\boldsymbol{r},t) \cdot \boldsymbol{H}_{scat}^d(\boldsymbol{r},t)\, dSdt \tag{5.1.16b}$$

$\boldsymbol{E}_{scat}^{BP}$ is called *back-propagated scattered electric field*. In view of Eq. (1.27), it can be observed that the integral equations (5.1.16) with $T \geq t \geq t'$ have the appropriate form for propagation with the adjoint Green's functions $\hat{\mathbf{G}}_b^{EJ}$ and $\hat{\mathbf{G}}_b^{EM}$. In fact, $\hat{\mathbf{G}}_b^{EJ}(\boldsymbol{r}',t';\boldsymbol{r},t)$ ($\hat{\mathbf{G}}_b^{EM}(\boldsymbol{r}',t';\boldsymbol{r},t)$) gives the electric field at $\boldsymbol{r}'$ and time t' caused by an electric (magnetic) current sources, here $\boldsymbol{E}_{scat}^d$ ($\boldsymbol{H}_{scat}^d$), radiating at $\boldsymbol{r}$ at a later time *t*.

Note that ordinary scattered fields, governed by the Maxwell's equations, propagate forward in time from scatterer to observation surface, whereas back-propagated scattered fields, governed by the adjoint Maxwell's equations, propagate backward in time from the observation surface to their original place, the scatterer.

In practice, the measurement is performed at discrete locations $\boldsymbol{r}_i \in \{\boldsymbol{r}_1,\ldots,\boldsymbol{r}_N\}$ on a planar observation surface. Then, the relations (5.1.16) can be written as:

$$\boldsymbol{E}_{Escat}^{BP}(\boldsymbol{r}',t') = \sum_{i=1}^{N} \int_T^{t'} \hat{\mathbf{G}}_b^{EJ}(\boldsymbol{r}',t';\boldsymbol{r}_i,t) \cdot \boldsymbol{E}_{scat}^d(\boldsymbol{r}_i,t)\, dt \tag{5.1.17a}$$

$$\boldsymbol{E}_{Hscat}^{BP}(\boldsymbol{r}',t') = \sum_{i=1}^{N} \int_{T}^{t'} \hat{\mathbf{G}}_{b}^{EM}(\boldsymbol{r}',t';\boldsymbol{r}_i,t) \cdot \boldsymbol{H}_{scat}^{d}(\boldsymbol{r}_i,t)\, dt \tag{5.1.17b}$$

The above equations represent the integral equation (IE) formalism of the back-propagated scattered electric fields. Considering the relations (1.27) and the adjoint field equations (1.22), it can be inferred that the back-propagated scattered electric fields $\boldsymbol{E}_{Escat}^{BP}(\boldsymbol{r}',t')$ and $\boldsymbol{E}_{Hscat}^{BP}(\boldsymbol{r}',t')$ satisfy equations adjoint to Maxwell's equations and that the source terms for these adjoint equations are the scattered electric and magnetic fields data at all the receiver locations radiating as electric and magnetic current sources in reverse time, respectively; i.e.,

$$\begin{cases} -\nabla \times \boldsymbol{E}_{Escat}^{BP}(\boldsymbol{r},t) = \boldsymbol{\mu}_{b}^{T} \cdot \dot{\boldsymbol{H}}_{Escat}^{BP}(\boldsymbol{r},t) \\ -\nabla \times \boldsymbol{H}_{Escat}^{BP}(\boldsymbol{r},t) = \boldsymbol{\sigma}_{b}^{T} \cdot \boldsymbol{E}_{Escat}^{BP}(\boldsymbol{r},t) - \boldsymbol{\varepsilon}_{b}^{T} \cdot \dot{\boldsymbol{E}}_{Escat}^{BP}(\boldsymbol{r},t) + \sum_{i=1}^{N} \boldsymbol{E}_{scat}^{d}(\boldsymbol{r}_i,t)\, \delta(\boldsymbol{r}-\boldsymbol{r}_i) \end{cases} \tag{5.1.18a}$$

$$\begin{cases} -\nabla \times \boldsymbol{E}_{Hscat}^{BP}(\boldsymbol{r},t) = \boldsymbol{\mu}_{b}^{T} \cdot \dot{\boldsymbol{H}}_{Hscat}^{BP}(\boldsymbol{r},t) - \sum_{i=1}^{N} \boldsymbol{H}_{scat}^{d}(\boldsymbol{r}_i,t)\, \delta(\boldsymbol{r}-\boldsymbol{r}_i) \\ -\nabla \times \boldsymbol{H}_{Hscat}^{BP}(\boldsymbol{r},t) = \boldsymbol{\sigma}_{b}^{T} \cdot \boldsymbol{E}_{Hscat}^{BP}(\boldsymbol{r},t) - \boldsymbol{\varepsilon}_{b}^{T} \cdot \dot{\boldsymbol{E}}_{Hscat}^{BP}(\boldsymbol{r},t) \end{cases} \tag{5.1.18b}$$

These equations represent the differential equation (DE) formalism of the back-propagated scattered fields. The back-propagated fields can thus be obtained by stepping these equations backward in time from $t = T$ to $t = 0$ with a finite difference algorithm, for instance. Although the ordinary Maxwell's equations are unstable when stepped backward in time, the adjoint equations (5.1.18) are stable.

Using similar procedures as applied for the apparent contrast permittivity, the apparent contrast conductivity and permeability can be obtained as:

$$\Delta\hat{\boldsymbol{\sigma}}_{E}(\boldsymbol{r}') = -\int_{0}^{T} \boldsymbol{E}_{Escat}^{BP}(\boldsymbol{r}',t')\, \boldsymbol{E}_{inc}(\boldsymbol{r}',t')\, dt' \tag{5.1.19a}$$

$$\Delta\hat{\boldsymbol{\sigma}}_{H}(\boldsymbol{r}') = -\int_{0}^{T} \boldsymbol{E}_{Hscat}^{BP}(\boldsymbol{r}',t')\, \boldsymbol{E}_{inc}(\boldsymbol{r}',t')\, dt' \tag{5.1.19b}$$

$$\Delta\hat{\boldsymbol{\mu}}_{E}(\boldsymbol{r}') = -\int_{0}^{T} \boldsymbol{H}_{Escat}^{BP}(\boldsymbol{r}',t')\, \dot{\boldsymbol{H}}_{inc}(\boldsymbol{r}',t')\, dt' \tag{5.1.20a}$$

$$\Delta\hat{\boldsymbol{\mu}}_H(\boldsymbol{r}') = -\int_0^T \boldsymbol{H}_{Hscat}^{BP}(\boldsymbol{r}',t')\ \dot{\boldsymbol{H}}_{inc}(\boldsymbol{r}',t')\ dt' \tag{5.1.20b}$$

where the IE formalism of the back-propagated scattered magnetic fields are:

$$\boldsymbol{H}_{Escat}^{BP}(\boldsymbol{r}',t') = \sum_{i=1}^{N}\int_T^{t'} \hat{\mathbf{G}}_b^{HJ}(\boldsymbol{r}',t';\boldsymbol{r}_i,t)\cdot\boldsymbol{E}_{scat}^{d}(\boldsymbol{r}_i,t)\,dt \tag{5.1.21a}$$

$$\boldsymbol{H}_{Hscat}^{BP}(\boldsymbol{r}',t') = \sum_{i=1}^{N}\int_T^{t'} \hat{\mathbf{G}}_b^{HM}(\boldsymbol{r}',t';\boldsymbol{r}_i,t)\cdot\boldsymbol{H}_{scat}^{d}(\boldsymbol{r}_i,t)\,dt \tag{5.1.21b}$$

Mathematically, the imaging formulas (5.1.15), (5.1.19) and (5.1.20) represent negative zero-lag cross correlation of the back-propagated scattered field with the incident field.

It should be noted that these imaging formulas will not provide complete geometry identification of the damages if only one actuator at a fixed location is used. The reason is that each actuator can illuminate only partial geometry of damages. Therefore, to illuminate more complete damages geometry, multiple actuators are needed. The final image is obtained by stacking the partial images. In the case of multiple actuator excitations with actuator positions at $\boldsymbol{s}_j \in \{\boldsymbol{s}_1,\ldots,\boldsymbol{s}_M\}$, the imaging formulas take the following forms:

$$\Delta\hat{\boldsymbol{\varepsilon}}_E(\boldsymbol{r}') = -\sum_{j=1}^{M}\int_0^T \boldsymbol{E}_{Escat;j}^{BP}(\boldsymbol{r}',t')\ \dot{\boldsymbol{E}}_{inc;j}(\boldsymbol{r}',t')\ dt' \tag{5.1.22a}$$

$$\Delta\hat{\boldsymbol{\varepsilon}}_H(\boldsymbol{r}') = -\sum_{j=1}^{M}\int_0^T \boldsymbol{E}_{Hscat;j}^{BP}(\boldsymbol{r}',t')\ \dot{\boldsymbol{E}}_{inc;j}(\boldsymbol{r}',t')\ dt' \tag{5.1.22b}$$

$$\Delta\hat{\boldsymbol{\sigma}}_E(\boldsymbol{r}') = -\sum_{j=1}^{M}\int_0^T \boldsymbol{E}_{Escat;j}^{BP}(\boldsymbol{r}',t')\ \boldsymbol{E}_{inc;j}(\boldsymbol{r}',t')\ dt' \tag{5.1.23a}$$

$$\Delta\hat{\boldsymbol{\sigma}}_H(\boldsymbol{r}') = -\sum_{j=1}^{M}\int_0^T \boldsymbol{E}_{Hscat;j}^{BP}(\boldsymbol{r}',t')\ \boldsymbol{E}_{inc;j}(\boldsymbol{r}',t')\ dt' \tag{5.1.23b}$$

$$\Delta\hat{\boldsymbol{\mu}}_E(\boldsymbol{r}') = -\sum_{j=1}^{M}\int_0^T \boldsymbol{H}_{Escat;j}^{BP}(\boldsymbol{r}',t')\ \dot{\boldsymbol{H}}_{inc;j}(\boldsymbol{r}',t')\ dt' \tag{5.1.24a}$$

$$\Delta\hat{\boldsymbol{\mu}}_H(\boldsymbol{r}') = -\sum_{j=1}^{M}\int_0^T \boldsymbol{H}_{Hscat;j}^{BP}(\boldsymbol{r}',t')\ \dot{\boldsymbol{H}}_{inc;j}(\boldsymbol{r}',t')\ dt' \tag{5.1.24b}$$

where the IE and DE formalisms of the back-propagated scattered fields are:

$$\begin{aligned}\boldsymbol{E}^{BP}_{Escat;j}(\boldsymbol{r}',t') &= \sum_{i=1}^{N}\int_{T}^{t'}\hat{\mathbf{G}}^{EJ}_{b}(\boldsymbol{r}',t';\boldsymbol{r}_i,t)\cdot\boldsymbol{E}^{d}_{scat;j}(\boldsymbol{r}_i,t)\,dt \\ \boldsymbol{H}^{BP}_{Escat;j}(\boldsymbol{r}',t') &= \sum_{i=1}^{N}\int_{T}^{t'}\hat{\mathbf{G}}^{HJ}_{b}(\boldsymbol{r}',t';\boldsymbol{r}_i,t)\cdot\boldsymbol{E}^{d}_{scat;j}(\boldsymbol{r}_i,t)\,dt\end{aligned} \tag{5.1.25a}$$

$$\begin{aligned}\boldsymbol{E}^{BP}_{Hscat;j}(\boldsymbol{r}',t') &= \sum_{i=1}^{N}\int_{T}^{t'}\hat{\mathbf{G}}^{EM}_{b}(\boldsymbol{r}',t';\boldsymbol{r}_i,t)\cdot\boldsymbol{H}^{d}_{scat;j}(\boldsymbol{r}_i,t)\,dt \\ \boldsymbol{H}^{BP}_{Hscat;j}(\boldsymbol{r}',t') &= \sum_{i=1}^{N}\int_{T}^{t'}\hat{\mathbf{G}}^{HM}_{b}(\boldsymbol{r}',t';\boldsymbol{r}_i,t)\cdot\boldsymbol{H}^{d}_{scat;j}(\boldsymbol{r}_i,t)\,dt\end{aligned} \tag{5.1.25b}$$

$$\begin{cases}-\nabla\times\boldsymbol{E}^{BP}_{Escat;j}(\boldsymbol{r},t) = \boldsymbol{\mu}^{T}_{b}\cdot\dot{\boldsymbol{H}}^{BP}_{Escat;j}(\boldsymbol{r},t) \\ -\nabla\times\boldsymbol{H}^{BP}_{Escat;j}(\boldsymbol{r},t) = \boldsymbol{\sigma}^{T}_{b}\cdot\boldsymbol{E}^{BP}_{Escat;j}(\boldsymbol{r},t) - \boldsymbol{\varepsilon}^{T}_{b}\cdot\dot{\boldsymbol{E}}^{BP}_{Escat;j}(\boldsymbol{r},t) + \sum_{i=1}^{N}\boldsymbol{E}^{d}_{scat;j}(\boldsymbol{r}_i,t)\,\delta(\boldsymbol{r}-\boldsymbol{r}_i)\end{cases} \tag{5.1.26a}$$

$$\begin{cases}-\nabla\times\boldsymbol{E}^{BP}_{Hscat;j}(\boldsymbol{r},t) = \boldsymbol{\mu}^{T}_{b}\cdot\dot{\boldsymbol{H}}^{BP}_{Hscat;j}(\boldsymbol{r},t) - \sum_{i=1}^{N}\boldsymbol{H}^{d}_{scat;j}(\boldsymbol{r}_i,t)\,\delta(\boldsymbol{r}-\boldsymbol{r}_i) \\ -\nabla\times\boldsymbol{H}^{BP}_{Hscat;j}(\boldsymbol{r},t) = \boldsymbol{\sigma}^{T}_{b}\cdot\boldsymbol{E}^{BP}_{Hscat;j}(\boldsymbol{r},t) - \boldsymbol{\varepsilon}^{T}_{b}\cdot\dot{\boldsymbol{E}}^{BP}_{Hscat;j}(\boldsymbol{r},t)\end{cases} \tag{5.1.26b}$$

The images constructed from Eq. (5.1.22) to (5.1.24) are called *permittivity*, *conductivity*, and *permeability images*, respectively

For isotropic structures, the imaging formulas can be derived in a similar manner as:

$$\Delta\hat{\varepsilon}_{E}(\boldsymbol{r}') = -\sum_{j=1}^{M}\int_{0}^{T}\boldsymbol{E}^{BP}_{Escat;j}(\boldsymbol{r}',t')\cdot\dot{\boldsymbol{E}}_{inc;j}(\boldsymbol{r}',t')\,dt' \tag{5.1.27a}$$

$$\Delta\hat{\varepsilon}_{H}(\boldsymbol{r}') = -\sum_{j=1}^{M}\int_{0}^{T}\boldsymbol{E}^{BP}_{Hscat;j}(\boldsymbol{r}',t')\cdot\dot{\boldsymbol{E}}_{inc;j}(\boldsymbol{r}',t')\,dt' \tag{5.1.27b}$$

$$\Delta\hat{\sigma}_{E}(\boldsymbol{r}') = -\sum_{j=1}^{M}\int_{0}^{T}\boldsymbol{E}^{BP}_{Escat;j}(\boldsymbol{r}',t')\cdot\boldsymbol{E}_{inc;j}(\boldsymbol{r}',t')\,dt' \tag{5.1.28a}$$

$$\Delta\hat{\sigma}_{H}(\boldsymbol{r}') = -\sum_{j=1}^{M}\int_{0}^{T}\boldsymbol{E}^{BP}_{Hscat;j}(\boldsymbol{r}',t')\cdot\boldsymbol{E}_{inc;j}(\boldsymbol{r}',t')\,dt' \tag{5.1.28b}$$

$$\Delta\hat{\mu}_E(\boldsymbol{r}') = -\sum_{j=1}^{M}\int_0^T \boldsymbol{H}^{BP}_{Escat;j}(\boldsymbol{r}',t')\cdot\dot{\boldsymbol{H}}_{inc;j}(\boldsymbol{r}',t')\,dt' \tag{5.1.29a}$$

$$\Delta\hat{\mu}_H(\boldsymbol{r}') = -\sum_{j=1}^{M}\int_0^T \boldsymbol{H}^{BP}_{Hscat;j}(\boldsymbol{r}',t')\cdot\dot{\boldsymbol{H}}_{inc;j}(\boldsymbol{r}',t')\,dt' \tag{5.1.29b}$$

It is worth mentioning that the imaging formula introduced by Leuschen and Plumb (2001) using the *Matched Filter* approach for an inhomogeneous isotropic and lossless host structure is equivalent to Eq. (5.1.27a).

5.2. The Relation between Adjoint Operators and Gradients

In this section, the relation between the adjoint operators derived in the previous section and the gradients of the following error functionals is established.

Consider multiple scatterers (damages) embedded in a host structure (background medium) with known EM properties $\boldsymbol{\sigma}_b(\boldsymbol{r})$, $\boldsymbol{\varepsilon}_b(\boldsymbol{r})$, and $\boldsymbol{\mu}_b(\boldsymbol{r})$. All scatterers are assumed to be enclosed by the scatterer region or domain of investigation *D*. The scatterers are illuminated by incident EM waves, which are generated by actuators (sources) placed at *M* distinct positions $\boldsymbol{s}_j \in \{\boldsymbol{s}_1,\ldots,\boldsymbol{s}_M\}$ outside *D*. For each incidence, the total transient electric or magnetic field is measured over a planar observation surface *S* outside *D* at discrete positions $\boldsymbol{r}_i \in \{\boldsymbol{r}_1,\ldots,\boldsymbol{r}_N\}$ and for the time interval $[0\,,T]$. It is also assumed that the sources and all fields are zero before $t=0$.

The goal of an iterative gradient-based inversion method is to find a model (conductivity $\boldsymbol{\sigma}(\boldsymbol{r})$, permittivity $\boldsymbol{\varepsilon}(\boldsymbol{r})$, and permeability $\boldsymbol{\mu}(\boldsymbol{r})$ distributions, where $\boldsymbol{r}$ denotes a point in the scatterer region *D* in which the model is allowed to vary) such that the transient field, $\boldsymbol{E}_j(\boldsymbol{r}_i,t)$ or $\boldsymbol{H}_j(\boldsymbol{r}_i,t)$, calculated from the model matches the measured field, $\boldsymbol{E}^d_j(\boldsymbol{r}_i,t)$ or $\boldsymbol{H}^d_j(\boldsymbol{r}_i,t)$, in some sense. The simplest choice is to match the data in a least-squares sense, which corresponds to finding a model that minimizes one of the following error functionals:

$$F_E(\boldsymbol{\sigma},\boldsymbol{\varepsilon},\boldsymbol{\mu}) = \frac{1}{2}\sum_{j=1}^{M}\sum_{i=1}^{N}\int_0^T \left|\boldsymbol{E}_j^d(\boldsymbol{r}_i,t) - \boldsymbol{E}_j(\boldsymbol{r}_i,t)\right|^2 dt = \frac{1}{2}\sum_{j=1}^{M}\sum_{i=1}^{N}\int_0^T \Delta\boldsymbol{E}_j(\boldsymbol{r}_i,t)\cdot\Delta\boldsymbol{E}_j(\boldsymbol{r}_i,t)dt \qquad (5.2.1a)$$

$$F_H(\boldsymbol{\sigma},\boldsymbol{\varepsilon},\boldsymbol{\mu}) = \frac{1}{2}\sum_{j=1}^{M}\sum_{i=1}^{N}\int_0^T \left|\boldsymbol{H}_j^d(\boldsymbol{r}_i,t) - \boldsymbol{H}_j(\boldsymbol{r}_i,t)\right|^2 dt = \frac{1}{2}\sum_{j=1}^{M}\sum_{i=1}^{N}\int_0^T \Delta\boldsymbol{H}_j(\boldsymbol{r}_i,t)\cdot\Delta\boldsymbol{H}_j(\boldsymbol{r}_i,t)dt \qquad (5.2.1b)$$

where

$$\Delta\boldsymbol{E}_j(\boldsymbol{r}_i,t) = \boldsymbol{E}_j^d(\boldsymbol{r}_i,t) - \boldsymbol{E}_j(\boldsymbol{r}_i,t) \qquad (5.2.2a)$$

$$\Delta\boldsymbol{H}_j(\boldsymbol{r}_i,t) = \boldsymbol{H}_j^d(\boldsymbol{r}_i,t) - \boldsymbol{H}_j(\boldsymbol{r}_i,t) \qquad (5.2.2b)$$

The dependence of the error functionals on the model parameters ($\boldsymbol{\sigma}$, $\boldsymbol{\varepsilon}$, and $\boldsymbol{\mu}$) arises from the implicit dependence of the calculated field $\boldsymbol{E}_j(\boldsymbol{r}_i,t)$ or $\boldsymbol{H}_j(\boldsymbol{r}_i,t)$ on these parameters.

The most direct method of minimizing the nonlinear error functionals is steepest descent method which is the simplest gradient method. Following similar procedures performed in section (4.1), the gradients of the error functionals $F_E(\boldsymbol{\sigma},\boldsymbol{\varepsilon},\boldsymbol{\mu})$ and $F_H(\boldsymbol{\sigma},\boldsymbol{\varepsilon},\boldsymbol{\mu})$ with respect to model parameters are obtained as:

$$\frac{\partial F_E}{\partial \boldsymbol{\sigma}} = \sum_{j=1}^{M}\int_0^T \boldsymbol{E}_{\Delta E;j}^{BP}(\boldsymbol{r}',t')\,\boldsymbol{E}_j(\boldsymbol{r}',t')\,dt' \qquad (5.2.3a)$$

$$\frac{\partial F_E}{\partial \boldsymbol{\varepsilon}} = \sum_{j=1}^{M}\int_0^T \boldsymbol{E}_{\Delta E;j}^{BP}(\boldsymbol{r}',t')\,\dot{\boldsymbol{E}}_j(\boldsymbol{r}',t')\,dt' \qquad (5.2.4a)$$

$$\frac{\partial F_E}{\partial \boldsymbol{\mu}} = \sum_{j=1}^{M}\int_0^T \boldsymbol{H}_{\Delta E;j}^{BP}(\boldsymbol{r}',t')\,\dot{\boldsymbol{H}}_j(\boldsymbol{r}',t')\,dt' \qquad (5.2.5a)$$

$$\frac{\partial F_H}{\partial \boldsymbol{\sigma}} = \sum_{j=1}^{M}\int_0^T \boldsymbol{E}_{\Delta H;j}^{BP}(\boldsymbol{r}',t')\,\boldsymbol{E}_j(\boldsymbol{r}',t')\,dt' \qquad (5.2.3b)$$

$$\frac{\partial F_H}{\partial \boldsymbol{\varepsilon}} = \sum_{j=1}^{M}\int_0^T \boldsymbol{E}_{\Delta H;j}^{BP}(\boldsymbol{r}',t')\,\dot{\boldsymbol{E}}_j(\boldsymbol{r}',t')\,dt' \qquad (5.2.4b)$$

$$\frac{\partial F_H}{\partial \boldsymbol{\mu}} = \sum_{j=1}^{M}\int_0^T \boldsymbol{H}_{\Delta H;j}^{BP}(\boldsymbol{r}',t')\,\dot{\boldsymbol{H}}_j(\boldsymbol{r}',t')\,dt' \qquad (5.2.5b)$$

where

$$\boldsymbol{E}^{BP}_{\Delta E;j}(\boldsymbol{r}',t') = \sum_{i=1}^{N}\int_{T}^{t'}\hat{\mathbf{G}}^{EJ}(\boldsymbol{r}',t';\boldsymbol{r}_i,t)\cdot\Delta\boldsymbol{E}_j(\boldsymbol{r}_i,t)\,dt$$
$$\boldsymbol{H}^{BP}_{\Delta E;j}(\boldsymbol{r}',t') = \sum_{i=1}^{N}\int_{T}^{t'}\hat{\mathbf{G}}^{HJ}(\boldsymbol{r}',t';\boldsymbol{r}_i,t)\cdot\Delta\boldsymbol{E}_j(\boldsymbol{r}_i,t)\,dt \qquad (5.2.6a)$$

$$\boldsymbol{E}^{BP}_{\Delta H;j}(\boldsymbol{r}',t') = \sum_{i=1}^{N}\int_{T}^{t'}\hat{\mathbf{G}}^{EM}(\boldsymbol{r}',t';\boldsymbol{r}_i,t)\cdot\Delta\boldsymbol{H}_j(\boldsymbol{r}_i,t)\,dt$$
$$\boldsymbol{H}^{BP}_{\Delta H;j}(\boldsymbol{r}',t') = \sum_{i=1}^{N}\int_{T}^{t'}\hat{\mathbf{G}}^{HM}(\boldsymbol{r}',t';\boldsymbol{r}_i,t)\cdot\Delta\boldsymbol{H}_j(\boldsymbol{r}_i,t)\,dt \qquad (5.2.6b)$$

Using the host structure as the initial guess for the model, the changes introduced in Eq. (4.1.20) hold. Then, equations (5.2.6) for the *back-propagated residual field* are changed into the following equations for the *back-propagated scattered field*:

$$\boldsymbol{E}^{BP}_{Escat;j}(\boldsymbol{r}',t') = \sum_{i=1}^{N}\int_{T}^{t'}\hat{\mathbf{G}}^{EJ}_{b}(\boldsymbol{r}',t';\boldsymbol{r}_i,t)\cdot\boldsymbol{E}^{d}_{scat;j}(\boldsymbol{r}_i,t)\,dt$$
$$\boldsymbol{H}^{BP}_{Escat;j}(\boldsymbol{r}',t') = \sum_{i=1}^{N}\int_{T}^{t'}\hat{\mathbf{G}}^{HJ}_{b}(\boldsymbol{r}',t';\boldsymbol{r}_i,t)\cdot\boldsymbol{E}^{d}_{scat;j}(\boldsymbol{r}_i,t)\,dt \qquad (5.2.7a)$$

$$\boldsymbol{E}^{BP}_{Hscat;j}(\boldsymbol{r}',t') = \sum_{i=1}^{N}\int_{T}^{t'}\hat{\mathbf{G}}^{EM}_{b}(\boldsymbol{r}',t';\boldsymbol{r}_i,t)\cdot\boldsymbol{H}^{d}_{scat;j}(\boldsymbol{r}_i,t)\,dt$$
$$\boldsymbol{H}^{BP}_{Hscat;j}(\boldsymbol{r}',t') = \sum_{i=1}^{N}\int_{T}^{t'}\hat{\mathbf{G}}^{HM}_{b}(\boldsymbol{r}',t';\boldsymbol{r}_i,t)\cdot\boldsymbol{H}^{d}_{scat;j}(\boldsymbol{r}_i,t)\,dt \qquad (5.2.7b)$$

Then, comparing Eq. (5.1.22) to (5.1.24) and (5.1.25) with Eq. (5.2.3) to (5.2.5) and (5.2.7), it is concluded that the negative gradients of the error functionals with respect to the model parameters in the first iteration of the gradient inversion method are indeed equal to the apparent contrast properties obtained from the Born imaging algorithm.

6. Imaging Steps in Electromagnetic Migration and Born Imaging Algorithms

By examining the EM migration and Born imaging formulas, it can be observed that both imaging algorithms consist of the following three steps; similar to *prestack migration* (Claerbout, 1971):

(1) Back-propagation (migration) of the scattered field data derived from the measured sensor data through integral equations (4.1.25) or (5.1.25) or differential equations (4.1.26), (4.1.27), or (5.1.26). In migration literature, data collection on observation surface by sensors due to a common actuator is called *common-source gather* (*experiment*).

(2) Zero-lag cross-correlation of the back-propagated (migrated) scattered field with the incident field through integral equations (4.1.22) - (4.1.24) or (5.1.22) - (5.1.24), which provides a partial image of damage geometry from an actuator. This step is generally called *zero-lag cross-correlation imaging condition* in migration literature (Claerbout, 1971).

(3) Summation of partial images obtained from individual actuators. In other words, each common-source gather is back-propagated (migrated) independently to produce a partial image; the final composite image is obtained from stacking over the partial images (Chang and McMechan, 1994). This stacking process after the back-propagation (migration) increases the signal-to-noise ratio (Lin and Yuan, 2005).

To expedite the imaging process, many researchers have addressed the zero-lag cross-correlation imaging condition performed in step (2). Chang and McMechan (1986) developed an *excitation-time imaging condition*. First, the *excitation time* (defined as the moment when a point in image area, called image point, is excited by the wave energy from the actuator) from an actuator to each image point is computed and kept in an *excitation-time* (*one-way traveltime*) *table*. Then, instead of applying zero-lag cross-correlation imaging condition which requires the computation of incident field or its time derivative at each image point at all times, the image at a specified point is considered to be the amplitude of the computed

migrated scattered field at that point at its excitation time. Although the excitation-time imaging condition does not truly reflect the zero-lag cross-correlation, it significantly reduces the computational cost.

Several methods have been suggested to calculate the excitation-time table in acoustic and elastic wave cases such as *ray tracing* (Chang and McMechan, 1986), finite difference (FD) solution of *eikonal equation* (Vidale, 1988 and Zhu and Lines, 1997), and FD solution of wave equation (Chang and McMechan, 1994 and Loewenthal and Hu, 1991). It should be noted that the results obtained by the third method is more accurate because it is based on the wave equation while the first two methods rely on the high-frequency ray approximation. Although the third method demands the highest computational cost, it remains a method of choice for SHM applications because the computation of the excitation-time table is performed before the monitoring stage is started.

Loewenthal and Hu (1991) suggested two criteria for calculating the excitation-time table using the FD solution of the acoustic wave equation:

(a) Maximum-amplitude criterion (*maximum-energy arrival criterion*): The traveltime of an image point is calculated at the moment the incident wave has maximum amplitude at that point.

(b) Minimum-time criterion (*first-arrival criterion*): The travel time of an image point is calculated at the moment the incident wave hits that point.

In order to enhance the resolution of the images obtained by the excitation-time imaging condition with the above criteria, a modified excitation-time imaging condition is introduced. In this modified condition, any component of the incident field (or its time derivative) at each image point is approximated by the following single-event function parameterized by not only a traveltime but an amplitude:

$$e_{inc;j}(\boldsymbol{r}',t') \cong A_{e_{inc;j}}(\boldsymbol{r}')\,\delta\left(t'-\tau_{e_{inc;j}}(\boldsymbol{r}')\right) \tag{6.1}$$

where $\boldsymbol{r}'$, $\tau_{e_{inc;j}}(\boldsymbol{r}')$, and $A_{e_{inc;j}}(\boldsymbol{r}')$ are an arbitrary image point position, the traveltime of the incident field component $e_{inc;j}$ from the j^{th} actuator to the image point, and the amplitude of

the $e_{inc;j}$ at $t' = \tau_{e_{inc;j}}(\boldsymbol{r}')$, respectively. Note that in the excitation-time imaging condition only the traveltime of the incident field is used, whereas in the modified condition both traveltime and amplitude of the field are taken into account.

Another way to reduce the computational cost of the imaging algorithms is to utilize poststack concept. In *poststack migration*, the sensor data should be collected in a monostatic (zero-offset) configuration, i.e., the actuators and the sensors are collocated.

The concept of poststack migration is based on the *exploding reflector model* (Scales, 1997): The data recorded in the zero-offset configuration is the same that would be recorded if actuators were placed along the damage boundary and were fired off with a strength proportional to the reflection coefficient at $t = 0$ in a medium having half the original velocity. This means that if the zero-offset wave field recorded at the surface was somehow run backward in time, then by evaluating the results at $t = 0$ (*zero-time imaging condition*), a picture of the reflection event would have been obtained, provided half the original velocity is used when the recorded field is back-propagated. Therefore, the image can be simply obtained by applying the zero-time imaging condition to the migrated scattered field computed in the pristine structure having half the original velocity (or a 2:1 scaled pristine structure).

Unfortunately, the exploding reflector model concept is not quantitatively correct. Some of its shortcomings are (Claerbout and Black, 2001 and Chen and Huang, 1998): It fails with multiple reflections; it fails where waves reflected from both sides of an interface are able to be seen. The exploding reflector model predicts the waves emitted by both sides have the same polarity. The physics of reflection coefficients dictates reflections from opposite sides have opposite polarities; and it fails when there is lateral velocity variation.

In practice, data collection in zero-offset configuration is very difficult. Therefore, the data is collected in common middle point (CMP) gathers (each CMP gather consists of the data associated with the same actuator-sensor midpoint). Each CMP gather must be first processed by a so-called normal-move out (NMO) correction and then stacked. Performing NMO/stack on all the CMP gathers yields a plausible estimate of the zero-offset data.

However, the assumptions made in the NMO correction stage, limit the ability of the algorithm to image steep boundaries of damages (Feng and Sato, 2004).

Gray (1999) proved that prestack migration had a higher signal-to-noise ratio (SNR) than that of the poststack migration. Moreover, Chen and Schuster (1999) showed in acoustic case that prestack images had better dynamic range than that of the poststack images. In spite of these drawbacks, the usage of the poststack concept in the proposed algorithms is also examined.

A simple way to compute the back-propagated (migrated) scattered field is to use FD discretization of the differential equations (4.1.26), (4.1.27) or (5.1.26). In migration literature, when back-propagation (migration) of the scattered field data is carried out by FD discretization of the full wave equation in time-space domain, the method is called *reverse-time migration* (*RTM*).

Ability to consider any inhomogeneities in the pristine structure, high accuracy and simple programming are some of the advantages in RTM. Zhu and Lines (1997) showed, in acoustic case, that reverse-time wave equation extrapolation procedure also possessed the capability of implicitly interpolating missing recorded traces (data) in FD grid, as long as net data sampling is not aliased locally either temporally or spatially. This healing characteristic is very important in a SHMS because not only will the system be able to operate with fewer numbers of sensors but it will be more robust when some of the sensors fail due to aging or surrounding environment.

On the other hand, RTM algorithm is considered to be the most computationally expensive migration algorithm. In addition, existence of any material discontinuity in the pristine structure will generate internal reflections during back-propagation (migration) of the scattered field data and forward propagation of incident field and thus causes artifacts in the image (Biondi, 2004). These artifacts are generated due to the use of full two-way wave equation. Several methods have been proposed to handle this problem in acoustic and elastic wave cases such as smoothing the pristine structure velocity or slowness model (Loewenthal *et al*., 1987), using two-way “non-reflecting” wave equation (Baysal *et al*., 1984 and Etgen, 1986), or using one-way wave equation algorithms such as phase-shift migration (Gazdag,

1978) and *f-k* migration (Stolt,1978). Note that the wavefield satisfying the one-way wave equation does not experience reflection at the interfaces of different media. It is expected that if the incident field (computed by a FD discretization of the full two-way wave equation) is approximated by Eq. (6.1) based on the first-arrival criterion, the artifacts related to the material discontinuity in the pristine structure will be reduced. Note that approximation of incident field in image area based on the first-arrival criterion eliminates all reflection events from the incident field.

Another technique to compute the back-propagated (migrated) scattered field is to use the integral equation (IE) formalisms (4.1.25) or (5.1.25). In this approach, the Green's functions of the pristine structure are required. For general 3-D cases, numerical solutions of these Green's functions may be computationally intensive when analytical solutions are not available. Fortunately, the numerical solutions of the Green's functions, if needed, can be carried out prior to the monitoring stage. Having calculated the Green's functions, the back-propagated (migrated) scattered field is computed by performing integral (summation) operations during the monitoring stage.

To further speed up the imaging algorithms using the IE formalism, in addition to the approximation made for the incident field in Eq. (6.1), similar approximations can be applied to the fields associated with the Green's functions of the pristine structure. By doing so, two time integrations involved in imaging steps (1) and (2) are removed from the imaging process. As a result, real-time 3-D imaging algorithms can be realized. Note that the artifacts related to the material discontinuity in the pristine structure are expected to be completely removed if the first-arrival criterion is used for the approximations of incident fields and the Green's functions.

The resulting real-time imaging algorithms bear a resemblance to the conventional Kirchhoff migration (KM). Computational efficiency, ability to handle irregular actuator and sensor spacing, and target-oriented capability (i.e., a desired part of the original domain of investigation can be imaged without the need to image the entire domain) are some of the features of KM (Fehler and Huang, 2002 and Audebert *et al.*, 1997) which can carry over into the proposed imaging algorithms in IE formalism as well. It is worth mentioning that a major shortcoming of conventional KM is that it may fail to produce accurate image in

complex structures. This shortcoming is not caused by the theory, but by the approximations (mostly high-frequency ray and far-field approximations) introduced in the presentation and calculation of the Green's function traveltime and amplitude functions (Audebert *et al.*, 1997). In high-frequency ray approximation, wave phenomena such as diffraction and multi-pathing (i.e., when many wavepaths connect a single actuator/sensor location with a single image point) in complex structures are not completely accounted for (Fehler and Huang, 2002). Nichols (1996) suggested that KM with traveltimes and amplitudes computed using wave equation and based on maximum-energy arrivals instead of the first arrivals, significantly improved the images specially in areas of complex structures.

In theory, scattered field data (measured incident field subtracted from measured total field) is used for damage imaging. In practice, however, it is desirable to only measure the response of the structure under inspection (measured total field) for detecting the damage without the need to measure the response of the pristine structure (measured incident field) because the measurements are collected at different times that are often subject to different environmental conditions. If the measured total field is directly used to perform back-propagation (migration), all the material interfaces in the structure will be imaged in addition to the geometry of the damage. In general, when the measured total field is used for damage imaging, *direct waves* (the waves received by the sensors directly from the actuator) and possible reflections from the upper surface of the structure (if non-contact EM sensors are used) should be removed from the data as a preprocessing step to highlight the image. However, by using the measured total field, the image of the damage may be obscured by the strong reflections from nearby material interfaces.

Generally, the smallest distance between two point scatterers that can be resolved in the image is known as the *spatial resolution limit* of the image. Chen and Schuster (1999) showed that in the far-field, where the depth was much greater than the sensor span, the horizontal resolution limit for migrated images was proportional to the depth of the scatterer and the wavelength and inversely proportional to the sensor span. The vertical resolution limit, however, does not depend on the sensor span and the depth of the scatterer and is proportional to the wavelength. Other factors affecting the spatial resolution of migration images can be found in Vermeer (1999).

It should be mentioned that actuator and sensor spacings, Δ_a and Δ_s, are important factors in image quality. A coarse actuator or sensor spacing will introduce *spatial aliasing artifacts* and lowers the dynamic range in the image (Chen and Schuster, 1999). In KM, time-reversal, and diffraction tomography algorithms, for instance, the sensor spacing should satisfy the *spatial Nyquist sampling criterion*: the spacing should not be more than one-half of the minimum wavelength of the signal propagating in the structure, i.e., $\Delta_s = \lambda_{\min}/2$ (Schneider, 1978, Alam *et al.*, 2004, Kak and Slaney, 1988, and Weedon *et al.*, 2000). Note that there is a trade-off between resolution and aliasing artifacts because of incomplete spatial sampling of the data. That is to say, for a given sensor spacing satisfying the Nyquist criterion, increasing the excitation frequency improves the image resolution but deteriorates the image quality with the aliasing artifacts.

Having examined several numerical simulations of the proposed imaging algorithms, it is believed that these algorithms share a typical shortcoming for damage imaging application. This shortcoming may prevail when there is a material interface in geometrical shadow of a damage. In such a case, the reflection events in the measured incident field associated with the parts of the interface that are located in the geometrical shadow of the damage may differ from those events in the measured total field due to the presence of the damage. Therefore, there may be some unwanted events in the scattered field data in addition to the damage events. As a result, a false damage near or on the interface location may be imaged in addition to the real damage. Note that this problem cannot be resolved by one-way wave equation approach.

7. Two-Dimensional Electromagnetic Field

A 2-D electromagnetic (EM) field can be generated when neither EM field excitation nor model geometry has any variation in one specified direction, say *y*-direction. Then, all partial derivatives of the field with respect to *y* are equal to zero and the Maxwell's equations (1.9) in rectangular coordinates reduce to:

$$\begin{cases} -\dfrac{\partial E_y}{\partial z} = -\mu_{xx}\dot{H}_x - \mu_{xy}\dot{H}_y - \mu_{xz}\dot{H}_z - M_x \\ \dfrac{\partial E_x}{\partial z} - \dfrac{\partial E_z}{\partial x} = -\mu_{yx}\dot{H}_x - \mu_{yy}\dot{H}_y - \mu_{yz}\dot{H}_z - M_y \\ \dfrac{\partial E_y}{\partial x} = -\mu_{zx}\dot{H}_x - \mu_{zy}\dot{H}_y - \mu_{zz}\dot{H}_z - M_z \\ -\dfrac{\partial H_y}{\partial z} = \sigma_{xx}E_x + \sigma_{xy}E_y + \sigma_{xz}E_z + \varepsilon_{xx}\dot{E}_x + \varepsilon_{xy}\dot{E}_y + \varepsilon_{xz}\dot{E}_z + J_x \\ \dfrac{\partial H_x}{\partial z} - \dfrac{\partial H_z}{\partial x} = \sigma_{yx}E_x + \sigma_{yy}E_y + \sigma_{yz}E_z + \varepsilon_{yx}\dot{E}_x + \varepsilon_{yy}\dot{E}_y + \varepsilon_{yz}\dot{E}_z + J_y \\ \dfrac{\partial H_y}{\partial x} = \sigma_{zx}E_x + \sigma_{zy}E_y + \sigma_{zz}E_z + \varepsilon_{zx}\dot{E}_x + \varepsilon_{zy}\dot{E}_y + \varepsilon_{zz}\dot{E}_z + J_z \end{cases} \tag{7.1}$$

By further assuming,

$$\boldsymbol{\sigma} \equiv \begin{bmatrix} \sigma_{xx} & 0 & \sigma_{xz} \\ 0 & \sigma_{yy} & 0 \\ \sigma_{zx} & 0 & \sigma_{zz} \end{bmatrix} \quad ; \quad \boldsymbol{\varepsilon} \equiv \begin{bmatrix} \varepsilon_{xx} & 0 & \varepsilon_{xz} \\ 0 & \varepsilon_{yy} & 0 \\ \varepsilon_{zx} & 0 & \varepsilon_{zz} \end{bmatrix} \quad ; \quad \boldsymbol{\mu} \equiv \begin{bmatrix} \mu_{xx} & 0 & \mu_{xz} \\ 0 & \mu_{yy} & 0 \\ \mu_{zx} & 0 & \mu_{zz} \end{bmatrix} \tag{7.2}$$

Eq. (7.1) can be separated into two independent systems; i.e.,

$$\text{TM}: \begin{cases} -\dfrac{\partial E_y}{\partial z} = -\mu_{xx}\dot{H}_x - \mu_{xz}\dot{H}_z - M_x \\ \dfrac{\partial H_x}{\partial z} - \dfrac{\partial H_z}{\partial x} = \sigma_{yy}E_y + \varepsilon_{yy}\dot{E}_y + J_y \\ \dfrac{\partial E_y}{\partial x} = -\mu_{zx}\dot{H}_x - \mu_{zz}\dot{H}_z - M_z \end{cases} \tag{7.3}$$

$$\text{TE}: \begin{cases} -\dfrac{\partial H_y}{\partial z} = \sigma_{xx} E_x + \sigma_{xz} E_z + \varepsilon_{xx} \dot{E}_x + \varepsilon_{xz} \dot{E}_z + J_x \\ \dfrac{\partial E_x}{\partial z} - \dfrac{\partial E_z}{\partial x} = -\mu_{yy} \dot{H}_y - M_y \\ \dfrac{\partial H_y}{\partial x} = \sigma_{zx} E_x + \sigma_{zz} E_z + \varepsilon_{zx} \dot{E}_x + \varepsilon_{zz} \dot{E}_z + J_z \end{cases} \tag{7.4}$$

The first system, equations (7.3), which is called *transverse magnetic mode* (*TM mode*) includes E_y, H_x, and H_z and the second system, equations (7.4), so called *transverse electric mode* (*TE mode*) includes H_y, E_x, and E_z. Because these two sets of equations are independent of each other, the total electromagnetic field reduces to the sum of TE and TM fields which propagate in the model independently. In TM field, the magnetic vector is transverse to the *y*-direction and perpendicular to the electric vector. The TM field can be excited by an electric current density $J_y(x,z,t)$.

In the following sections, the imaging formulas are simplified for 2-D TM case in isotropic and biaxial anisotropic structures. The *z*-axis is considered to be downward from the upper surface toward the pristine structure and the measurement line parallel to the *x*-axis.

7.1. Born Imaging Formulas in TM Field

For TM mode in biaxial structures, the Born imaging formulas (5.1.22)-(5.1.24) are reduced to:

$$\Delta\hat{\varepsilon}_{yy;\Phi}(x',z') = -\sum_{j=1}^{M} \int_0^T E^{BP}_{y;\Phi_{scat};j}(x',z',t')\, \dot{E}_{y;inc;j}(x',z',t')\, dt' \tag{7.1.1}$$

$$\Delta\hat{\sigma}_{yy;\Phi}(x',z') = -\sum_{j=1}^{M} \int_0^T E^{BP}_{y;\Phi_{scat};j}(x',z',t')\, E_{y;inc;j}(x',z',t')\, dt' \tag{7.1.2}$$

$$\Delta\hat{\mu}_{xx;\Phi}(x',z') = -\sum_{j=1}^{M} \int_0^T H^{BP}_{x;\Phi_{scat};j}(x',z',t')\, \dot{H}_{x;inc;j}(x',z',t')\, dt' \tag{7.1.3}$$

$$\Delta\hat{\mu}_{zz;\Phi}(x',z') = -\sum_{j=1}^{M}\int_0^T H^{BP}_{z;\Phi_{scat};j}(x',z',t')\,\dot{H}_{z;inc;j}(x',z',t')\,dt' \qquad (\Phi = E_y, H_x, H_z) \tag{7.1.4}$$

Where the differential equation (DE) formalisms of the back-propagated scattered fields are given by:

$$\begin{cases} \dfrac{\partial E^{BP}_{y;\Phi_{scat};j}}{\partial z} = \mu_{xx;b}\dot{H}^{BP}_{x;\Phi_{scat};j} - \hat{M}_{x;j} \\ -\dfrac{\partial H^{BP}_{x;\Phi_{scat};j}}{\partial z} + \dfrac{\partial H^{BP}_{z;\Phi_{scat};j}}{\partial x} = \sigma_{yy;b}E^{BP}_{y;\Phi_{scat};j} - \varepsilon_{yy;b}\dot{E}^{BP}_{y;\Phi_{scat};j} + \hat{J}_{y;j} \\ -\dfrac{\partial E^{BP}_{y;\Phi_{scat};j}}{\partial x} = \mu_{zz;b}\dot{H}^{BP}_{z;\Phi_{scat};j} - \hat{M}_{z;j} \end{cases} \tag{7.1.5}$$

For $\Phi = E_y$: $\hat{M}_{x;j} = 0;\quad \hat{J}_{y;j} = \sum_{i=1}^{N} E^{d}_{y;scat;j}(x_i,z_i,t)\,\delta(x-x_i)\delta(z-z_i);\quad \hat{M}_{z;j} = 0;$

For $\Phi = H_x$: $\hat{M}_{x;j} = \sum_{i=1}^{N} H^{d}_{x;scat;j}(x_i,z_i,t)\,\delta(x-x_i)\delta(z-z_i);\quad \hat{J}_{y;j} = 0;\quad \hat{M}_{z;j} = 0;$

For $\Phi = H_z$: $\hat{M}_{x;j} = 0;\quad \hat{J}_{y;j} = 0;\quad \hat{M}_{z;j} = \sum_{i=1}^{N} H^{d}_{z;scat;j}(x_i,z_i,t)\,\delta(x-x_i)\delta(z-z_i);$

The corresponding integral equation (IE) formalisms of the back-propagated scattered fields also assume the following forms

$$E^{BP}_{y;Ey_{scat};j}(x',z',t') = \sum_{i=1}^{N}\int_T^{t'} \hat{G}^{EJ}_{yy;b}(x',z',t';x_i,z_i,t)\,E^{d}_{y;scat;j}(x_i,z_i,t)dt \tag{7.1.6a}$$

$$H^{BP}_{x;Ey_{scat};j}(x',z',t') = \sum_{i=1}^{N}\int_T^{t'} \hat{G}^{HJ}_{xy;b}(x',z',t';x_i,z_i,t)\,E^{d}_{y;scat;j}(x_i,z_i,t)dt \tag{7.1.7a}$$

$$H^{BP}_{z;Ey_{scat};j}(x',z',t') = \sum_{i=1}^{N}\int_T^{t'} \hat{G}^{HJ}_{zy;b}(x',z',t';x_i,z_i,t)\,E^{d}_{y;scat;j}(x_i,z_i,t)dt \tag{7.1.8a}$$

$$E^{BP}_{y;Hx_{scat};j}(x',z',t') = \sum_{i=1}^{N}\int_T^{t'} \hat{G}^{EM}_{yx;b}(x',z',t';x_i,z_i,t)\,H^{d}_{x;scat;j}(x_i,z_i,t)\,dt \tag{7.1.6b}$$

$$H^{BP}_{x;Hx_{scat};j}(x',z',t') = \sum_{i=1}^{N}\int_{T}^{t'} \hat{G}^{HM}_{xx;b}(x',z',t';x_i,z_i,t)\, H^{d}_{x;scat;j}(x_i,z_i,t)\, dt \tag{7.1.7b}$$

$$H^{BP}_{z;Hx_{scat};j}(x',z',t') = \sum_{i=1}^{N}\int_{T}^{t'} \hat{G}^{HM}_{zx;b}(x',z',t';x_i,z_i,t)\, H^{d}_{x;scat;j}(x_i,z_i,t)\, dt \tag{7.1.8b}$$

$$E^{BP}_{y;Hz_{scat};j}(x',z',t') = \sum_{i=1}^{N}\int_{T}^{t'} \hat{G}^{EM}_{yz;b}(x',z',t';x_i,z_i,t)\, H^{d}_{z;scat;j}(x_i,z_i,t)\, dt \tag{7.1.6c}$$

$$H^{BP}_{x;Hz_{scat};j}(x',z',t') = \sum_{i=1}^{N}\int_{T}^{t'} \hat{G}^{HM}_{xz;b}(x',z',t';x_i,z_i,t)\, H^{d}_{z;scat;j}(x_i,z_i,t)\, dt \tag{7.1.7c}$$

$$H^{BP}_{z;Hz_{scat};j}(x',z',t') = \sum_{i=1}^{N}\int_{T}^{t'} \hat{G}^{HM}_{zz;b}(x',z',t';x_i,z_i,t)\, H^{d}_{z;scat;j}(x_i,z_i,t)\, dt \tag{7.1.8c}$$

In isotropic structures, the Born imaging formulas are reduced to:

$$\Delta\hat{\varepsilon}_{\Phi}(x',z') = -\sum_{j=1}^{M}\int_{0}^{T} E^{BP}_{y;\Phi_{scat};j}(x',z',t')\, \dot{E}_{y;inc;j}(x',z',t')\, dt' \tag{7.1.9}$$

$$\Delta\hat{\sigma}_{\Phi}(x',z') = -\sum_{j=1}^{M}\int_{0}^{T} E^{BP}_{y;\Phi_{scat};j}(x',z',t')\, E_{y;inc;j}(x',z',t')\, dt' \tag{7.1.10}$$

$$\begin{aligned}\Delta\hat{\mu}_{\Phi}(x',z') = -\sum_{j=1}^{M}\int_{0}^{T} [&H^{BP}_{x;\Phi_{scat};j}(x',z',t')\, \dot{H}_{x;inc;j}(x',z',t') + \\ &H^{BP}_{z;\Phi_{scat};j}(x',z',t')\, \dot{H}_{z;inc;j}(x',z',t')]\, dt'\end{aligned} \tag{7.1.11}$$

with the following DE formalisms of the back-propagated scattered fields:

$$\begin{cases} \dfrac{\partial E^{BP}_{y;\Phi_{scat};j}}{\partial z} = \mu_b \dot{H}^{BP}_{x;\Phi_{scat};j} - \hat{M}_{x;j} \\ -\dfrac{\partial H^{BP}_{x;\Phi_{scat};j}}{\partial z} + \dfrac{\partial H^{BP}_{z;\Phi_{scat};j}}{\partial x} = \sigma_b E^{BP}_{y;\Phi_{scat};j} - \varepsilon_b \dot{E}^{BP}_{y;\Phi_{scat};j} + \hat{J}_{y;j} \\ -\dfrac{\partial E^{BP}_{y;\Phi_{scat};j}}{\partial x} = \mu_b \dot{H}^{BP}_{z;\Phi_{scat};j} - \hat{M}_{z;j} \end{cases} \tag{7.1.12}$$

Applying the approximation defined in Eq. (6.1) on the incident field components, Eq. (7.1.1) to (7.1.4) and Eq. (7.1.9) to (7.1.11) are simplified to:

$$\Delta\hat{\varepsilon}_{yy;\Phi}(x',z') \cong -\sum_{j=1}^{M} A_{\dot{E}_{y;inc;j}}(x',z')\, E^{BP}_{y;\Phi_{scat};j}(x',z',\tau_{\dot{E}_{y;inc;j}}(x',z')) \tag{7.1.13}$$

$$\Delta\hat{\sigma}_{yy;\Phi}(x',z') \cong -\sum_{j=1}^{M} A_{E_{y;inc;j}}(x',z')\, E^{BP}_{y;\Phi_{scat};j}(x',z',\tau_{E_{y;inc;j}}(x',z')) \tag{7.1.14}$$

$$\Delta\hat{\mu}_{xx;\Phi}(x',z') \cong -\sum_{j=1}^{M} A_{\dot{H}_{x;inc;j}}(x',z')\, H^{BP}_{x;\Phi_{scat};j}(x',z',\tau_{\dot{H}_{x;inc;j}}(x',z')) \tag{7.1.15}$$

$$\Delta\hat{\mu}_{zz;\Phi}(x',z') \cong -\sum_{j=1}^{M} A_{\dot{H}_{z;inc;j}}(x',z')\, H^{BP}_{z;\Phi_{scat};j}(x',z',\tau_{\dot{H}_{z;inc;j}}(x',z')) \tag{7.1.16}$$

$$\Delta\hat{\varepsilon}_{\Phi}(x',z') \cong -\sum_{j=1}^{M} A_{\dot{E}_{y;inc;j}}(x',z')\, E^{BP}_{y;\Phi_{scat};j}(x',z',\tau_{\dot{E}_{y;inc;j}}(x',z')) \tag{7.1.17}$$

$$\Delta\hat{\sigma}_{\Phi}(x',z') \cong -\sum_{j=1}^{M} A_{E_{y;inc;j}}(x',z')\, E^{BP}_{y;\Phi_{scat};j}(x',z',\tau_{E_{y;inc;j}}(x',z')) \tag{7.1.18}$$

$$\begin{aligned}\Delta\hat{\mu}_{\Phi}(x',z') \cong -\sum_{j=1}^{M} [&A_{\dot{H}_{x;inc;j}}(x',z')\, H^{BP}_{x;\Phi_{scat};j}(x',z',\tau_{\dot{H}_{x;inc;j}}(x',z')) + \\ &A_{\dot{H}_{z;inc;j}}(x',z')\, H^{BP}_{z;\Phi_{scat};j}(x',z',\tau_{\dot{H}_{z;inc;j}}(x',z'))]\end{aligned} \tag{7.1.19}$$

Using relations (1.29) and applying similar approximation on the Green's functions, the back-propagated scattered fields can be simplified as:

$$E^{BP}_{y;Ey_{scat};j}(x',z',t') \cong -\sum_{i=1}^{N} A_{G^{EJ}_{yy;b;i}}(x',z')\, E^{d}_{y;scat;j}(x_i,z_i,\, t'+\tau_{G^{EJ}_{yy;b;i}}(x',z')) \tag{7.1.20a}$$

$$H^{BP}_{x;Ey_{scat};j}(x',z',t') \cong +\sum_{i=1}^{N} A_{G^{HJ}_{xy;b;i}}(x',z')\, E^{d}_{y;scat;j}(x_i,z_i,\, t'+\tau_{G^{HJ}_{xy;b;i}}(x',z')) \tag{7.1.21a}$$

$$H^{BP}_{z;Ey_{scat};j}(x',z',t') \cong +\sum_{i=1}^{N} A_{G^{HJ}_{zy;b;i}}(x',z')\, E^{d}_{y;scat;j}(x_i,z_i,\, t'+\tau_{G^{HJ}_{zy;b;i}}(x',z')) \tag{7.1.22a}$$

$$E^{BP}_{y;Hx_{scat};j}(x',z',t') \cong +\sum_{i=1}^{N} A_{G^{EM}_{yx;b;i}}(x',z')\, H^{d}_{x;scat;j}(x_i,z_i,\, t'+\tau_{G^{EM}_{yx;b;i}}(x',z')) \tag{7.1.20b}$$

$$H^{BP}_{x;Hx_{scat};j}(x',z',t') \cong -\sum_{i=1}^{N} A_{G^{HM}_{xx;b;i}}(x',z')\, H^{d}_{x;scat;j}(x_i,z_i,\, t'+\tau_{G^{HM}_{xx;b;i}}(x',z')) \tag{7.1.21b}$$

$$H^{BP}_{z;Hx_{scat};j}(x',z',t') \cong -\sum_{i=1}^{N} A_{G^{HM}_{zx;b;i}}(x',z')\, H^{d}_{x;scat;j}(x_i, z_i,\, t' + \tau_{G^{HM}_{zx;b;i}}(x',z')) \tag{7.1.22b}$$

$$E^{BP}_{y;Hz_{scat};j}(x',z',t') \cong +\sum_{i=1}^{N} A_{G^{EM}_{yz;b;i}}(x',z')\, H^{d}_{z;scat;j}(x_i, z_i,\, t' + \tau_{G^{EM}_{yz;b;i}}(x',z')) \tag{7.1.20c}$$

$$H^{BP}_{x;Hz_{scat};j}(x',z',t') \cong -\sum_{i=1}^{N} A_{G^{HM}_{xz;b;i}}(x',z')\, H^{d}_{z;scat;j}(x_i, z_i,\, t' + \tau_{G^{HM}_{xz;b;i}}(x',z')) \tag{7.1.21c}$$

$$H^{BP}_{z;Hz_{scat};j}(x',z',t') \cong -\sum_{i=1}^{N} A_{G^{HM}_{zz;b;i}}(x',z')\, H^{d}_{z;scat;j}(x_i, z_i,\, t' + \tau_{G^{HM}_{zz;b;i}}(x',z')) \tag{7.1.22c}$$

Substitution of the above back-propagated scattered fields into Eq. (7.1.13) to (7.1.19) results in the following real-time imaging formulas:

$$\Delta\hat{\varepsilon}_{yy;Ey}(x',z') \cong +\sum_{j=1}^{M} A_{\dot{E}_{y;inc;j}} \sum_{i=1}^{N} A_{G^{EJ}_{yy;b;i}} E^{d}_{y;scat;j}(x_i, z_i,\, \tau_{\dot{E}_{y;inc;j}} + \tau_{G^{EJ}_{yy;b;i}}) \tag{7.1.23a}$$

$$\Delta\hat{\varepsilon}_{yy;Hx}(x',z') \cong -\sum_{j=1}^{M} A_{\dot{E}_{y;inc;j}} \sum_{i=1}^{N} A_{G^{EM}_{yx;b;i}} H^{d}_{x;scat;j}(x_i, z_i,\, \tau_{\dot{E}_{y;inc;j}} + \tau_{G^{EM}_{yx;b;i}}) \tag{7.1.23b}$$

$$\Delta\hat{\varepsilon}_{yy;Hz}(x',z') \cong -\sum_{j=1}^{M} A_{\dot{E}_{y;inc;j}} \sum_{i=1}^{N} A_{G^{EM}_{yz;b;i}} H^{d}_{z;scat;j}(x_i, z_i,\, \tau_{\dot{E}_{y;inc;j}} + \tau_{G^{EM}_{yz;b;i}}) \tag{7.1.23c}$$

$$\Delta\hat{\sigma}_{yy;Ey}(x',z') \cong +\sum_{j=1}^{M} A_{E_{y;inc;j}} \sum_{i=1}^{N} A_{G^{EJ}_{yy;b;i}} E^{d}_{y;scat;j}(x_i, z_i,\, \tau_{E_{y;inc;j}} + \tau_{G^{EJ}_{yy;b;i}}) \tag{7.1.24a}$$

$$\Delta\hat{\sigma}_{yy;Hx}(x',z') \cong -\sum_{j=1}^{M} A_{E_{y;inc;j}} \sum_{i=1}^{N} A_{G^{EM}_{yx;b;i}} H^{d}_{x;scat;j}(x_i, z_i,\, \tau_{E_{y;inc;j}} + \tau_{G^{EM}_{yx;b;i}}) \tag{7.1.24b}$$

$$\Delta\hat{\sigma}_{yy;Hz}(x',z') \cong -\sum_{j=1}^{M} A_{E_{y;inc;j}} \sum_{i=1}^{N} A_{G^{EM}_{yz;b;i}} H^{d}_{z;scat;j}(x_i, z_i,\, \tau_{E_{y;inc;j}} + \tau_{G^{EM}_{yz;b;i}}) \tag{7.1.24c}$$

$$\Delta\hat{\mu}_{xx;Ey}(x',z') \cong -\sum_{j=1}^{M} A_{\dot{H}_{x;inc;j}} \sum_{i=1}^{N} A_{G^{HJ}_{xy;b;i}} E^{d}_{y;scat;j}(x_i, z_i,\, \tau_{\dot{H}_{x;inc;j}} + \tau_{G^{HJ}_{xy;b;i}}) \tag{7.1.25a}$$

$$\Delta\hat{\mu}_{xx;Hx}(x',z') \cong +\sum_{j=1}^{M} A_{\dot{H}_{x;inc;j}} \sum_{i=1}^{N} A_{G^{HM}_{xx;b;i}} H^{d}_{x;scat;j}(x_i, z_i,\, \tau_{\dot{H}_{x;inc;j}} + \tau_{G^{HM}_{xx;b;i}}) \tag{7.1.25b}$$

$$\Delta\hat{\mu}_{xx;Hz}(x',z') \cong +\sum_{j=1}^{M} A_{\dot{H}_{x;inc;j}} \sum_{i=1}^{N} A_{G^{HM}_{xz;b;i}} H^{d}_{z;scat;j}(x_i, z_i, \tau_{\dot{H}_{x;inc;j}} + \tau_{G^{HM}_{xz;b;i}}) \tag{7.1.25c}$$

$$\Delta\hat{\mu}_{zz;Ey}(x',z') \cong -\sum_{j=1}^{M} A_{\dot{H}_{z;inc;j}} \sum_{i=1}^{N} A_{G^{HJ}_{zy;b;i}} E^{d}_{y;scat;j}(x_i, z_i, \tau_{\dot{H}_{z;inc;j}} + \tau_{G^{HJ}_{zy;b;i}}) \tag{7.1.26a}$$

$$\Delta\hat{\mu}_{zz;Hx}(x',z') \cong +\sum_{j=1}^{M} A_{\dot{H}_{z;inc;j}} \sum_{i=1}^{N} A_{G^{HM}_{zx;b;i}} H^{d}_{x;scat;j}(x_i, z_i, \tau_{\dot{H}_{z;inc;j}} + \tau_{G^{HM}_{zx;b;i}}) \tag{7.1.26b}$$

$$\Delta\hat{\mu}_{zz;Hz}(x',z') \cong +\sum_{j=1}^{M} A_{\dot{H}_{z;inc;j}} \sum_{i=1}^{N} A_{G^{HM}_{zz;b;i}} H^{d}_{z;scat;j}(x_i, z_i, \tau_{\dot{H}_{z;inc;j}} + \tau_{G^{HM}_{zz;b;i}}) \tag{7.1.26c}$$

$$\Delta\hat{\varepsilon}_{Ey}(x',z') \cong +\sum_{j=1}^{M} A_{\dot{E}_{y;inc;j}} \sum_{i=1}^{N} A_{G^{EJ}_{yy;b;i}} E^{d}_{y;scat;j}(x_i, z_i, \tau_{\dot{E}_{y;inc;j}} + \tau_{G^{EJ}_{yy;b;i}}) \tag{7.1.27a}$$

$$\Delta\hat{\varepsilon}_{Hx}(x',z') \cong -\sum_{j=1}^{M} A_{\dot{E}_{y;inc;j}} \sum_{i=1}^{N} A_{G^{EM}_{yx;b;i}} H^{d}_{x;scat;j}(x_i, z_i, \tau_{\dot{E}_{y;inc;j}} + \tau_{G^{EM}_{yx;b;i}}) \tag{7.1.27b}$$

$$\Delta\hat{\varepsilon}_{Hz}(x',z') \cong -\sum_{j=1}^{M} A_{\dot{E}_{y;inc;j}} \sum_{i=1}^{N} A_{G^{EM}_{yz;b;i}} H^{d}_{z;scat;j}(x_i, z_i, \tau_{\dot{E}_{y;inc;j}} + \tau_{G^{EM}_{yz;b;i}}) \tag{7.1.27c}$$

$$\Delta\hat{\sigma}_{Ey}(x',z') \cong +\sum_{j=1}^{M} A_{E_{y;inc;j}} \sum_{i=1}^{N} A_{G^{EJ}_{yy;b;i}} E^{d}_{y;scat;j}(x_i, z_i, \tau_{E_{y;inc;j}} + \tau_{G^{EJ}_{yy;b;i}}) \tag{7.1.28a}$$

$$\Delta\hat{\sigma}_{Hx}(x',z') \cong -\sum_{j=1}^{M} A_{E_{y;inc;j}} \sum_{i=1}^{N} A_{G^{EM}_{yx;b;i}} H^{d}_{x;scat;j}(x_i, z_i, \tau_{E_{y;inc;j}} + \tau_{G^{EM}_{yx;b;i}}) \tag{7.1.28b}$$

$$\Delta\hat{\sigma}_{Hz}(x',z') \cong -\sum_{j=1}^{M} A_{E_{y;inc;j}} \sum_{i=1}^{N} A_{G^{EM}_{yz;b;i}} H^{d}_{z;scat;j}(x_i, z_i, \tau_{E_{y;inc;j}} + \tau_{G^{EM}_{yz;b;i}}) \tag{7.1.28c}$$

$$\begin{aligned}\Delta\hat{\mu}_{Ey}(x',z') \cong -\sum_{j=1}^{M} \{ & A_{\dot{H}_{x;inc;j}} \sum_{i=1}^{N} A_{G^{HJ}_{xy;b;i}} E^{d}_{y;scat;j}(x_i, z_i, \tau_{\dot{H}_{x;inc;j}} + \tau_{G^{HJ}_{xy;b;i}}) + \\ & A_{\dot{H}_{z;inc;j}} \sum_{i=1}^{N} A_{G^{HJ}_{zy;b;i}} E^{d}_{y;scat;j}(x_i, z_i, \tau_{\dot{H}_{z;inc;j}} + \tau_{G^{HJ}_{zy;b;i}}) \}\end{aligned} \tag{7.1.29a}$$

$$\begin{aligned}\Delta\hat{\mu}_{Hx}(x',z') \cong +\sum_{j=1}^{M} \{ & A_{\dot{H}_{x;inc;j}} \sum_{i=1}^{N} A_{G^{HM}_{xx;b;i}} H^{d}_{x;scat;j}(x_i, z_i, \tau_{\dot{H}_{x;inc;j}} + \tau_{G^{HM}_{xx;b;i}}) + \\ & A_{\dot{H}_{z;inc;j}} \sum_{i=1}^{N} A_{G^{HM}_{zx;b;i}} H^{d}_{x;scat;j}(x_i, z_i, \tau_{\dot{H}_{z;inc;j}} + \tau_{G^{HM}_{zx;b;i}}) \}\end{aligned} \tag{7.1.29b}$$

$$\Delta\hat{\mu}_{Hz}(x',z') \cong +\sum_{j=1}^{M}\{A_{\dot{H}_{x;inc;j}}\sum_{i=1}^{N}A_{G^{HM}_{xz;b;i}}H^{d}_{z;scat;j}(x_i,z_i,\tau_{\dot{H}_{x;inc;j}}+\tau_{G^{HM}_{xz;b;i}})+ \\ A_{\dot{H}_{z;inc;j}}\sum_{i=1}^{N}A_{G^{HM}_{zz;b;i}}H^{d}_{z;scat;j}(x_i,z_i,\tau_{\dot{H}_{z;inc;j}}+\tau_{G^{HM}_{zz;b;i}})\} \tag{7.1.29c}$$

In the above relations, the dependency of all amplitudes and traveltimes on x' and z' is not shown for the sake of brevity.

7.2. Electromagnetic Migration Imaging Formulas in TM Field

Based on the assumed coordinate axis configuration, the unit normal vector pointing outward of the measurement line is $\boldsymbol{n}=-\boldsymbol{k}$, where $\boldsymbol{k}$ is the z-axis unit vector. Then, the migration imaging formulas (4.1.22) to (4.1.24) for biaxial structures are reduced to:

$$\Delta\hat{\varepsilon}_{yy}(x',z') = -\sum_{j=1}^{M}\int_0^T E^{m}_{y;scat;j}(x',z',t')\,\dot{E}_{y;inc;j}(x',z',t')\,dt' \tag{7.2.1}$$

$$\Delta\hat{\sigma}_{yy}(x',z') = -\sum_{j=1}^{M}\int_0^T E^{m}_{y;scat;j}(x',z',t')\,E_{y;inc;j}(x',z',t')\,dt' \tag{7.2.2}$$

$$\Delta\hat{\mu}_{xx}(x',z') = -\sum_{j=1}^{M}\int_0^T H^{m}_{x;scat;j}(x',z',t')\,\dot{H}_{x;inc;j}(x',z',t')\,dt' \tag{7.2.3}$$

$$\Delta\hat{\mu}_{zz}(x',z') = -\sum_{j=1}^{M}\int_0^T H^{m}_{z;scat;j}(x',z',t')\,\dot{H}_{z;inc;j}(x',z',t')\,dt' \tag{7.2.4}$$

Where the DE formalisms of the migrated scattered field, Eq.(4.1.26) or Eq. (4.1.27), take the following forms, respectively.

$$\begin{cases} \dfrac{\partial E^{m}_{y;scat;j}}{\partial z} = \mu_{xx;b}\dot{H}^{m}_{x;scat;j} - \sum_{i=1}^{N}E^{d}_{y;scat;j}(x_i,z_i,t)\,\delta(x-x_i)\delta(z-z_i) \\ -\dfrac{\partial H^{m}_{x;scat;j}}{\partial z} + \dfrac{\partial H^{m}_{z;scat;j}}{\partial x} = \sigma_{yy;b}E^{m}_{y;scat;j} - \varepsilon_{yy;b}\dot{E}^{m}_{y;scat;j} + \sum_{i=1}^{N}H^{d}_{x;scat;j}(x_i,z_i,t)\,\delta(x-x_i)\delta(z-z_i) \\ -\dfrac{\partial E^{m}_{y;scat;j}}{\partial x} = \mu_{zz;b}\dot{H}^{m}_{z;scat;j} \end{cases} \tag{7.2.5}$$

$$\begin{cases} \dfrac{\partial E^{m}_{y;scat;j}}{\partial z} = \mu_{xx;b}\dot{H}^{m}_{x;scat;j} \\ -\dfrac{\partial H^{m}_{x;scat;j}}{\partial z} + \dfrac{\partial H^{m}_{z;scat;j}}{\partial x} = \sigma_{yy;b}E^{m}_{y;scat;j} - \varepsilon_{yy;b}\dot{E}^{m}_{y;scat;j} \\ -\dfrac{\partial E^{m}_{y;scat;j}}{\partial x} = \mu_{zz;b}\dot{H}^{m}_{z;scat;j} \end{cases} \tag{7.2.6a}$$

$$\text{BC}: \begin{cases} E^{m}_{y;scat;j}(x_i, z_i, t) = E^{d}_{y;scat;j}(x_i, z_i, t) \\ H^{m}_{x;scat;j}(x_i, z_i, t) = H^{d}_{x;scat;j}(x_i, z_i, t) \end{cases} \tag{7.2.6b}$$

Also, the corresponding IE formalism of the migrated scattered field, Eq. (4.1.25), is expressed as:

$$E^{m}_{y;scat}(x', z', t') = \sum_{i=1}^{N}\int_{T}^{t'} [\hat{G}^{EM}_{yx;b}(x', z', t'; x_i, z_i, t)\, E^{d}_{y;scat;j}(x_i, z_i, t) + \hat{G}^{EJ}_{yy;b}(x', z', t'; x_i, z_i, t)\, H^{d}_{x;scat;j}(x_i, z_i, t)]\, dt \tag{7.2.7}$$

$$H^{m}_{x;scat}(x', z', t') = \sum_{i=1}^{N}\int_{T}^{t'} [\hat{G}^{HM}_{xx;b}(x', z', t'; x_i, z_i, t)\, E^{d}_{y;scat;j}(x_i, z_i, t) + \hat{G}^{HJ}_{xy;b}(x', z', t'; x_i, z_i, t)\, H^{d}_{x;scat;j}(x_i, z_i, t)]\, dt \tag{7.2.8}$$

$$H^{m}_{z;scat}(x', z', t') = \sum_{i=1}^{N}\int_{T}^{t'} [\hat{G}^{HM}_{zx;b}(x', z', t'; x_i, z_i, t)\, E^{d}_{y;scat;j}(x_i, z_i, t) + \hat{G}^{HJ}_{zy;b}(x', z', t'; x_i, z_i, t)\, H^{d}_{x;scat;j}(x_i, z_i, t)]\, dt \tag{7.2.9}$$

For isotropic structures, the migration imaging formulas are simplified to:

$$\Delta\hat{\varepsilon}(x', z') = -\sum_{j=1}^{M}\int_{0}^{T} E^{m}_{y;scat;j}(x', z', t')\, \dot{E}_{y;inc;j}(x', z', t')\, dt' \tag{7.2.10}$$

$$\Delta\hat{\sigma}(x', z') = -\sum_{j=1}^{M}\int_{0}^{T} E^{m}_{y;scat;j}(x', z', t')\, E_{y;inc;j}(x', z', t')\, dt' \tag{7.2.11}$$

$$\Delta\hat{\mu}(x', z') = -\sum_{j=1}^{M}\int_{0}^{T} [H^{m}_{x;scat;j}(x', z', t')\, \dot{H}_{x;inc;j}(x', z', t') + H^{m}_{z;scat;j}(x', z', t')\, \dot{H}_{z;inc;j}(x', z', t')]\, dt' \tag{7.2.12}$$

with the following DE formalisms of the migrated scattered field:

$$\begin{cases} \dfrac{\partial E^{m}_{y;scat;j}}{\partial z} = \mu_b \dot{H}^{m}_{x;scat;j} - \sum_{i=1}^{N} E^{d}_{y;scat;j}(x_i, z_i, t)\,\delta(x - x_i)\delta(z - z_i) \\ -\dfrac{\partial H^{m}_{x;scat;j}}{\partial z} + \dfrac{\partial H^{m}_{z;scat;j}}{\partial x} = \sigma_b E^{m}_{y;scat;j} - \varepsilon_b \dot{E}^{m}_{y;scat;j} + \sum_{i=1}^{N} H^{d}_{x;scat;j}(x_i, z_i, t)\,\delta(x - x_i)\delta(z - z_i) \\ -\dfrac{\partial E^{m}_{y;scat;j}}{\partial x} = \mu_b \dot{H}^{m}_{z;scat;j} \end{cases} \quad (7.2.13)$$

$$\begin{cases} \dfrac{\partial E^{m}_{y;scat;j}}{\partial z} = \mu_b \dot{H}^{m}_{x;scat;j} \\ -\dfrac{\partial H^{m}_{x;scat;j}}{\partial z} + \dfrac{\partial H^{m}_{z;scat;j}}{\partial x} = \sigma_b E^{m}_{y;scat;j} - \varepsilon_b \dot{E}^{m}_{y;scat;j} \\ -\dfrac{\partial E^{m}_{y;scat;j}}{\partial x} = \mu_b \dot{H}^{m}_{z;scat;j} \end{cases} \quad (7.2.14a)$$

$$\text{BC}: \begin{cases} E^{m}_{y;scat;j}(x_i, z_i, t) = E^{d}_{y;scat;j}(x_i, z_i, t) \\ H^{m}_{x;scat;j}(x_i, z_i, t) = H^{d}_{x;scat;j}(x_i, z_i, t) \end{cases} \quad (7.2.14b)$$

Applying the approximation defined in Eq. (6.1) on the incident field components, Eq. (7.2.1) to (7.2.4) and Eq. (7.2.10) to (7.2.12) are simplified to:

$$\Delta\hat{\varepsilon}_{yy}(x', z') \cong -\sum_{j=1}^{M} A_{\dot{E}_{y;inc;j}}(x', z')\; E^{m}_{y;scat;j}(x', z', \tau_{\dot{E}_{y;inc;j}}(x', z')) \quad (7.2.15)$$

$$\Delta\hat{\sigma}_{yy}(x', z') \cong -\sum_{j=1}^{M} A_{E_{y;inc;j}}(x', z')\; E^{m}_{y;scat;j}(x', z', \tau_{E_{y;inc;j}}(x', z')) \quad (7.2.16)$$

$$\Delta\hat{\mu}_{xx}(x', z') \cong -\sum_{j=1}^{M} A_{\dot{H}_{x;inc;j}}(x', z')\; H^{m}_{x;scat;j}(x', z', \tau_{\dot{H}_{x;inc;j}}(x', z')) \quad (7.2.17)$$

$$\Delta\hat{\mu}_{zz}(x', z') \cong -\sum_{j=1}^{M} A_{\dot{H}_{z;inc;j}}(x', z')\; H^{m}_{z;scat;j}(x', z', \tau_{\dot{H}_{z;inc;j}}(x', z')) \quad (7.2.18)$$

$$\Delta\hat{\varepsilon}(x', z') \cong -\sum_{j=1}^{M} A_{\dot{E}_{y;inc;j}}(x', z')\; E^{m}_{y;scat;j}(x', z', \tau_{\dot{E}_{y;inc;j}}(x', z')) \quad (7.2.19)$$

$$\Delta\hat{\sigma}(x',z') \cong -\sum_{j=1}^{M} A_{E_{y;inc;j}}(x',z')\, E^{m}_{y;scat;j}(x',z',\tau_{E_{y;inc;j}}(x',z')) \tag{7.2.20}$$

$$\begin{aligned}\Delta\hat{\mu}(x',z') \cong -\sum_{j=1}^{M} [&A_{\dot{H}_{x;inc;j}}(x',z')\, H^{m}_{x;scat;j}(x',z',\tau_{\dot{H}_{x;inc;j}}(x',z')) + \\ &A_{\dot{H}_{z;inc;j}}(x',z')\, H^{m}_{z;scat;j}(x',z',\tau_{\dot{H}_{z;inc;j}}(x',z'))]\end{aligned} \tag{7.2.21}$$

Using relations (1.29) and applying similar approximation on the Green's functions, the real-time imaging formulas take the following forms:

$$\begin{aligned}\Delta\hat{\varepsilon}_{yy}(x',z') \cong -\sum_{j=1}^{M} A_{\dot{E}_{y;inc;j}} \sum_{i=1}^{N} [&A_{G^{EM}_{yx;b;i}} E^{d}_{y;scat;j}(x_i,z_i,\tau_{\dot{E}_{y;inc;j}} + \tau_{G^{EM}_{yx;b;i}}) - \\ &A_{G^{EJ}_{yy;b;i}} H^{d}_{x;scat;j}(x_i,z_i,\tau_{\dot{E}_{y;inc;j}} + \tau_{G^{EJ}_{yy;b;i}})]\end{aligned} \tag{7.2.22}$$

$$\begin{aligned}\Delta\hat{\sigma}_{yy}(x',z') \cong -\sum_{j=1}^{M} A_{E_{y;inc;j}} \sum_{i=1}^{N} [&A_{G^{EM}_{yx;b;i}} E^{d}_{y;scat;j}(x_i,z_i,\tau_{E_{y;inc;j}} + \tau_{G^{EM}_{yx;b;i}}) - \\ &A_{G^{EJ}_{yy;b;i}} H^{d}_{x;scat;j}(x_i,z_i,\tau_{E_{y;inc;j}} + \tau_{G^{EJ}_{yy;b;i}})]\end{aligned} \tag{7.2.23}$$

$$\begin{aligned}\Delta\hat{\mu}_{xx}(x',z') \cong -\sum_{j=1}^{M} A_{\dot{H}_{x;inc;j}} \sum_{i=1}^{N} [&-A_{G^{HM}_{xx;b;i}} E^{d}_{y;scat;j}(x_i,z_i,\tau_{\dot{H}_{x;inc;j}} + \tau_{G^{HM}_{xx;b;i}}) + \\ &A_{G^{HJ}_{xy;b;i}} H^{d}_{x;scat;j}(x_i,z_i,\tau_{\dot{H}_{x;inc;j}} + \tau_{G^{HJ}_{xy;b;i}})]\end{aligned} \tag{7.2.24}$$

$$\begin{aligned}\Delta\hat{\mu}_{zz}(x',z') \cong -\sum_{j=1}^{M} A_{\dot{H}_{z;inc;j}} \sum_{i=1}^{N} [&-A_{G^{HM}_{zx;b;i}} E^{d}_{y;scat;j}(x_i,z_i,\tau_{\dot{H}_{z;inc;j}} + \tau_{G^{HM}_{zx;b;i}}) + \\ &A_{G^{HJ}_{zy;b;i}} H^{d}_{x;scat;j}(x_i,z_i,\tau_{\dot{H}_{z;inc;j}} + \tau_{G^{HJ}_{zy;b;i}})]\end{aligned} \tag{7.2.25}$$

$$\begin{aligned}\Delta\hat{\varepsilon}(x',z') \cong -\sum_{j=1}^{M} A_{\dot{E}_{y;inc;j}} \sum_{i=1}^{N} [&A_{G^{EM}_{yx;b;i}} E^{d}_{y;scat;j}(x_i,z_i,\tau_{\dot{E}_{y;inc;j}} + \tau_{G^{EM}_{yx;b;i}}) - \\ &A_{G^{EJ}_{yy;b;i}} H^{d}_{x;scat;j}(x_i,z_i,\tau_{\dot{E}_{y;inc;j}} + \tau_{G^{EJ}_{yy;b;i}})]\end{aligned} \tag{7.2.26}$$

$$\begin{aligned}\Delta\hat{\sigma}(x',z') \cong -\sum_{j=1}^{M} A_{E_{y;inc;j}} \sum_{i=1}^{N} [&A_{G^{EM}_{yx;b;i}} E^{d}_{y;scat;j}(x_i,z_i,\tau_{E_{y;inc;j}} + \tau_{G^{EM}_{yx;b;i}}) - \\ &A_{G^{EJ}_{yy;b;i}} H^{d}_{x;scat;j}(x_i,z_i,\tau_{E_{y;inc;j}} + \tau_{G^{EJ}_{yy;b;i}})]\end{aligned} \tag{7.2.27}$$

$$\Delta\hat{\mu}(x',z') \cong -\sum_{j=1}^{M}\{A_{\dot{H}_{x;inc;j}}\sum_{i=1}^{N}[-A_{G^{HM}_{xx;b;i}}E^{d}_{y;scat;j}(x_i,z_i,\tau_{\dot{H}_{x;inc;j}}+\tau_{G^{HM}_{xx;b;i}})+ A_{G^{HJ}_{xy;b;i}}H^{d}_{x;scat;j}(x_i,z_i,\tau_{\dot{H}_{x;inc;j}}+\tau_{G^{HJ}_{xy;b;i}})]+ A_{\dot{H}_{z;inc;j}}\sum_{i=1}^{N}[-A_{G^{HM}_{zx;b;i}}E^{d}_{y;scat;j}(x_i,z_i,\tau_{\dot{H}_{z;inc;j}}+\tau_{G^{HM}_{zx;b;i}})+ A_{G^{HJ}_{zy;b;i}}H^{d}_{x;scat;j}(x_i,z_i,\tau_{\dot{H}_{z;inc;j}}+\tau_{G^{HJ}_{zy;b;i}})]\} \quad (7.2.28)$$

8. Numerical Results

The effectiveness of the electromagnetic (EM) migration and Born imaging algorithms for 2-D damage imaging of both isotropic and anisotropic structures is demonstrated in this chapter. For isotropic case, a reinforced concrete slab with horizontal crack and debonding damages and for anisotropic case, a glass/epoxy composite plate with two delaminations, are considered.

For each case, the imaging quality of both differential equation (DE) and integral equation (IE) formalisms of the proposed algorithms are examined. In addition, the imaging quality of the DE formalism of the algorithms utilizing the poststack concept is investigated.

A finite difference time-domain (FDTD) method based on *Yee algorithm* (Yee, 1966) with second–order of accuracy in both time and space is used for generating all synthetic sensor data, incident field, the fields associated with the Green's functions of the pristine structure, and back-propagated (migrated) scattered field. The grid sizes in both *x* and *z* directions are assumed equal ($\Delta x = \Delta z$). In order to ensure numerical stability, the time step is chosen (Taflov, 1995): $\Delta t = 0.9\Delta x/(c_0\sqrt{2})$, where $c_0 = 3\times10^8$ m/s is the velocity of the EM waves in vacuum.

The transverse magnetic (TM) field is excited by an electric current density line source $J_y(x,z,t) = \delta(x-x_j)\,\delta(z-z_j)\,f(t)$, a *y*-directed line source passing through the point (x_j, z_j). The time history of the current density (unit in Amperes) is considered to be a Hanning window modulated sinusoid:

$$f(t) = [H(t) - H(t - N_p / f_c)]\,[1-\cos(2\pi f_c t / N_p)]\,\sin(2\pi f_c t) \tag{8.1}$$

Where *H*(*t*) is Heaviside function, $N_p = 1$, and f_c is the dominant (central) frequency. Note that in real application, the radiation pattern and directivity of the transmitter and receiver antennas, actuators and sensors, should be accounted for in the modeling.

As previously mentioned, the sensor data must be collected in a zero-offset configuration when the poststack concept is to be used in the proposed algorithms. However, the synthetic

data generated based on the exploding reflector model does not correctly represent the zero-offset data. Therefore, instead of solving the forward problem one time using exploding reflector model, the problem should be solved as many times as the number of sensor/actuator pairs using the actual damaged model to obtain the correct synthetic zero-offset data. In order to use the poststack concept in the algorithms, zero-time imaging condition is applied to the back-propagated (migrated) scattered field components $E^{BP}_{y;scat}$, $H^{BP}_{x;scat}$, and $H^{BP}_{z;scat}$ ($E^{m}_{y;scat}$, $H^{m}_{x;scat}$, and $H^{m}_{z;scat}$) computed in a 2:1 scaled pristine structure. Therefore, three different images can be obtained.

To show the robustness of the imaging algorithms to measurement noise, the sensor data is contaminated by an additive white Gaussian noise with zero mean and standard deviation σ (not confused with the conductivity). Signal-to-noise ratio (SNR) is considered to be equal to 5 with the following definition for $E^{d}_{y;scat}$, for instance:

$$SNR = 10\log_{10}\left\{ \frac{Mean\left[(E^{d}_{y;scat})^2\right]}{\sigma^2} \right\} \tag{8.2}$$

It should be noted that the artifacts in images are generally due to several factors some of which are coarse actuator/sensor spacing, limited sensor span, limited bandwidth of the excitation signal, and material discontinuity in the pristine structure. In the following, the effect of the actuator/sensor spacing and the material discontinuity in the pristine structure are investigated.

8.1. Isotropic Case

A reinforced concrete slab (depth: 5 cm) with three square rebars having 11 mm diameters and center locations (1, 2.5), (5, 2.5), and (9, 2.5) cm is considered as the pristine structure. Fig. 8.1.1 illustrates the cross section of the damaged structure having a horizontal crack (crack area: $11\,\text{mm}\times 2\,\text{mm}$) with the center at (3, 3) cm and a debonding between the middle rebar and concrete with the debonding thickness of 2 mm. It is assumed that above and below the slab is air and actuators and sensors are uniformly located on the upper surface of the concrete slab with a sensor span of 108 mm.

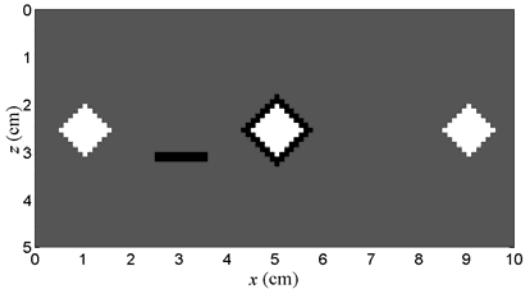

Fig. 8.1.1. Cross section of a reinforced concrete slab with multiple damages

The central frequency of the excitation signal is assumed to be $f_c = 7.65\,\text{GHz}$. Fig. 8.1.2 and 3 show the time history of the excitation signal and its amplitude spectrum, respectively.

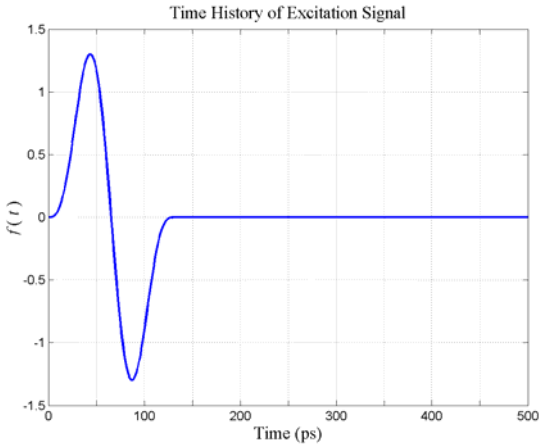

Fig. 8.1.2. The time history of the excitation signal

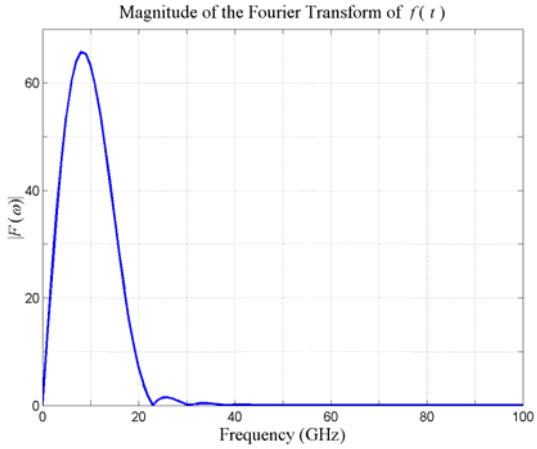

Fig. 8.1.3. The amplitude spectrum of the excitation signal

Considering relative dielectric constant and conductivity of the concrete to be $\varepsilon_r = 5.3$ and $\sigma = 0.05$ S/m , the central wavelength of the excitation signal in concrete is about 17 mm ($\lambda_c \cong c_0/(\sqrt{\varepsilon_r}\, f_c)$). Also, based on 3% of the maximum amplitude of the excitation signal spectrum, the maximum frequency and minimum wavelength of the signal in concrete are found to be about 21.7 GHz and 6 mm, respectively. It is also assumed that the properties of the rebars are $\varepsilon_r = 1$ and $\sigma = 1.03\times10^7$ S/m . Considering the minimum wavelength, the grid size is chosen equal to 1 mm ($\Delta x = \Delta z = 1$mm).

Fig. 8.1.4 to 6 illustrate three components of the scattered field data (the measured incident field subtracted from the measured total field) excited from an actuator located at $x = 50$mm with sensor spacing of $\Delta_s = 6$ mm .

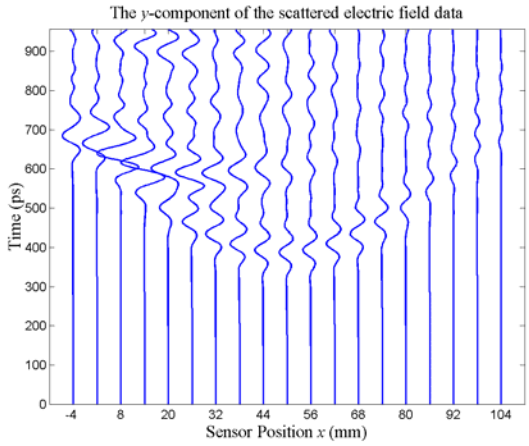

Fig. 8.1.4. The *y*-component of the scattered electric field data, $E^d_{y;\,scat}$, excited from an actuator at $x = 50$mm with sensor spacing of $\Delta_s = 6$ mm

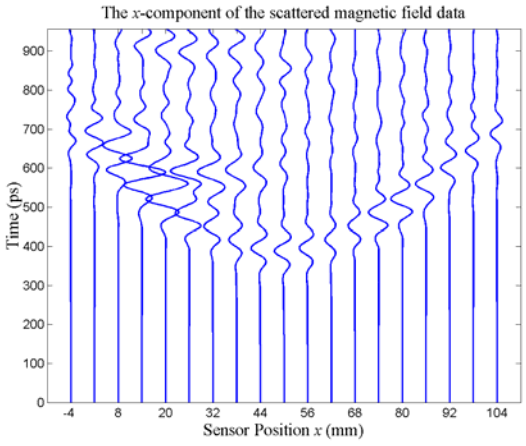

Fig. 8.1.5. The *x*-component of the scattered magnetic field data, $H^d_{x;\,scat}$, excited from an actuator at $x = 50$mm with sensor spacing of $\Delta_s = 6$ mm

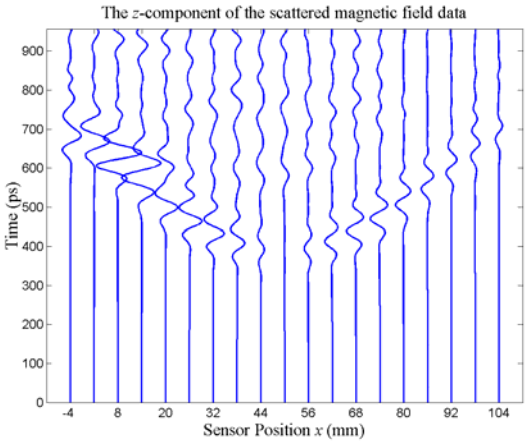

Fig. 8.1.6. The *z*-component of the scattered magnetic field data, $H^{d}_{z;\ scat}$, excited from an actuator at $x = 50\,\text{mm}$ with sensor spacing of $\Delta_s = 6$ mm

Note that the actuator-sensor array can only reconstruct the upper part of the debonding due to the total reflection of EM waves by the metal rebars.

To observe the negative effect of the material discontinuity in the pristine structure, the resulting images are compared with the images from a new damaged structure including a half-space concrete without rebars and the original damages.

As mentioned in Chapter 6, there are several methods for reducing the artifacts related to the material discontinuity in the pristine structure. Here, in order to remove undesired internal reflections, a modified pristine structure, a half-space concrete, instead of the actual pristine structure, is used for the computation of the incident field, Green's functions, and back-propagated (migrated) scattered fields in the image area. Obviously, the measured incident and total fields are obtained from the actual pristine and damaged structures, respectively. Note that by using this method, no information about the positions of the rebars inside the pristine concrete structure has to be known *a priori* which is valuable in real applications.

Finally, to observe the typical shortcoming of the algorithms mentioned in Chapter 6, another damaged structure including a concrete slab without the rebars and the original damages is investigated.

8.1.1. Born Imaging (DE Formalism)

Eq. (7.1.9) - (7.1.11) represent the imaging formulas with zero-lag cross-correlation imaging condition. The corresponding imaging formulas with modified excitation-time imaging condition are Eq. (7.1.17) - (7.1.19); the imaging formulas with ordinary excitation-time imaging condition are easily obtained by setting the amplitudes to unity. Note that the back-propagated scattered fields are computed by FD discretization of differential equations (7.1.12) for the pristine structure. Also, the application of both first and maximum-energy arrival criteria for the calculation of the traveltimes and amplitudes are examined.

To show the effects of different measurement scenarios, actuator/sensor spacing, measurement noise, and material discontinuity in the pristine structure on the quality of the images, the following cases are investigated (in all cases $\Delta_{s,a} = 6 \text{ mm} = \lambda_{\min}$ unless otherwise stated):

(A) $H^d_{x;scat}$

(B) $E^d_{y;scat}$

(C) $H^d_{z;scat}$

(D) $H^d_{x;scat}$ (contaminated by noise with SNR=5)

(E) $H^d_{x;scat}$ ($\Delta_{s,a} = 9 \text{ mm} = 1.5\lambda_{\min}$)

(F) $H^d_{x;scat}$ ($\Delta_{s,a} = 12 \text{ mm} = 2\lambda_{\min}$)

(G) $H^d_{x;scat}$ (damaged structure: half-space concrete without rebars and the original damages)

(H) $H^d_{x;scat}$ (modified pristine structure: half-space concrete without rebars)

(I) $H^d_{x;scat}$ (damaged structure: concrete slab without rebars and the original damages)

Fig. 8.1.1.1 to 15 show the images obtained by the Born imaging algorithm in DE formalism with different imaging conditions in Case (A). The geometries of the damages have been correctly identified with the least artifacts in the permittivity images shown in Fig. 8.1.1.1 and 3. It is also observed that when the zero-lag cross-correlation imaging condition has been approximated by the ordinary or modified excitation-time imaging condition, the application of the maximum-energy arrival criterion for the calculation of the traveltimes (and amplitudes) has provided better damage identification (specially for the debonding damage) than the application of the first-arrival criterion. Notice that the images obtained by the modified excitation-time imaging condition with maximum-energy arrival criterion are comparable in quality to the images obtained by the zero-lag cross-correlation imaging condition.

Fig. 8.1.1.16 to 21 show the images obtained by the modified excitation-time imaging condition with maximum-energy arrival criterion for different measurement scenarios in Cases (B) and (C),.

Fig. 8.1.1.22 and 23 illustrate the effect of the measurement noise with SNR=5 on the permittivity images in Case (D). These figures show that the algorithm is quite robust against the measurement noise. To show the effect of the actuator/sensor spacing on the images quality, the permittivity images with $\Delta_{s,a}$ =1.5 $\lambda_{\min}$, 2 $\lambda_{\min}$ are shown in Fig. 8.1.1.24 to 25. The artifacts resulting from the increase in the actuator/sensor spacing can be easily observed in these figures.

Fig. 8.1.1.26 to 31 illustrate the images for a new damaged structure including a half-space concrete without rebars and the original damages in Case (G). Due to the simplicity of the pristine structure in this case (i.e., half-space concrete), all permittivity, permeability, and conductivity images obtained by different imaging conditions have provided good damage identification. The best damage identification has been still provided by the modified excitation-time imaging condition with maximum-energy arrival criterion. Notice how the artifacts related to the material discontinuity in the pristine structure in Case (A) images, have disappeared on the corresponding images in Case (G).

Fig. 8.1.1.32 to 37 present the images when a modified pristine structure (a half-space concrete) instead of the actual pristine structure (the concrete slab with the rebars) has been used for the computation of the incident and back-propagated fields in the image area. Notice how the artifacts related to the material discontinuity in the actual pristine structure in Case (A) images have been eliminated.

Fig. 8.1.1.38 shows the permeability image for a damaged structure including a concrete slab without the rebars and the original damages. Notice how a false damage related to the typical shortcoming of the algorithm has been imaged near the lower interface of the slab.

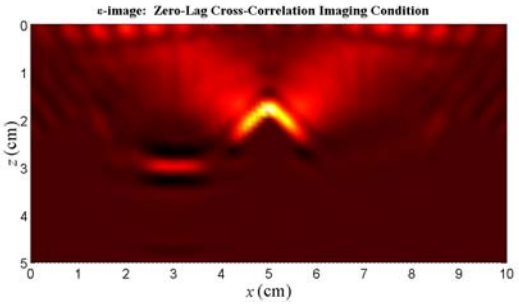

Fig. 8.1.1.1. Case (A); Permittivity image; Zero-lag cross-correlation imaging condition;

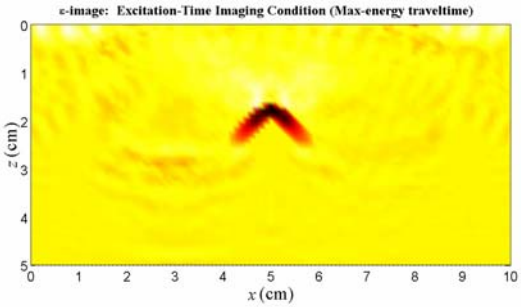

Fig. 8.1.1.2. Case (A); Permittivity image; Excitation-time imaging condition (Max-energy arrival);

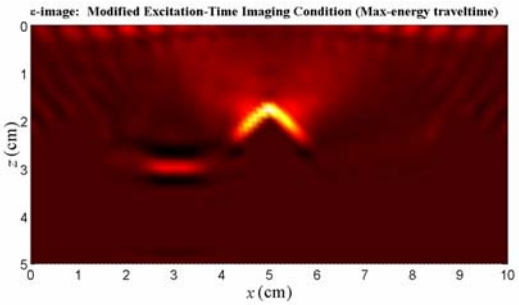

Fig. 8.1.1.3. Case (A); Permittivity image; Modified excitation-time imaging condition (Max-energy arrival);

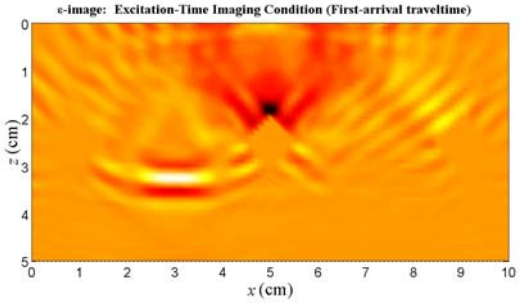

Fig. 8.1.1.4. Case (A); Permittivity image; Excitation-time imaging condition (First-arrival);

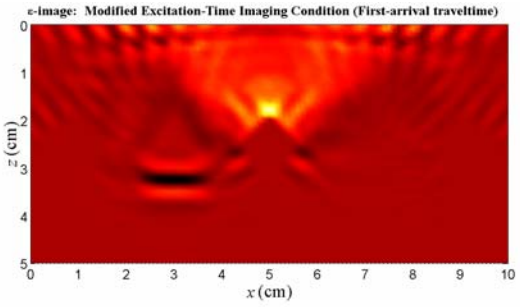

Fig. 8.1.1.5. Case (A); Permittivity image; Modified excitation-time imaging condition (First-arrival);

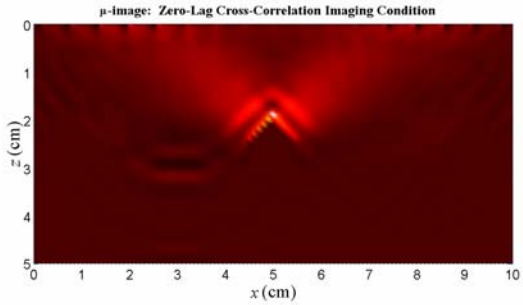

Fig. 8.1.1.6. Case (A); Permeability image; Zero-lag cross-correlation imaging condition;

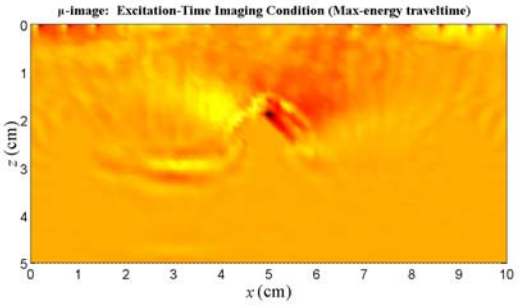

Fig. 8.1.1.7. Case (A); Permeability image; Excitation-time imaging condition (Max-energy arrival);

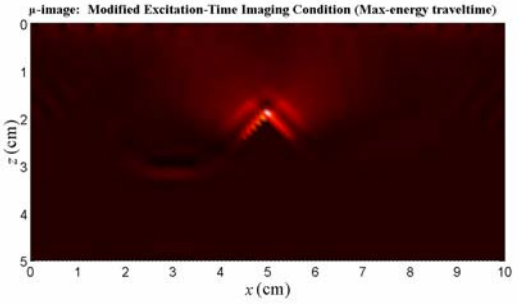

Fig. 8.1.1.8. Case (A); Permeability image; Modified excitation-time imaging condition (Max-energy arrival);

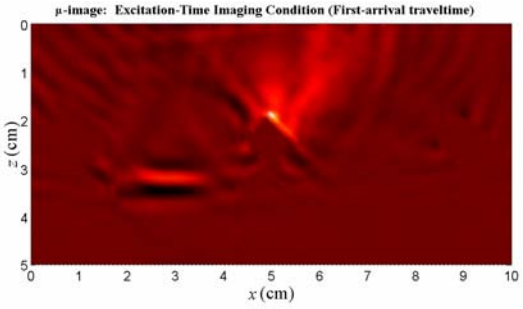

Fig. 8.1.1.9. Case (A); Permeability image; Excitation-time imaging condition (First-arrival);

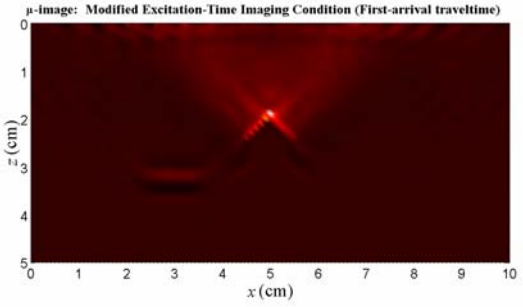

Fig. 8.1.1.10. Case (A); Permeability image; Modified excitation-time imaging condition (First-arrival);

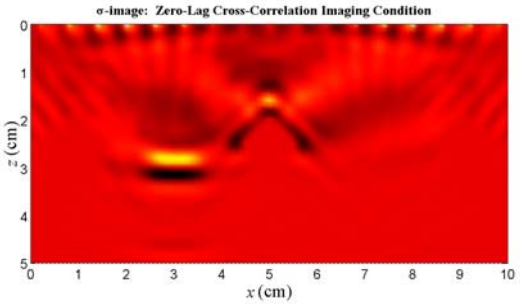

Fig. 8.1.1.11. Case (A); Conductivity image; Zero-lag cross-correlation imaging condition;

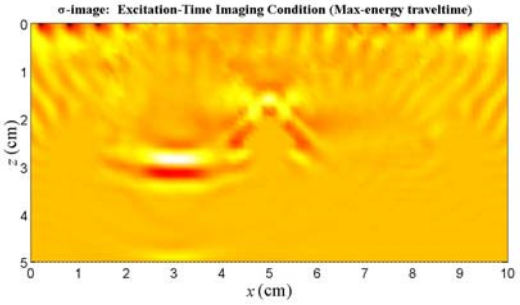

Fig. 8.1.1.12. Case (A); Conductivity image; Excitation-time imaging condition (Max-energy arrival);

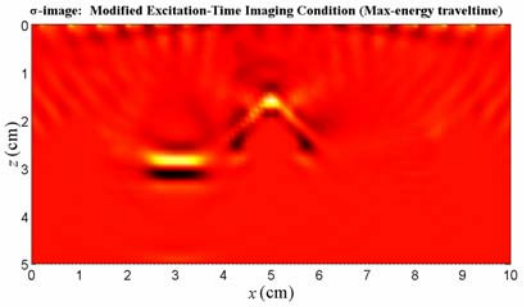

Fig. 8.1.1.13. Case (A); Conductivity image; Modified excitation-time imaging condition (Max-energy arrival);

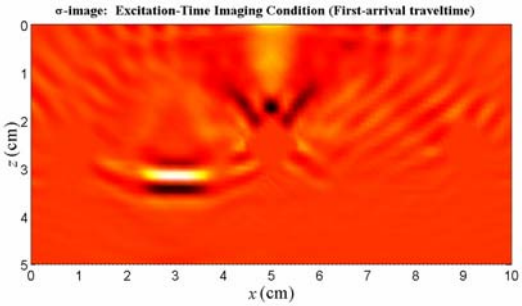

Fig. 8.1.1.14. Case (A); Conductivity image; Excitation-time imaging condition (First-arrival);

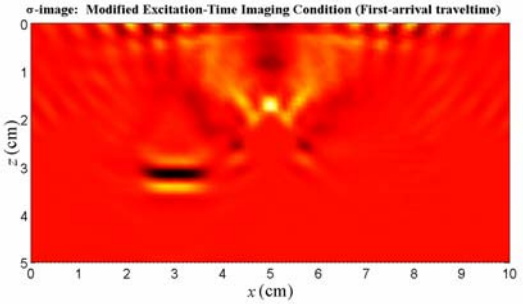

Fig. 8.1.1.15. Case (A); Conductivity image; Modified excitation-time imaging condition (First-arrival);

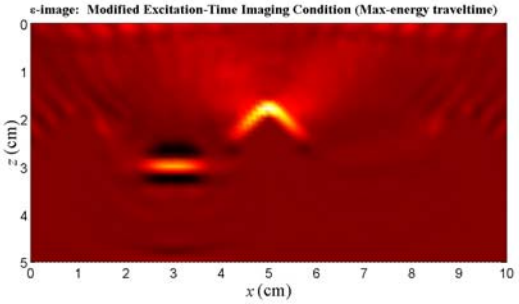

Fig. 8.1.1.16. Case (B); Permittivity image; Modified excitation-time imaging condition (Max-energy arrival);

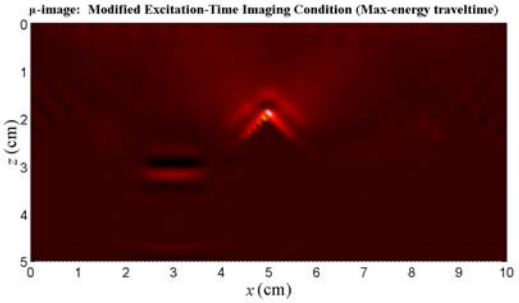

Fig. 8.1.1.17. Case (B); Permeability image; Modified excitation-time imaging condition (Max-energy arrival);

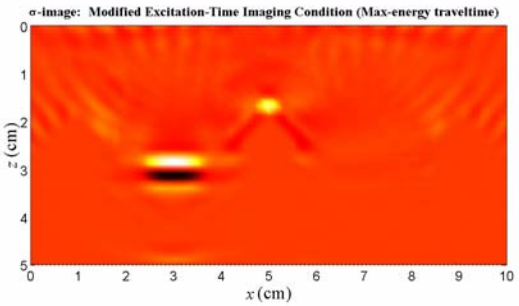

Fig. 8.1.1.18. Case (B); Conductivity image; Modified excitation-time imaging condition (Max-energy arrival);

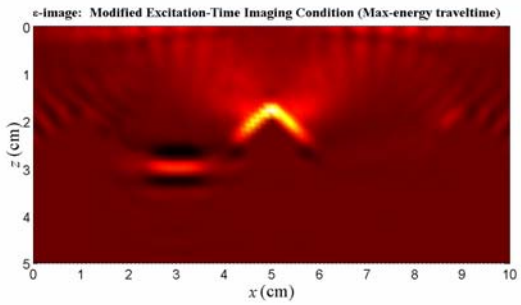

Fig. 8.1.1.19. Case (C); Permittivity image; Modified excitation-time imaging condition (Max-energy arrival);

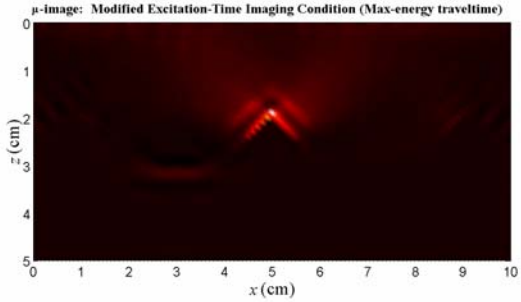

Fig. 8.1.1.20. Case (C); Permeability image; Modified excitation-time imaging condition (Max-energy arrival);

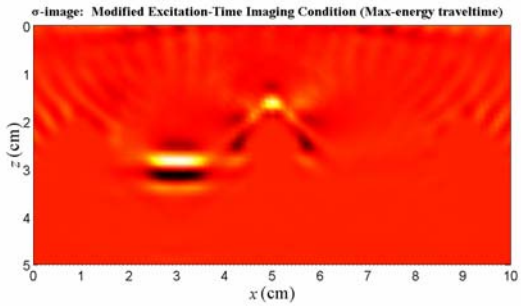

Fig. 8.1.1.21. Case (C); Conductivity image; Modified excitation-time imaging condition (Max-energy arrival);

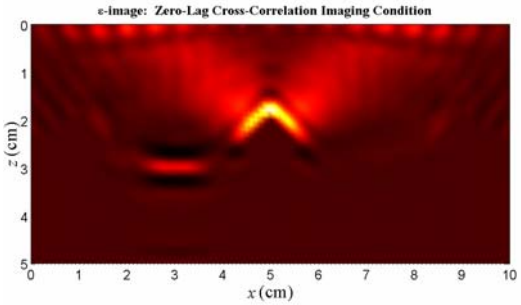

Fig. 8.1.1.22. Case (D); Permittivity image; Zero-lag cross-correlation imaging condition; Noisy data SNR=5;

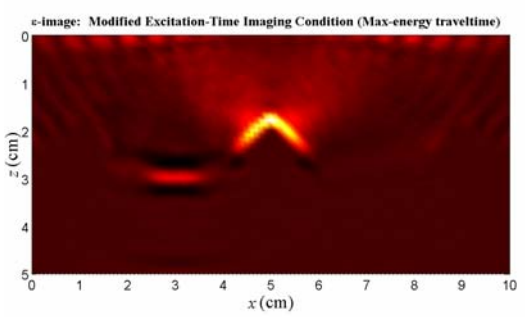

Fig. 8.1.1.23. Case (D); Permittivity image; Modified excitation-time imaging condition (Max-energy arrival); Noisy data SNR=5;

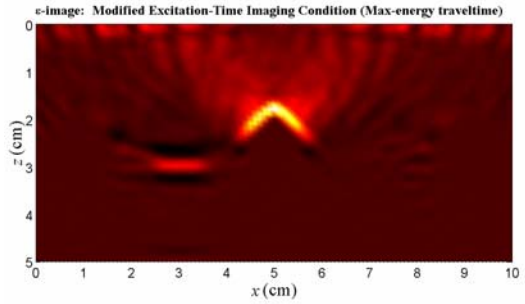

Fig. 8.1.1.24. Case (E); Permittivity image; Modified excitation-time imaging condition (Max-energy arrival); $\Delta_{s,a} = 1.5\,\lambda_{\min}$;

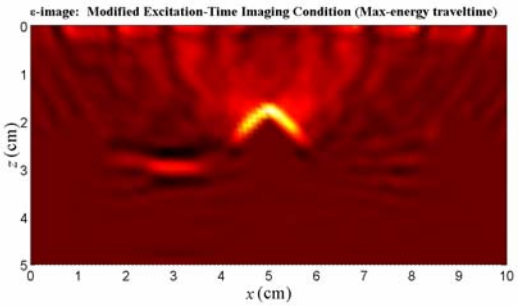

Fig. 8.1.1.25. Case (F); Permittivity image; Modified excitation-time imaging condition (Max-energy arrival); $\Delta_{s,a} = 2\,\lambda_{\min}$;

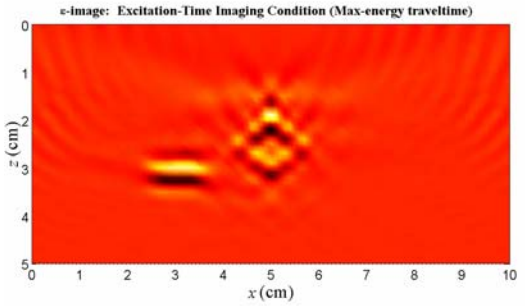

Fig. 8.1.1.26. Case (G); Permittivity image; Excitation-time imaging condition (Max-energy arrival); Half-space concrete;

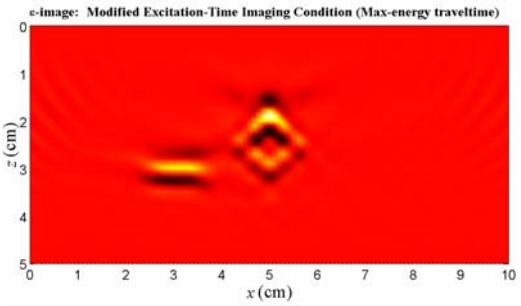

Fig. 8.1.1.27. Case (G); Permittivity image; Modified excitation-time imaging condition (Max-energy arrival); Half-space concrete;

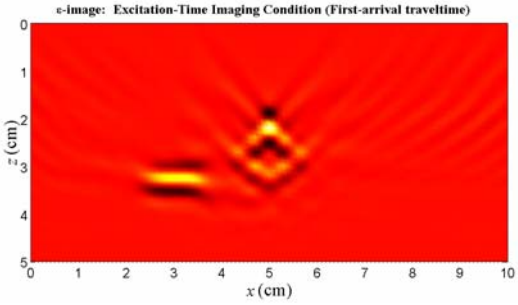

Fig. 8.1.1.28. Case (G); Permittivity image; Excitation-time imaging condition (First-arrival); Half-space concrete;

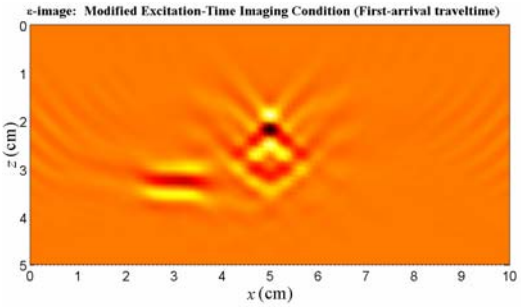

Fig. 8.1.1.29. Case (G); Permittivity image; Modified excitation-time imaging condition (First-arrival); Half-space concrete;

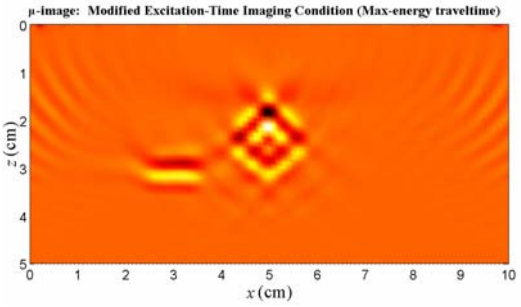

Fig. 8.1.1.30. Case (G); Permeability image; Modified excitation-time imaging condition (Max-energy arrival); Half-space concrete;

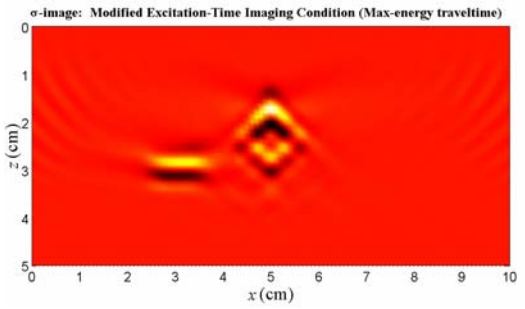

Fig. 8.1.1.31. Case (G); Conductivity image; Modified excitation-time imaging condition (Max-energy arrival); Half-space concrete;

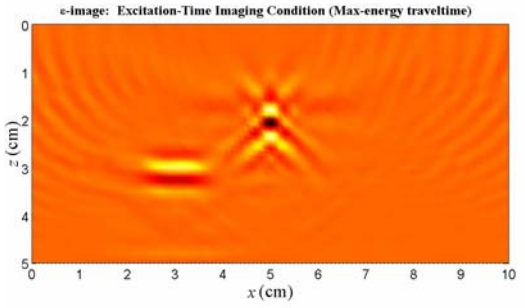

Fig. 8.1.1.32. Case (H); Permittivity image; Excitation-time imaging condition (Max-energy arrival); Modified pristine structure;

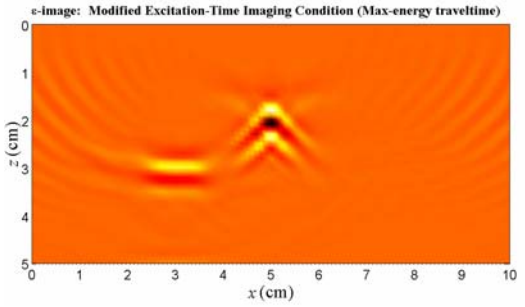

Fig. 8.1.1.33. Case (H); Permittivity image; Modified excitation-time imaging condition (Max-energy arrival); Modified pristine structure;

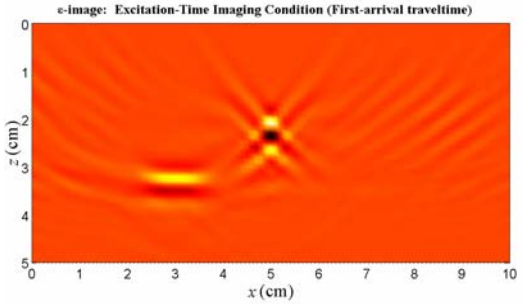

Fig. 8.1.1.34. Case (H); Permittivity image; Excitation-time imaging condition (First-arrival); Modified pristine structure;

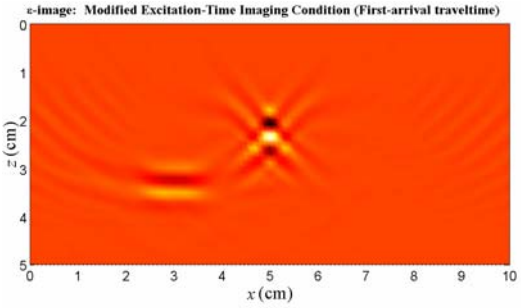

Fig. 8.1.1.35. Case (H); Permittivity image; Modified excitation-time imaging condition (First-arrival); Modified pristine structure;

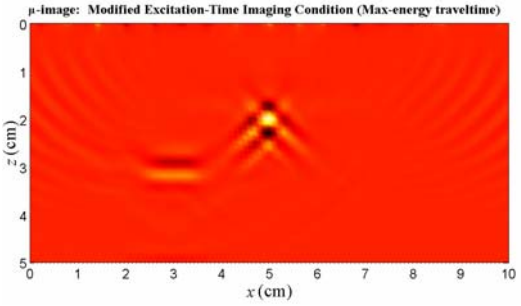

Fig. 8.1.1.36. Case (H); Permeability image; Modified excitation-time imaging condition (Max-energy arrival); Modified pristine structure;

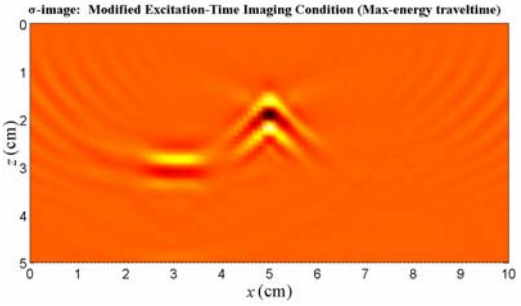

Fig. 8.1.1.37. Case (H); Conductivity image; Modified excitation-time imaging condition (Max-energy arrival); Modified pristine structure;

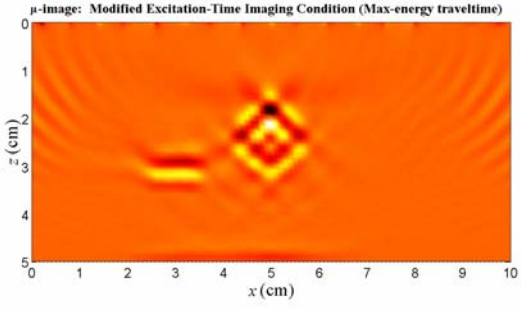

Fig. 8.1.1.38. Case (I); Permeability image; Modified excitation-time imaging condition (Max-energy arrival); Concrete slab without rebars;

8.1.2. Born Imaging (DE Formalism; Poststack)

The three different images for each type of measurement can be obtained by applying the zero-time imaging condition to the back-propagated scattered field components $E^{BP}_{y;scat}$, $H^{BP}_{x;scat}$, and $H^{BP}_{z;scat}$ computed by FD discretization of differential equations (7.1.12) for a 2:1 scaled pristine structure.

To show the effects of different measurement scenarios, actuator/sensor spacing, measurement noise, and material discontinuity in the pristine structure on the quality of the images, the following cases are investigated (in all cases $\Delta = 3\text{ mm} = 0.5\,\lambda_{\min}$ unless otherwise stated):

(A) $E^{d}_{y;scat}$

(B) $H^{d}_{x;scat}$

(C) $H^{d}_{z;scat}$

(D) $H^{d}_{x;scat}$ (contaminated by noise with SNR=5)

(E) $H^{d}_{x;scat}$ ($\Delta = 6\text{ mm} = \lambda_{\min}$)

(F) $H^{d}_{x;scat}$ (damaged structure: half-space concrete without rebars and the original damages)

(G) $H^{d}_{x;scat}$ (modified pristine structure: half-space concrete without rebars)

(H) $H^{d}_{x;scat}$ (damaged structure: concrete slab without rebars and the original damages)

Fig. 8.1.2.1 to 9 show the images obtained by the Born imaging algorithm in DE formalism using the poststack concept in Cases (A) to (C). The $E^{BP}_{y;scat}$-images have provided the best damage identification among the images. Also, the horizontal crack has not been completely imaged in the $H^{BP}_{z;scat}$-images. Moreover, when $H^{d}_{z;scat}$ has been used as the data, the horizontal crack has not been completely identified.

Fig. 8.1.2.10 illustrates the effect of the measurement noise with SNR=5 on the $E^{BP}_{y;scat}$-image in Case (D). This figure shows that the algorithm is quite robust against the measurement noise. Fig. 8.1.2.11 shows the $E^{BP}_{y;scat}$-image with the actuator/sensor spacing of $\Delta = \lambda_{\min}$. The artifacts resulting from the increase in the actuator/sensor spacing can be easily observed in this figure.

Fig. 8.1.2.12 to 14 illustrate the images for a new damaged structure including a half-space concrete without rebars and the original damages in Case (F). Due to the simplicity of the pristine structure in this case (i.e., half-space concrete), all three images have provided good damage identification. Note that the horizontal crack still has not been completely identified in the $H^{BP}_{z;scat}$-image.

Fig. 8.1.2.15 to 17 present the images when a modified pristine structure (a half-space concrete) instead of the actual pristine structure (the concrete slab with the rebars) has been used for the computation of the back-propagated field. Notice that the damage identification has been improved in the $H^{BP}_{z;scat}$ and $H^{BP}_{x;scat}$-images compared to the corresponding images in Case (B).

Fig. 8.1.2.18 shows the $E^{BP}_{y;scat}$-image for a damaged structure including a concrete slab without the rebars and the original damages. Notice how two false damages related to the typical shortcoming of the algorithm have been imaged near the lower interface of the slab.

It is worth mentioning that Sanada and Ashida (1998) applied a 2-D TM poststack RTM using FDTD method. However, the synthetic sensor data was generated based on incorrect exploding reflector model.

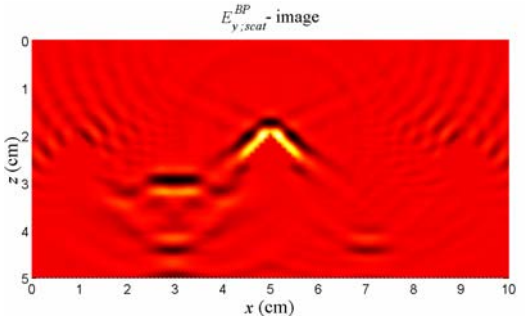

Fig. 8.1.2.1. Case (A); $E^{BP}_{y;scat}$ -image obtained by poststack Born imaging;

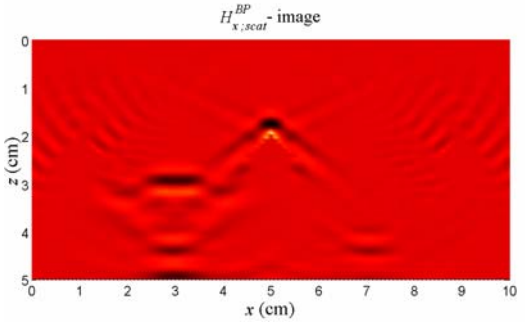

Fig. 8.1.2.2. Case (A); $H^{BP}_{x;scat}$ -image obtained by poststack Born imaging;

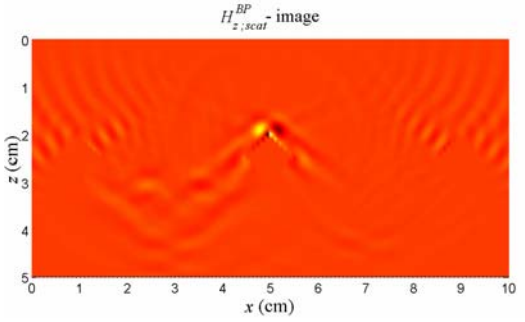

Fig. 8.1.2.3. Case (A); $H^{BP}_{z;scat}$ -image obtained by poststack Born imaging;

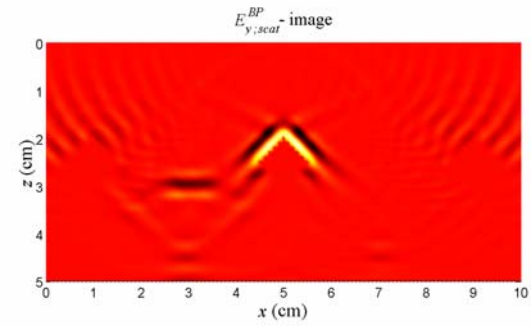

Fig. 8.1.2.4. Case (B); $E^{BP}_{y;scat}$ -image obtained by poststack Born imaging;

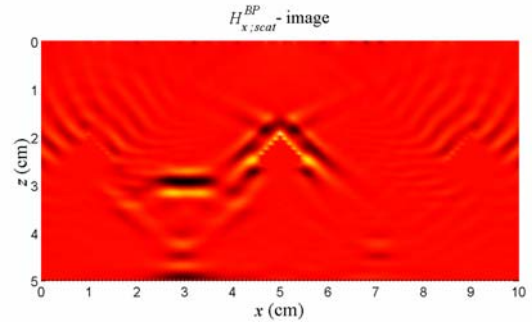

Fig. 8.1.2.5. Case (B); $H^{BP}_{x;scat}$ -image obtained by poststack Born imaging;

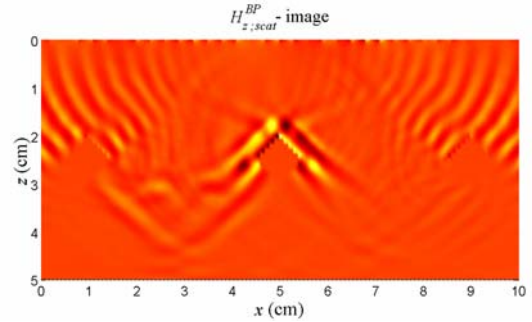

Fig. 8.1.2.6. Case (B); $H^{BP}_{z;scat}$ -image obtained by poststack Born imaging;

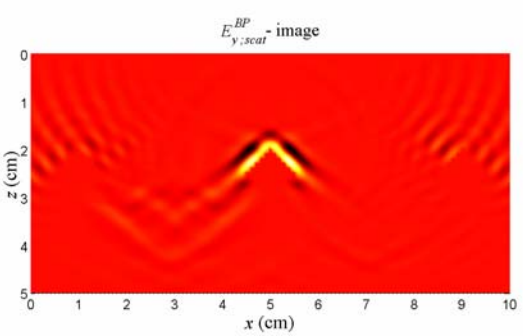

Fig. 8.1.2.7. Case (C); $E^{BP}_{y;scat}$ -image obtained by poststack Born imaging;

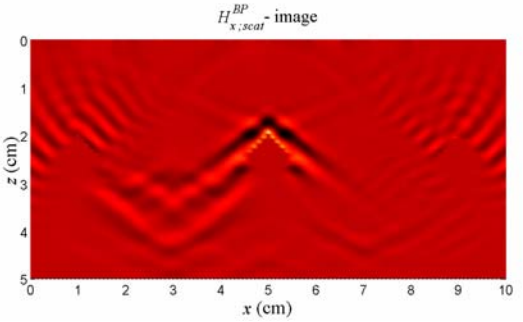

Fig. 8.1.2.8. Case (C); $H^{BP}_{x;scat}$ -image obtained by poststack Born imaging;

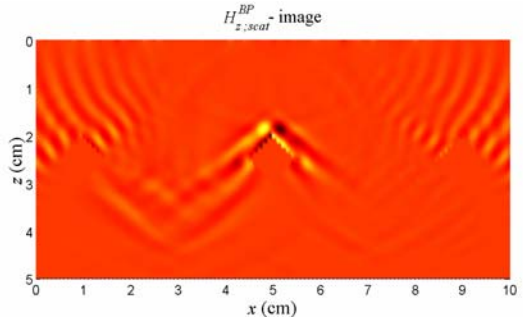

Fig. 8.1.2.9. Case (C); $H^{BP}_{z;scat}$ -image obtained by poststack Born imaging;

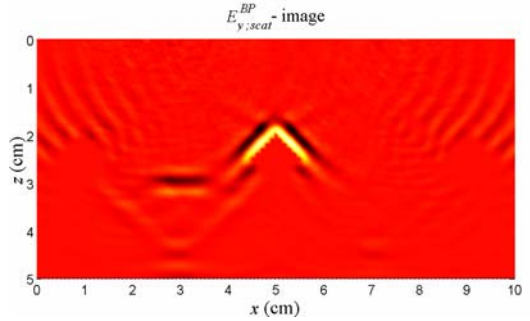

Fig. 8.1.2.10. Case (D); $E^{BP}_{y;scat}$ -image obtained by poststack Born imaging; Noisy data SNR=5;

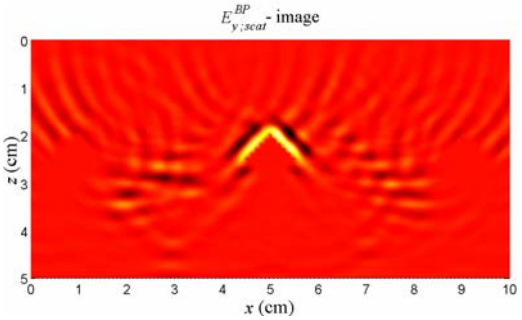

Fig. 8.1.2.11. Case (E); $E^{BP}_{y;scat}$ -image obtained by poststack Born imaging; $\Delta = \lambda_{\min}$;

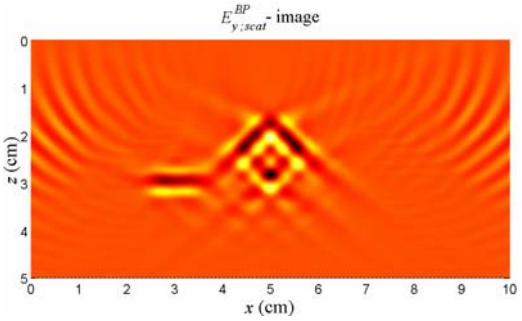

Fig. 8.1.2.12. Case (F); $E^{BP}_{y;scat}$ -image obtained by poststack Born imaging; Half-space concrete;

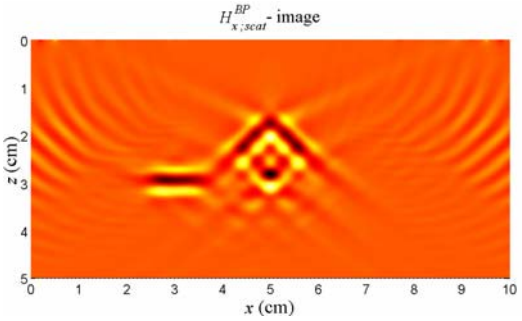

Fig. 8.1.2.13. Case (F); $H^{BP}_{x;scat}$ -image obtained by poststack Born imaging; Half-space concrete;

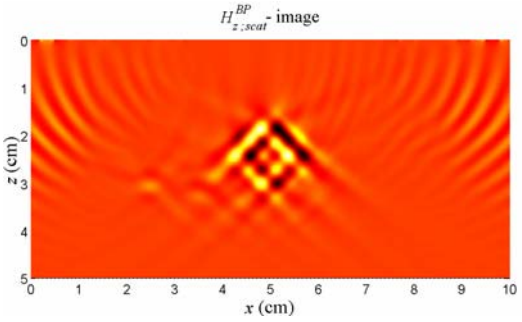

Fig. 8.1.2.14. Case (F); $H^{BP}_{z;scat}$ -image obtained by poststack Born imaging; Half-space concrete;

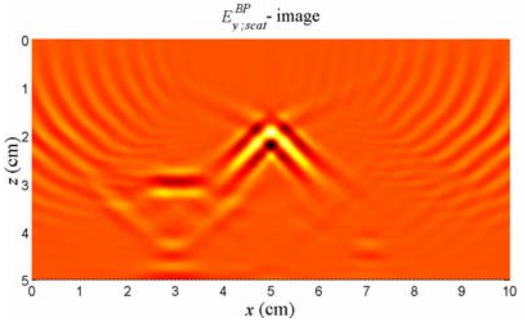

Fig. 8.1.2.15. Case (G); $E^{BP}_{y;scat}$ -image obtained by poststack Born imaging; Modified pristine structure;

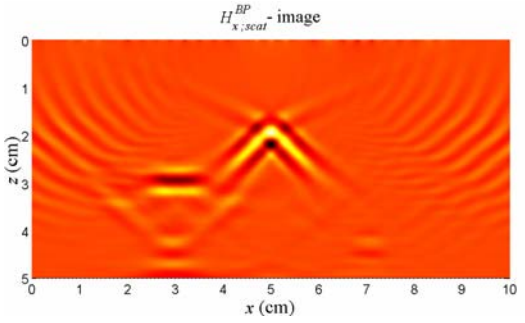

Fig. 8.1.2.16. Case (G); $H^{BP}_{x;scat}$ -image obtained by poststack Born imaging; Modified pristine structure;

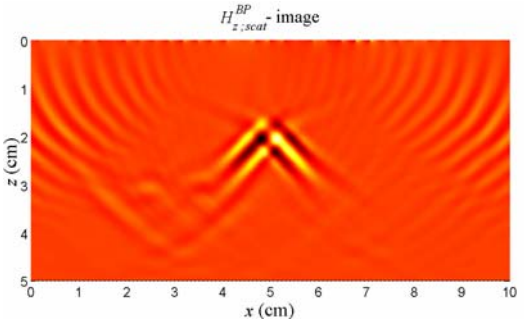

Fig. 8.1.2.17. Case (G); $H^{BP}_{z;scat}$ -image obtained by poststack Born imaging; Modified pristine structure;

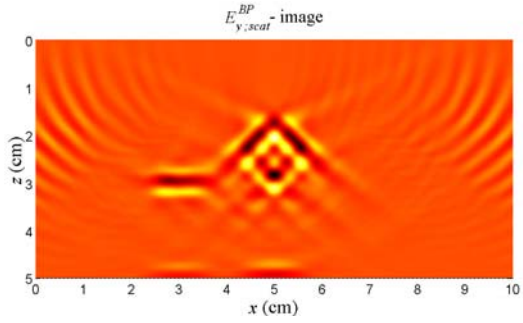

Fig. 8.1.2.18. Case (H); $E^{BP}_{y;scat}$ -image obtained by poststack Born imaging; Concrete slab without rebars;

8.1.3. Born Imaging (IE Formalism)

Eq. (7.1.27) - (7.1.29) represent the real-time imaging formulas in the IE formalism of the Born imaging algorithm. The amplitudes and traveltimes of the incident field and Green's functions are computed by FD discretization of ordinary Maxwell's equations for the pristine structure. The application of both first-arrival and maximum-energy arrival criteria for the calculation of these traveltimes and amplitudes are examined as well.

To show the effects of different measurement scenarios, actuator/sensor spacing, measurement noise, and material discontinuity in the pristine structure on the quality of the images, the following cases are investigated (in all cases $\Delta_{s,a} = 6 \text{ mm} = \lambda_{\min}$ unless otherwise stated):

(A) $H^d_{x;scat}$

(B) $E^d_{y;scat}$

(C) $H^d_{z;scat}$

(D) $H^d_{x;scat}$ (contaminated by noise with SNR=5)

(E) $H^d_{x;scat}$ ($\Delta_{s,a} = 9 \text{ mm} = 1.5\lambda_{\min}$)

(F) $H^d_{x;scat}$ ($\Delta_{s,a} = 12 \text{ mm} = 2\lambda_{\min}$)

(G) $H^d_{x;scat}$ (damaged structure: half-space concrete without rebars and the original damages)

(H) $H^d_{x;scat}$ (modified pristine structure: half-space concrete without rebars)

(I) $H^d_{x;scat}$ (damaged structure: concrete slab without rebars and the original damages)

Fig. 8.1.3.1 to 8 show the images obtained by the Born imaging algorithm in the IE formalism in Case (A). The geometries of the damages have been correctly identified with the least artifacts in the permittivity image shown in Fig. 8.1.3.2. It is also observed that

including the amplitude in addition to the traveltimes in the approximation of the incident field and Green's functions has significantly improved the images quality (only shown for the permittivity images). Notice that the images obtained based on the maximum-energy arrival criterion for the calculation of the traveltimes and amplitudes have provided better damage identification (specially for the debonding damage) than those of based on the first-arrival criterion. However, the images obtained based on the first-arrival criterion contain fewer artifacts.

Fig. 8.1.3.9 to 14 show the images obtained based on the maximum-energy arrival criterion for different measurement scenarios in Cases (B) and (C).

Fig. 8.1.3.15 illustrates the effect of the measurement noise with SNR=5 on the permittivity image in Case (D). This figure shows that the algorithm is quite robust against the measurement noise. To show the effect of the actuator/sensor spacing on the images quality, the permittivity images with $\Delta_{s,a}$ =1.5 $\lambda_{\min}$, 2 $\lambda_{\min}$ are shown in Fig. 8.1.3.16 and 17. The artifacts resulting from the increase in the actuator/sensor spacing can be easily observed in these figures.

Fig. 8.1.3.18 to 23 illustrate the images for a new damaged structure including a half-space concrete without rebars and the original damages in Case (G). Due to the simplicity of the pristine structure in this case (i.e., half-space concrete), all permittivity, permeability, and conductivity images obtained based on both first and maximum-energy arrival criteria have provided good damage identification. The best damage identification has been still provided by the maximum-energy arrival criterion. Notice how the artifacts related to the material discontinuity in the pristine structure in the images obtained based on the maximum-energy arrival criterion in Case (A), have disappeared on the corresponding images in Case (G).

Fig. 8.1.3.24 to 29 present the images when a modified pristine structure (a half-space concrete) instead of the actual pristine structure (the concrete slab with the rebars) has been used for the computation of the incident and Green's functions in the image area. Notice how the artifacts related to the material discontinuity in the actual pristine structure in the images obtained based on the maximum-energy arrival criterion in Case (A) have been eliminated.

Fig. 8.1.3.30 shows the permeability image for a damaged structure including a concrete slab without the rebars and the original damages. Notice how some false damages related to the typical shortcoming of the algorithm have been imaged near the lower interface of the slab.

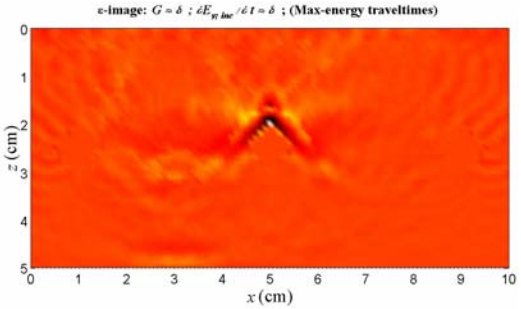

Fig. 8.1.3.1. Case (A); Permittivity image; Both $G_{yx;b}^{EM}$ and $\dot{E}_{y;inc}$ are approximated based on maximum-energy arrival criterion; Without amplitude;

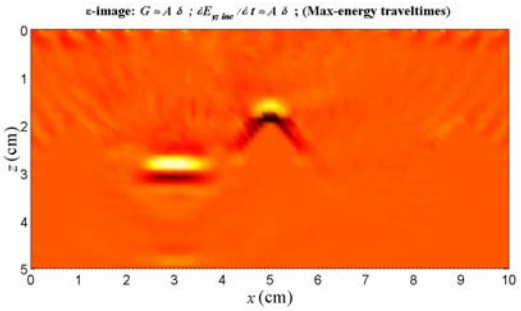

Fig. 8.1.3.2. Case (A); Permittivity image; Both $G_{yx;b}^{EM}$ and $\dot{E}_{y;inc}$ are approximated based on maximum-energy arrival criterion; With amplitude;

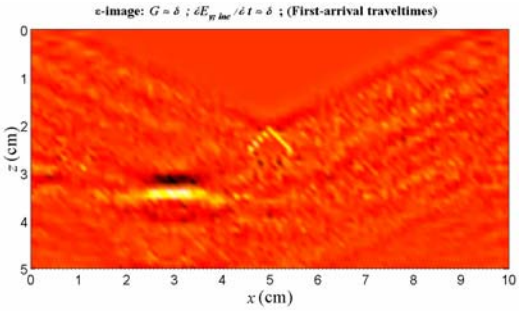

Fig. 8.1.3.3. Case (A); Permittivity image; Both $G_{yx;b}^{EM}$ and $\dot{E}_{y;inc}$ are approximated based on first-arrival criterion; Without amplitude;

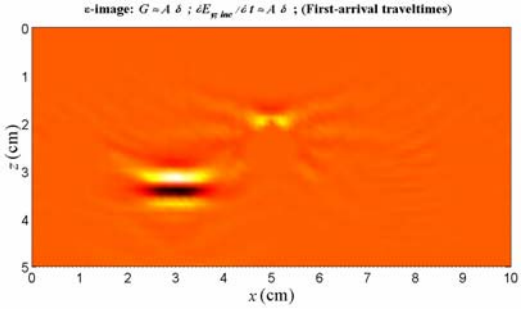

Fig. 8.1.3.4. Case (A); Permittivity image; Both $G_{yx;b}^{EM}$ and $\dot{E}_{y;inc}$ are approximated based on first-arrival criterion; With amplitude;

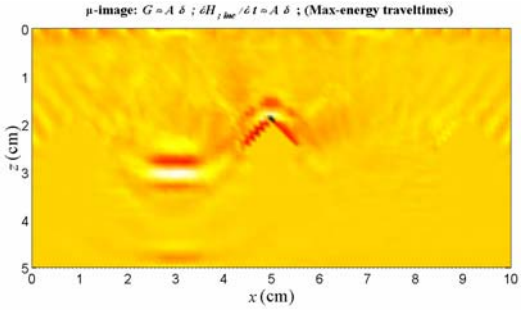

Fig. 8.1.3.5. Case (A); Permeability image; All $G_{xx;b}^{HM}$, $G_{zx;b}^{HM}$, $\dot{H}_{x;inc}$, and $\dot{H}_{z;inc}$ are approximated based on maximum-energy arrival criterion; With amplitude;

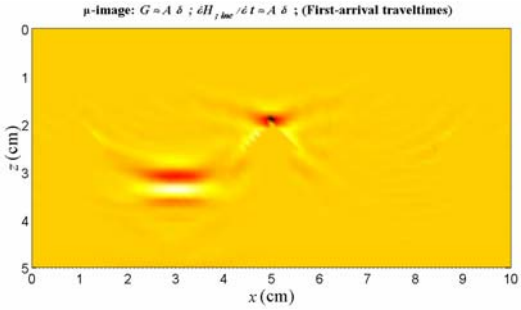

Fig. 8.1.3.6. Case (A); Permeability image; All $G_{xx;b}^{HM}$, $G_{zx;b}^{HM}$, $\dot{H}_{x;inc}$, and $\dot{H}_{z;inc}$ are approximated based on first-arrival criterion; With amplitude;

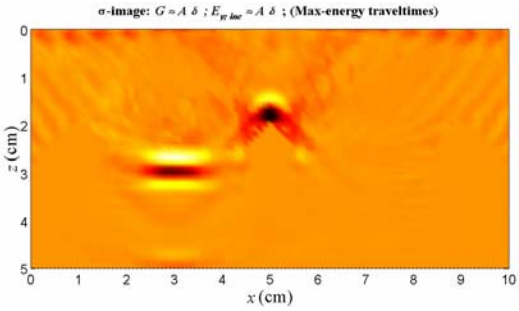

Fig. 8.1.3.7. Case (A); Conductivity image; Both $G^{EM}_{yx;b}$ and $E_{y;inc}$ are approximated based on maximum-energy arrival criterion; With amplitude;

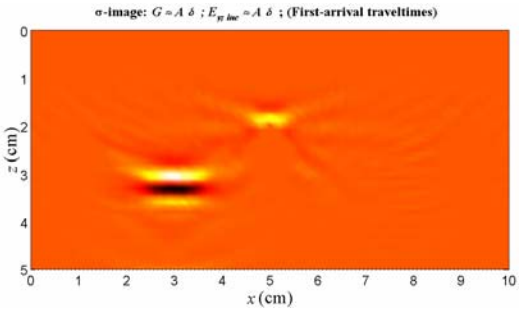

Fig. 8.1.3.8. Case (A); Conductivity image; Both $G^{EM}_{yx;b}$ and $E_{y;inc}$ are approximated based on first-arrival criterion; With amplitude;

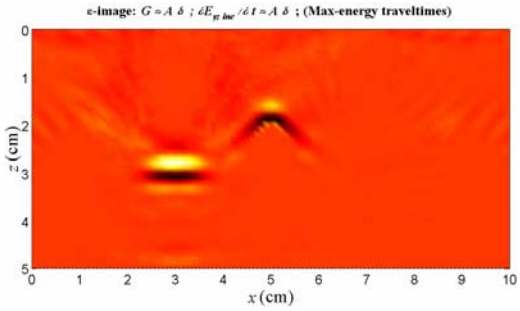

Fig. 8.1.3.9. Case (B); Permittivity image; Both $G^{EJ}_{yy;b}$ and $\dot{E}_{y;inc}$ are approximated based on maximum-energy arrival criterion; With amplitude;

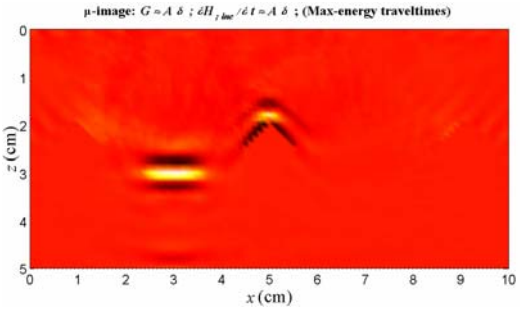

Fig. 8.1.3.10. Case (B); Permeability image; All $G^{HJ}_{xy;b}$, $G^{HJ}_{zy;b}$, $\dot{H}_{x;inc}$, and $\dot{H}_{z;inc}$ are approximated based on maximum-energy arrival criterion; With amplitude;

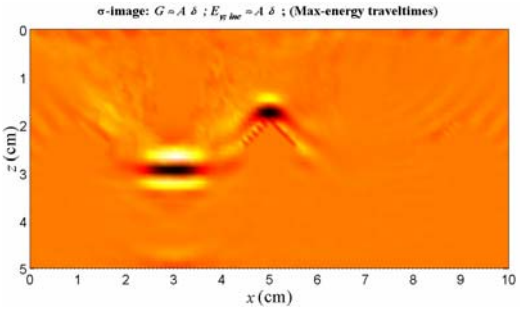

Fig. 8.1.3.11. Case (B); Conductivity image; Both $G^{EJ}_{yy;b}$ and $E_{y;inc}$ are approximated based on maximum-energy arrival criterion; With amplitude;

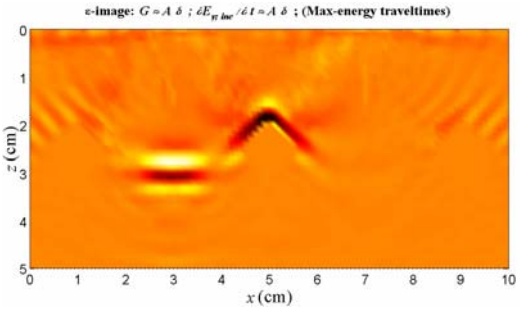

Fig. 8.1.3.12. Case (C); Permittivity image; Both $G^{EM}_{yz;b}$ and $\dot{E}_{y;inc}$ are approximated based on maximum-energy arrival criterion; With amplitude;

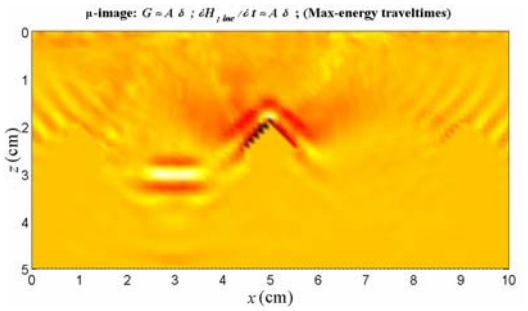

Fig. 8.1.3.13. Case (C); Permeability image; All $G^{HM}_{xz;b}$, $G^{HM}_{zz;b}$, $\dot{H}_{x;inc}$, and $\dot{H}_{z;inc}$ are approximated based on maximum-energy arrival criterion; With amplitude;

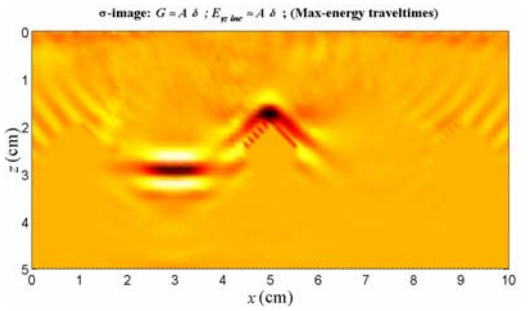

Fig. 8.1.3.14. Case (C); Conductivity image; Both $G^{EM}_{yz;b}$ and $E_{y;inc}$ are approximated based on maximum-energy arrival criterion; With amplitude;

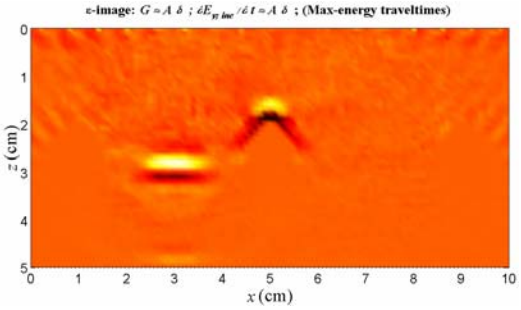

Fig. 8.1.3.15. Case (D); Permittivity image; Both $G^{EM}_{yx;b}$ and $\dot{E}_{y;inc}$ are approximated based on maximum-energy arrival criterion; With amplitude; Noisy data SNR=5;

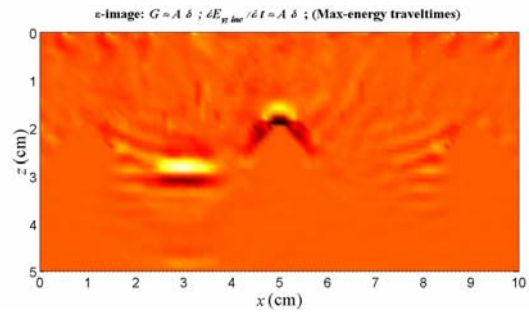

Fig. 8.1.3.16. Case (E); Permittivity image; Both $G^{EM}_{yx;b}$ and $\dot{E}_{y;inc}$ are approximated based on maximum-energy arrival criterion; With amplitude; $\Delta_{s,a} = 1.5\lambda_{\min}$;

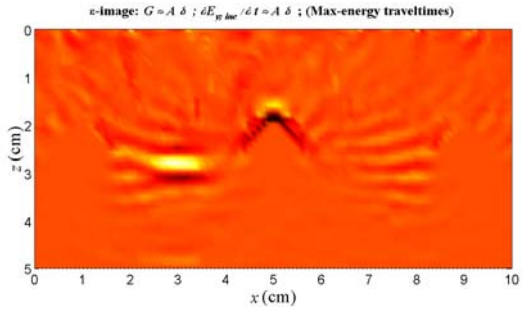

Fig. 8.1.3.17. Case (F); Permittivity image; Both $G^{EM}_{yx;b}$ and $\dot{E}_{y;inc}$ are approximated based on maximum-energy arrival criterion; With amplitude; $\Delta_{s,a} = 2\lambda_{\min}$;

Fig. 8.1.3.18. Case (G); Permittivity image; Both $G^{EM}_{yx;b}$ and $\dot{E}_{y;inc}$ are approximated based on maximum-energy arrival criterion; Without amplitude; Half-space concrete;

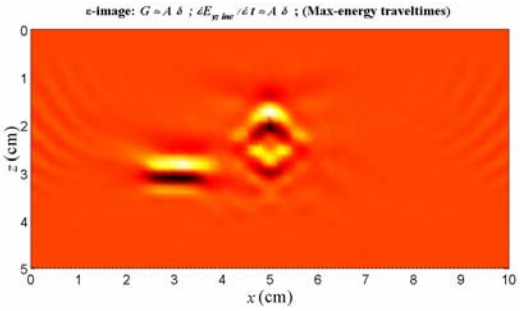

Fig. 8.1.3.19. Case (G); Permittivity image; Both $G^{EM}_{yx;b}$ and $\dot{E}_{y;inc}$ are approximated based on maximum-energy arrival criterion; With amplitude; Half-space concrete;

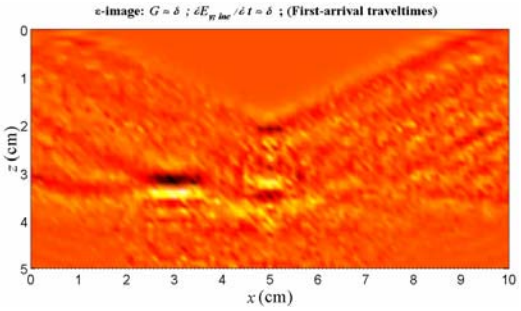

Fig. 8.1.3.20. Case (G); Permittivity image; Both $G^{EM}_{yx;b}$ and $\dot{E}_{y;inc}$ are approximated based on first-arrival criterion; Without amplitude; Half-space concrete;

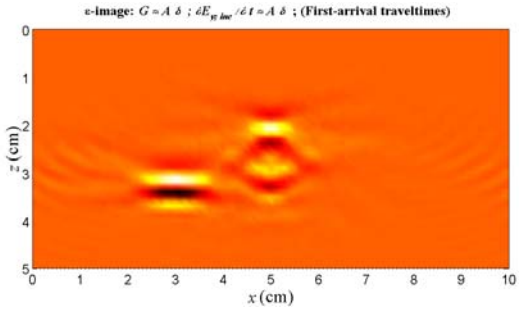

Fig. 8.1.3.21. Case (G); Permittivity image; Both $G^{EM}_{yx;b}$ and $\dot{E}_{y;inc}$ are approximated based on first-arrival criterion; With amplitude; Half-space concrete;

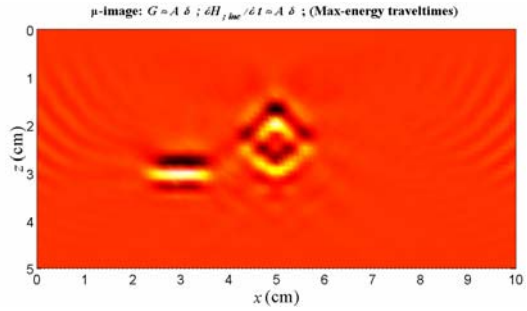

Fig. 8.1.3.22. Case (G); Permeability image; All $G^{HM}_{xx;b}$, $G^{HM}_{zx;b}$, $\dot{H}_{x;inc}$, and $\dot{H}_{z;inc}$ are approximated based on maximum-energy arrival criterion; With amplitude; Half-space concrete;

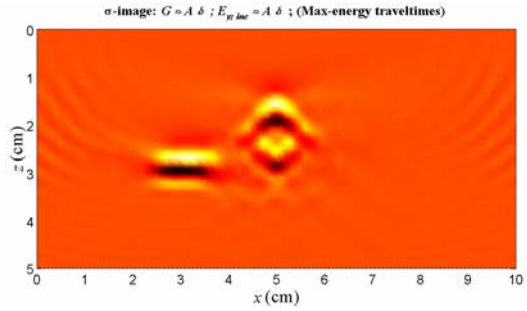

Fig. 8.1.3.23. Case (G); Conductivity image; Both $G^{EM}_{yx;b}$ and $E_{y;inc}$ are approximated based on maximum-energy arrival criterion; With amplitude; Half-space concrete;

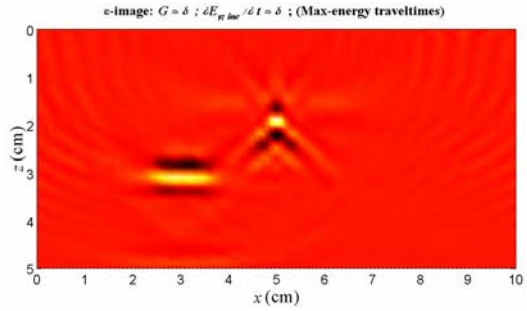

Fig. 8.1.3.24. Case (H); Permittivity image; Both $G^{EM}_{yx;b}$ and $\dot{E}_{y;inc}$ are approximated based on maximum-energy arrival criterion; Without amplitude; Modified pristine structure;

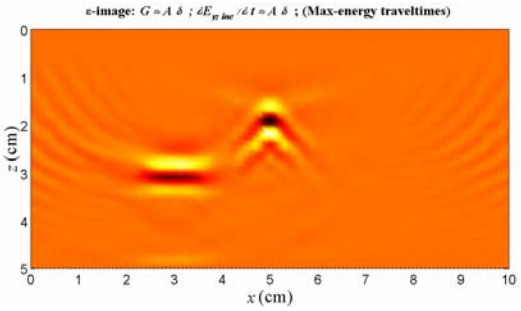

Fig. 8.1.3.25. Case (H); Permittivity image; Both $G^{EM}_{yx;b}$ and $\dot{E}_{y;inc}$ are approximated based on maximum-energy arrival criterion; With amplitude; Modified pristine structure;

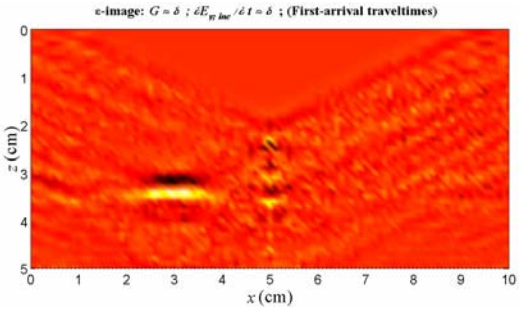

Fig. 8.1.3.26. Case (H); Permittivity image; Both $G^{EM}_{yx;b}$ and $\dot{E}_{y;inc}$ are approximated based on first-arrival criterion; Without amplitude; Modified pristine structure;

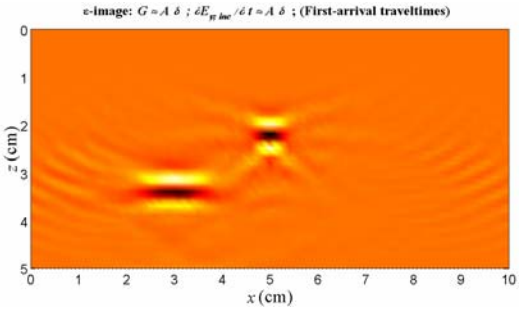

Fig. 8.1.3.27. Case (H); Permittivity image; Both $G^{EM}_{yx;b}$ and $\dot{E}_{y;inc}$ are approximated based on first-arrival criterion; With amplitude; Modified pristine structure;

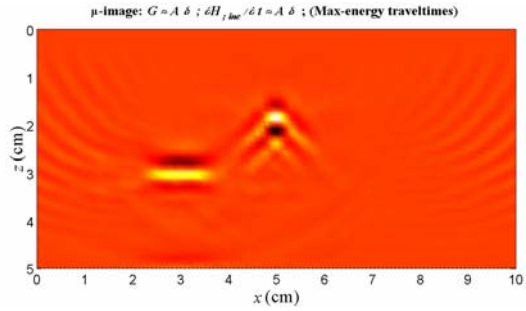

Fig. 8.1.3.28. Case (H); Permeability image; All $G^{HM}_{xx;b}$, $G^{HM}_{zx;b}$, $\dot{H}_{x;inc}$, and $\dot{H}_{z;inc}$ are approximated based on maximum-energy arrival criterion; With amplitude; Modified pristine structure;

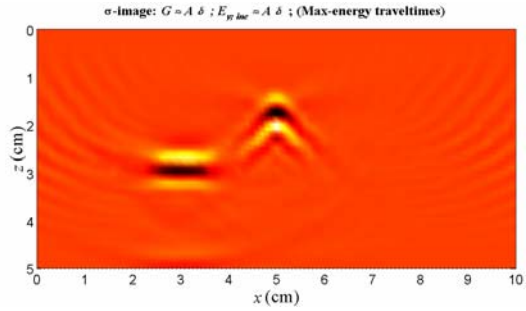

Fig. 8.1.3.29. Case (H); Conductivity image; Both $G^{EM}_{yx;b}$ and $E_{y;inc}$ are approximated based on maximum-energy arrival criterion; With amplitude; Modified pristine structure;

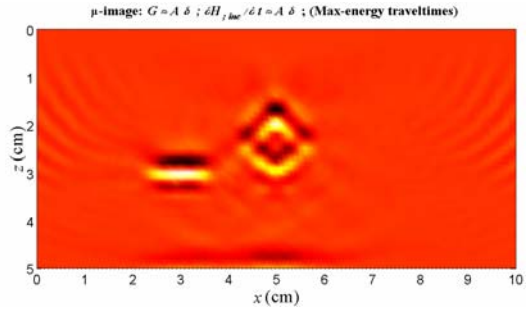

Fig. 8.1.3.30. Case (I); Permeability image; All $G^{HM}_{xx;b}$, $G^{HM}_{zx;b}$, $\dot{H}_{x;inc}$, and $\dot{H}_{z;inc}$ are approximated based on maximum-energy arrival criterion; With amplitude; Concrete slab without rebars;

8.1.4. EM Migration (DE Formalism)

Eq. (7.2.10) - (7.2.12) represent the imaging formulas with zero-lag cross correlation imaging condition. The corresponding imaging formulas with modified excitation-time imaging condition are Eq. (7.2.19) - (7.2.21); the imaging formulas with ordinary excitation-time imaging condition are easily obtained by setting the amplitudes to unity. Note that the migrated scattered fields are computed by FD discretization of differential equations (7.2.13) or (7.2.14) for the pristine structure depending on weather the sensor data is treated as sources or as time-dependent boundary conditions, respectively. Also, the application of both first and maximum-energy arrival criteria for the calculation of the traveltimes and amplitudes are examined.

To show the effects of different measurement scenarios, actuator/sensor spacing, measurement noise, and material discontinuity in the pristine structure on the quality of the images, the following cases are investigated (in all cases $\Delta_{s,a} = 6 \text{ mm} = \lambda_{\min}$ and data is treated as time-dependent boundary conditions, unless otherwise stated):

(A) $E^d_{y;scat}$ and $H^d_{x;scat}$

(B) $E^d_{y;scat}$ and $H^d_{x;scat}$ (as sources)

(C) Only $E^d_{y;scat}$

(D) Only $H^d_{x;scat}$

(E) $E^d_{y;scat}$ and $H^d_{x;scat}$ (contaminated by noise with SNR=5)

(F) $E^d_{y;scat}$ and $H^d_{x;scat}$ ($\Delta_{s,a} = 9 \text{ mm} = 1.5\lambda_{\min}$)

(G) $E^d_{y;scat}$ and $H^d_{x;scat}$ ($\Delta_{s,a} = 12 \text{ mm} = 2\lambda_{\min}$)

(H) $E^d_{y;scat}$ and $H^d_{x;scat}$ (damaged structure: half-space concrete without rebars and the original damages)

(I) $E^d_{y;scat}$ and $H^d_{x;scat}$ (modified pristine structure: half-space concrete without rebars)

(J) $E^{d}_{y;scat}$ and $H^{d}_{x;scat}$ (damaged structure: concrete slab without rebars and the original damages)

Fig. 8.1.4.1 to 15 show the images obtained by the EM migration algorithm in DE formalism with different imaging conditions in Case (A). The geometries of the damages have been correctly identified with the least artifacts in the conductivity images shown in Fig. 8.1.4.11 and 13. Notice that the images obtained by the modified excitation-time imaging condition with maximum-energy arrival criterion are comparable in quality to the images obtained by the zero-lag cross-correlation imaging condition. In addition, the modified excitation-time imaging condition has often improved the images quality compared to the images obtained by the ordinary excitation-time imaging condition.

When the sensor data has been treated as sources instead of time-dependent boundary conditions in the EM migration in Case (B), the quality of images has been slightly deteriorated as shown in Fig. 8.1.4.16 to 18. Surprisingly, the usage of only $E^{d}_{y;scat}$ or $H^{d}_{x;scat}$ instead of both in the algorithm in Cases (C) and (D) has improved the quality of images as shown in Fig. 8.1.4.19 to 24.

Fig. 8.1.4.25 and 26 illustrate the effect of the measurement noise with SNR=5 on conductivity images. These figures show that the algorithm is quite robust against the measurement noise. To show the effect of the actuator/sensor spacing on the images quality, the conductivity images with $\Delta_{s,a}$ =1.5 $\lambda_{\min}$, 2 $\lambda_{\min}$ are shown in Fig. 8.1.4.27 and 28. The artifacts resulting from the increase in the actuator/sensor spacing can be easily observed in these figures.

Fig. 8.1.4.29 to 34 illustrate the images for a new damaged structure including a half-space concrete without rebars and the original damages in Case (H). Due to the simplicity of the pristine structure in this case (i.e., half-space concrete), all permittivity, permeability, and conductivity images obtained by different imaging conditions have provided good damage identification. The best damage identification has been still provided by the modified excitation-time imaging condition with maximum-energy arrival criterion. Notice how the

artifacts related to the material discontinuity in the pristine structure in Case (A) images, have disappeared on the corresponding images in Case (G).

Fig. 8.1.4.35 to 40 present the images when a modified pristine structure (a half-space concrete) instead of the actual pristine structure (the concrete slab with the rebars) has been used for the computation of the incident and migrated scattered fields in the image area. Notice how the artifacts related to the material discontinuity in the actual pristine structure in Case (A) images have been eliminated.

Fig. 8.1.4.41 shows the conductivity image for a damaged structure including a concrete slab without the rebars and the original damages. Notice how a false damage related to the typical shortcoming of the algorithm has been imaged near the lower interface of the slab.

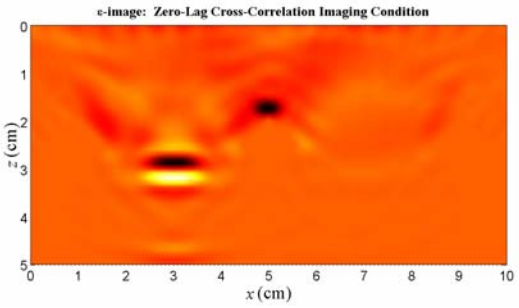

Fig. 8.1.4.1. Case (A); Permittivity image; Zero-lag cross-correlation imaging condition;

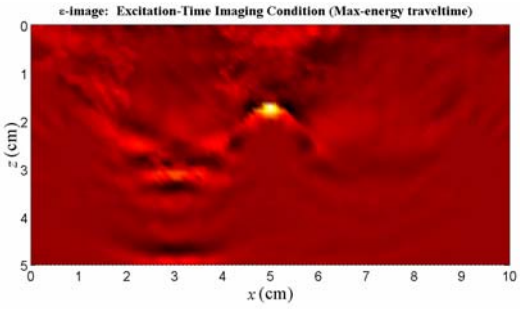

Fig. 8.1.4.2. Case (A); Permittivity image; Excitation-time imaging condition (Max-energy arrival);

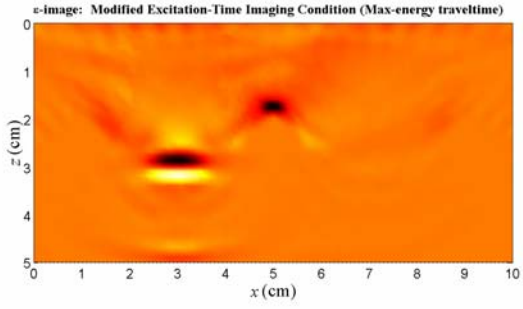

Fig. 8.1.4.3. Case (A); Permittivity image; Modified excitation-time imaging condition (Max-energy arrival);

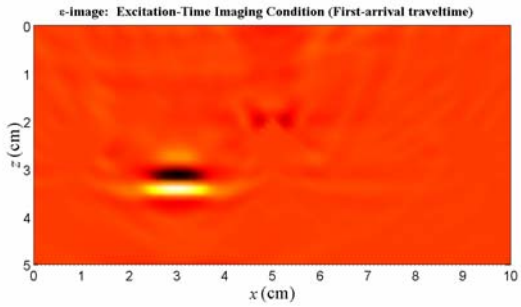

Fig. 8.1.4.4. Case (A); Permittivity image; Excitation-time imaging condition (First-arrival);

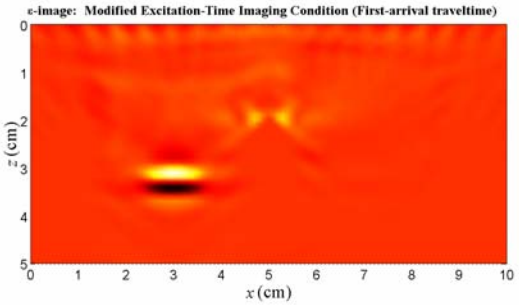

Fig. 8.1.4.5. Case (A); Permittivity image; Modified excitation-time imaging condition (First-arrival);

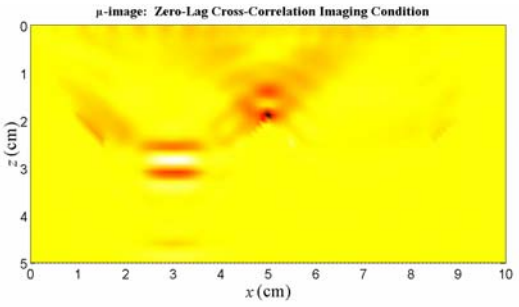

Fig. 8.1.4.6. Case (A); Permeability image; Zero-lag cross-correlation imaging condition;

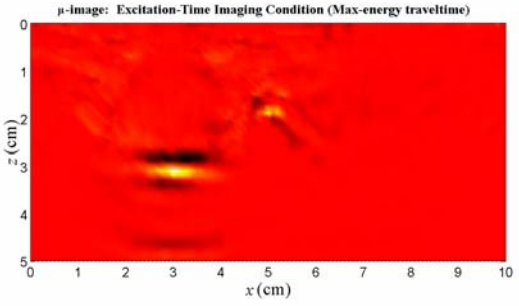

Fig. 8.1.4.7. Case (A); Permeability image; Excitation-time imaging condition (Max-energy arrival);

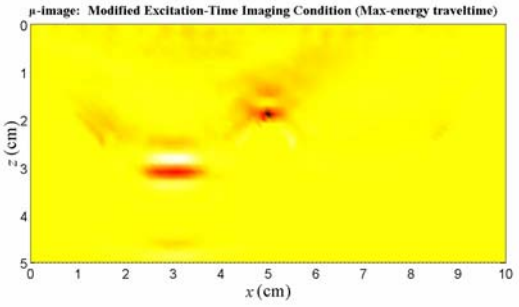

Fig. 8.1.4.8. Case (A); Permeability image; Modified excitation-time imaging condition (Max-energy arrival);

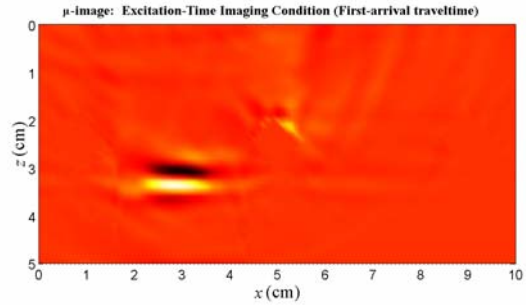

Fig. 8.1.4.9. Case (A); Permeability image; Excitation-time imaging condition (First-arrival);

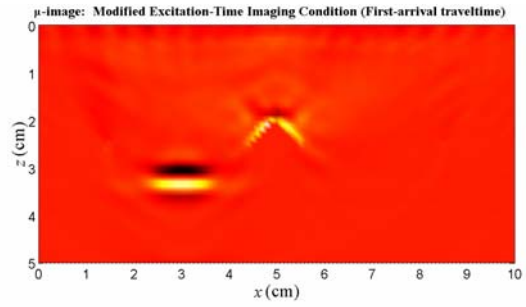

Fig. 8.1.4.10. Case (A); Permeability image; Modified excitation-time imaging condition (First-arrival);

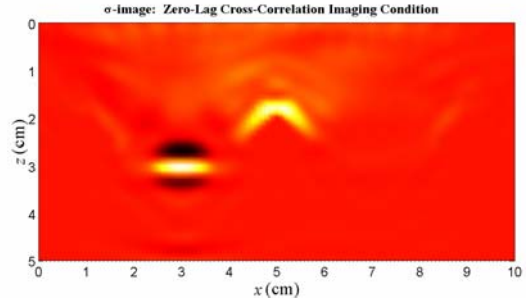

Fig. 8.1.4.11. Case (A); Conductivity image; Zero-lag cross-correlation imaging condition;

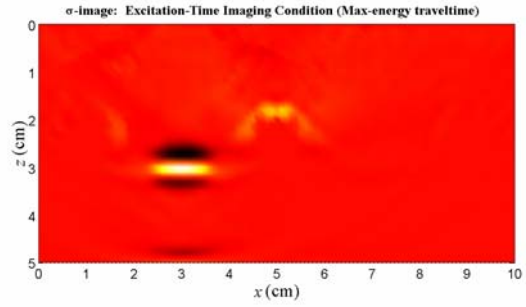

Fig. 8.1.4.12. Case (A); Conductivity image; Excitation-time imaging condition (Max-energy arrival);

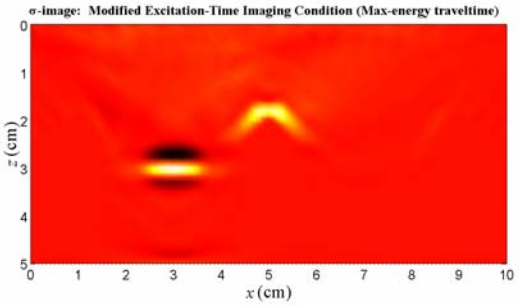

Fig. 8.1.4.13. Case (A); Conductivity image; Modified excitation-time imaging condition (Max-energy arrival);

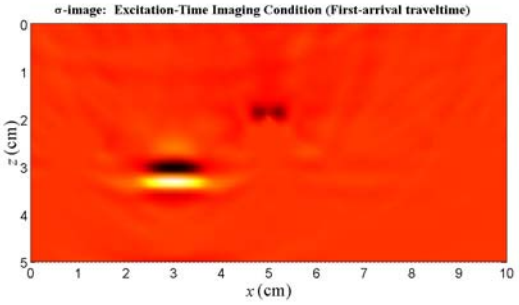

Fig. 8.1.4.14. Case (A); Conductivity image; Excitation-time imaging condition (First-arrival);

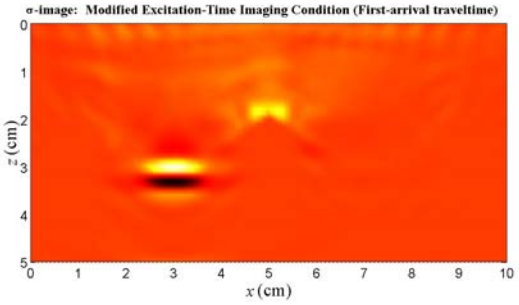

Fig. 8.1.4.15. Case (A); Conductivity image; Modified excitation-time imaging condition (First-arrival);

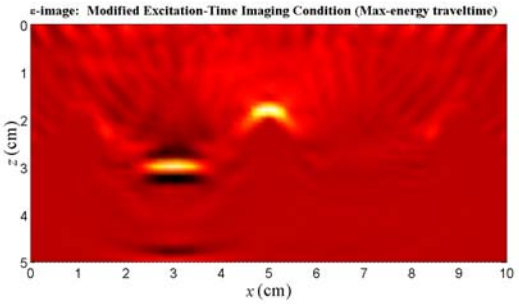

Fig. 8.1.4.16. Case (B); Permittivity image; Modified excitation-time imaging condition (Max-energy arrival); Data treated as sources;

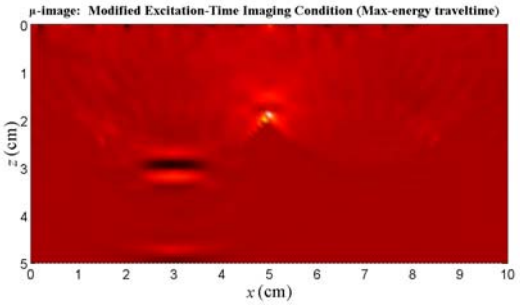

Fig. 8.1.4.17. Case (B); Permeability image; Modified excitation-time imaging condition (Max-energy arrival); Data treated as sources;

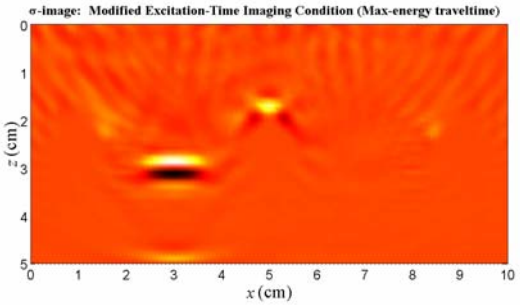

Fig. 8.1.4.18. Case (B); Conductivity image; Modified excitation-time imaging condition (Max-energy arrival); Data treated as sources;

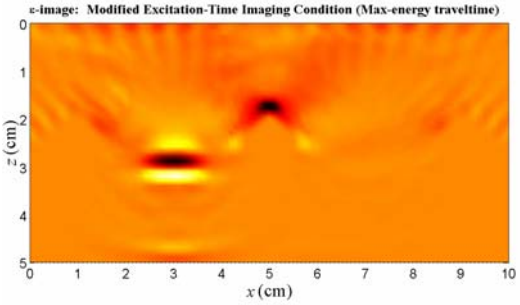

Fig. 8.1.4.19. Case (C); Permittivity image; Modified excitation-time imaging condition (Max-energy arrival); Only $E^{d}_{y;scat}$ as BC;

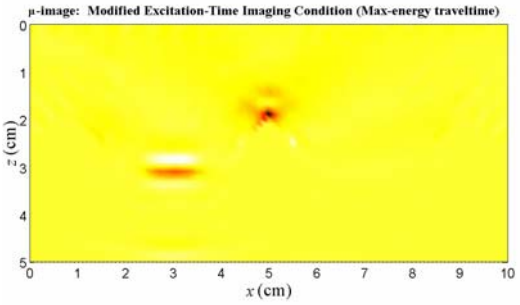

Fig. 8.1.4.20. Case (C); Permeability image; Modified excitation-time imaging condition (Max-energy arrival); Only $E^{d}_{y;scat}$ as BC;

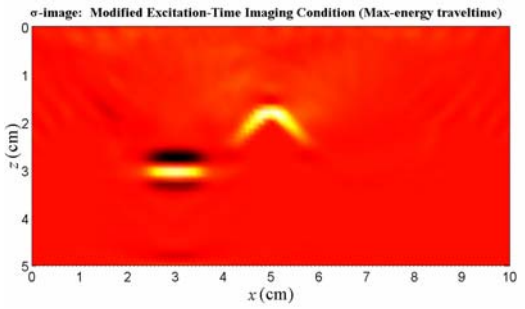

Fig. 8.1.4.21. Case (C); Conductivity image; Modified excitation-time imaging condition (Max-energy arrival); Only $E^d_{y;scat}$ as BC;

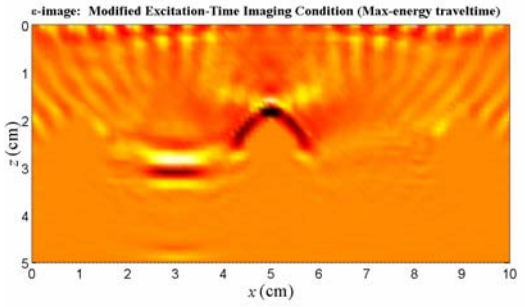

Fig. 8.1.4.22. Case (D); Permittivity image; Modified excitation-time imaging condition (Max-energy arrival); Only $H^d_{x;scat}$ as BC;

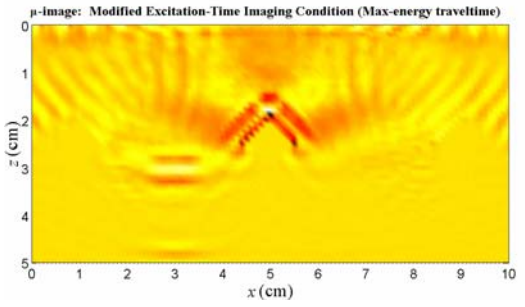

Fig. 8.1.4.23. Case (D); Permeability image; Modified excitation-time imaging condition (Max-energy arrival); Only $H^d_{x;scat}$ as BC;

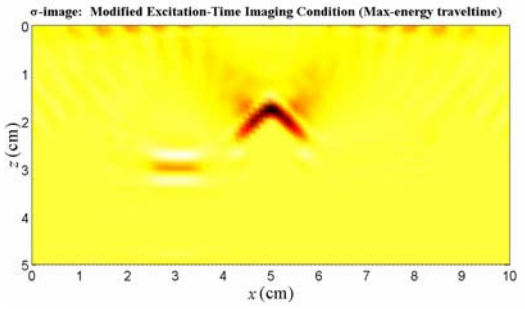

Fig. 8.1.4.24. Case (D); Conductivity image; Modified excitation-time imaging condition (Max-energy arrival); Only $H^d_{x;scat}$ as BC;

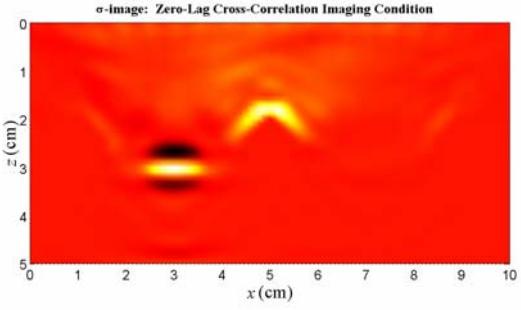

Fig. 8.1.4.25. Case (E); Conductivity image; Zero-lag cross-correlation imaging condition; Noisy data SNR=5;

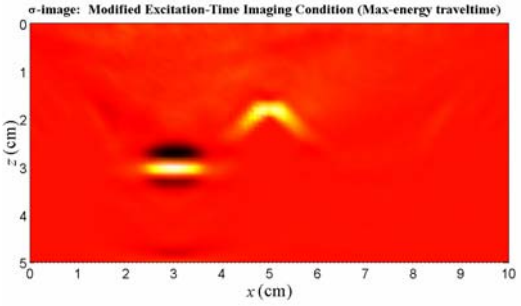

Fig. 8.1.4.26. Case (E); Conductivity image; Modified excitation-time imaging condition (Max-energy arrival); Noisy data SNR=5;

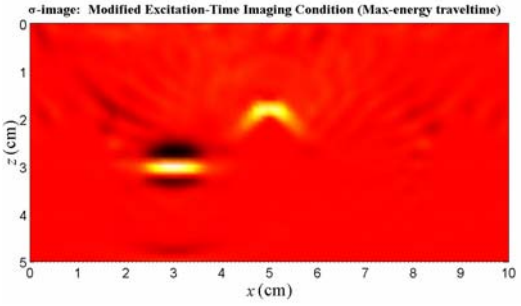

Fig. 8.1.4.27. Case (F); Conductivity image; Modified excitation-time imaging condition (Max-energy arrival); $\Delta_{s,a} = 1.5\lambda_{\min}$;

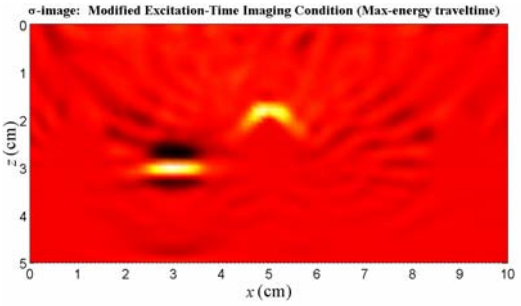

Fig. 8.1.4.28. Case (G); Conductivity image; Modified excitation-time imaging condition (Max-energy arrival); $\Delta_{s,a} = 2\lambda_{\min}$;

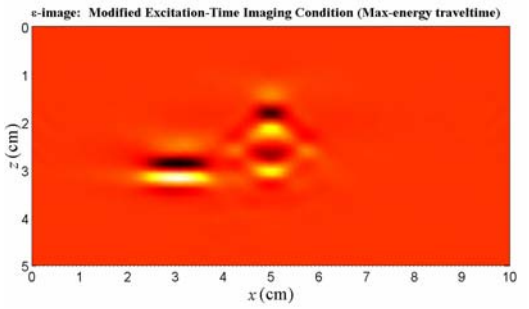

Fig. 8.1.4.29. Case (H); Permittivity image; Modified excitation-time imaging condition (Max-energy arrival); Half-space concrete;

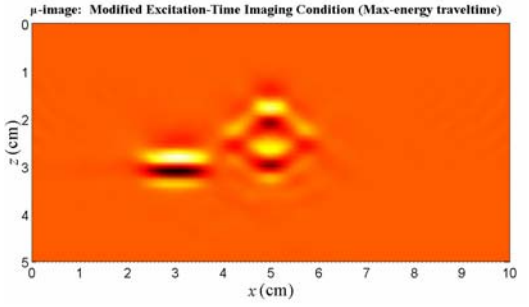

Fig. 8.1.4.30. Case (H); Permeability image; Modified excitation-time imaging condition (Max-energy arrival); Half-space concrete;

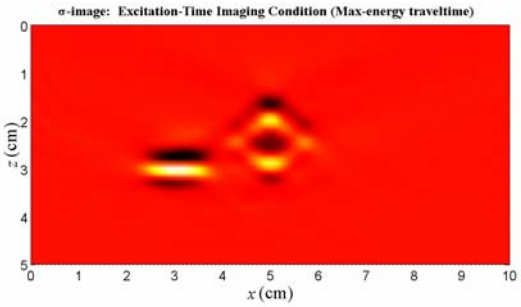

Fig. 8.1.4.31. Case (H); Conductivity image; Excitation-time imaging condition (Max-energy arrival); Half-space concrete;

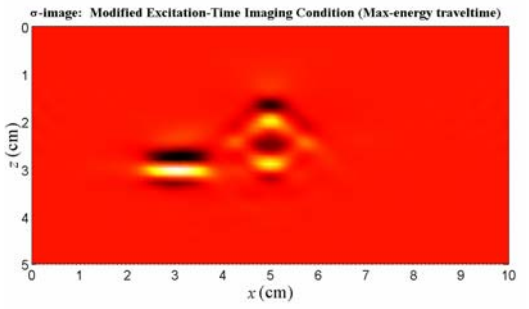

Fig. 8.1.4.32. Case (H); Conductivity image; Modified excitation-time imaging condition (Max-energy arrival); Half-space concrete;

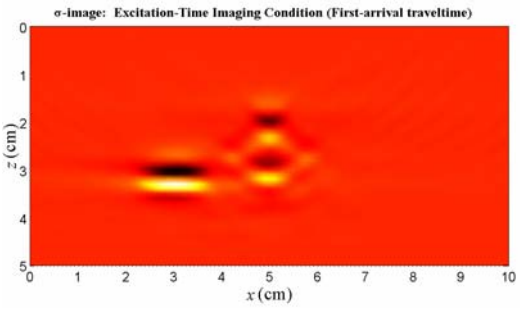

Fig. 8.1.4.33. Case (H); Conductivity image; Excitation-time imaging condition (First-arrival); Half-space concrete;

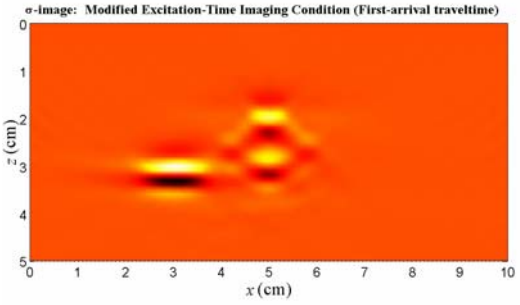

Fig. 8.1.4.34. Case (H); Conductivity image; Modified excitation-time imaging condition (First-arrival); Half-space concrete;

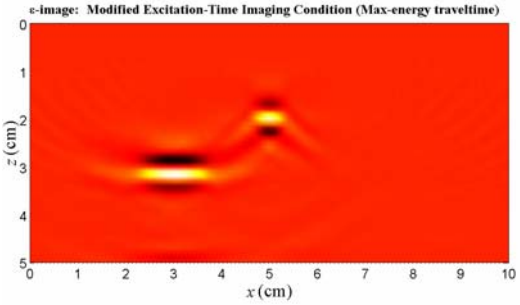

Fig. 8.1.4.35. Case (I); Permittivity image; Modified excitation-time imaging condition (Max-energy arrival); Modified pristine structure;

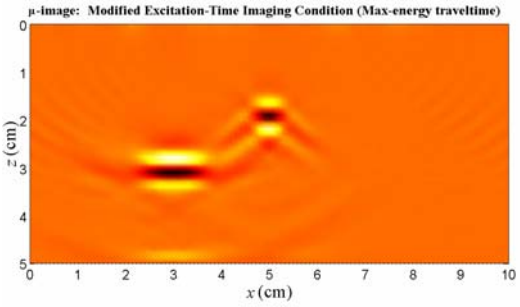

Fig. 8.1.4.36. Case (I); Permeability image; Modified excitation-time imaging condition (Max-energy arrival); Modified pristine structure;

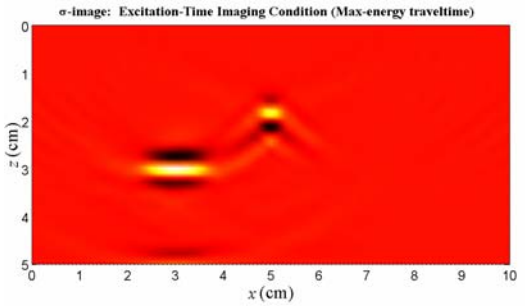

Fig. 8.1.4.37. Case (I); Conductivity image; Excitation-time imaging condition (Max-energy arrival); Modified pristine structure;

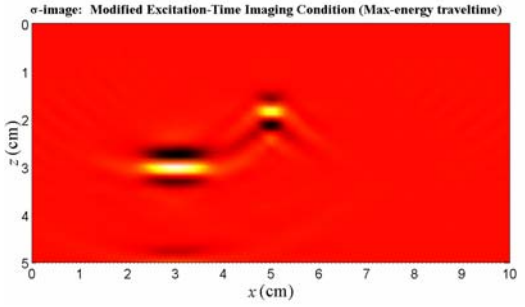

Fig. 8.1.4.38. Case (I); Conductivity image; Modified excitation-time imaging condition (Max-energy arrival); Modified pristine structure;

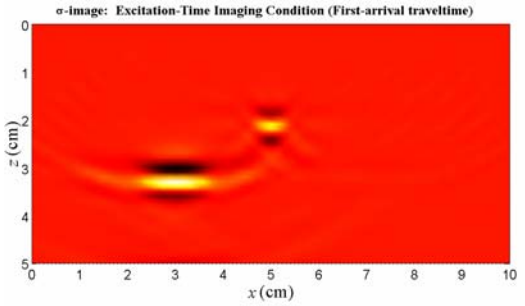

Fig. 8.1.4.39. Case (I); Conductivity image; Excitation-time imaging condition (First-arrival); Modified pristine structure;

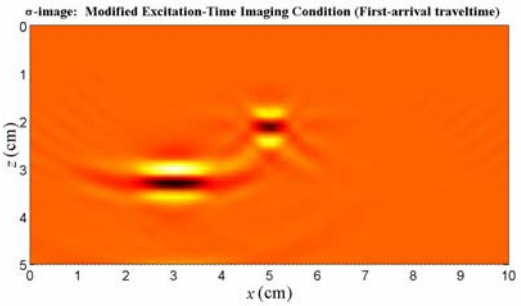

Fig. 8.1.4.40. Case (I); Conductivity image; Modified excitation-time imaging condition (First-arrival); Modified pristine structure;

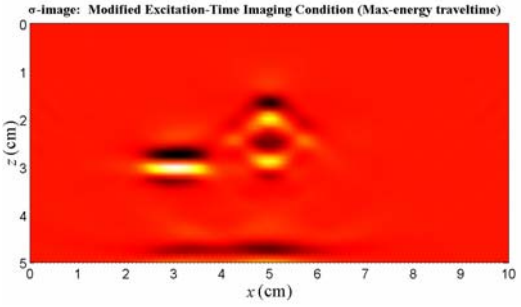

Fig. 8.1.4.41. Case (J); Conductivity image; Modified excitation-time imaging condition (Max-energy arrival); Concrete slab without rebars;

8.1.5. EM Migration (DE Formalism; Poststack)

The three different images for each type of measurement can be obtained by applying the zero-time imaging condition to the migrated scattered field components $E^m_{y;scat}$, $H^m_{x;scat}$, and $H^m_{z;scat}$ computed by FD discretization of differential equations (7.2.13) or (7.2.14) for a 2:1 scaled pristine structure depending on weather the sensor data is treated as sources or as time-dependent boundary conditions, respectively.

To show the effects of different measurement scenarios, actuator/sensor spacing, measurement noise, and material discontinuity in the pristine structure on the quality of the images, the following cases are investigated (in all cases $\Delta = 3\text{ mm} = 0.5\,\lambda_{\min}$ and data is treated as time-dependent boundary conditions, unless otherwise stated):

(A) $E^d_{y;scat}$ and $H^d_{x;scat}$

(B) $E^d_{y;scat}$ and $H^d_{x;scat}$ (as sources)

(C) Only $E^d_{y;scat}$

(D) Only $H^d_{x;scat}$

(E) $E^d_{y;scat}$ and $H^d_{x;scat}$ (contaminated by noise with SNR=5)

(F) $E^d_{y;scat}$ and $H^d_{x;scat}$ ($\Delta = 6\text{ mm} = \lambda_{\min}$)

(G) $E^d_{y;scat}$ and $H^d_{x;scat}$ (damaged structure: half-space concrete without rebars and the original damages)

(H) $E^d_{y;scat}$ and $H^d_{x;scat}$ (modified pristine structure: half-space concrete without rebars)

(I) $E^d_{y;scat}$ and $H^d_{x;scat}$ (damaged structure: concrete slab without rebars and the original damages)

Fig. 8.1.5.1 to 3 show the images obtained by the EM migration algorithm in DE formalism using the poststack concept in Case (A). The $H^m_{x;scat}$-images have provided the best damage identification. Also, the horizontal crack has not been completely identified in the $H^m_{z;scat}$-images.

When the sensor data has been treated as sources instead of time-dependent boundary conditions in the EM migration in Case (B), the quality of images has been deteriorated as shown in Fig. 8.1.5.4 to 6.

The images for different measurement scenarios in Cases (C) and (D) are shown in Fig. 8.1.5.7 to 12. Surprisingly, the usage of only $E^d_{y;scat}$ or $H^d_{x;scat}$ instead of both in the algorithm has improved the quality of images.

Fig. 8.1.5.13 illustrates the effect of the measurement noise with SNR=5 on the $H^m_{x;scat}$-image. This figure shows that the algorithm is quite robust against the measurement noise. Fig. 8.1.5.14 shows the $H^m_{x;scat}$-image with the actuator/sensor spacing of $\Delta = \lambda_{\min}$. The artifacts resulting from the increase in the actuator/sensor spacing can be easily observed in this figure.

Fig. 8.1.5.15 to 17 illustrate the images for a new damaged structure including a half-space concrete without rebars and the original damages in Case (G). Due to the simplicity of the pristine structure in this case (i.e., half-space concrete), all three images have provided good damage identification. Note that the horizontal crack still has not been completely identified in the $H^m_{z;scat}$-image.

Fig. 8.1.5.18 to 20 present the images when a modified pristine structure (a half-space concrete) instead of the actual pristine structure (the concrete slab with the rebars) has been used for the computation of the migrated scattered field. Notice that the damage identification has been improved in the $E^m_{y;scat}$-image compared to the corresponding image in Case (A).

Fig. 8.1.5.21 shows the $H^m_{x;scat}$-image for a damaged structure including a concrete slab without the rebars and the original damages. Notice how two false damages related to the typical shortcoming of the algorithm have been imaged near the lower interface of the slab.

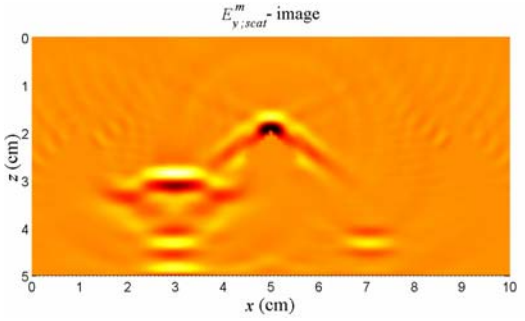

Fig. 8.1.5.1. Case (A); $E^m_{y;scat}$-image obtained by poststack EM migration;

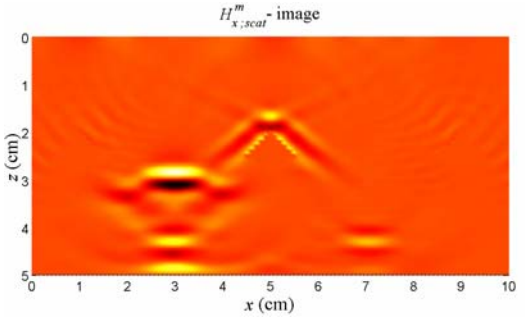

Fig. 8.1.5.2. Case (A); $H^m_{x;scat}$-image obtained by poststack EM migration;

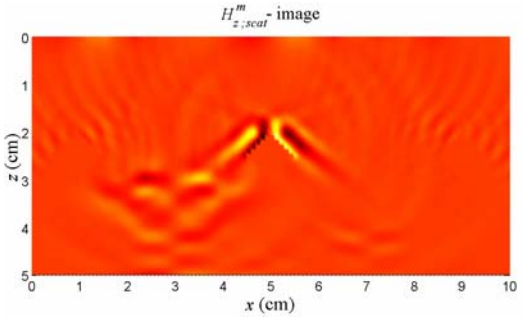

Fig. 8.1.5.3. Case (A); $H^m_{z;scat}$-image obtained by poststack EM migration;

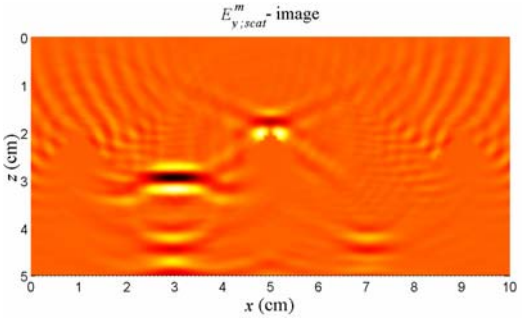

Fig. 8.1.5.4. Case (B); $E^m_{y;scat}$-image obtained by poststack EM migration; Data treated as sources;

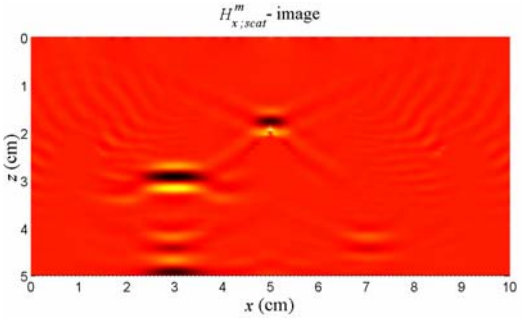

Fig. 8.1.5.5. Case (B); $H^m_{x;scat}$-image obtained by poststack EM migration; Data treated as sources;

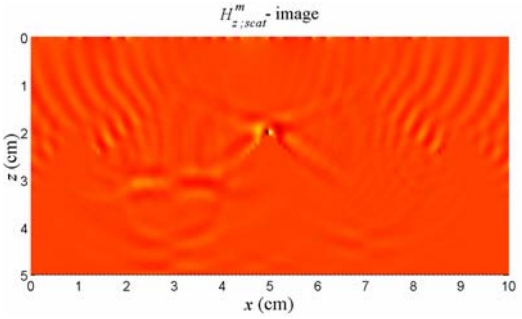

Fig. 8.1.5.6. Case (B); $H^m_{z;scat}$-image obtained by poststack EM migration; Data treated as sources;

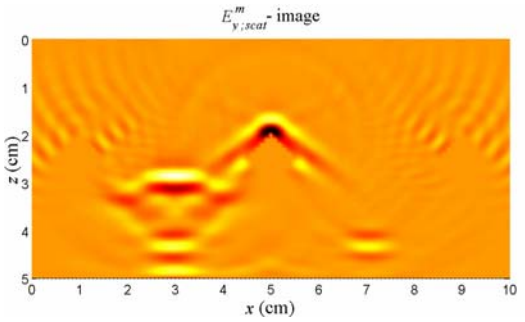

Fig. 8.1.5.7. Case (C); $E^m_{y;scat}$-image obtained by poststack EM migration; Only $E^d_{y;scat}$ as BC;

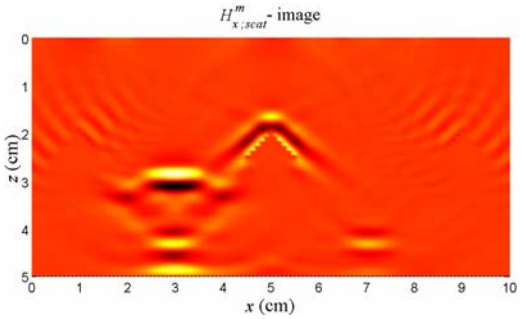

Fig. 8.1.5.8. Case (C); $H^m_{x;scat}$-image obtained by poststack EM migration; Only $E^d_{y;scat}$ as BC;

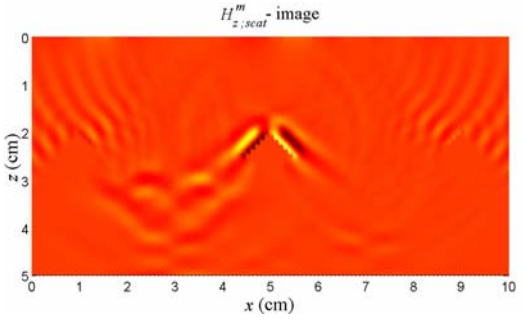

Fig. 8.1.5.9. Case (C); $H^m_{z;scat}$-image obtained by poststack EM migration; Only $E^d_{y;scat}$ as BC;

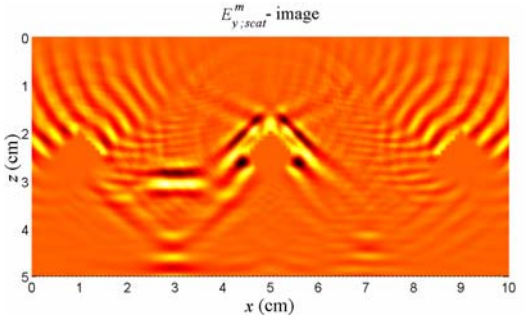

Fig. 8.1.5.10. Case (D); $E^m_{y;scat}$-image obtained by poststack EM migration; Only $H^d_{x;scat}$ as BC;

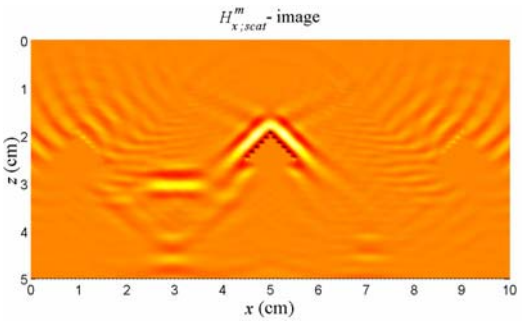

Fig. 8.1.5.11. Case (D); $H^m_{x;scat}$-image obtained by poststack EM migration; Only $H^d_{x;scat}$ as BC;

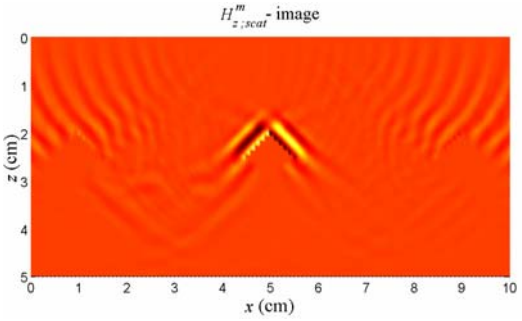

Fig. 8.1.5.12. Case (D); $H^m_{z;scat}$-image obtained by poststack EM migration; Only $H^d_{x;scat}$ as BC;

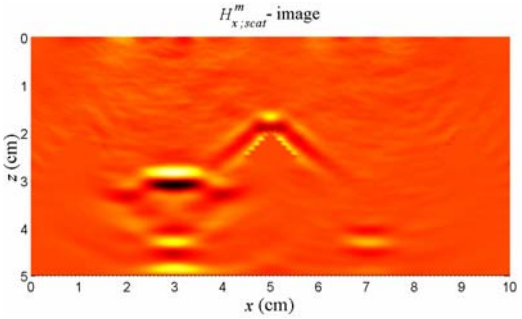

Fig. 8.1.5.13. Case (E); $H^m_{x;scat}$-image obtained by poststack EM migration; Noisy data SNR=5;

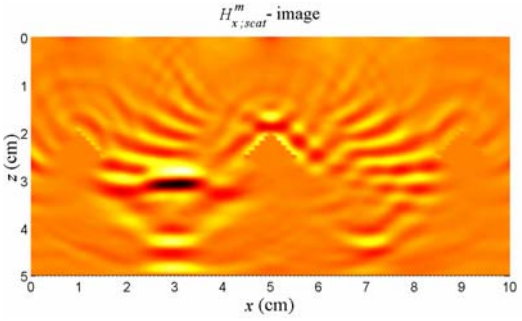

Fig. 8.1.5.14. Case (F); $H^m_{x;scat}$-image obtained by poststack EM migration; $\Delta = \lambda_{\min}$;

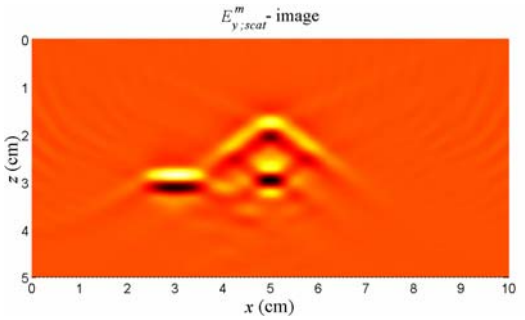

Fig. 8.1.5.15. Case (G); $E^m_{y;scat}$ -image obtained by poststack EM migration; Half-space concrete;

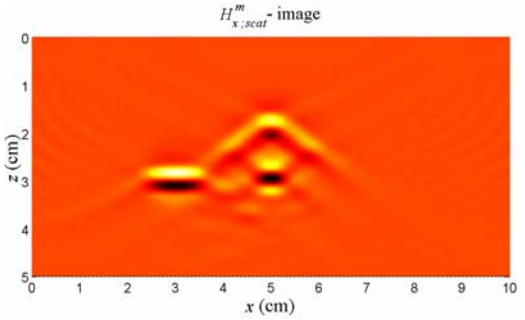

Fig. 8.1.5.16. Case (G); $H^m_{x;scat}$ -image obtained by poststack EM migration; Half-space concrete;

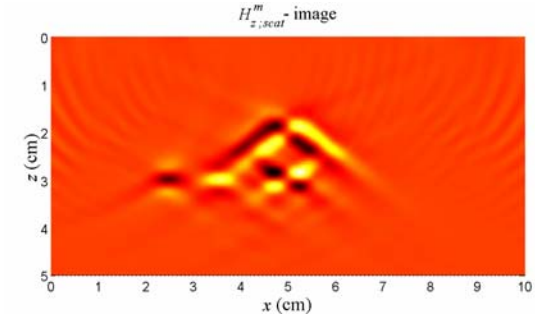

Fig. 8.1.5.17. Case (G); $H^m_{z;scat}$ -image obtained by poststack EM migration; Half-space concrete;

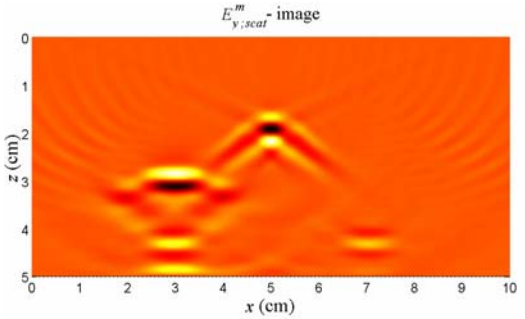

Fig. 8.1.5.18. Case (H); $E^m_{y;scat}$ -image obtained by poststack EM migration; Modified pristine structure;

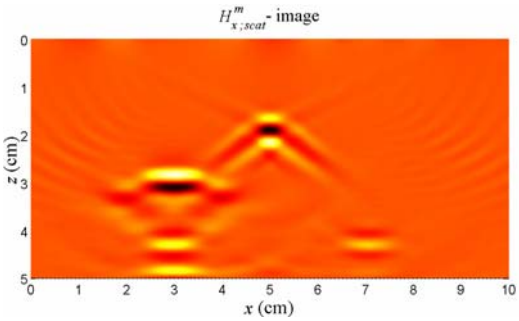

Fig. 8.1.5.19. Case (H); $H^m_{x;scat}$ -image obtained by poststack EM migration; Modified pristine structure;

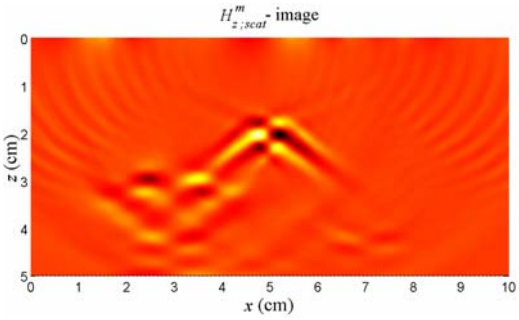

Fig. 8.1.5.20. Case (H); $H^m_{z;scat}$ -image obtained by poststack EM migration; Modified pristine structure;

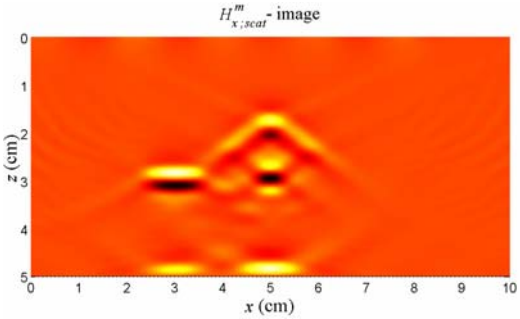

Fig. 8.1.5.21. Case (I); $H^m_{x;scat}$ -image obtained by poststack EM migration; Concrete slab without rebars;

8.1.6. EM Migration (IE Formalism)

Eq. (7.2.26) - (7.2.28) represent the real-time imaging formulas in the IE formalism of the EM migration algorithm. The amplitudes and traveltimes of the incident field and Green's functions are computed by FD discretization of ordinary Maxwell's equations for the pristine structure. The application of both first and maximum-energy arrival criteria for the calculation of these traveltimes and amplitudes are examined as well.

To show the effects of different measurement scenarios, actuator/sensor spacing, measurement noise, and material discontinuity in the pristine structure on the quality of the images, the following cases are investigated (in all cases $\Delta_{s,a} = 6 \text{ mm} = \lambda_{\min}$ unless otherwise stated):

(A) $E^d_{y;scat}$ and $H^d_{x;scat}$

(B) Only $E^d_{y;scat}$

(C) Only $H^d_{x;scat}$

(D) $E^d_{y;scat}$ and $H^d_{x;scat}$ (contaminated by noise with SNR=5)

(E) $E^d_{y;scat}$ and $H^d_{x;scat}$ ($\Delta_{s,a} = 9 \text{ mm} = 1.5\lambda_{\min}$)

(F) $E^d_{y;scat}$ and $H^d_{x;scat}$ ($\Delta_{s,a} = 12 \text{ mm} = 2\lambda_{\min}$)

(G) $E^d_{y;scat}$ and $H^d_{x;scat}$ (damaged structure: half-space concrete without rebars and the original damages)

(H) $E^d_{y;scat}$ and $H^d_{x;scat}$ (modified pristine structure: half-space concrete without rebars)

(I) $E^d_{y;scat}$ and $H^d_{x;scat}$ (damaged structure: concrete slab without rebars and the original damages)

Fig. 8.1.6.1 to 8 show the images obtained by the EM migration algorithm in IE formalism in Case (A). The geometries of the damages have been correctly identified with

the least artifacts in the permittivity image shown in Fig. 8.1.6.2. It is also observed that by excluding the amplitude in the approximation of the incident field and Green's functions, correct damage identification cannot be obtained (only shown for the permittivity images). Notice that the images obtained based on the maximum-energy arrival criterion for the for the calculation of the traveltimes and amplitudes have provided much better damage identification (specially for the debonding damage) than those of based on the first-arrival criterion. However, the images obtained based on the first-arrival criterion contain fewer artifacts.

Fig. 8.1.6.9 to 14 show the images obtained based on the maximum-energy arrival criterion when only $E^d_{y;scat}$ or $H^d_{x;scat}$ instead of both has been used in the algorithm. Notice that the images in Case (C) are quite similar to images in Case (A).

Fig. 8.1.6.15 illustrates the effect of the measurement noise with SNR=5 on the permittivity image. This figure shows that the algorithm is quite robust against the measurement noise. To show the effect of the actuator/sensor spacing on the images quality, the permittivity images with $\Delta_{s,a}$ =1.5 $\lambda_{\min}$, 2 $\lambda_{\min}$ are shown in Fig. 8.1.6.16 and 17. The artifacts resulting from the increase in the actuator/sensor spacing can be easily observed in these figures.

Fig. 8.1.6.18 to 21 illustrate the images for a new damaged structure including a half-space concrete without rebars and the original damages in Case (G). Due to the simplicity of the pristine structure in this case (i.e., half-space concrete), all permittivity, permeability, and conductivity images obtained based on the maximum-energy arrival criterion have provided excellent damage identification. Notice how the artifacts related to the material discontinuity in the pristine structure in Case (A) images have disappeared on the corresponding images in Case (G).

Fig. 8.1.6.22 to 25 present the images when a modified pristine structure (a half-space concrete) instead of the actual pristine structure (the concrete slab with the rebars) has been used for the computation of the incident and Green's functions in the image area. Notice how the artifacts related to the material discontinuity in the actual pristine structure in Case (A) images have been eliminated.

Fig. 8.1.6.26 shows the permittivity image for a damaged structure including a concrete slab without the rebars and the original damages. Notice how some false damages related to the typical shortcoming of the algorithm have been imaged near the lower interface of the slab.

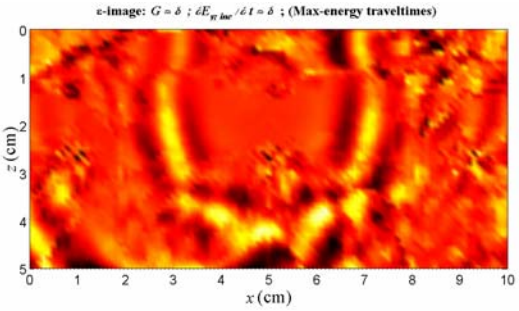

Fig. 8.1.6.1. Case (A); Permittivity image; All $G^{EM}_{yx;b}$, $G^{EJ}_{yy;b}$, and $\dot{E}_{y;inc}$ are approximated based on maximum-energy arrival criterion; Without amplitude;

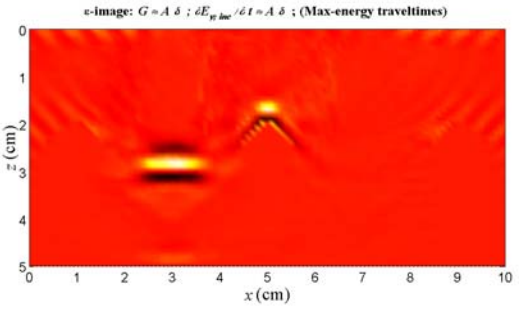

Fig. 8.1.6.2. Case (A); Permittivity image; All $G^{EM}_{yx;b}$, $G^{EJ}_{yy;b}$, and $\dot{E}_{y;inc}$ are approximated based on maximum-energy arrival criterion; With amplitude;

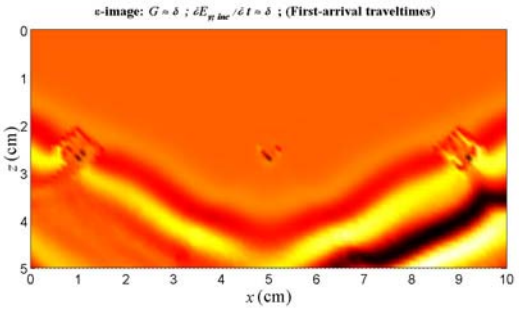

Fig. 8.1.6.3. Case (A); Permittivity image; All $G^{EM}_{yx;b}$, $G^{EJ}_{yy;b}$, and $\dot{E}_{y;inc}$ are approximated based on first-arrival criterion; Without amplitude;

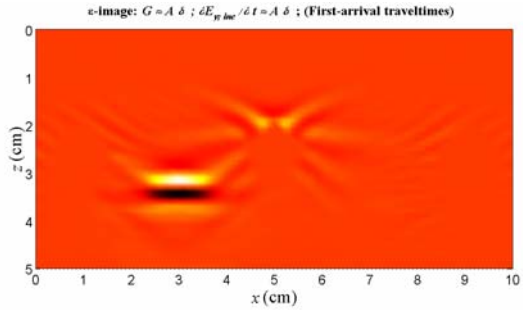

Fig. 8.1.6.4. Case (A); Permittivity image; All $G^{EM}_{yx;b}$, $G^{EJ}_{yy;b}$, and $\dot{E}_{y;inc}$ are approximated based on first-arrival criterion; With amplitude;

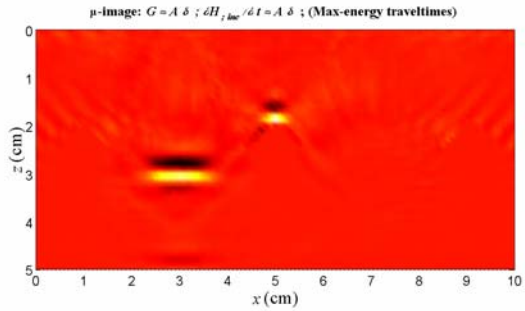

Fig. 8.1.6.5. Case (A); Permeability image; All $G^{HJ}_{xy;b}$, $G^{HJ}_{zy;b}$, $G^{HM}_{xx;b}$, $G^{HM}_{zx;b}$, $\dot{H}_{x;inc}$, and $\dot{H}_{z;inc}$ are approximated based on maximum-energy arrival criterion; With amplitude;

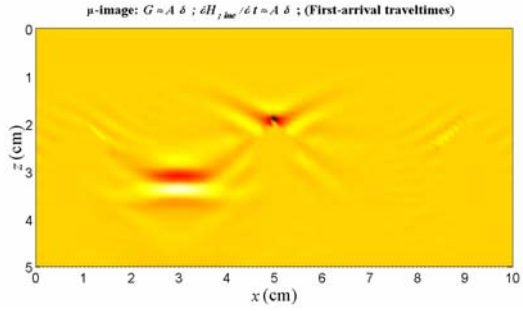

Fig. 8.1.6.6. Case (A); Permeability image; All $G^{HJ}_{xy;b}$, $G^{HJ}_{zy;b}$, $G^{HM}_{xx;b}$, $G^{HM}_{zx;b}$, $\dot{H}_{x;inc}$, and $\dot{H}_{z;inc}$ are approximated based on first-arrival criterion; With amplitude;

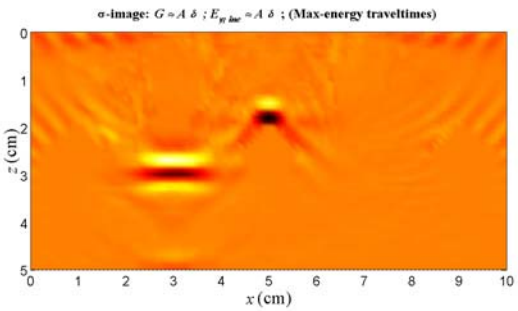

Fig. 8.1.6.7. Case (A); Conductivity image; All $G^{EM}_{yx;b}$, $G^{EJ}_{yy;b}$, and $E_{y;inc}$ are approximated based on maximum-energy arrival criterion; With amplitude;

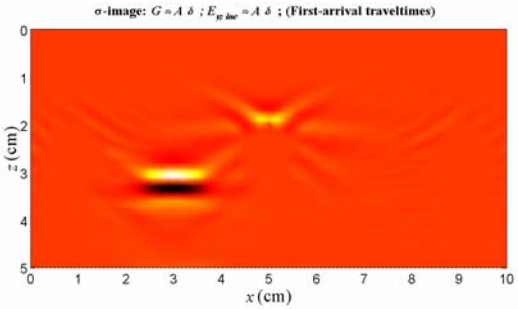

Fig. 8.1.6.8. Case (A); Conductivity image; All $G^{EM}_{yx;b}$, $G^{EJ}_{yy;b}$, and $E_{y;inc}$ are approximated based on first-arrival criterion; With amplitude;

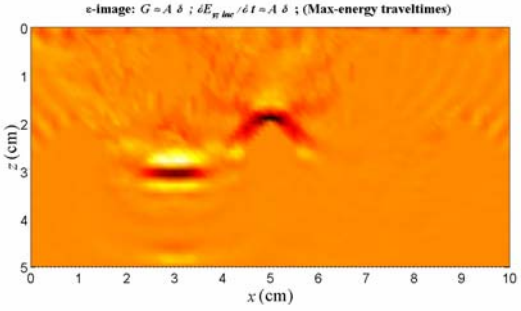

Fig. 8.1.6.9. Case (B); Permittivity image; Both $G^{EM}_{yx;b}$ and $\dot{E}_{y;inc}$ are approximated based on maximum-energy arrival criterion; With amplitude; Only $E^{d}_{y;scat}$;

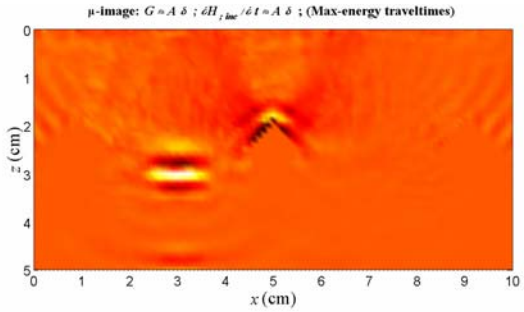

Fig. 8.1.6.10. Case (B); Permeability image; All $G^{HM}_{xx;b}$, $G^{HM}_{zx;b}$, $\dot{H}_{x;inc}$, and $\dot{H}_{z;inc}$ are approximated based on maximum-energy arrival criterion; With amplitude; Only $E^{d}_{y;scat}$;

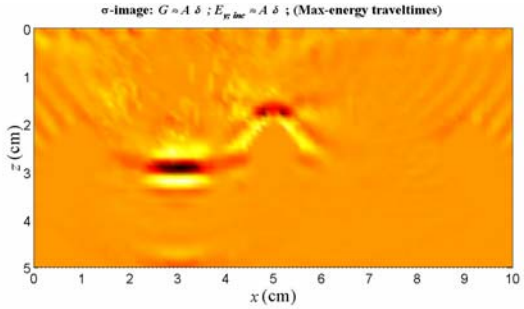

Fig. 8.1.6.11. Case (B); Conductivity image; Both $G^{EM}_{yx;b}$ and $E_{y;inc}$ are approximated based on maximum-energy arrival criterion; With amplitude; Only $E^{d}_{y;scat}$;

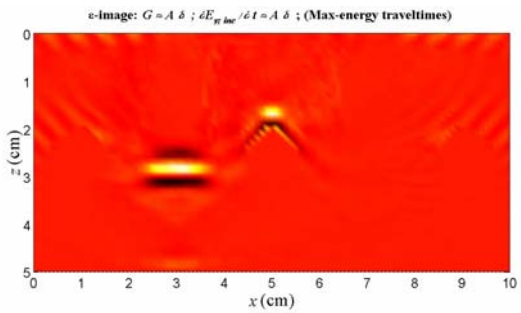

Fig. 8.1.6.12. Case (C); Permittivity image; Both $G^{EJ}_{yy;b}$ and $\dot{E}_{y;inc}$ are approximated based on maximum-energy arrival criterion; With amplitude; Only $H^{d}_{x;scat}$;

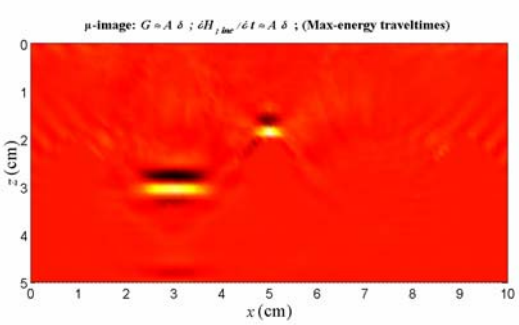

Fig. 8.1.6.13. Case (C); Permeability image; All $G^{HJ}_{xy;b}$, $G^{HJ}_{zy;b}$, $\dot{H}_{x;inc}$, and $\dot{H}_{z;inc}$ are approximated based on maximum-energy arrival criterion; With amplitude; Only $H^{d}_{x;scat}$;

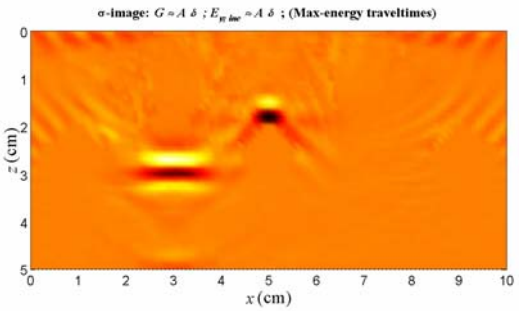

Fig. 8.1.6.14. Case (C); Conductivity image; Both $G^{EJ}_{yy;b}$ and $E_{y;inc}$ are approximated based on maximum-energy arrival criterion; With amplitude; Only $H^{d}_{x;scat}$;

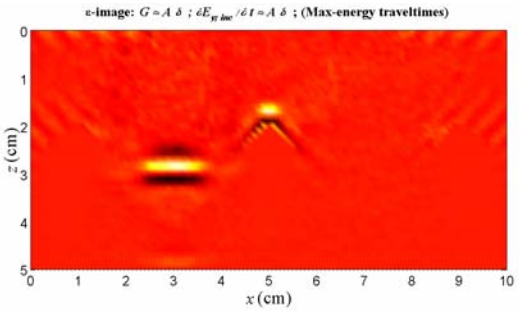

Fig. 8.1.6.15. Case (D); Permittivity image; All $G^{EM}_{yx;b}$, $G^{EJ}_{yy;b}$, and $\dot{E}_{y;inc}$ are approximated based on maximum-energy arrival criterion; With amplitude; Noisy data SNR=5;

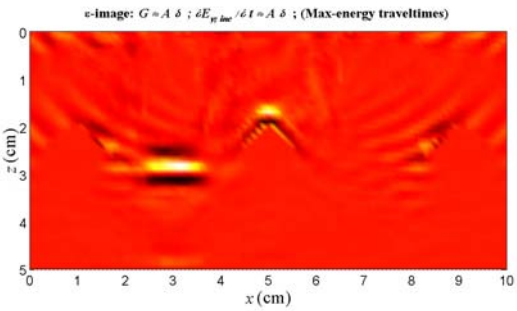

Fig. 8.1.6.16. Case (E); Permittivity image; All $G^{EM}_{yx;b}$, $G^{EJ}_{yy;b}$, and $\dot{E}_{y;inc}$ are approximated based on maximum-energy arrival criterion; With amplitude; $\Delta_{s,a} = 1.5\lambda_{\min}$;

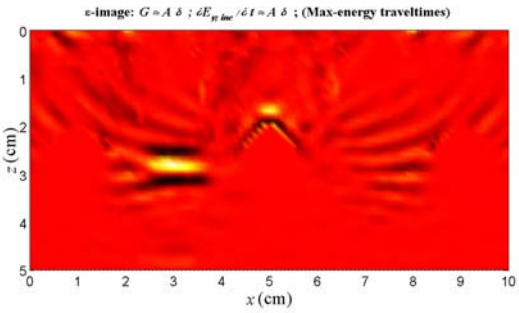

Fig. 8.1.6.17. Case (F); Permittivity image; All $G^{EM}_{yx;b}$, $G^{EJ}_{yy;b}$, and $\dot{E}_{y;inc}$ are approximated based on maximum-energy arrival criterion; With amplitude; $\Delta_{s,a} = 2\lambda_{\min}$;

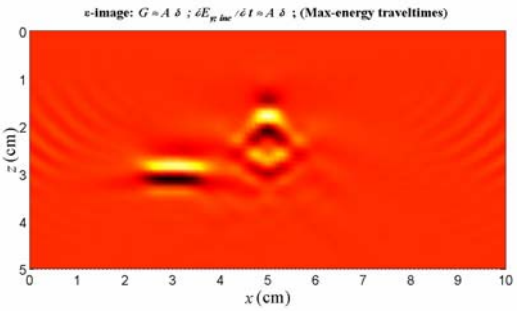

Fig. 8.1.6.18. Case (G); Permittivity image; All $G^{EM}_{yx;b}$, $G^{EJ}_{yy;b}$, and $\dot{E}_{y;inc}$ are approximated based on maximum-energy arrival criterion; With amplitude; Half-space concrete;

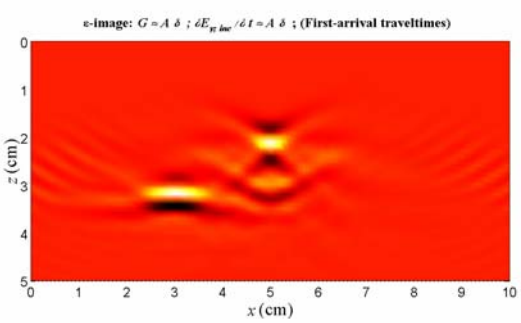

Fig. 8.1.6.19. Case (G); Permittivity image; All $G^{EM}_{yx;b}$, $G^{EJ}_{yy;b}$, and $\dot{E}_{y;inc}$ are approximated based on first-arrival criterion; With amplitude; Half-space concrete;

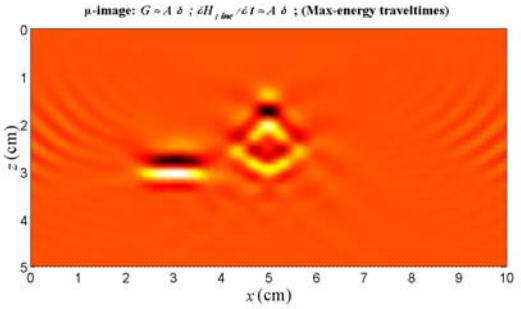

Fig. 8.1.6.20. Case (G); Permeability image; All $G^{HJ}_{xy;b}$, $G^{HJ}_{zy;b}$, $G^{HM}_{xx;b}$, $G^{HM}_{zx;b}$, $\dot{H}_{x;inc}$, and $\dot{H}_{z;inc}$ are approximated based on maximum-energy arrival criterion; With amplitude; Half-space concrete;

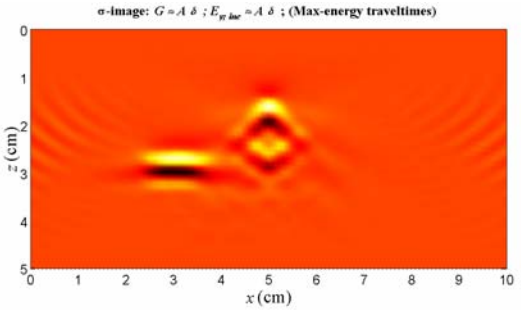

Fig. 8.1.6.21. Case (G); Conductivity image; All $G^{EM}_{yx;b}$, $G^{EJ}_{yy;b}$, and $E_{y;inc}$ are approximated based on maximum-energy arrival criterion; With amplitude; Half-space concrete;

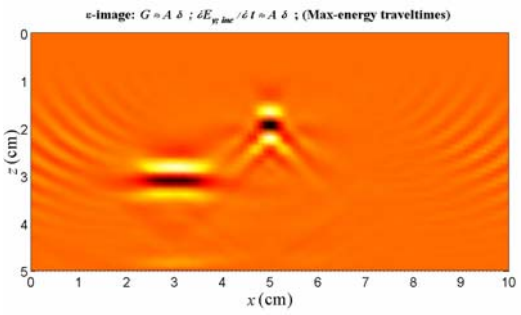

Fig. 8.1.6.22. Case (H); Permittivity image; All $G^{EM}_{yx;b}$, $G^{EJ}_{yy;b}$, and $\dot{E}_{y;inc}$ are approximated based on maximum-energy arrival criterion; With amplitude; Modified pristine structure;

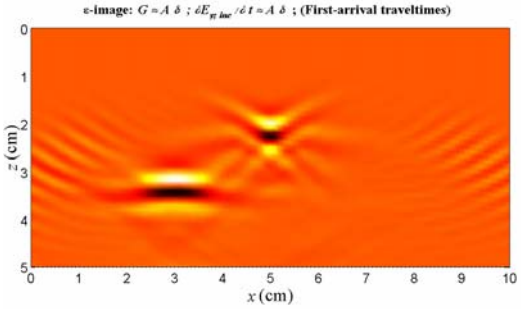

Fig. 8.1.6.23. Case (H); Permittivity image; All $G^{EM}_{yx;b}$, $G^{EJ}_{yy;b}$, and $\dot{E}_{y;inc}$ are approximated based on first-arrival criterion; With amplitude; Modified pristine structure;

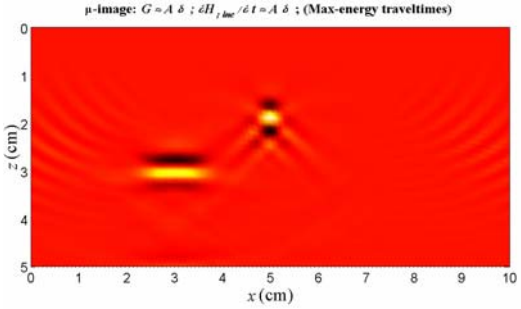

Fig. 8.1.6.24. Case (H); Permeability image; All $G^{HJ}_{xy;b}$, $G^{HJ}_{zy;b}$, $G^{HM}_{xx;b}$, $G^{HM}_{zx;b}$, $\dot{H}_{x;inc}$, and $\dot{H}_{z;inc}$ are approximated based on maximum-energy arrival criterion; With amplitude; Modified pristine structure;

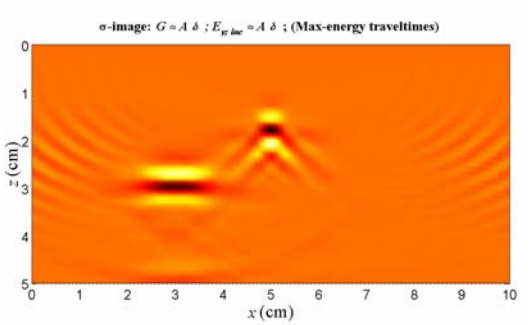

Fig. 8.1.6.25. Case (H); Conductivity image; All $G^{EM}_{yx;b}$, $G^{EJ}_{yy;b}$, and $E_{y;inc}$ are approximated based on maximum-energy arrival criterion; With amplitude; Modified pristine structure;

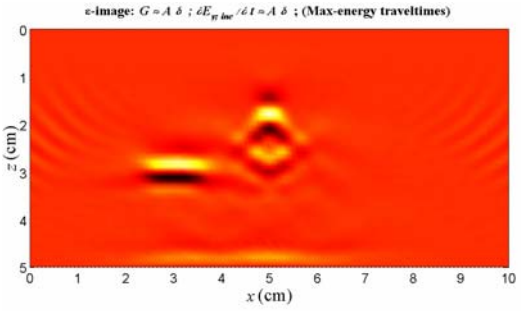

Fig. 8.1.6.26. Case (I); Permittivity image; All $G^{EM}_{yx;b}$, $G^{EJ}_{yy;b}$, and $\dot{E}_{y;inc}$ are approximated based on maximum-energy arrival criterion; With amplitude; Concrete slab without rebars;

8.2. Anisotropic Case

A glass/epoxy composite plate composed of 10 transversely isotropic (uniaxial) layers with stacking sequence of $[(0^o/90^o)_2/0^o]_s$ and equal thickness of 1mm is considered as the pristine structure. Fig. 8.2.1 illustrates the cross section of the damaged structure having two delaminations (area: $10\,\text{mm}\times 0.25\,\text{mm}$) with the centers at (15, 4) and (35, 6) mm. It is assumed that above and below the plate is air and actuators and sensors are uniformly located on the upper surface of the concrete slab with a sensor span of 48 mm.

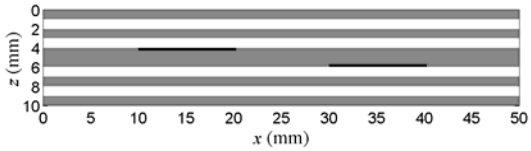

Fig. 8.2.1. Cross section of a glass/epoxy composite plate with two delaminations

The central frequency of the excitation signal is assumed to be $f_c = 36\,\text{GHz}$. Fig. 8.2.2 and 3 show the time history of the excitation signal and its amplitude spectrum, respectively.

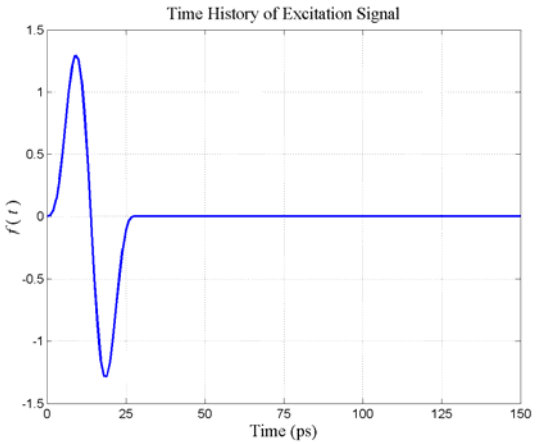

Fig. 8.2.2. The time history of the excitation signal

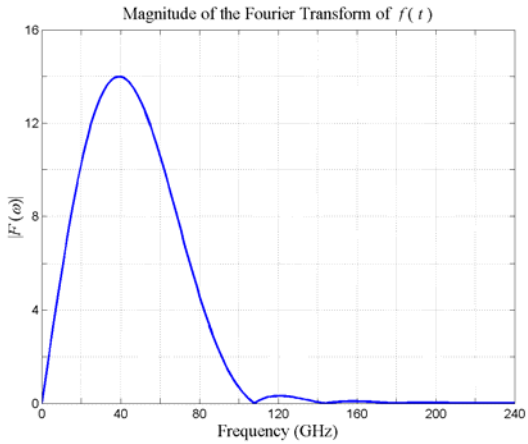

Fig. 8.2.3. The amplitude spectrum of the excitation signal

Relative dielectric constant and conductivity of the transversely isotropic glass/epoxy lamina are: $\sigma_L = 0.023$ S/m ; $\varepsilon_L = 3.84$ and $\sigma_T = 0.012$ S/m ; $\varepsilon_T = 3.40$, where subscripts L and T denote the direction along and transverse to the fibers, respectively.

Based on 3% of the maximum amplitude of the excitation signal spectrum, the maximum frequency and minimum wavelength of the signal in the plate are found to be about 102 GHz and 1.5 mm, respectively. Considering the minimum wavelength, the grid size is chosen equal to 0.25 mm ($\Delta x = \Delta z = 0.25$ mm).

Fig. 8.2.4 to 6 illustrate three components of the scattered field data (the measured incident field subtracted from the measured total field) excited from an actuator located at $x = 25$ mm with sensor spacing of $\Delta_s = 2$ mm .

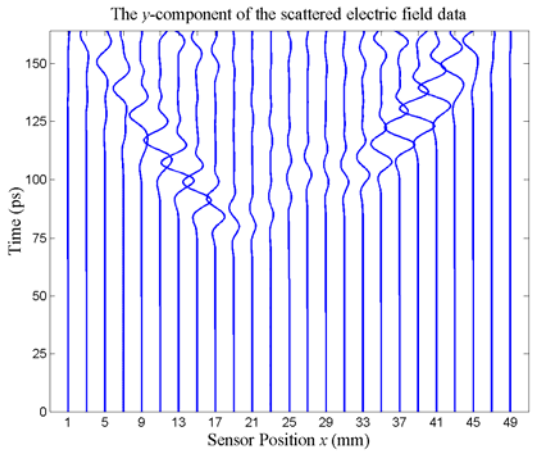

Fig. 8.2.4. The *y*-component of the scattered electric field data, $E^{d}_{y;\,scat}$, excited from an actuator at $x = 25$mm with sensor spacing of $\Delta_s = 2$ mm

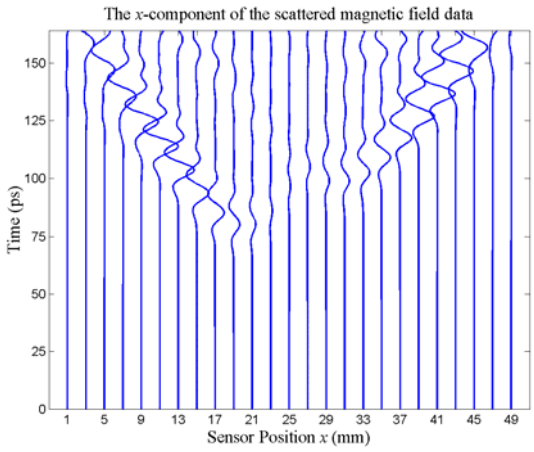

Fig. 8.2.5. The *x*-component of the scattered magnetic field data, $H^{d}_{x;\,scat}$, excited from an actuator at $x = 25$mm with sensor spacing of $\Delta_s = 2$ mm

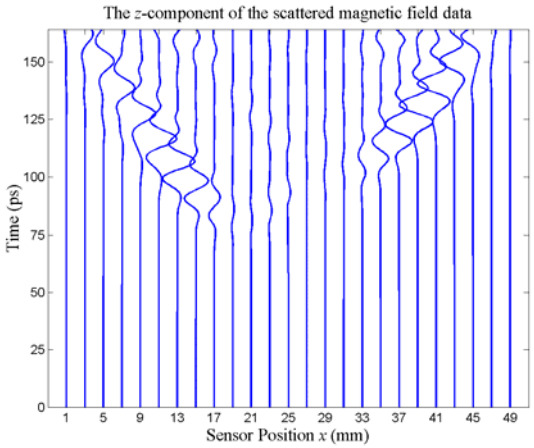

Fig. 8.2.6. The *z*-component of the scattered magnetic field data, $H^{d}_{z;\ scat}$, excited from an actuator at $x = 25\text{mm}$ with sensor spacing of $\Delta_s = 2$ mm

As mentioned in Chapter 6, there are several methods for reducing the artifacts related to the material discontinuity in the pristine structure. Here, in order to remove undesired internal reflections, a modified pristine structure, a half-space homogenized orthotropic medium, instead of the actual layered pristine structure, is used for the computation of the incident field, Green's functions, and back-propagated (migrated) scattered fields in the image area. Obviously, the measured incident and total fields are obtained from the actual pristine and damaged structures, respectively. This approach is also valuable in real applications when precise information about the layered structure may not be known *a priori*. Note that a drawback of this homogenization assumption prevails when the material properties of the layers are very distinct; as a result, the location of the damages may not be accurately identified because the velocity field of the actual structure for the back-propagation (migration) differs significantly from layer to layer.

8.2.1. Born Imaging (DE Formalism)

Eq. (7.1.1) - (7.1.4) represent the imaging formulas with zero-lag cross-correlation imaging condition. The corresponding imaging formulas with modified excitation-time imaging condition are Eq. (7.1.13) - (7.1.16); the imaging formulas with ordinary excitation-time imaging condition are easily obtained by setting the amplitudes to unity. Note that the back-propagated scattered fields are computed by FD discretization of differential equations (7.1.5) for the pristine structure. Also, the application of both first and maximum-energy arrival criteria for the calculation of the traveltimes and amplitudes are examined.

To show the effects of different measurement scenarios, actuator/sensor spacing, measurement noise, and material discontinuity in the pristine structure on the quality of the images, the following cases are investigated (in all cases $\Delta_{s,a} = 2 \text{ mm} = 1.33\, \lambda_{\min}$, unless otherwise stated):

(A) $E^d_{y;scat}$

(B) $H^d_{x;scat}$

(C) $H^d_{z;scat}$

(D) $E^d_{y;scat}$ (contaminated by noise with SNR=5)

(E) $E^d_{y;scat}$ ($\Delta_{s,a} = 3 \text{ mm} = 2\, \lambda_{\min}$)

(F) $E^d_{y;scat}$ ($\Delta_{s,a} = 4 \text{ mm} = 2.67\, \lambda_{\min}$)

(G) $E^d_{y;scat}$ (longer measurement time span)

(H) $E^d_{y;scat}$ (longer measurement time span; modified pristine structure)

(I) E^d_{y} (modified pristine structure)

Fig. 8.2.1.1 to 14 show the images obtained by the Born imaging algorithm in DE formalism with different imaging conditions in Case (A). It is observed that the images

obtained by the modified excitation-time imaging condition with either first or maximum-energy arrival criterion for the calculation of the traveltimes and amplitudes are comparable in quality to the images obtained by the zero-lag cross-correlation imaging condition. Also, the modified excitation-time imaging condition has significantly improved the images quality compared to the images obtained by the ordinary excitation-time imaging condition (only shown for the ε_{yy}-images). Notice how two false damages related to the typical shortcoming of the algorithm have been imaged near the lower surface of the plate.

Fig. 8.2.1.15 to 18 show the μ_{xx}-images for different measurement scenarios in Cases (B) and (C).

The effect of the measurement noise with SNR=5 on the μ_{xx}-images is illustrated in Fig. 8.2.1.19 and 20. These figures show that the algorithm is quite robust against the measurement noise. To show the effect of the actuator/sensor spacing on the images quality, the μ_{xx}-images with $\Delta_{s,a} = 2\,\lambda_{\min}$, $2.67\,\lambda_{\min}$ are shown in Fig. 8.2.1.21 to 24. The artifacts resulting from the increase in the actuator/sensor spacing can be easily observed in these figures.

To highlight the negative effect of the material discontinuity in the pristine structure on the images quality, the measurement time span has been increased from 164 ps to 196 ps in Case (G). The strong artifacts can be clearly observed in Fig. 8.2.1.25 and 26. The artifacts related to the material discontinuity in the actual pristine structure have been eliminated in Fig. 8.2.1.27 and 28 when a modified pristine structure (a half-space homogenized orthotropic medium) has been used for the computation of the incident and back-propagated fields in the image area.

Fig. 8.2.1.29 and 30 illustrate the μ_{xx}-images when E_y^d instead of $E_{y;scat}^d$ has been used for damage imaging. It should be mentioned that the events associated with direct waves and reflections from the upper surface of the plate have been removed from E_y^d as a preprocessing step. Notice how the material interfaces of the laminated plate have been imaged in addition to the delaminations.

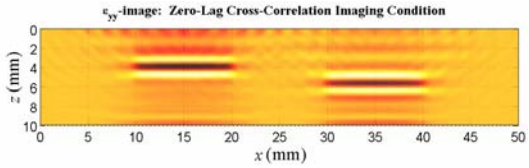

Fig. 8.2.1.1. Case (A); ε_{yy} -image; Zero-lag cross-correlation imaging condition;

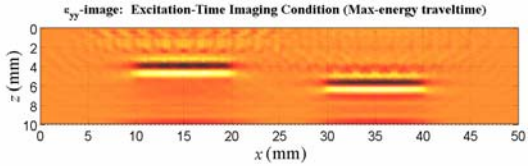

Fig. 8.2.1.2. Case (A); ε_{yy} -image; Excitation-time imaging condition (Max-energy arrival);

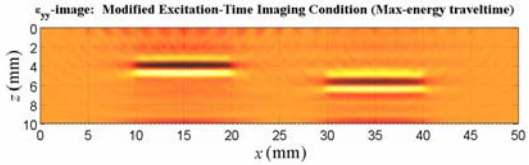

Fig. 8.2.1.3. Case (A); ε_{yy} -image; Modified excitation-time imaging condition (Max-energy arrival);

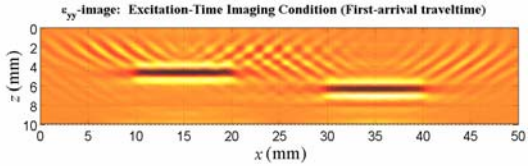

Fig. 8.2.1.4. Case (A); ε_{yy} -image; Excitation-time imaging condition (First-arrival);

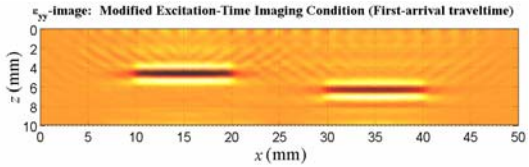

Fig. 8.2.1.5. Case (A); ε_{yy} -image; Modified excitation-time imaging condition (First-arrival);

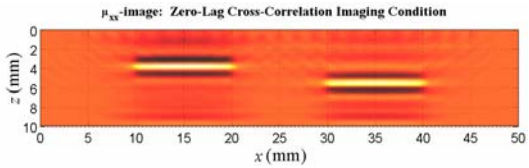

Fig. 8.2.1.6. Case (A); μ_{xx} -image; Zero-lag cross-correlation imaging condition;

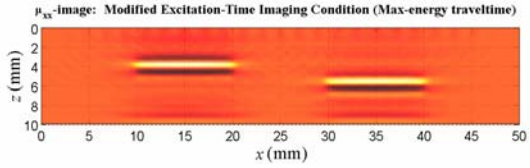

Fig. 8.2.1.7. Case (A); μ_{xx} -image; Modified excitation-time imaging condition (Max-energy arrival);

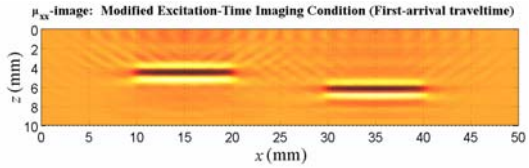

Fig. 8.2.1.8. Case (A); μ_{xx} -image; Modified excitation-time imaging condition (First-arrival);

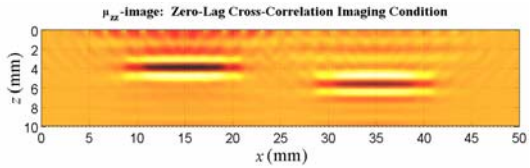

Fig. 8.2.1.9. Case (A); μ_{zz} -image; Zero-lag cross-correlation imaging condition;

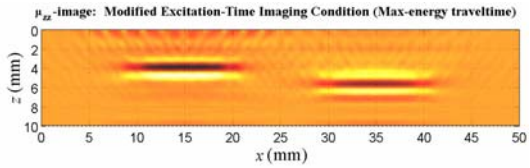

Fig. 8.2.1.10. Case (A); μ_{zz} -image; Modified excitation-time imaging condition (Max-energy arrival);

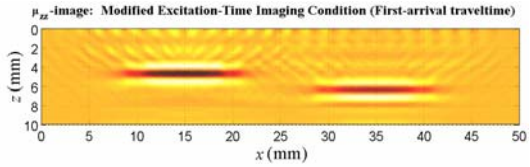

Fig. 8.2.1.11. Case (A); μ_{zz} -image; Modified excitation-time imaging condition (First-arrival);

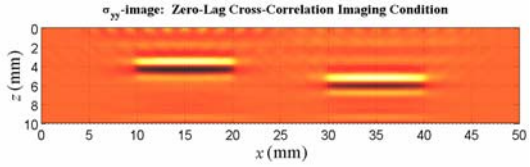

Fig. 8.2.1.12. Case (A); σ_{yy} -image; Zero-lag cross-correlation imaging condition;

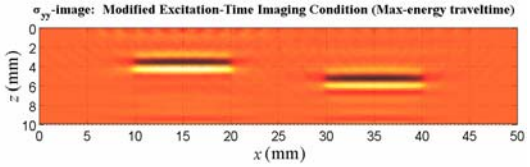

Fig. 8.2.1.13. Case (A); σ_{yy} -image; Modified excitation-time imaging condition (Max-energy arrival);

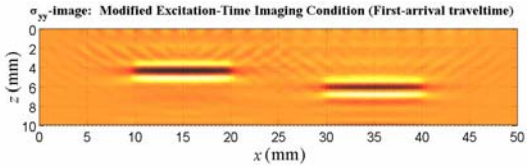

Fig. 8.2.1.14. Case (A); σ_{yy} -image; Modified excitation-time imaging condition (First-arrival);

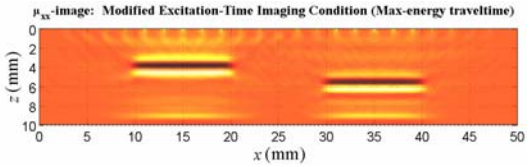

Fig. 8.2.1.15. Case (B); μ_{xx} -image; Modified excitation-time imaging condition (Max-energy arrival);

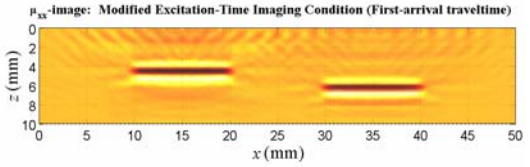

Fig. 8.2.1.16. Case (B); μ_{xx} -image; Modified excitation-time imaging condition (First-arrival);

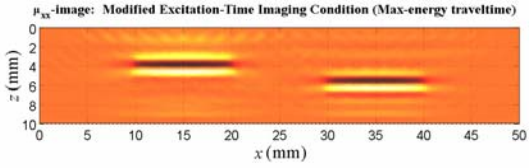

Fig. 8.2.1.17. Case (C); μ_{xx} -image; Modified excitation-time imaging condition (Max-energy arrival);

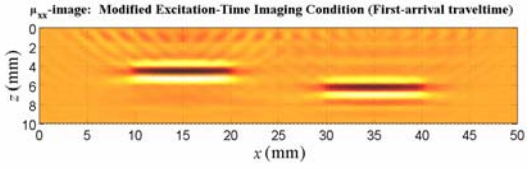

Fig. 8.2.1.18. Case (C); μ_{xx} -image; Modified excitation-time imaging condition (First-arrival);

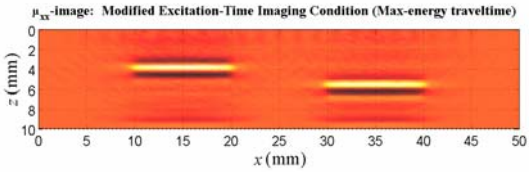

Fig. 8.2.1.19. Case (D); μ_{xx} -image; Modified excitation-time imaging condition (Max-energy arrival); Noisy data SNR=5;

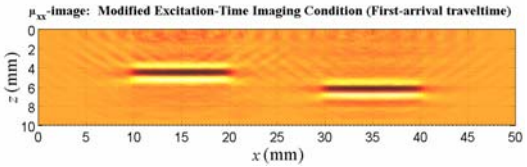

Fig. 8.2.1.20. Case (D); μ_{xx} -image; Modified excitation-time imaging condition (First-arrival); Noisy data SNR=5;

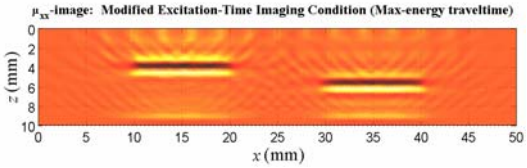

Fig. 8.2.1.21. Case (E); μ_{xx} -image; Modified excitation-time imaging condition (Max-energy arrival); $\Delta_{s,a} = 2\lambda_{\min}$;

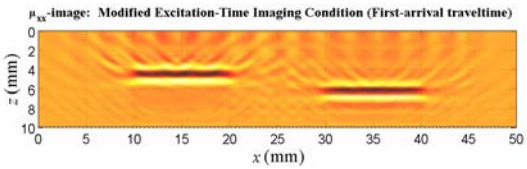

Fig. 8.2.1.22. Case (E); μ_{xx} -image; Modified excitation-time imaging condition (First-arrival); $\Delta_{s,a} = 2\lambda_{\min}$;

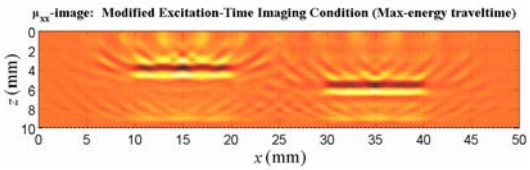

Fig. 8.2.1.23. Case (F); μ_{xx} -image; Modified excitation-time imaging condition (Max-energy arrival); $\Delta_{s,a} = 2.67\lambda_{\min}$;

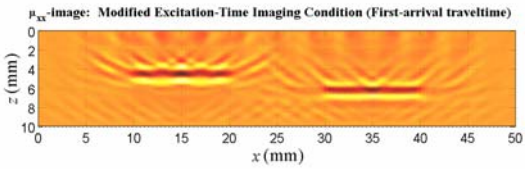

Fig. 8.2.1.24. Case (F); μ_{xx} -image; Modified excitation-time imaging condition (First-arrival); $\Delta_{s,a} = 2.67\lambda_{\min}$;

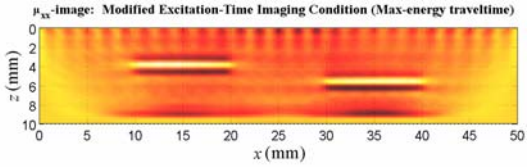

Fig. 8.2.1.25. Case (G); μ_{xx} -image; Modified excitation-time imaging condition (Max-energy arrival); Longer data time span;

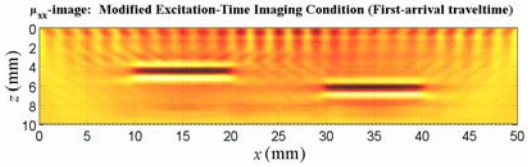

Fig. 8.2.1.26. Case (G); μ_{xx} -image; Modified excitation-time imaging condition (First-arrival); Longer data time span;

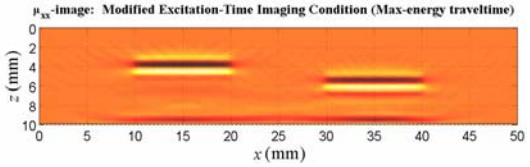

Fig. 8.2.1.27. Case (H); μ_{xx} -image; Modified excitation-time imaging condition (Max-energy arrival); Longer data time span; Modified pristine structure;

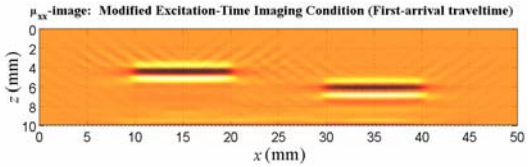

Fig. 8.2.1.28. Case (H); μ_{xx} -image; Modified excitation-time imaging condition (First-arrival); Longer data time span; Modified pristine structure;

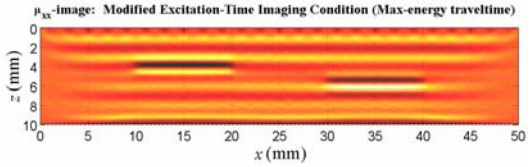

Fig. 8.2.1.29. Case (I); μ_{xx} -image; Modified excitation-time imaging condition (Max-energy arrival); E_y^d ; Modified pristine structure;

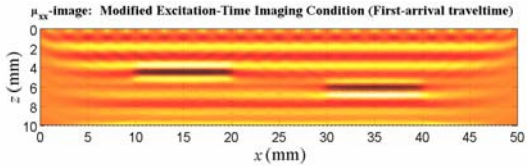

Fig. 8.2.1.30. Case (I); μ_{xx} -image; Modified excitation-time imaging condition (First-arrival); E_y^d ; Modified pristine structure;

8.2.2. Born Imaging (DE Formalism; Poststack)

The three different images for each type of measurement can be obtained by applying the zero-time imaging condition to the back-propagated scattered field components $E^{BP}_{y;scat}$, $H^{BP}_{x;scat}$, and $H^{BP}_{z;scat}$ computed by FD discretization of differential equations (7.1.5) for a 2:1 scaled pristine structure.

To show the effects of different measurement scenarios, actuator/sensor spacing, measurement noise, and material discontinuity in the pristine structure on the quality of the images, the following cases are investigated (in all cases $\Delta = 1\,\text{mm} = 0.67\,\lambda_{\min}$ unless otherwise stated):

(A) $E^{d}_{y;scat}$

(B) $H^{d}_{x;scat}$

(C) $H^{d}_{z;scat}$

(D) $E^{d}_{y;scat}$ (contaminated by noise with SNR=5)

(E) $E^{d}_{y;scat}$ ($\Delta = 1.5\,\text{mm} = \lambda_{\min}$)

(F) $E^{d}_{y;scat}$ ($\Delta = 2\,\text{mm} = 1.33\,\lambda_{\min}$)

(G) $E^{d}_{y;scat}$ (longer measurement time span)

(H) $E^{d}_{y;scat}$ (longer measurement time span; modified pristine structure)

(I) E^{d}_{y} (modified pristine structure)

Fig. 8.2.2.1 to 9 show the images obtained by the Born imaging algorithm in DE formalism using poststack concept in Cases (A) to (C). The $H^{BP}_{x;scat}$-images have provided the best damage identification among the images. Also, the delaminations have not been completely imaged in the $H^{BP}_{z;scat}$-images. Moreover, when $H^{d}_{z;scat}$ has been used as data, the

damages have not been completely identified. Notice how two false damages related to the typical shortcoming of the algorithm have been imaged near the lower surface of the plate

The effect of the measurement noise with SNR=5 on the $H^{BP}_{x;scat}$-image is shown in Fig. 8.2.2.10. This figure shows that the algorithm is quite robust against the measurement noise.

Fig. 8.2.2.11 and 12 show $H^{BP}_{x;scat}$-images with the actuator/sensor spacing of $\Delta = \lambda_{\min}$, $1.33\,\lambda_{\min}$. The artifacts resulting from the increase in the actuator/sensor spacing can be easily observed in these figures.

To highlight the effect of the material discontinuity in the pristine structure on the images quality, the measurement time span has been increased from 164 ps to 196 ps, Fig. 8.2.2.13. This image has not been affected by the artifacts related to the material discontinuity as opposed to the corresponding image in the prestack form of the algorithm. Fig. 8.2.2.14 also shows the $H^{BP}_{x;scat}$-image when a modified pristine structure (a half-space homogenized orthotropic medium) has been used for the computation of the back-propagated field. It is concluded that the poststack images are more robust than the prestack images to the artifacts related to the material discontinuity in the pristine structure. This is because the incident field in the image area is not needed in constructing the poststack images. The difference between data collected in common-source and zero-offset configurations may be another reason.

Fig. 8.2.2.15 illustrates the $H^{BP}_{x;scat}$-image when E^{d}_{y} instead of $E^{d}_{y;scat}$ has been used for damage imaging. It should be mentioned that the events associated with direct waves and reflections from the upper surface of the plate have been removed from E^{d}_{y} as a preprocessing step. Notice how the material interfaces of the laminated plate have been imaged in addition to the delaminations.

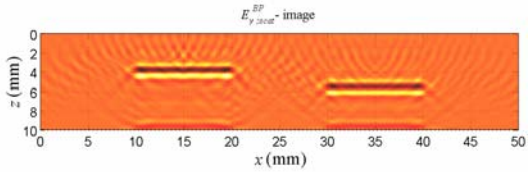

Fig. 8.2.2.1. Case (A); $E^{BP}_{y;scat}$ -image obtained by poststack Born imaging;

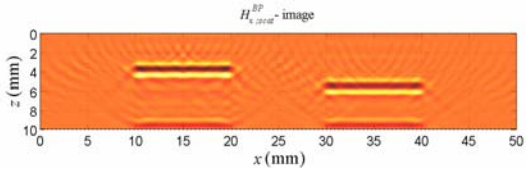

Fig. 8.2.2.2. Case (A); $H^{BP}_{x;scat}$ -image obtained by poststack Born imaging;

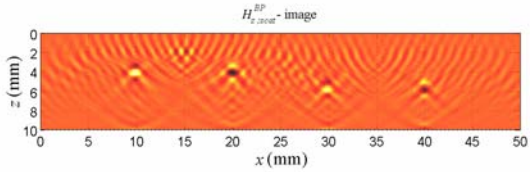

Fig. 8.2.2.3. Case (A); $H^{BP}_{z;scat}$ -image obtained by poststack Born imaging;

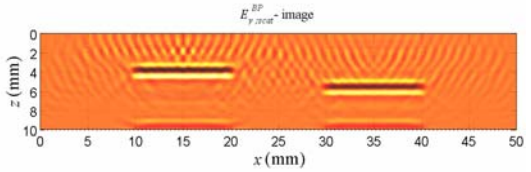

Fig. 8.2.2.4. Case (B); $E^{BP}_{y;scat}$ -image obtained by poststack Born imaging;

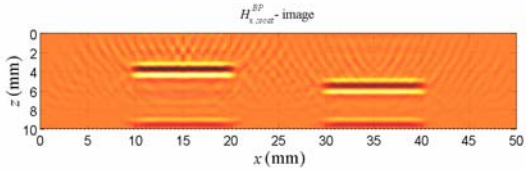

Fig. 8.2.2.5. Case (B); $H^{BP}_{x;scat}$ -image obtained by poststack Born imaging;

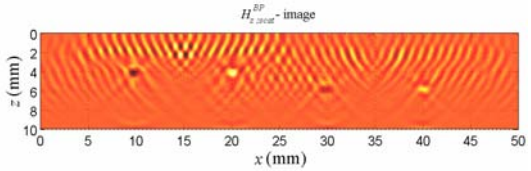

Fig. 8.2.2.6. Case (B); $H^{BP}_{z;scat}$ -image obtained by poststack Born imaging;

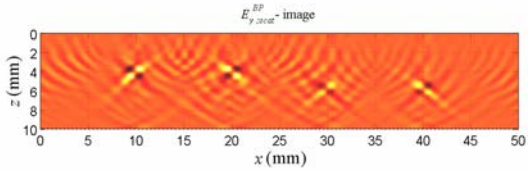

Fig. 8.2.2.7. Case (C); $E^{BP}_{y;scat}$ -image obtained by poststack Born imaging;

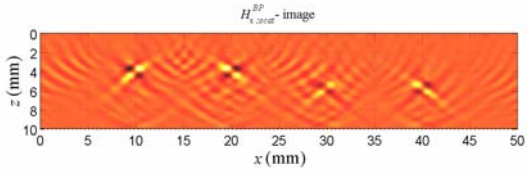

Fig. 8.2.2.8. Case (C); $H^{BP}_{x;scat}$ -image obtained by poststack Born imaging;

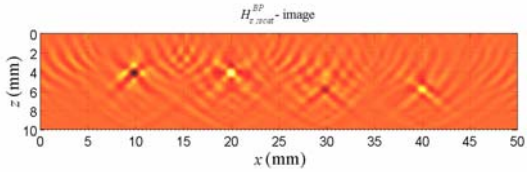

Fig. 8.2.2.9. Case (C); $H^{BP}_{z;scat}$ -image obtained by poststack Born imaging;

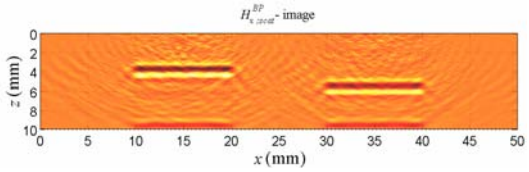

Fig. 8.2.2.10. Case (D); $H^{BP}_{x;scat}$ -image obtained by poststack Born imaging; Noisy data SNR=5;

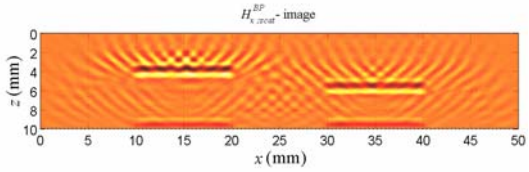

Fig. 8.2.2.11. Case (E); $H^{BP}_{x;scat}$ -image obtained by poststack Born imaging; $\Delta = \lambda_{\min}$;

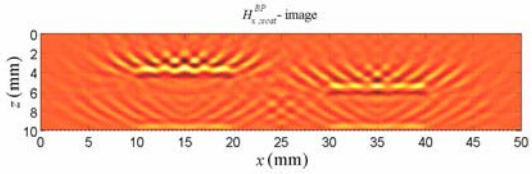

Fig. 8.2.2.12. Case (F); $H^{BP}_{x;scat}$ -image obtained by poststack Born imaging; $\Delta = 1.33\lambda_{\min}$;

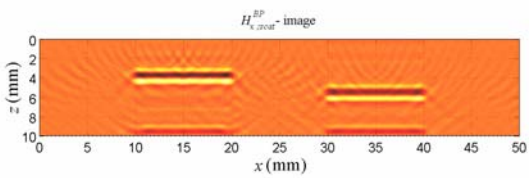

Fig. 8.2.2.13. Case (G); $H^{BP}_{z;scat}$ -image obtained by poststack Born imaging; Longer data time span;

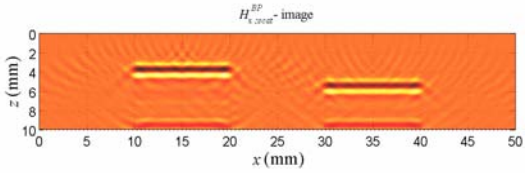

Fig. 8.2.2.14. Case (H); $H^{BP}_{z;scat}$ -image obtained by poststack Born imaging; Longer data time span; Modified pristine structure;

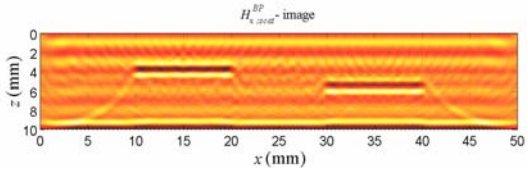

Fig. 8.2.2.15. Case (I); $H^{BP}_{z;scat}$ -image obtained by poststack Born imaging; E^{d}_{y} ; Modified pristine structure;

8.2.3. Born Imaging (IE Formalism)

Eq. (7.1.23) - (7.1.26) represent the real-time imaging formulas in the IE formalism of the Born imaging algorithm. The amplitudes and traveltimes of the incident field and Green's functions are computed by FD discretization of ordinary Maxwell's equations for the pristine structure. The application of both first and maximum-energy arrival criteria for the calculation of these traveltimes and amplitudes are examined as well.

To show the effects of different measurement scenarios, actuator/sensor spacing, measurement noise, and material discontinuity in the pristine structure on the quality of the images, the following cases are investigated (in all cases $\Delta_{s,a} = 2 \text{ mm} = 1.33\,\lambda_{\min}$, unless otherwise stated):

(A) $E^{d}_{y;scat}$

(B) $H^{d}_{x;scat}$

(C) $H^{d}_{z;scat}$

(D) $E^{d}_{y;scat}$ (contaminated by noise with SNR=5)

(E) $E^{d}_{y;scat}$ ($\Delta_{s,a} = 3 \text{ mm} = 2\,\lambda_{\min}$)

(F) $E^{d}_{y;scat}$ ($\Delta_{s,a} = 4 \text{ mm} = 2.67\,\lambda_{\min}$)

(G) $E^{d}_{y;scat}$ (longer measurement time span)

(H) $E^{d}_{y;scat}$ (longer measurement time span; modified pristine structure)

(I) E^{d}_{y} (modified pristine structure)

Fig. 8.2.3.1 to 10 show the images obtained by the Born imaging algorithm in IE formalism in Case (A). It is observed that including the amplitude in the approximation of the incident field and Green's functions has significantly improved the images quality (only shown for the ε_{yy}-images). Notice how two false damages related to the typical shortcoming

of the imaging algorithm discussed in Chapter 6 have been imaged near the lower surface of the plate specially in the images obtained based on the maximum-energy arrival criterion.

Fig. 8.2.3.11 to 14 show the μ_{xx}-images for different measurement scenarios in Cases (B) and (C).

The effect of the measurement noise with SNR=5 on the μ_{xx}-images is illustrated in Fig. 8.2.3.15 and 16. These figures show that the algorithm is quite robust against the measurement noise.

To show the effect of the actuator/sensor spacing on the images quality, the μ_{xx}-images with $\Delta_{s,a} = 2\,\lambda_{\min}$, $2.67\,\lambda_{\min}$ are shown in Fig. 8.2.3.17 to 20. The artifacts resulting from the increase in the actuator/sensor spacing can be easily observed in these figures. Notice how the images obtained based on the first-arrival criterion are more sensitive to the actuator/sensor spacing.

To highlight the negative effect of the material discontinuity in the pristine structure on the images quality, the measurement time span has been increased from 164 ps to 196 ps in Case (G). The strong artifacts are observed in the μ_{xx}-image obtained based on the maximum-energy arrival criterion, Fig. 8.2.3.21. As discussed in Chapter 6, the images obtained based on the first-arrival criterion are not affected by the artifacts related to the material discontinuity in the actual pristine structure, see Fig. 8.2.3.22. Fig. 8.2.3.23 and 24 show the μ_{xx}-images when a modified pristine structure (a half-space homogenized orthotropic medium) has been used for the computation of the incident field and Green's functions in the image area. Notice how the artifacts related to the material discontinuity in the actual pristine structure have been eliminated in Fig. 8.2.3.23.

Fig. 8.2.3.25 and 26 illustrate the μ_{xx}-images when E_y^d instead of $E_{y;scat}^d$ has been used for damage imaging. It should be mentioned that the events associated with direct waves and reflections from the upper surface of the plate have been removed from E_y^d as a preprocessing step. Notice how the material interfaces of the laminated plate have been imaged in addition to the delaminations.

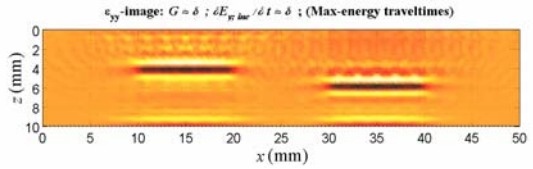

Fig. 8.2.3.1. Case (A); ε_{yy} -image; Both $G^{EJ}_{yy;b}$ and $\dot{E}_{y;inc}$ are approximated based on maximum-energy arrival criterion; Without amplitude;

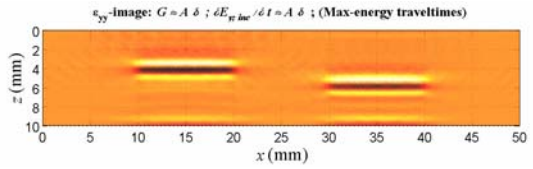

Fig. 8.2.3.2. Case (A); ε_{yy} -image; Both $G^{EJ}_{yy;b}$ and $\dot{E}_{y;inc}$ are approximated based on maximum-energy arrival criterion; With amplitude;

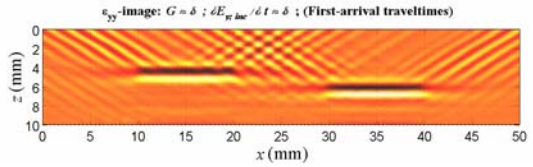

Fig. 8.2.3.3. Case (A); ε_{yy} -image; Both $G^{EJ}_{yy;b}$ and $\dot{E}_{y;inc}$ are approximated based on first-arrival criterion; Without amplitude;

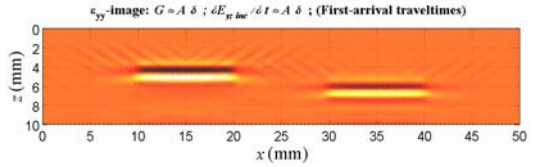

Fig. 8.2.3.4. Case (A); ε_{yy} -image; Both $G^{EJ}_{yy;b}$ and $\dot{E}_{y;inc}$ are approximated based on first-arrival criterion; With amplitude;

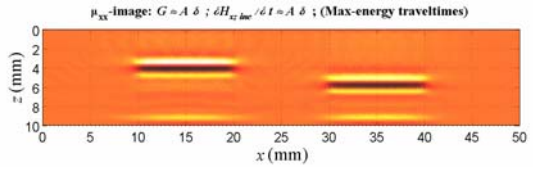

Fig. 8.2.3.5. Case (A); μ_{xx} -image; Both $G^{HJ}_{xy;b}$ and $\dot{H}_{x;inc}$ are approximated based on maximum-energy arrival criterion; With amplitude;

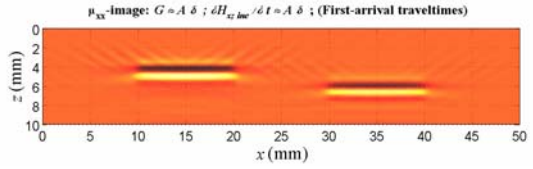

Fig. 8.2.3.6. Case (A); μ_{xx} -image; Both $G^{HJ}_{xy;b}$ and $\dot{H}_{x;inc}$ are approximated based on first-arrival criterion; With amplitude;

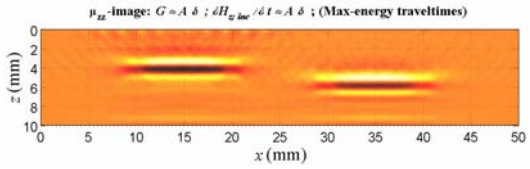

Fig. 8.2.3.7. Case (A); μ_{zz} -image; Both $G^{HJ}_{zy;b}$ and $\dot{H}_{z;inc}$ are approximated based on maximum-energy arrival criterion; With amplitude;

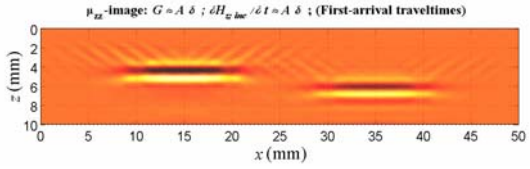

Fig. 8.2.3.8. Case (A); μ_{zz} -image; Both $G^{HJ}_{zy;b}$ and $\dot{H}_{z;inc}$ are approximated based on first-arrival criterion; With amplitude;

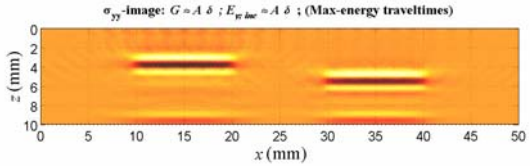

Fig. 8.2.3.9. Case (A); σ_{yy} -image; Both $G^{EJ}_{yy;b}$ and $E_{y;inc}$ are approximated based on maximum-energy arrival criterion; With amplitude;

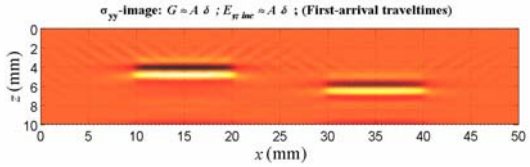

Fig. 8.2.3.10. Case (A); σ_{yy} -image; Both $G^{EJ}_{yy;b}$ and $E_{y;inc}$ are approximated based on first-arrival criterion; With amplitude;

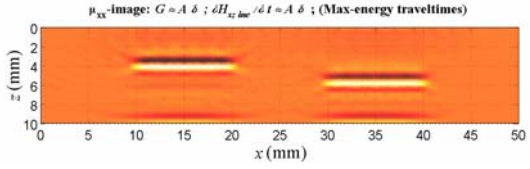

Fig. 8.2.3.11. Case (B); μ_{xx} -image; Both $G^{HM}_{xx;b}$ and $\dot{H}_{x;inc}$ are approximated based on maximum-energy arrival criterion; With amplitude;

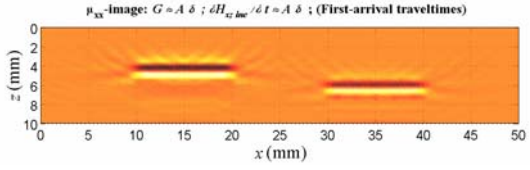

Fig. 8.2.3.12. Case (B); μ_{xx} -image; Both $G^{HM}_{xx;b}$ and $\dot{H}_{x;inc}$ are approximated based on first-arrival criterion; With amplitude;

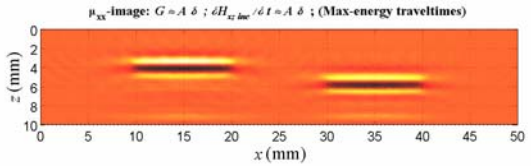

Fig. 8.2.3.13. Case (C); μ_{xx}-image; Both $G^{HM}_{xx;b}$ and $\dot{H}_{x;inc}$ are approximated based on maximum-energy arrival criterion; With amplitude;

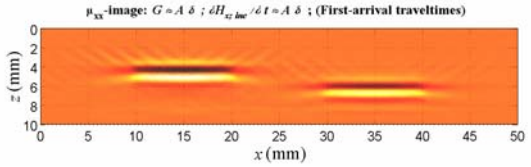

Fig. 8.2.3.14. Case (C); μ_{xx}-image; Both $G^{HM}_{xx;b}$ and $\dot{H}_{x;inc}$ are approximated based on first-arrival criterion; With amplitude;

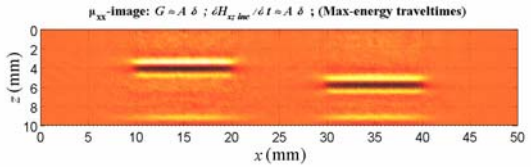

Fig. 8.2.3.15. Case (D); μ_{xx}-image; Both $G^{HJ}_{xy;b}$ and $\dot{H}_{x;inc}$ are approximated based on maximum-energy arrival criterion; With amplitude; Noisy data SNR=5;

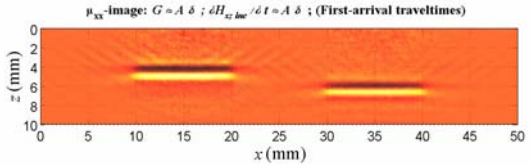

Fig. 8.2.3.16. Case (D); μ_{xx}-image; Both $G^{HJ}_{xy;b}$ and $\dot{H}_{x;inc}$ are approximated based on first-arrival criterion; With amplitude; Noisy data SNR=5;

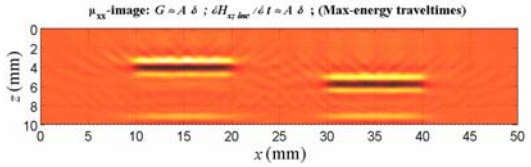

Fig. 8.2.3.17. Case (E); μ_{xx}-image; Both $G^{HJ}_{xy;b}$ and $\dot{H}_{x;inc}$ are approximated based on maximum-energy arrival criterion; With amplitude; $\Delta_{s,a} = 2\,\lambda_{\min}$;

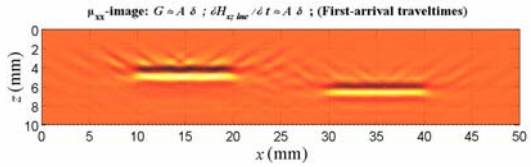

Fig. 8.2.3.18. Case (E); μ_{xx}-image; Both $G^{HJ}_{xy;b}$ and $\dot{H}_{x;inc}$ are approximated based on first-arrival criterion; With amplitude; $\Delta_{s,a} = 2\,\lambda_{\min}$;

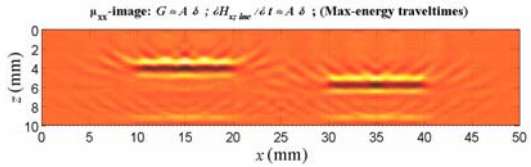

Fig. 8.2.3.19. Case (F); μ_{xx}-image; Both $G^{HJ}_{xy;b}$ and $\dot{H}_{x;inc}$ are approximated based on maximum-energy arrival criterion; With amplitude; $\Delta_{s,a} = 2.67\,\lambda_{\min}$;

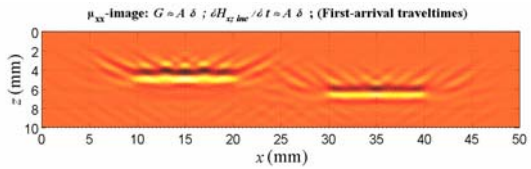

Fig. 8.2.3.20. Case (F); μ_{xx}-image; Both $G^{HJ}_{xy;b}$ and $\dot{H}_{x;inc}$ are approximated based on first-arrival criterion; With amplitude; $\Delta_{s,a} = 2.67\,\lambda_{\min}$;

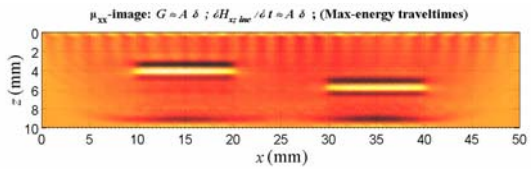

Fig. 8.2.3.21. Case (G); μ_{xx}-image; Both $G^{HM}_{xx;b}$ and $\dot{H}_{x;inc}$ are approximated based on maximum-energy arrival criterion; With amplitude; Longer data time span;

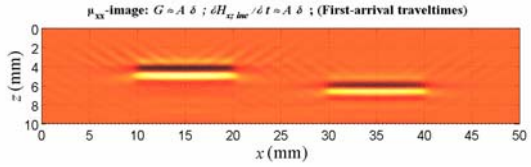

Fig. 8.2.3.22. Case (G); μ_{xx}-image; Both $G^{HM}_{xx;b}$ and $\dot{H}_{x;inc}$ are approximated based on first-arrival criterion; With amplitude; Longer data time span;

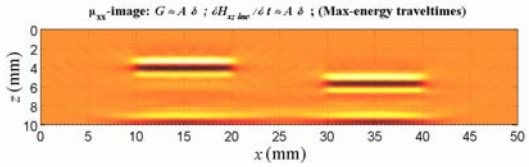

Fig. 8.2.3.23. Case (H); μ_{xx}-image; Both $G^{HM}_{xx;b}$ and $\dot{H}_{x;inc}$ are approximated based on maximum-energy arrival criterion; With amplitude; Longer data time span; Modified pristine structure;

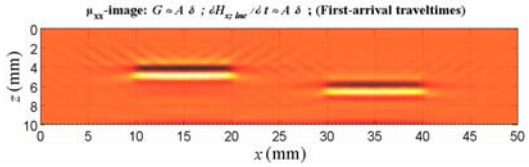

Fig. 8.2.3.24. Case (H); μ_{xx}-image; Both $G^{HM}_{xx;b}$ and $\dot{H}_{x;inc}$ are approximated based on first-arrival criterion; With amplitude; Longer data time span; Modified pristine structure;

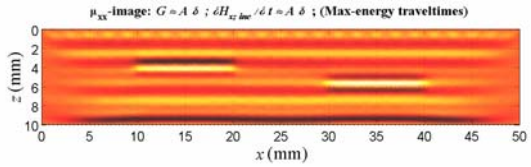

Fig. 8.2.3.25. Case (I); μ_{xx}-image; Both $G^{HM}_{xx;b}$ and $\dot{H}_{x;inc}$ are approximated based on maximum-energy arrival criterion; With amplitude; E^d_y; Modified pristine structure;

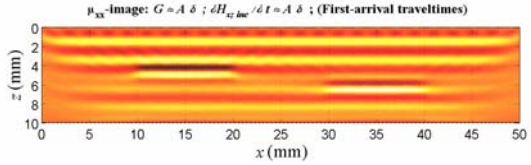

Fig. 8.2.3.26. Case (I); μ_{xx}-image; Both $G^{HM}_{xx;b}$ and $\dot{H}_{x;inc}$ are approximated based on first-arrival criterion; With amplitude; E^d_y; Modified pristine structure;

8.2.4. EM Migration (DE Formalism)

Eq. (7.2.1) - (7.2.4) represent the imaging formulas with zero-lag cross-correlation imaging condition. The corresponding imaging formulas with modified excitation-time imaging condition are Eq. (7.2.15) - (7.2.18); the imaging formulas with ordinary excitation-time imaging condition are easily obtained by setting the amplitudes to unity. Note that the migrated scattered fields are computed by FD discretization of differential equations (7.2.5) or (7.2.6) for the pristine structure depending on weather the sensor data is treated as sources or as time-dependent boundary conditions, respectively. Also, the application of both first and maximum-energy arrival criteria for the calculation of the traveltimes and amplitudes are examined.

To show the effects of different measurement scenarios, actuator/sensor spacing, measurement noise, and material discontinuity in the pristine structure on the quality of the images, the following cases are investigated (in all cases $\Delta_{s,a} = 2 \text{ mm} = 1.33\, \lambda_{\min}$ and data is treated as time-dependent boundary conditions, unless otherwise stated):

(A) $E^d_{y;scat}$ and $H^d_{x;scat}$

(B) $E^d_{y;scat}$ and $H^d_{x;scat}$ (as sources)

(C) Only $E^d_{y;scat}$

(D) Only $H^d_{x;scat}$

(E) $E^d_{y;scat}$ and $H^d_{x;scat}$ (contaminated by noise with SNR=5)

(F) $E^d_{y;scat}$ and $H^d_{x;scat}$ ($\Delta_{s,a} = 3 \text{ mm} = 2\, \lambda_{\min}$)

(G) $E^d_{y;scat}$ and $H^d_{x;scat}$ ($\Delta_{s,a} = 4 \text{ mm} = 2.67\, \lambda_{\min}$)

(H) $E^d_{y;scat}$ and $H^d_{x;scat}$ (longer measurement time span)

(I) $E^d_{y;scat}$ and $H^d_{x;scat}$ (longer measurement time span; modified pristine structure)

(J) E_y^d and H_x^d (modified pristine structure)

Fig. 8.2.4.1 to 14 show the images obtained by the EM migration algorithm in DE formalism with different imaging conditions in Case (A). It is observed that the images obtained by the modified excitation-time imaging condition with either first or maximum-energy arrival criterion for the calculation of the traveltimes and amplitudes are comparable in quality to the images obtained by the zero-lag cross-correlation imaging condition. Also, the modified excitation-time imaging condition has significantly improved the images compared to the images obtained by the ordinary excitation-time imaging condition (only shown for the ε_{yy}-images). Notice how two false damages related to the typical shortcoming of the algorithm have been imaged near the lower surface of the plate.

When the sensor data has been treated as sources instead of time-dependent boundary conditions in the EM migration in Case (B), the quality of images has been deteriorated, specially in the μ_{zz}-images as shown in Fig. 8.2.4.15 to 18.

The usage of only $E_{y;scat}^d$ or $H_{x;scat}^d$ instead of both in the algorithm in Cases (C) and (D) has still provided good damage identification as shown in Fig. 8.2.4.19 to 22.

The effect of the measurement noise with SNR=5 on the μ_{xx}-images is illustrated in Fig. 8.2.4.23 and 24. These figures show that the algorithm is quite robust against the measurement noise.

To show the effect of the actuator/sensor spacing on the images quality, the μ_{xx}-images with $\Delta_{s,a} = 2\,\lambda_{\min}$, $2.67\,\lambda_{\min}$ are shown in Fig. 8.2.4.25 to 28. The artifacts resulting from the increase in the actuator/sensor spacing can be easily observed in these figures.

To highlight the negative effect of the material discontinuity in the pristine structure on the images quality, the measurement time span has been increased from 164 ps to 196 ps in Case (H). The strong artifacts can be clearly observed in Fig. 8.2.4.29 and 30. The artifacts related to the material discontinuity in the actual pristine structure have been eliminated in Fig. 8.2.4.31 and 32 when a modified pristine structure (a half-space homogenized orthotropic medium) has been used for the computation of the incident and migrated fields in

the image area. Note that the false images near the lower surface of the plate, related to the typical shortcoming of the imaging algorithm mentioned in Chapter 6, cannot be eliminated by this approach.

Fig. 8.2.4.33 and 34 illustrate the μ_{xx}-images when E_y^d and H_x^d instead of $E_{y;scat}^d$ and $H_{x;scat}^d$ have been used for damage imaging. It should be mentioned that the events associated with direct waves and reflections from the upper surface of the plate have been removed from E_y^d and H_x^d as a preprocessing step. Notice how the material interfaces of the laminated plate have been imaged in addition to the delaminations.

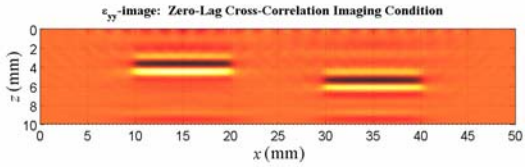

Fig. 8.2.4.1. Case (A); ε_{yy}-image; Zero-lag cross-correlation imaging condition;

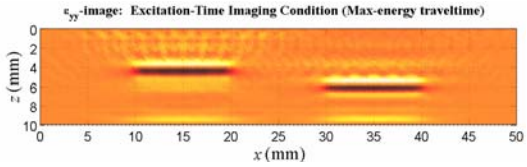

Fig. 8.2.4.2. Case (A); ε_{yy}-image; Excitation-time imaging condition (Max-energy arrival);

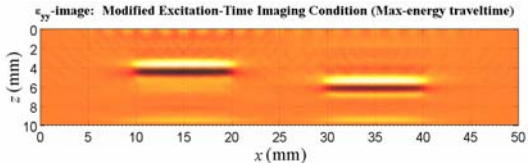

Fig. 8.2.4.3. Case (A); ε_{yy}-image; Modified excitation-time imaging condition (Max-energy arrival);

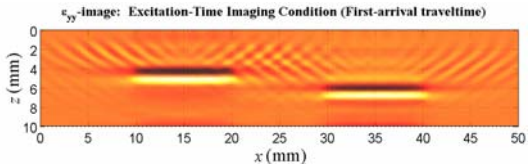

Fig. 8.2.4.4. Case (A); ε_{yy}-image; Excitation-time imaging condition (First-arrival);

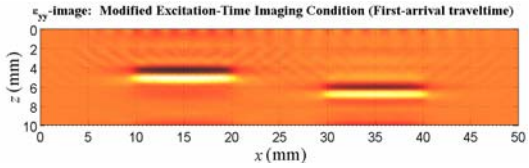

Fig. 8.2.4.5. Case (A); ε_{yy}-image; Modified excitation-time imaging condition (First-arrival);

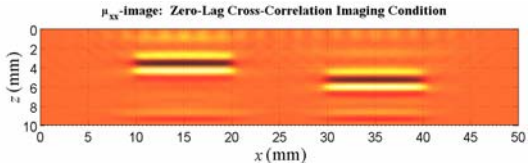

Fig. 8.2.4.6. Case (A); μ_{xx}-image; Zero-lag cross-correlation imaging condition;

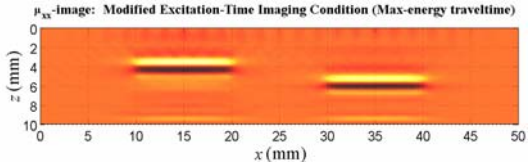

Fig. 8.2.4.7. Case (A); μ_{xx}-image; Modified excitation-time imaging condition (Max-energy arrival);

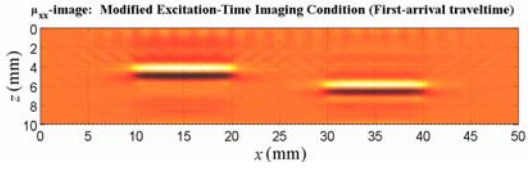

Fig. 8.2.4.8. Case (A); μ_{xx}-image; Modified excitation-time imaging condition (First-arrival);

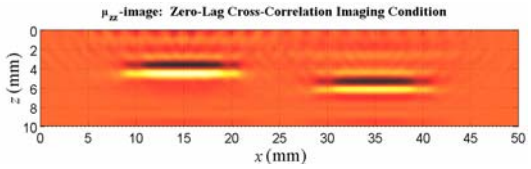

Fig. 8.2.4.9. Case (A); μ_{zz} -image; Zero-lag cross-correlation imaging condition;

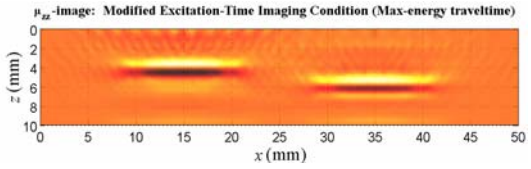

Fig. 8.2.4.10. Case (A); μ_{zz} -image; Modified excitation-time imaging condition (Max-energy arrival);

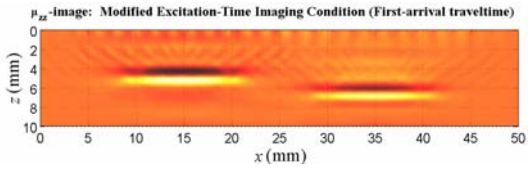

Fig. 8.2.4.11. Case (A); μ_{zz} -image; Modified excitation-time imaging condition (First-arrival);

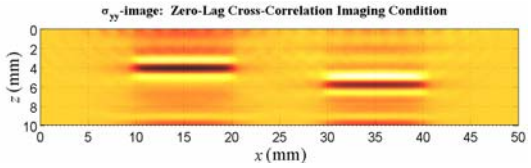

Fig. 8.2.4.12. Case (A); σ_{yy} -image; Zero-lag cross-correlation imaging condition;

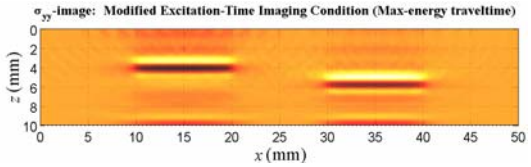

Fig. 8.2.4.13. Case (A); σ_{yy} -image; Modified excitation-time imaging condition (Max-energy arrival);

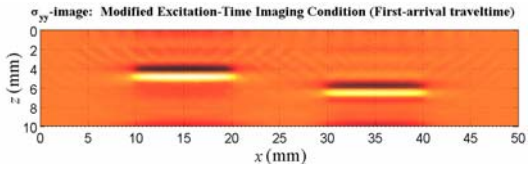

Fig. 8.2.4.14. Case (A); σ_{yy} -image; Modified excitation-time imaging condition (First-arrival);

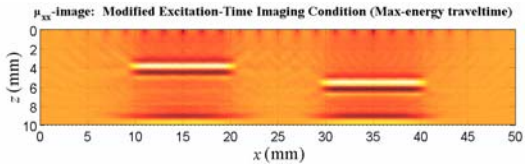

Fig. 8.2.4.15. Case (B); μ_{xx} -image; Modified excitation-time imaging condition (Max-energy arrival); Data treated as sources;

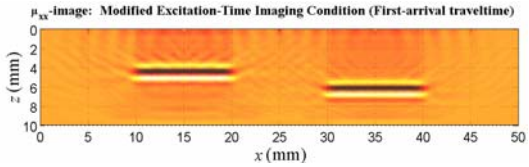

Fig. 8.2.4.16. Case (B); μ_{xx} -image; Modified excitation-time imaging condition (First-arrival); Data treated as sources;

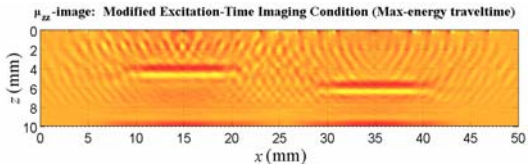

Fig. 8.2.4.17. Case (B); μ_{zz} -image; Modified excitation-time imaging condition (Max-energy arrival); Data treated as sources;

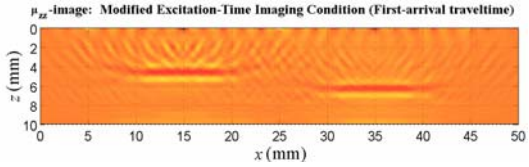

Fig. 8.2.4.18. Case (B); μ_{zz} -image; Modified excitation-time imaging condition (First-arrival); Data treated as sources;

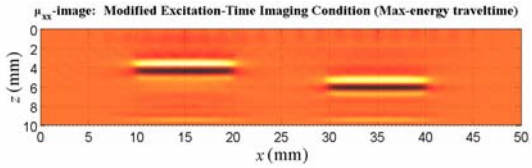

Fig. 8.2.4.19. Case (C); μ_{xx} -image; Modified excitation-time imaging condition (Max-energy arrival); Only $E^{d}_{y;scat}$ as BC;

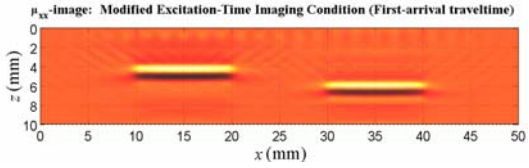

Fig. 8.2.4.20. Case (C); μ_{xx} -image; Modified excitation-time imaging condition (First-arrival); Only $E^{d}_{y;scat}$ as BC;

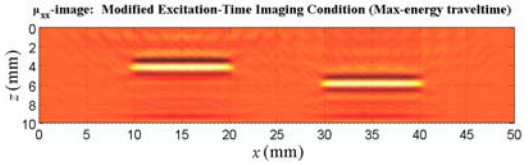

Fig. 8.2.4.21. Case (D); μ_{xx} -image; Modified excitation-time imaging condition (Max-energy arrival); Only $H^{d}_{x;scat}$ as BC;

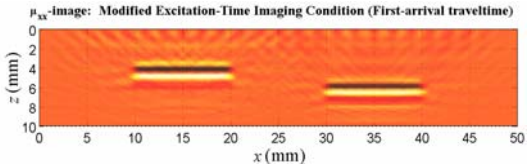

Fig. 8.2.4.22. Case (D); μ_{xx} -image; Modified excitation-time imaging condition (First-arrival); Only $H^{d}_{x;scat}$ as BC;

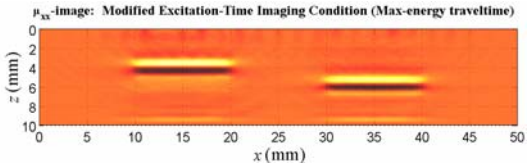

Fig. 8.2.4.23. Case (E); μ_{xx} -image; Modified excitation-time imaging condition (Max-energy arrival); Noisy data SNR=5;

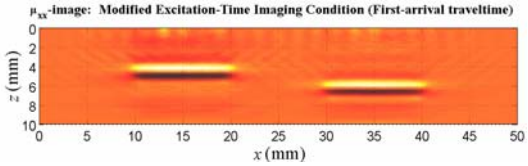

Fig. 8.2.4.24. Case (E); μ_{xx} -image; Modified excitation-time imaging condition (First-arrival); Noisy data SNR=5;

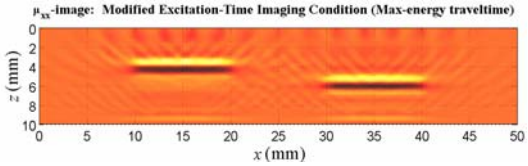

Fig. 8.2.4.25. Case (F); μ_{xx} -image; Modified excitation-time imaging condition (Max-energy arrival); $\Delta_{s,a} = 2\,\lambda_{\min}$;

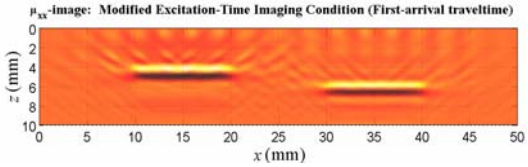

Fig. 8.2.4.26. Case (F); μ_{xx} -image; Modified excitation-time imaging condition (First-arrival); $\Delta_{s,a} = 2\,\lambda_{\min}$;

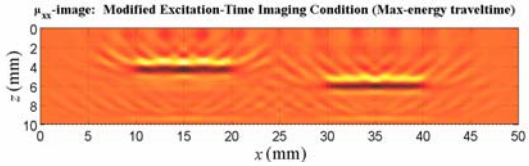

Fig. 8.2.4.27. Case (G); μ_{xx} -image; Modified excitation-time imaging condition (Max-energy arrival); $\Delta_{s,a} = 2.67\,\lambda_{\min}$;

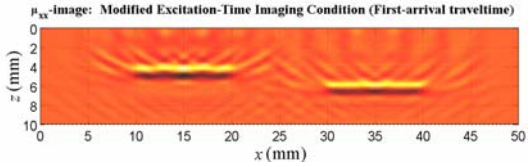

Fig. 8.2.4.28. Case (G); μ_{xx} -image; Modified excitation-time imaging condition (First-arrival); $\Delta_{s,a} = 2.67\,\lambda_{\min}$;

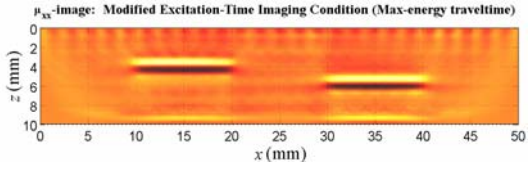

Fig. 8.2.4.29. Case (H); μ_{xx} -image; Modified excitation-time imaging condition (Max-energy arrival); Longer data time span;

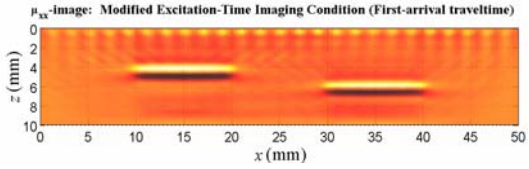

Fig. 8.2.4.30. Case (H); μ_{xx} -image; Modified excitation-time imaging condition (First-arrival); Longer data time span;

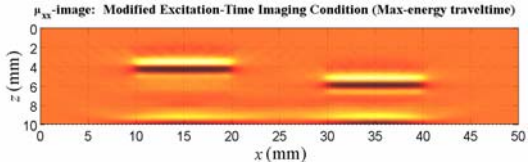

Fig. 8.2.4.31. Case (I); μ_{xx} -image; Modified excitation-time imaging condition (Max-energy arrival); Longer data time span; Modified pristine structure;

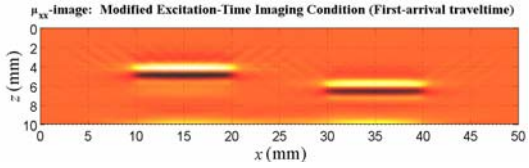

Fig. 8.2.4.32. Case (I); μ_{xx} -image; Modified excitation-time imaging condition (First-arrival); Longer data time span; Modified pristine structure;

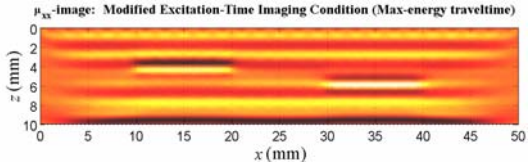

Fig. 8.2.4.33. Case (J); μ_{xx}-image; Modified excitation-time imaging condition (Max-energy arrival); E_y^d and H_x^d; Modified pristine structure;

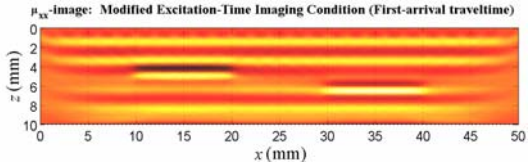

Fig. 8.2.4.34. Case (J); μ_{xx}-image; Modified excitation-time imaging condition (First-arrival); E_y^d and H_x^d; Modified pristine structure;

8.2.5. EM Migration (DE Formalism; Poststack)

The three different images for each type of measurement can be obtained by applying the zero-time imaging condition to the migrated scattered field components $E^m_{y;scat}$, $H^m_{x;scat}$, and $H^m_{z;scat}$ computed by FD discretization of differential equations (7.2.5) or (7.2.6) for a 2:1 scaled pristine structure depending on weather the sensor data is treated as sources or as time-dependent boundary conditions, respectively.

To show the effects of different measurement scenarios, actuator/sensor spacing, measurement noise, and material discontinuity in the pristine structure on the quality of the images, the following cases are investigated (in all cases $\Delta = 1\text{ mm} = 0.67\,\lambda_{\min}$ and the data is treated as time-dependent boundary conditions, unless otherwise stated):

(A) $E^d_{y;scat}$ and $H^d_{x;scat}$

(B) $E^d_{y;scat}$ and $H^d_{x;scat}$ (treated as sources)

(C) Only $E^d_{y;scat}$

(D) Only $H^d_{x;scat}$

(E) $E^d_{y;scat}$ and $H^d_{x;scat}$ (contaminated by noise with SNR=5)

(F) $E^d_{y;scat}$ and $H^d_{x;scat}$ ($\Delta = 1.5\text{ mm} = \lambda_{\min}$)

(G) $E^d_{y;scat}$ and $H^d_{x;scat}$ ($\Delta = 2\text{ mm} = 1.33\,\lambda_{\min}$)

(H) $E^d_{y;scat}$ and $H^d_{x;scat}$ (longer measurement time span)

(I) $E^d_{y;scat}$ and $H^d_{x;scat}$ (longer measurement time span; modified pristine structure)

(J) E^d_y and H^d_x (modified pristine structure)

Fig. 8.2.5.1 to 3 show the images obtained by the EM migration algorithm in DE formalism using the poststack concept in Case (A). The $H^m_{x;scat}$-image has provided the best

damage identification. In addition, the delaminations have not been completely imaged in the $H^m_{z;scat}$-image. Notice how two false damages related to the typical shortcoming of the imaging algorithm have been imaged near the lower surface of the plate.

Treating the data as sources instead of time-dependent boundary conditions in the EM migration algorithm in Case (B), has not changed the quality of images tangibly as shown in Fig. 8.2.5.4 to 6.

The usage of only $E^d_{y;scat}$ or $H^d_{x;scat}$ instead of both in the algorithm in Cases (C) and (D) has still provided good damage identification as shown in Fig. 8.2.5.7 to 12.

The effect of the measurement noise with SNR=5 on the $H^m_{x;scat}$-image is shown in Fig. 8.2.5.13. This figure shows that the algorithm is quite robust against the measurement noise. Fig. 8.2.5.14 and 15 show the $H^m_{x;scat}$-images with the actuator/sensor spacings of $\Delta = \lambda_{\min}$, $1.33\,\lambda_{\min}$ in Cases (F) and (G). The artifacts resulting from the increase in the actuator/sensor spacing can be easily observed in these figures.

To highlight the effect of the material discontinuity in the pristine structure on the images quality, the measurement time span has been increased from 164 ps to 196 ps, Fig. 8.2.5.16. This image has not been affected by the artifacts related to the material discontinuity as opposed to the corresponding image in the prestack form of the algorithm. Fig. 8.2.5.17 also shows the $H^m_{x;scat}$-image when a modified pristine structure (a half-space homogenized orthotropic medium) has been used for the computation of the migrated field. It is concluded that the poststack images are more robust than the prestack images to the artifacts related to the material discontinuity in the pristine structure. This is because the incident field in the image area is not needed in constructing the poststack images. The difference between data collected in common-source and zero-offset configurations may be another reason.

Fig. 8.2.5.18 illustrates the $H^m_{x;scat}$-image when E^d_y and H^d_x instead of $E^d_{y;scat}$ and $H^d_{x;scat}$ have been used for damage imaging. It should be mentioned that the events associated with direct waves and reflections from the upper surface of the plate have been removed

from E_y^d and H_x^d as a preprocessing step. Notice how the material interfaces of the plate have been imaged in addition to the delaminations.

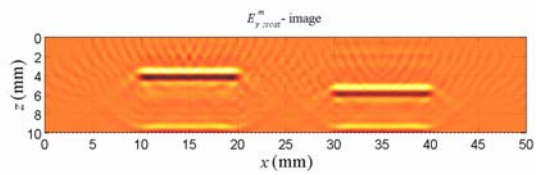

Fig. 8.2.5.1. Case (A); $E^m_{y;scat}$ -image obtained by poststack EM migration;

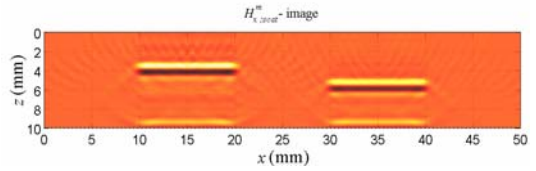

Fig. 8.2.5.2. Case (A); $H^m_{x;scat}$ -image obtained by poststack EM migration;

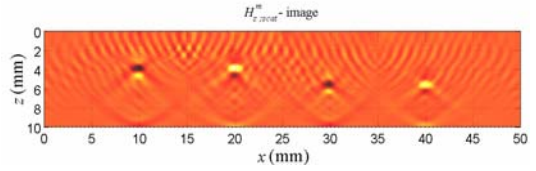

Fig. 8.2.5.3. Case (A); $H^m_{z;scat}$ -image obtained by poststack EM migration;

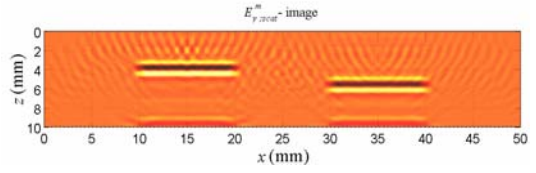

Fig. 8.2.5.4. Case (B); $E^m_{y;scat}$ -image obtained by poststack EM migration; Data treated as sources;

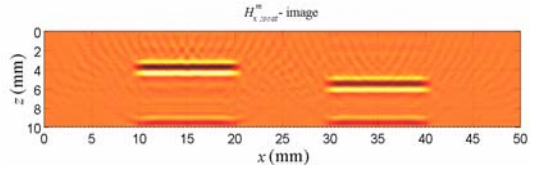

Fig. 8.2.5.5. Case (B); $H^m_{x;scat}$ -image obtained by poststack EM migration; Data treated as sources;

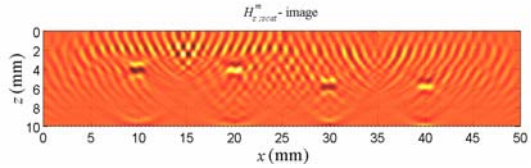

Fig. 8.2.5.6. Case (B); $H^m_{z;scat}$ -image obtained by poststack EM migration; Data treated as sources;

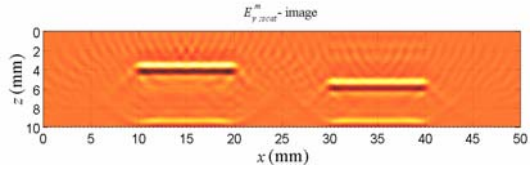

Fig. 8.2.5.7. Case (C); $E^m_{y;scat}$ -image obtained by poststack EM migration; Only $E^d_{y;scat}$ as BC's;

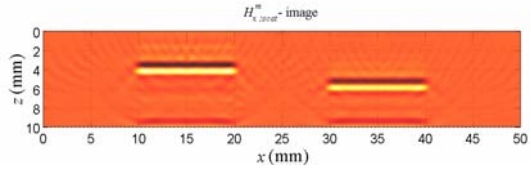

Fig. 8.2.5.8. Case (C); $H^m_{x;scat}$ -image obtained by poststack EM migration; Only $E^d_{y;scat}$ as BC's;

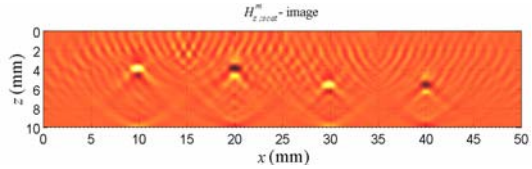

Fig. 8.2.5.9. Case (C); $H^m_{z;scat}$ -image obtained by poststack EM migration; Only $E^d_{y;scat}$ as BC's;

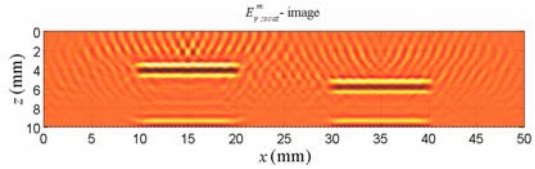

Fig. 8.2.5.10. Case (D); $E^m_{y;scat}$ -image obtained by poststack EM migration; Only $H^d_{x;scat}$ as BC's;

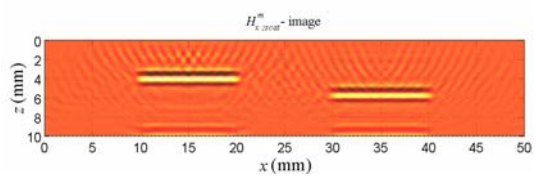

Fig. 8.2.5.11. Case (D); $H^m_{x;scat}$ -image obtained by poststack EM migration; Only $H^d_{x;scat}$ as BC's;

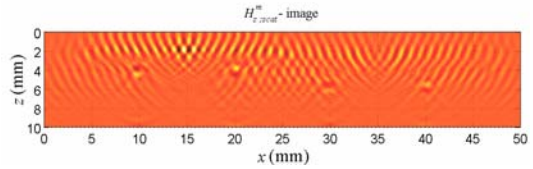

Fig. 8.2.5.12. Case (D); $H^m_{z;scat}$ -image obtained by poststack EM migration; Only $H^d_{x;scat}$ as BC's;

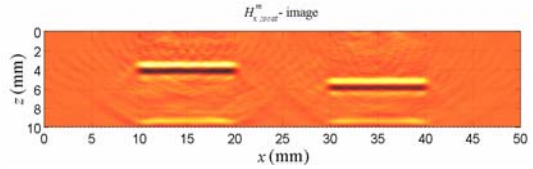

Fig. 8.2.5.13. Case (E); $H^m_{x;scat}$ -image obtained by poststack EM migration; Noisy data SNR=5;

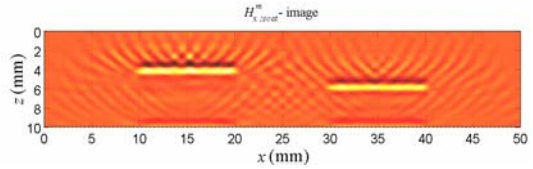

Fig. 8.2.5.14. Case (F); $H^m_{x;scat}$ -image obtained by poststack EM migration; $\Delta = \lambda_{\min}$;

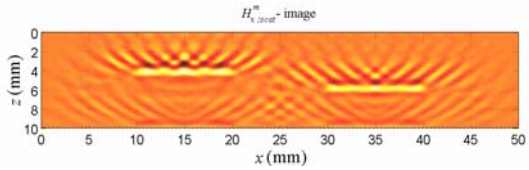

Fig. 8.2.5.15. Case (G); $H^m_{x;scat}$ -image obtained by poststack EM migration; $\Delta = 1.33\lambda_{\min}$;

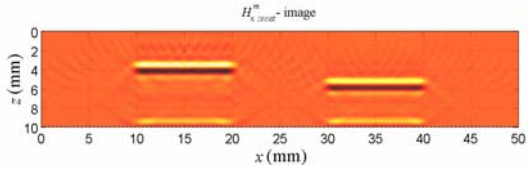

Fig. 8.2.5.16. Case (H); $H^m_{x;scat}$ -image obtained by poststack EM migration; Longer data time span;

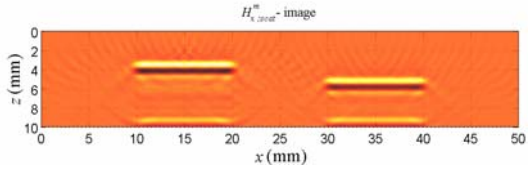

Fig. 8.2.5.17. Case (I); $H^m_{x;scat}$ -image obtained by poststack EM migration; Longer data time span; Modified pristine structure;

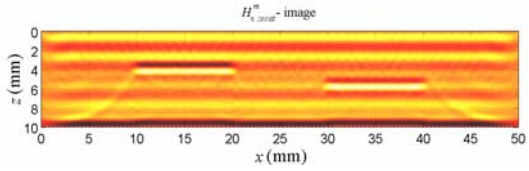

Fig. 8.2.5.18. Case (J); $H^m_{x;scat}$ -image obtained by poststack EM migration; E^d_y and H^d_x ; Modified pristine structure;

8.2.6. EM Migration (IE Formalism)

Eq. (7.2.22) - (7.2.25) represent the real-time imaging formulas in the IE formalism of the EM migration algorithm. The amplitudes and traveltimes of the incident field and Green's functions are computed by FD discretization of ordinary Maxwell's equations for the pristine structure. The application of both first and maximum-energy arrival criteria for the calculation of these traveltimes and amplitudes are examined as well.

To show the effects of different measurement scenarios, actuator/sensor spacing, measurement noise, and material discontinuity in the pristine structure on the quality of the images, the following cases are investigated (in all cases $\Delta_{s,a} = 2 \text{ mm} = 1.33\,\lambda_{\min}$, unless otherwise stated):

(A) $E^d_{y;scat}$ and $H^d_{x;scat}$

(B) Only $E^d_{y;scat}$

(C) Only $H^d_{x;scat}$

(D) $E^d_{y;scat}$ and $H^d_{x;scat}$ (contaminated by noise with SNR=5)

(E) $E^d_{y;scat}$ and $H^d_{x;scat}$ ($\Delta_{s,a} = 3 \text{ mm} = 2\,\lambda_{\min}$)

(F) $E^d_{y;scat}$ and $H^d_{x;scat}$ ($\Delta_{s,a} = 4 \text{ mm} = 2.67\,\lambda_{\min}$)

(G) $E^d_{y;scat}$ and $H^d_{x;scat}$ (longer measurement time span)

(H) $E^d_{y;scat}$ and $H^d_{x;scat}$ (longer measurement time span; modified pristine structure)

(I) E^d_y and H^d_x (modified pristine structure)

Fig. 8.2.6.1 to 10 show the images obtained by the EM migration algorithm in IE formalism in Case (A). It is observed that by excluding the amplitude in the approximation of the incident field and Green's functions, correct damage identification cannot be obtained (only shown for the ε_{yy}-images). In addition, the images obtained based on the first-arrival

or maximum-energy arrival criterion for the calculation of the traveltimes and amplitudes have provided close damage identification. Notice how two false damages related to the typical shortcoming of the imaging algorithm have been imaged near the lower surface of the plate.

Fig. 8.2.6.11 to 14 show μ_{xx}-images when only $E^d_{y;scat}$ or $H^d_{x;scat}$ instead of both is used in the algorithm. Notice that the images in Case (C) are quite similar to corresponding images in Case (A).

Fig. 8.2.6.15 and 16 illustrate the effect of the measurement noise with SNR=5 on the μ_{xx}-images. These figures show that the algorithm is quite robust against the measurement noise.

To show the effect of the actuator/sensor spacing on the images quality, the μ_{xx}-images with $\Delta_{s,a} = 2\,\lambda_{\min}$, $2.67\,\lambda_{\min}$ are shown in Fig. 8.2.6.17 to 20. The artifacts resulting from the increase in the actuator/sensor spacing can be easily observed in these figures. Notice that the images obtained based on the first-arrival criterion are more sensitive to the actuator/sensor spacing.

To highlight the negative effect of the material discontinuity in the pristine structure on the images quality, the measurement time span has been increased from 164 ps to 196 ps in Case (G). The strong artifacts can be observed in the μ_{xx}-image obtained based on the maximum-energy arrival criterion, Fig. 8.2.6.21. As discussed in Chapter 6, the images based on the first-arrival criterion are not affected by the artifacts related to the material discontinuity in the pristine structure, see Fig. 8.2.6.22. Fig. 8.2.6.23 and 24 show the μ_{xx}-images when a modified pristine structure (a half-space homogenized orthotropic medium) has been used for the computation of the incident field and Green's functions in the image area. Notice how the artifacts related to the material discontinuity in the pristine structure have been eliminated in Fig. 8.2.6.23.

Fig. 8.2.6.25 and 26 illustrate the μ_{xx}-images when E^d_y and H^d_x instead of $E^d_{y;scat}$ and $H^d_{x;scat}$ have been used for damage imaging. It should be mentioned that the events associated

with direct waves and reflections from the upper surface of the plate have been removed from E_y^d and H_x^d as a preprocessing step. Notice how the material interfaces of the laminated plate have been imaged in addition to the delaminations.

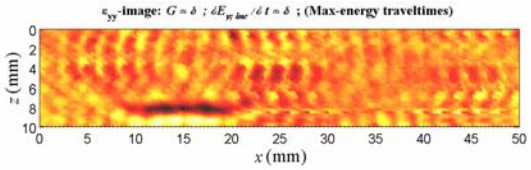

Fig. 8.2.6.1. Case (A); ε_{yy} -image; All $G_{yx;b}^{EM}$, $G_{yy;b}^{EJ}$, and $\dot{E}_{y;inc}$ are approximated based on maximum-energy arrival criterion; Without amplitude;

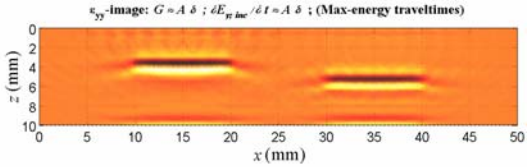

Fig. 8.2.6.2. Case (A); ε_{yy} -image; All $G_{yx;b}^{EM}$, $G_{yy;b}^{EJ}$, and $\dot{E}_{y;inc}$ are approximated based on maximum-energy arrival criterion; With amplitude;

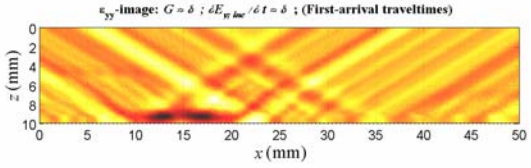

Fig. 8.2.6.3. Case (A); ε_{yy} -image; All $G_{yx;b}^{EM}$, $G_{yy;b}^{EJ}$, and $\dot{E}_{y;inc}$ are approximated based on first-arrival criterion; Without amplitude;

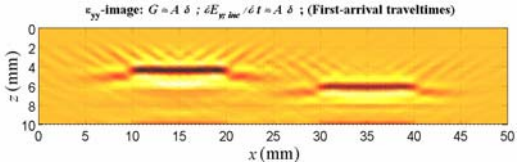

Fig. 8.2.6.4. Case (A); ε_{yy} -image; All $G_{yx;b}^{EM}$, $G_{yy;b}^{EJ}$, and $\dot{E}_{y;inc}$ are approximated based on first-arrival criterion; With amplitude;

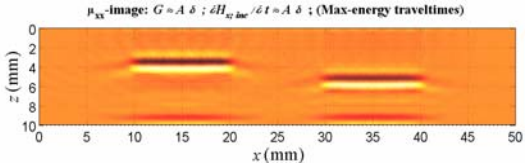

Fig. 8.2.6.5. Case (A); μ_{xx} -image; All $G_{xy;b}^{HJ}$, $G_{xx;b}^{HM}$, and $\dot{H}_{x;inc}$ are approximated based on maximum-energy arrival criterion; With amplitude;

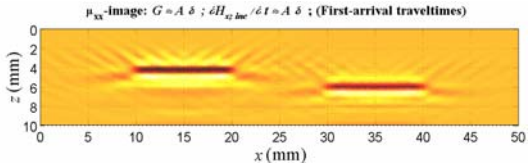

Fig. 8.2.6.6. Case (A); μ_{xx} -image; All $G_{xy;b}^{HJ}$, $G_{xx;b}^{HM}$, and $\dot{H}_{x;inc}$ are approximated based on first-arrival criterion; With amplitude;

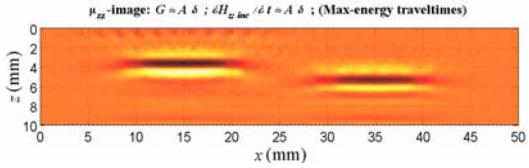

Fig. 8.2.6.7. Case (A); μ_{zz} -image; All $G_{zy;b}^{HJ}$, $G_{zx;b}^{HM}$, and $\dot{H}_{z;inc}$ are approximated based on maximum-energy arrival criterion; With amplitude;

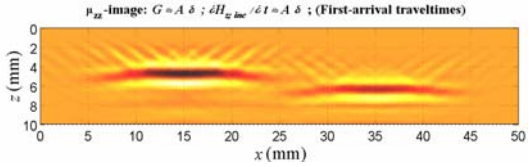

Fig. 8.2.6.8. Case (A); μ_{zz} -image; All $G_{zy;b}^{HJ}$, $G_{zx;b}^{HM}$, and $\dot{H}_{z;inc}$ are approximated based on first-arrival criterion; With amplitude;

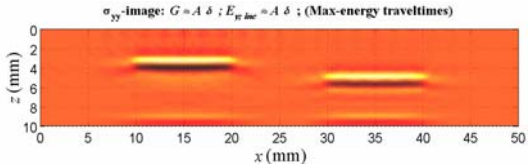

Fig. 8.2.6.9. Case (A); σ_{yy} -image; All $G_{yx;b}^{EM}$, $G_{yy;b}^{EJ}$, and $E_{y;inc}$ are approximated based on maximum-energy arrival criterion; With amplitude;

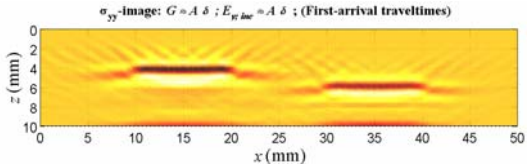

Fig. 8.2.6.10. Case (A); σ_{yy} -image; All $G_{yx;b}^{EM}$, $G_{yy;b}^{EJ}$, and $E_{y;inc}$ are approximated based on first-arrival criterion; With amplitude;

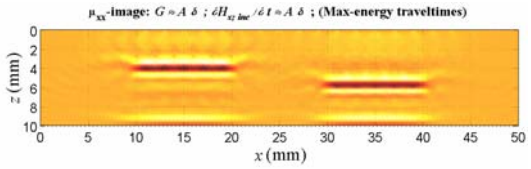

Fig. 8.2.6.11. Case (B); μ_{xx}-image; Both $G^{HM}_{xx;b}$ and $\dot{H}_{x;inc}$ are approximated based on maximum-energy arrival criterion; With amplitude; Only $E^{d}_{y;scat}$;

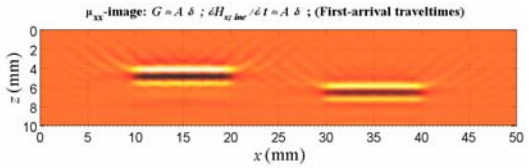

Fig. 8.2.6.12. Case (B); μ_{xx}-image; Both $G^{HM}_{xx;b}$ and $\dot{H}_{x;inc}$ are approximated based on first-arrival criterion; With amplitude; Only $E^{d}_{y;scat}$;

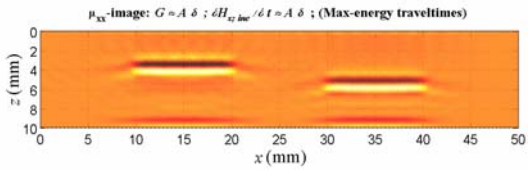

Fig. 8.2.6.13. Case (C); μ_{xx}-image; Both $G^{HJ}_{xy;b}$ and $\dot{H}_{x;inc}$ are approximated based on maximum-energy arrival criterion; With amplitude; Only $H^{d}_{x;scat}$;

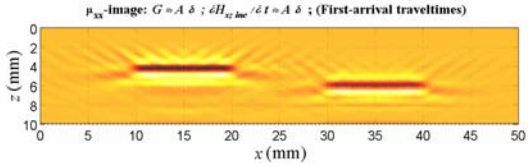

Fig. 8.2.6.14. Case (C); μ_{xx}-image; Both $G^{HJ}_{xy;b}$ and $\dot{H}_{x;inc}$ are approximated based on first-arrival criterion; With amplitude; Only $H^{d}_{x;scat}$;

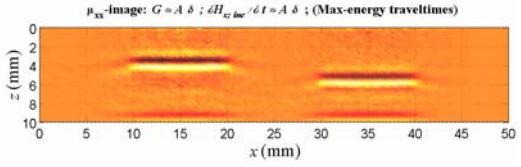

Fig. 8.2.6.15. Case (D); μ_{xx}-image; All $G^{HJ}_{xy;b}$, $G^{HM}_{xx;b}$, and $\dot{H}_{x;inc}$ are approximated based on maximum-energy arrival criterion; With amplitude; Noisy data SNR=5;

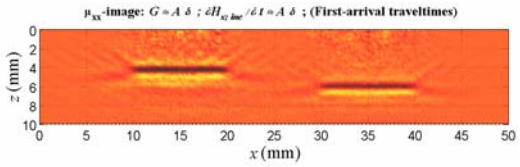

Fig. 8.2.6.16. Case (D); μ_{xx}-image; All $G^{HJ}_{xy;b}$, $G^{HM}_{xx;b}$, and $\dot{H}_{x;inc}$ are approximated based on first-arrival criterion; With amplitude; Noisy data SNR=5;

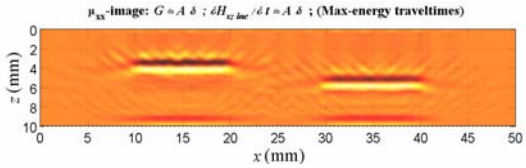

Fig. 8.2.6.17. Case (E); μ_{xx}-image; All $G^{HJ}_{xy;b}$, $G^{HM}_{xx;b}$, and $\dot{H}_{x;inc}$ are approximated based on maximum-energy arrival criterion; With amplitude; $\Delta_{s,a} = 2\,\lambda_{\min}$;

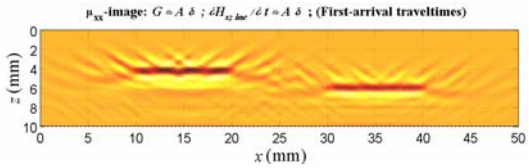

Fig. 8.2.6.18. Case (E); μ_{xx}-image; All $G^{HJ}_{xy;b}$, $G^{HM}_{xx;b}$, and $\dot{H}_{x;inc}$ are approximated based on first-arrival criterion; With amplitude; $\Delta_{s,a} = 2\,\lambda_{\min}$;

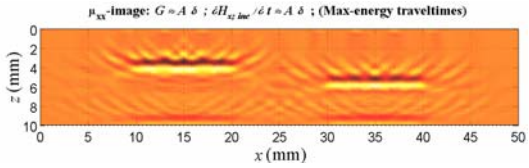

Fig. 8.2.6.19. Case (F); μ_{xx}-image; All $G^{HJ}_{xy;b}$, $G^{HM}_{xx;b}$, and $\dot{H}_{x;inc}$ are approximated based on maximum-energy arrival criterion; With amplitude; $\Delta_{s,a} = 2.67\,\lambda_{\min}$;

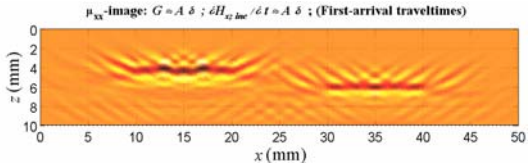

Fig. 8.2.6.20. Case (F); μ_{xx}-image; All $G^{HJ}_{xy;b}$, $G^{HM}_{xx;b}$, and $\dot{H}_{x;inc}$ are approximated based on first-arrival criterion; With amplitude; $\Delta_{s,a} = 2.67\,\lambda_{\min}$;

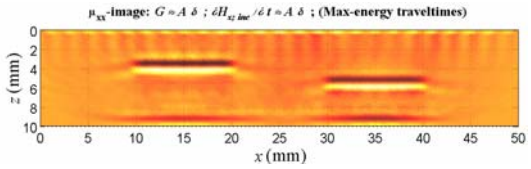

Fig. 8.2.6.21. Case (G); μ_{xx} -image; All $G^{HJ}_{xy;b}$, $G^{HM}_{xx;b}$, and $\dot{H}_{x;inc}$ are approximated based on maximum-energy arrival criterion; With amplitude; Longer data time span;

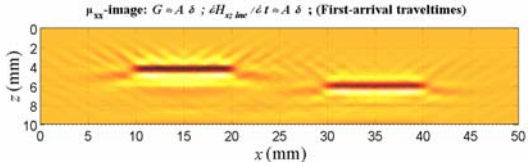

Fig. 8.2.6.22. Case (G); μ_{xx} -image; All $G^{HJ}_{xy;b}$, $G^{HM}_{xx;b}$, and $\dot{H}_{x;inc}$ are approximated based on first-arrival criterion; With amplitude; Longer data time span;

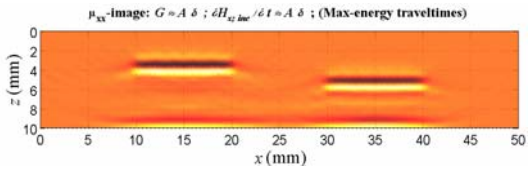

Fig. 8.2.6.23. Case (H); μ_{xx} -image; All $G^{HJ}_{xy;b}$, $G^{HM}_{xx;b}$, and $\dot{H}_{x;inc}$ are approximated based on maximum-energy arrival criterion; With amplitude; Longer data time span; Modified pristine structure;

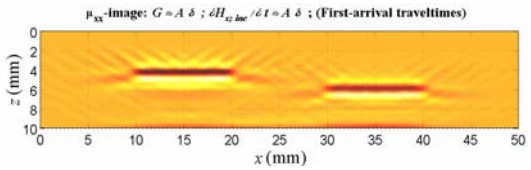

Fig. 8.2.6.24. Case (H); μ_{xx} -image; All $G^{HJ}_{xy;b}$, $G^{HM}_{xx;b}$, and $\dot{H}_{x;inc}$ are approximated based on first-arrival criterion; With amplitude; Longer data time span; Modified pristine structure;

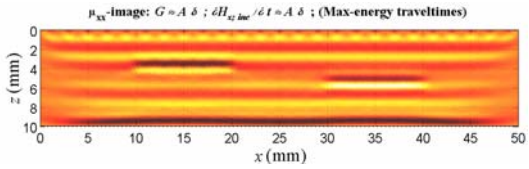

Fig. 8.2.6.25. Case (I); μ_{xx} -image; All $G^{HJ}_{xy;b}$, $G^{HM}_{xx;b}$, and $\dot{H}_{x;inc}$ are approximated based on maximum-energy arrival criterion; With amplitude; E^d_y and H^d_x; Modified pristine structure;

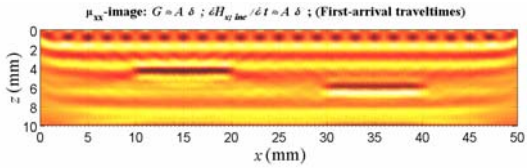

Fig. 8.2.6.26. Case (I); μ_{xx} -image; All $G^{HJ}_{xy;b}$, $G^{HM}_{xx;b}$, and $\dot{H}_{x;inc}$ are approximated based on first-arrival criterion; With amplitude; E^d_y and H^d_x; Modified pristine structure;

9. Conclusions

Knowing that identifying geometries of damages with efficient and effective algorithms is the primary and minimum goal of a structural health monitoring (SHM) system, electromagnetic (EM) migration and Born imaging algorithms have been formulated for real-time 3-D damage imaging of structures using EM waves. These algorithms have been driven in both differential equation (DE) and integral equation (IE) formalisms in time-domain for inhomogeneous anisotropic and lossy structures. To speed up the imaging process, various approximations on the incident field and the Green's functions of the pristine structure have been introduced and their effectiveness has also been examined. Moreover, the images obtained using the poststack concept has been compared with the prestack images.

To show the performance of the DE and IE formalisms of the imaging algorithms, numerical simulations in 2-D transverse magnetic (TM) case for a reinforced concrete slab and a glass/epoxy composite plate with multiple damages have been performed. In this simulated study, all sensor data, incident field, back-propagated (migrated) field, and Green's functions have been generated *via* a finite difference time-domain method with second–order of accuracy in time and space.

Examining the resulting images, the following conclusions may be drawn:

- Both DE and IE formalisms of EM migration and Born imaging algorithms are able to effectively identify the damages geometries and are quite robust against the measurement noise.
- The Born imaging algorithm provides superior damage identification over the EM migration, specially for complex damage geometries. Note that unlike the Born imaging, theoretically, the EM migration requires the measurement of both electric and magnetic components ($E^{d}_{y;scat}$ and $H^{d}_{x;scat}$).
- Although, in theory, both $E^{d}_{y;scat}$ and $H^{d}_{x;scat}$ measurements are required in the EM migration, the images obtained by using only one data component can still provide good damage identification.

- Treating the sensor data as time-dependent boundary conditions rather than sources in DE formalism of the EM migration usually improves images quality.
- Target-oriented capability (i.e., a desired part of the original domain of investigation can be imaged without the need to image the entire domain), which is only feasible using the IE formalism of the algorithms, can significantly reduce the computational cost.
- The numerical evaluation of the zero-lag cross-correlation of the back-propagated (migrated) scattered field with the incident field (zero-lag cross-correlation imaging condition), which is the second step of the imaging process for both DE and IE formalisms, is prohibitively expensive for a practical SHMS. The computational cost of this step can be significantly reduced by approximating the incident field in the image area by a proper single-event function. When this single-event function is parameterized by both traveltime and amplitude (modified excitation-time imaging condition) rather than only the traveltime (excitation-time imaging condition), the images quality is usually improved. Note that the images obtained by the modified excitation-time imaging condition with the maximum-energy arrival criterion are similar in quality to the images obtained without applying the incident field approximation.
- Note that despite having applied the above approximation to the incident field, the implementation of the DE formalism of the algorithms for a SHMS may be still impractical because the back-propagation (migration) of the scattered field data, the first step of the imaging process, is performed by solving the associated DEs during the monitoring stage which may be computationally expensive. In the IE formalism of the algorithms, however, the back-propagation step is performed by integral operations involving the Green's functions of the pristine structure and the scattered field data. Fortunately, the numerical solutions of the Green's functions (if analytical solutions are not available) can be carried out prior to the monitoring stage. Furthermore, by applying similar approximations to the fields associated with the Green's functions, real-time 3-D damage imaging algorithms suitable for SHM application can be

realized. In this case, the parameterization of the single-event functions by both traveltime and amplitude rather than only the traveltime significantly improves the quality of images. Note that the images obtained from the IE formalism of the algorithms with the approximated incident field and Green's functions are comparable in quality to the images obtained without any approximations.

- Employing the maximum-energy arrival criterion rather than the first-arrival criterion for calculating the traveltimes and amplitudes provides superior damage identification specially for complex damage geometries.

- When the pristine structure contains material discontinuity and the incident field and back-propagated scattered fields (or Green's functions for IE formalism of the algorithms) in image area are computed *via* Maxwell's equations (full two-way wave equations), strong artifacts may be generated in the resulting images due to undesired internal reflections. These artifacts can be completely eliminated when both incident field and Green's functions are approximated by single-event functions based on the first-arrival criterion.

- A remedy for reducing the artifacts related to the material discontinuity in the pristine structure is to modify the pristine structure such that the material discontinuities are removed or smoothed out. This modified pristine structure is used only for the computation of the incident field and back-propagated scattered field (or Green's functions for the IE formalism of the algorithms) in the image area. For instance, a half-space concrete and a half-space homogenized orthotropic medium have been assumed as the modified pristine structures for imaging the damages illustrated in Chapter 8. It should be mentioned that this scheme is also valuable in real applications since precise information about material properties and/or geometries of the pristine structure may not be known *a priori*.

- Examining the poststack images, it is observed that for obtaining images quality comparable to the quality of the prestack images, denser actuator/sensor is required (at least twice). In addition, the poststack images obtained by using the $H^{d}_{z;scat}$ do not provide complete damage identification, as opposed to the prestack images. On the

other hand, the algorithms based on the poststack concept are computationally more efficient and are much more robust to the problem related to the material discontinuity in the pristine structure.

- In theory, scattered field data (measured incident field subtracted from measured total field) is used for damage imaging. In practice, however, it is desirable to only measure the response of the structure under inspection (measured total field) for detecting the damage without the need to measure the response of the pristine structure (measured incident field) because the measurements are collected at different times that are often subject to different environmental conditions. If the measured total field is directly used for damage imaging in both DE and IE formalisms, all the material interfaces in the structure will be imaged in addition to the geometry of the damage. However, the image of the damage may be obscured by the strong reflections from nearby material interfaces. In general, when the measured total field is used for damage imaging, *direct waves* (the waves received by the sensors directly from the actuator) and possible reflections from the upper surface of the structure (if non-contact EM sensors are used) should be removed from the data as a preprocessing step to highlight the image.
- The proposed imaging algorithms in IE formalism can be considered "base-free" algorithms if the measured total field is directly used for damage imaging. Note that the algorithms in IE formalism do not require information about the pristine structure during the monitoring stage.
- The proposed imaging algorithms have a typical shortcoming for damage imaging application. This shortcoming may prevail when there is a material interface in geometrical shadow of a damage. In this case, a false damage near or on the interface location may be imaged in addition to the real damage. In other words, these algorithms may overestimate the severity of damages inside a structure. The application of linearized inversion method may resolve this problem.

References

Abubakar, A. and van den Berg, P.M., 2002, The contrast source inversion method for location and shape reconstructions, Inverse Problems, 18, 495–510.

Alam, M., McClellan, J.H., Norville, P., and Scott, W.R., 2004, Time-reverse imaging for detection of landmines, In: Proceedings of SPIE, Detection and Remediation Technologies for Mines and Minelike Targets IX, Harmon, R.S., Broach, J.T., and Holloway, J.H. (Ed.), 5415, 167-174.

Audebert, F., Nichols, D., Rekdal, T., Biondi, B., Lumley, D., and Urdaneta, H., 1997, Imaging complex geologic structure with single-arrival Kirchhoff prestack depth migration, Geophysics, 62(5), 1533-1543.

Bahr, A.J., 1995, Experimental techniques in microwave NDE, Review of Progress in Quantitative Nondestructive Evaluation, 14, 593-600.

Balanis, C.A., 1989, Advanced Engineering Electromagnetics, John Wiley & Sons, Inc.

Barkeshli, S., Radecki, D.J. and Sabbagh, H.A., 1992, On the linearized inverse scattering model for a three dimensional flaw embedded in anisotropic advanced composite materials, IEEE Transactions on Geoscience and Remote Sensing, 30(1), Jan. 1992, 71-80.

Baysal, E., Kosloff, D.D., and Sherwood, J.W.C., 1984, A two-way non-reflecting wave equation, Geophysics, 49, 132-141.

Belkebir, K., Kleinman, R.E., and Pichot, C., 1997, Microwave imaging - location and shape reconstruction from multifrequency scattering data, IEEE Transactions on Microwave Theory and Techniques, 45(4), April 1997, 469-476.

Bermani, E., Boni, A., Caorsi, S., Donelli, M., and Massa, A., 2004, A multi-source strategy based on a learning-by-example technique for buried object detection, Progress In Electromagnetics Research, PIER 48, 185–200.

Biondi, B.L., 2004, 3-D Seismic Imaging, Stanford University.

Bojarski, N.N., 1982, A survey of the physical optics inverse scattering identity, IEEE Transactions on Antennas and Propagation, 30(5), Sep. 1982, 980-989.

Bray, D.E. and McBride, D., 1992, Nondestructive Testing Techniques, John Wiley & Sons, Inc., New York.

Büyüköztürk, O., 1998, Imaging of concrete structures, NDT&E Int., 31(4), 233-243.

Büyüköztürk, O., Park, J., and Au, C., 2003, Non-destructive evaluation of FRP- confined concrete using microwaves, International Symposium: Non-Destructive Testing in Civil Engineering 2003.

Chang, F.K., 1997, Structural health monitoring: a summary report, 1st International Workshop on Structural Health Monitoring, Stanford University, Sept 18-20, 1997, xix-xxix.

Chang, W.F. and McMechan, G.A., 1986, Reverse time migration of offset vertical seismic profiling data using the excitation time imaging condition, Geophysics, 51(1), 67-84.

Chang, W.F. and McMechan, G.A., 1994, 3-D elastic prestack reverse time depth migration, Geophysics, 59(4), 597-609.

Chaturvedi, P. and Plumb, R.G., 1995, Electromagnetic imaging of underground targets using constrained optimization, IEEE Transactions on Geoscience and Remote Sensing, 33(3), May 1995, 551-561.

Chen, H.W. and Huang, T.M., 1998, Finite-difference time-domain simulation of GPR data, Journal of Applied Geophysics, 40, 139-163.

Chen J. and Schuster, G.T., 1999, Resolution limits of migrated images, Geophysics, 64, 1046–1053.

Chew, W.C., 1995, Waves and Fields in Inhomogeneous Media, IEEE Press.

Chien, W., Chiu, C.C., and Li, C.L., 2005, Image and conductivity reconstruction of a variable conducting cylinder in a half-space, International Journal of Applied Electromagnetics and Mechanics, 21, 51–62.

Claerbout, J.F., 1971, Toward a unified theory of reflector mapping, Geophysics, 36(3), 467-481.

Claerbout, J.F., 1992, Earth Sounding Analysis: Processing Versus Inversion, Blackwell Scientific Publications, Inc.

Claerbout, J.F. and Black, J.L., 2001, Basic Earth Imaging, © December 7, 2001, Version 2.4.

Colton, D. and Monk, P., 1994, The detection and monitoring of leukemia using electromagnetic waves: mathematical theory, Inverse Problems, 10, 1235-1251.

Colton, D., Haddar, H., and Piana, M., 2003, The linear sampling method in inverse electromagnetic scattering theory, Inverse Problems, 19, S105–S137.

Cui, T.J. and Chew, W.C., 2002, Diffraction tomographic algorithm for the detection of 3D objects buried in a lossy half-space, IEEE Transaction on Antennas and Propagation, 50(1), 42-49.

De Hoop, A.T., 1995, Handbook of Radiation and Scattering of Waves, Academic Press.

Deming, R.W. and Devaney, A.J., 1997, Diffraction tomography for multi-monostatic ground penetration radar, Inverse Problems, 13, 29-45.

Di, Q. and Wang, M., 2004, Migration of ground penetrating radar data with a finite element method that considers attenuation and dispersion, Geophysics, 69(2), 472-477.

Etgen(1), J.T., 1986, High-order finite difference reverse time migration with the 2-way non-reflecting wave equation, SEP Report 48.

Etgen(2), J.T., 1986, Prestack reverse time migration of shot profiles, SEP Report 50.

Fear, E.C., Li, X., Hagness, S.C., and Stuchly, M.A., 2002, Confocal microwave imaging for breast cancer detection: localization of tumors in three dimensions, IEEE Transactions on Biomedical Engineering, 49(8), August 2002, 812-821.

Fehler, M.C. and Huang, L., 2002, Modern imaging using seismic reflection data, Annual Rev. Earth Planet Sci., 30, 259-284.

Felsen, L. and Marcuvitz, N., 1994, Radiation and Scattering of Waves, IEEE Press, New York.

Feng, X. and Sato, M., 2004, Pre-stack migration applied to GPR for landmine detection, Inverse Problems, 20, S99–S115.

Gazdag, J., 1978, Wave equation migration with the phase-shift method, Geophysics, 43(7), 1342–1351.

Gray, S.H., 1999, Speed and accuracy of seismic migration methods, Depth Imaging of Foothills Seismic Data, Ed. L. R. Lines, D. C. Lawton, and S. H. Gray.

Guo, Y., Ko, H.W., and White, D.M., 1998, 3-D localization of buried objects by near-field electromagnetic holography, Geophysics, 63(3), 880-889.

Haberman, R., 1987, Elementary Applied Partial Differential Equations, Prentice-Hall International Edition.

Hadamard, J., 1923, Lectures on the Cauchy Problem in Linear Partial Differential Equations, Yale University Press.

Haykin, S., 1999, Neural Networks: A Comprehensive Foundation, Prentice Hall, New Jersey, 2nd edition.

Iyer, S.R., Sinha, S.K., and Schokker, A.J., 2005, Ultrasonic C-scan imaging of post-tensioned concrete bridge structures for detection of corrosion and voids, Computer-Aided Civil and Infrastructure Engineering, 20, 79-94.

Johansson, E.M. and Mast, J.E., 1994, Three dimensional ground penetration radar imaging using synthetic aperture time-domain focusing, Proceedings SPIE, Vol. 2275, July 25-26, 1994, 205-214.

Johnson, E.A., Lam, H.F., Katafygiotis, L.S., and Beck, J.L., 2004, Phase I IASC-ASCE structural health monitoring benchmark problem using simulated data, J. of Engineering Mechanics, 130(1), 3-15.

Kak, A.C. and Slaney, M., 1988, Principles of Computerized Tomographic Imaging, IEEE PRESS.

Kim, Y.J., Jofre, L., Flaviis, F.D., and Feng, M.Q., 2004, Microwave subsurface imaging technology for damage detection, Journal of Engineering Mechanics, 130(7), July 1, 2004, 858-866.

Kirsch, A., 2004, The factorization method for Maxwell's equations, Inverse Problems, 20, S117–S134.

Kosmas, P. and Rappaport, C.M., 2005, Time reversal with the FDTD method for microwave breast cancer detection, IEEE Transactions on Microwave Theory and Techniques, 53(7), July 2005, 2317-2323.

Krautkramer, J. and Krautkramer, H., 1990, Ultrasonic Testing of Materials, Springer-Verlag, Berlin.

Langenberg, K.J., 1989, Introduction to the special issue on inverse problems, Wave Motion, 11, 99-112.

Langenberg, K.J., Bärmann, R., Marklein, R., Irmer, S., Müller, H., Brandfaß, M., and Potzkai, B., 1997, Electromagnetic and elastic wave scattering and inverse scattering applied to concrete, NDT&E International, 30(4), 205-210.

Langenberg, K.J., Fischer, M., Berger, M., and Weinfurter, G., 1986, Imaging performance of generalized holography, J. Opt. Soc. Am. A, 3(3), March 1986, 329-339.

Lemistre, M.B. and Balageas, D.L., 2004, A hybrid electromagnetic acousto-ultrasonic method for SHM of carbon/epoxy structures, Structural Health Monitoring, 2(2), 153-160.

Leone, G., Persico, R., and Pierri, R., 1999, Inverse scattering under the distorted Born approximation for cylindrical geometries, J. Opt. Soc. Am. A, 16(7), July 1999, 1779-1787.

Leuschen, C. and Plumb, R., 2001, A matched-filter-based reverse-time migration algorithm for GPR data, IEEE Transaction on Geoscience and Remote Sensing, 39(5), May 2001, 929-936.

Lin, X. and Yuan, F.G., 2001, Detection of multiple damages by prestack reverse-time migration technique, AIAA Journal 39 (11), 2206-2215.

Lin, X. and Yuan, F.G., 2005, Experimental study of applying migration technique in structural health monitoring, To appear in International Journal of Structural Health Monitoring.

Liseno, A. and Pierri, R., 2004, Imaging of voids by means of a physical-optics-based shape-reconstruction algorithm, J. Opt. Soc. Am. A, 21(6), 968-974.

Liu, J. and Bethesda, W., 1998, Microwave and ultrasonic NDE of thick glass-fiber-reinforcement composites, Proceedings of SPIE on NDE on materials and composites II, Vol. 3396, 135-146.

Liu, Q.H., Zhang, Z.Q., Wang, T.T., Bryan, J.A., Ybarra, G.A., Nolte, L.W., and Joines, W.T., 2002, Active microwave imaging I: 2D forward and inverse scattering methods, IEEE Transactions on Microwave Theory and Techniques, 50(1), Jan. 2002, 123-133.

Loewenthal, D., Stoffa, P.L., and Faria, E.L., 1987, Suppressing the unwanted reflections of the full wave equation, Geophysics, 52(7), 1007-1012.

Loewenthal, D. and Hu, L.Z., 1991, Two methods for computing the imaging condition for common-shot prestack migration, Geophysics, 56(3), 378-381.

Marklein, R., Mayer, K., Hannemann, R., Kraylow, T., Balasubramanian, K., Langenberg, K.J. and Schmitz, V., 2002, Linear and nonlinear inversion algorithms applied in nondestructive evaluation, Inverse Problems, 18, 1733-1759.

Nichols, D.E., 1996, Maximum energy traveltimes calculated in the seismic frequency band, Geophysics, 61(1), 253-263.

Oristaglio, M. and Blok, H., 1994, Wave Field Imaging and Inversion in Electromagnetics and Acoustics," Lecture Notes.

Peng, Y., Jia-Lin, W., and Jian-Sheng, W., 2001, Multi-parameter migration imaging of magnetotelluric data using finite difference, Chinese J. of Geophysics, 44(4), 548-559.

Pierri, R., Brancaccio, A., and De Blasio, F., 2000, Multifrequency dielectric profile inversion for a cylindrically stratified medium, IEEE Transactions on Geoscience and Remote Sensing, 38(4), July 2000, 1716-1724.

Ramananjaona, C., Lambert, M., and Lesselier, D., 2001, Shape inversion from TM and TE real data by controlled evolution of level sets, Inverse Problems, 17, 1585–1595.

Ramm, A.G., Gutman, S., 2005, Analysis of a linear sampling method for identification of obstacles, Acta Mathematicae Applicatae Sinica, English Series, 21(3), 399–404.

Rekanos, I.T. and Räisänen, A., 2003, Microwave imaging in the time domain of buried multiple scatterers by using an FTDT-based optimization technique, IEEE Transactions on Magnetics, 39(3), Mar. 2003, 1381-1384.

Rekanos, I.T., 2002, Neural-network-based inverse-scattering technique for online microwave medical imaging, IEEE Transactions on Magnetics, 38(2), Mar. 2002, 1061-1064.

Sanada, Y. and Ashida, Y., 1998, Reverse time migration for ground penetration radar using finite difference time domain method, Proceedings of the 3rd Int. Symposium on Recent advances in Exploration Geophysics in Kyoto, 145-154.

Scales, J.A., 1997, Theory of Seismic Imaging, Samizdat Press, Golden .White River Junction.

Schneider, W.A., 1978, Integral formulation for migration in two and three dimensions, Geophysics, 43(1), 49-76.

Slaney, M., Kak, A.C., and Larsen, L.E., 1984, Limitation of imaging with first-order diffraction tomography, IEEE Transactions on Microwave and Techniques, 32(8), Aug. 1984, 860-874.

Soldovieri, F., Brancaccio, A., Leone, G., and Pierri, R., Shape reconstruction of perfectly conducting objects by multiview experimental data, IEEE Transactions on Geoscience and Remote Sensing, 43(1), Jan 2005, 65-71.

Stolt, R.H., 1978, Migration by Fourier transform, Geophysics, 43(1), 23–48.

Taflove, A., 1995, Computational Electrodynamics: the Finite Difference Time Domain Method, Boston: Artech House.

Takenaka, T., Zhou, H., and Tanaka, T., 2003, Inverse scattering for a three-dimensional object in the time domain, J. of Optical Society of America, 20(10), October 2003, 1867-1874.

Tarokh, A.B., Miller, E.L., and Boas, D., 2004, A new, flexible parameterization for the estimation of 3D shape structure from scattered field data, Proc. of SPIE-IS&T Electronic Imaging, Computational Imaging II, edited by Bouman, C.A. and Miller, E.L., Vol. 5299, 304-314.

Tseng, H.W., Leez, K.H., and Becker, A., 2003, 3D interpretation of electromagnetic data using a modified extended Born approximation, Geophysics, 68(1), 127-137.

Van den Berg, P.M. and Kleinman, R.E., 1997, A contrast source inversion method, Inverse Problems, 13, 1607-1620.

Van der Kurk, J., Wapenaar, C.P.A., Fokkema, J.T., and van den Berg, P.M., 2003, Three dimensional imaging of multi-component ground penetration radar data, Geophysics, 68(4), 1241-1254.

Vermeer, G.J.O., 1999, Factors affecting spatial resolution, Geophysics, 64(3), 942-953.

Vidale, J.E., 1988, Finite difference traveltime calculation, Bull. Seis. Soc. Am., 78, 2062-2076.

Wang, T. and Oristaglio, M.L., 2000, GPR imaging using the generalized Radon transform, Geophysics, 65(5), 1553-1559.

Wang, L. and Yuan, F.G., 2005, Damage identification in a composite plate using prestack reverse-time migration technique, Structural Health Monitoring, 4 (3), 195-211.

Weedon, W.H., Chew, W.C., and Mayes, P.E., 2000, A step-frequency radar imaging system for microwave nondestructive evaluation, Progress in Electromagnetics Research, PIER 28, 121-146.

Welch, W.J., 1960, Reciprocity theorems for electromagnetic fields whose time dependence is arbitrary, IEEE Transactions on Antennas and Propagation, 8(1), Jan 1960, 68-73.

Welch, W.J., 1961, Comment on reciprocity theorems for electromagnetic fields whose time dependence is arbitrary, IEEE Transactions on Antennas and Propagation, 9(1), 114-115.

Xu, X., Miller, E.L., and Rappaport, C.M., 2003, Minimum entropy regularization in frequency-wavenumber migration to localize subsurface objects, IEEE Transactions on Geoscience and Remote Sensing, 41(8), Aug. 2003, 1804-1812.

Yavuz, M.E. and Teixeira, F.L., 2005, A numerical study of time-reversed UWB electromagnetic waves in continuous random media, IEEE Antennas and Wireless Propagation Letters, 4, 43-46.

Yee, K.S., 1966, Numerical solution of initial boundary value problems involving Maxwell's equations in isotropic media, IEEE Transactions on Antennas and Propagation, 14, 302-307.

Zhdanov, M. and Hursan, G., 2000, 3D electromagnetic inversion based on quasi-analytical approximation, Inverse Problems, 16, 1297-1322.

Zhdanov, M. and Tartaras, E., 2002, 3D inversion of multi-transmitter electromagnetic data based on the localized quasi-linear approximation, Geophysics J. Int., 148, 506-519.

Zhdanov, M.S. and Portniaguine, O., 1997, Time domain electromagnetic migration in the solution of inverse problem, Geophysics J. Int., 131, 293-309.

Zhdanov, M.S. and Li, W., 1997, 2D finite difference time domain electromagnetic migration, SEG Expanded Abstracts, 67th Annual Meeting, Dallas, TEX., 370-373.

Zhdanov, M.S. and Li, W., 1998, Preconditioned time domain electromagnetic migration, SEG Expanded Abstracts.

Zhdanov, M.S., Traynin, P., and Booker, J.R., 1996, Underground imaging by frequency-domain electromagnetic migration, Geophysics, 61(3), 666-682.

Zhdanov, M.S., 2002, Geophysical Inverse Theory and Regularization Problems, Amsterdam, Oxford, Elsevier Science.

Zhdanov, M.S., 2001, Method of broad band electromagnetic holographic imaging, U.S. Patent # 6,253,100.

Zhdanov, M.S., 1988, Integral Transforms in Geophysics, Springer-Verlag, Berlin.

Zhou, C. and Liu, L., 2000, Radar-diffraction tomography using the modified quasi-linear approximation, IEEE Transactions on Geoscience and Remote Sensing, 38(1), Jan. 2000, 404-415.

Zhu, J. and Lines, L.R., 1997, Implicit interpolation in reverse time migration, Geophysics, 62, 906-917.

Zoghi, R., 2000, Microwave Non-Destructive Testing and Evaluation, Kluwer Academic Pub.

Appendices

Appendix A

Dyadic Green's Functions in an Infinite Homogeneous Isotropic and Lossless Media

For unbounded homogeneous isotropic and lossless media having permittivity ε and permeability μ, the four dyadic Green's functions can be expressed in terms of a single scalar Green's function (Felsen and Marcuvitz, 1994), i.e.,

$$\begin{aligned}
\mathbf{G}^{EJ}(\boldsymbol{r},t;\boldsymbol{r}',t') &= \left(\mu\frac{\partial}{\partial t}\mathbf{I}-\frac{\nabla\nabla}{\varepsilon(\partial/\partial t)}\right)g(\boldsymbol{r},t;\boldsymbol{r}',t') \\
\mathbf{G}^{HM}(\boldsymbol{r},t;\boldsymbol{r}',t') &= \left(\varepsilon\frac{\partial}{\partial t}\mathbf{I}-\frac{\nabla\nabla}{\mu(\partial/\partial t)}\right)g(\boldsymbol{r},t;\boldsymbol{r}',t') \\
\mathbf{G}^{EM}(\boldsymbol{r},t;\boldsymbol{r}',t') &= \nabla\times\mathbf{I}\,g(\boldsymbol{r},t;\boldsymbol{r}',t') \\
\mathbf{G}^{HJ}(\boldsymbol{r},t;\boldsymbol{r}',t') &= -\nabla\times\mathbf{I}\,g(\boldsymbol{r},t;\boldsymbol{r}',t')
\end{aligned} \tag{A.1}$$

Where $\frac{1}{\partial/\partial t}f(t)=\int_{-\infty}^{t}f(t)\,dt$ and $\mathbf{I}$ is identity tensor. The scalar Green's function $g(\boldsymbol{r},t;\boldsymbol{r}',t')$ satisfies $\left(\nabla^2-\frac{1}{c^2}\frac{\partial^2}{\partial t^2}\right)g(\boldsymbol{r},t;\boldsymbol{r}',t')=\delta(\boldsymbol{r}-\boldsymbol{r}')\,\delta(t-t')$, causality condition, and radiation boundary conditions, and can be derived as:

$$g(\boldsymbol{r},t;\boldsymbol{r}',t')=\frac{1}{4\pi|\boldsymbol{r}-\boldsymbol{r}'|}\,\delta\left(t-t'-\frac{|\boldsymbol{r}-\boldsymbol{r}'|}{c}\right) \tag{A.2}$$

where $c=\frac{1}{\sqrt{\mu\varepsilon}}$ is medium velocity.

Appendix B

Reciprocity Theorems in Electromagnetic

A reciprocity theorem interrelates in a specific way the field quantities associated with two admissible physical states that could occur in one and the same domain of space. These reciprocity theorems apply to a time-invariant configuration; the media in the physical states are also assumed to be time-invariant and linear in their physical behavior (constitutive properties).

Generally, in the time domain, there is a distinction between reciprocity theorems of *convolution type* and reciprocity theorems of *correlation type*. Their frequency domain counterparts are the *classical* reciprocity theorem (which in electromagnetic is named after H.A. Lorentz and in acoustics, after Lord Rayleigh) and the *power* reciprocity theorem, respectively (Oristaglio and Blok, 1994).

Here, an inhomogeneous, anisotropic, and dissipative medium described by the constitutive equations (1.8) is considered.

Consider two sets of finite sources, $\{\boldsymbol{J}(\boldsymbol{r},t),\boldsymbol{M}(\boldsymbol{r},t)\}$ and $\{\hat{\boldsymbol{J}}(\boldsymbol{r},t),\hat{\boldsymbol{M}}(\boldsymbol{r},t)\}$ in an unbounded medium, and their corresponding fields, $\{\boldsymbol{E}(\boldsymbol{r},t),\boldsymbol{H}(\boldsymbol{r},t)\}$ and $\{\hat{\boldsymbol{E}}(\boldsymbol{r},t),\hat{\boldsymbol{H}}(\boldsymbol{r},t)\}$, where hat denotes adjoint. They satisfy the equations (1.9) and (1.22), i.e.,

$$\begin{cases}\nabla\times\boldsymbol{E}=-\boldsymbol{\mu}\cdot\dot{\boldsymbol{H}}-\boldsymbol{M}\\ \nabla\times\boldsymbol{H}=\boldsymbol{\sigma}\cdot\boldsymbol{E}+\boldsymbol{\varepsilon}\cdot\dot{\boldsymbol{E}}+\boldsymbol{J}\end{cases} \tag{B.1}$$

$$\begin{cases}-\nabla\times\hat{\boldsymbol{E}}=\boldsymbol{\mu}^{T}\cdot\dot{\hat{\boldsymbol{H}}}-\hat{\boldsymbol{M}}\\ -\nabla\times\hat{\boldsymbol{H}}=\boldsymbol{\sigma}^{T}\cdot\hat{\boldsymbol{E}}-\boldsymbol{\varepsilon}^{T}\cdot\dot{\hat{\boldsymbol{E}}}+\hat{\boldsymbol{J}}\end{cases} \tag{B.2}$$

Using the identity

$$\nabla\cdot(\boldsymbol{A}\times\boldsymbol{B})=\boldsymbol{B}\cdot\nabla\times\boldsymbol{A}-\boldsymbol{A}\cdot\nabla\times\boldsymbol{B} \tag{B.3}$$

and Eq. (B.1) and (B.2), the following relation can be obtained:

$$\nabla\cdot\left(\boldsymbol{E}\times\hat{\boldsymbol{H}}+\hat{\boldsymbol{E}}\times\boldsymbol{H}\right)=\hat{\boldsymbol{H}}\cdot\nabla\times\boldsymbol{E}-\boldsymbol{E}\cdot\nabla\times\hat{\boldsymbol{H}}+\boldsymbol{H}\cdot\nabla\times\hat{\boldsymbol{E}}-\hat{\boldsymbol{E}}\cdot\nabla\times\boldsymbol{H}$$
$$=-\hat{\boldsymbol{H}}\cdot\left(\boldsymbol{\mu}\cdot\dot{\boldsymbol{H}}\right)-\hat{\boldsymbol{H}}\cdot\boldsymbol{M}+\boldsymbol{E}\cdot\left(\boldsymbol{\sigma}^{T}\cdot\hat{\boldsymbol{E}}\right)-\boldsymbol{E}\cdot\left(\boldsymbol{\varepsilon}^{T}\cdot\dot{\hat{\boldsymbol{E}}}\right)+\boldsymbol{E}\cdot\hat{\boldsymbol{J}}- \tag{B.4}$$
$$\boldsymbol{H}\cdot\left(\boldsymbol{\mu}^{T}\cdot\dot{\hat{\boldsymbol{H}}}\right)+\boldsymbol{H}\cdot\hat{\boldsymbol{M}}-\hat{\boldsymbol{E}}\cdot\left(\boldsymbol{\sigma}\cdot\boldsymbol{E}\right)-\hat{\boldsymbol{E}}\cdot\left(\boldsymbol{\varepsilon}\cdot\dot{\boldsymbol{E}}\right)-\hat{\boldsymbol{E}}\cdot\boldsymbol{J}$$

Using the identity $\boldsymbol{A}\cdot(\mathbf{B}\cdot\boldsymbol{C})=\boldsymbol{C}\cdot(\mathbf{B}^{T}\cdot\boldsymbol{A})$, the last relation is simplified to:

$$\nabla\cdot\left(\boldsymbol{E}\times\hat{\boldsymbol{H}}+\hat{\boldsymbol{E}}\times\boldsymbol{H}\right)=-\frac{\partial}{\partial t}\left[\hat{\boldsymbol{H}}\cdot\left(\boldsymbol{\mu}\cdot\boldsymbol{H}\right)+\hat{\boldsymbol{E}}\cdot\left(\boldsymbol{\varepsilon}\cdot\boldsymbol{E}\right)\right]+\boldsymbol{E}\cdot\hat{\boldsymbol{J}}+\boldsymbol{H}\cdot\hat{\boldsymbol{M}}-\hat{\boldsymbol{E}}\cdot\boldsymbol{J}-\hat{\boldsymbol{H}}\cdot\boldsymbol{M} \tag{B.5}$$

Now, both sides of the above relation are integrated over a volume which contains both sources and over a time interval $T_1<t<T_2$. Then with the application of the divergence theorem to the left-hand side, it follows that

$$\int_{T_1}^{T_2}\oiint_S\left(\boldsymbol{E}\times\hat{\boldsymbol{H}}+\hat{\boldsymbol{E}}\times\boldsymbol{H}\right)\cdot\boldsymbol{n}\,dS\,dt=\iiint_V-\left[\hat{\boldsymbol{H}}\cdot\left(\boldsymbol{\mu}\cdot\boldsymbol{H}\right)+\hat{\boldsymbol{E}}\cdot\left(\boldsymbol{\varepsilon}\cdot\boldsymbol{E}\right)\right]_{T_1}^{T_2}dV+$$
$$\int_{T_1}^{T_2}\iiint_V\left(\boldsymbol{E}\cdot\hat{\boldsymbol{J}}+\boldsymbol{H}\cdot\hat{\boldsymbol{M}}-\hat{\boldsymbol{E}}\cdot\boldsymbol{J}-\hat{\boldsymbol{H}}\cdot\boldsymbol{M}\right)dV\,dt \tag{B.6}$$

Let T_1 be some time prior to the sources and T_2 some time after the sources are both off. At time T_1 the *retarded* (*ordinary*) fields are everywhere zero (causality), and at time T_2 the *advanced* (*adjoint*) fields are everywhere zero (anti-causality). Therefore, for this choice of T_1 and T_2, the first volume integral on the right-hand side vanishes identically. An inspection of (B.6) shows that the value of the surface integral is independent of the size or shape of the surface, as long as the surface is large enough to enclose completely both sources. Let the surface be a large sphere of radius *R*. Then, if, for example, $R>>c\left(|T_1|+|T_2|\right)$, where *c* is the speed, the retarded field will not reach the surface *S* during the interval $T_1<t<T_2$, and the surface integral will be identically zero (Welch, 1960 and 1961). In fact, the time interval may be infinite and the contribution from the surface integral at infinity will be zero, as long as the sources are of finite spatial extent. It follows then that if the integrations over space and time completely enclose the sources,

$$\int_{T_1}^{T_2}\iiint_V\left(\boldsymbol{E}\cdot\hat{\boldsymbol{J}}+\boldsymbol{H}\cdot\hat{\boldsymbol{M}}-\hat{\boldsymbol{E}}\cdot\boldsymbol{J}-\hat{\boldsymbol{H}}\cdot\boldsymbol{M}\right)dV\,dt=0 \tag{B.7}$$

To utilize the *reciprocity relation* (B.7) for deriving the relations between dyadic Green's functions and their adjoints, a number of different choices of excitation for the ordinary and adjoint fields are considered (Felsen and Marcuvitz, 1994). For example, if

$$\begin{aligned} \boldsymbol{J} &= \boldsymbol{e}'\delta(\boldsymbol{r}-\boldsymbol{r}')\delta(t-t') \; ; \quad \hat{\boldsymbol{J}} = \boldsymbol{e}''\delta(\boldsymbol{r}-\boldsymbol{r}'')\delta(t-t'') \\ \boldsymbol{M} &= \boldsymbol{0} \qquad\qquad\qquad\quad ; \quad \hat{\boldsymbol{M}} = \boldsymbol{0} \end{aligned} \tag{B.8}$$

Then, the corresponding fields can be obtained using relations (1.13) and (1.27) as

$$\begin{aligned} \boldsymbol{E}(\boldsymbol{r},t) &= \mathbf{G}^{EJ}(\boldsymbol{r},t;\boldsymbol{r}',t')\cdot\boldsymbol{e}' \; ; \quad \hat{\boldsymbol{E}}(\boldsymbol{r},t) = \hat{\mathbf{G}}^{EJ}(\boldsymbol{r},t;\boldsymbol{r}'',t'')\cdot\boldsymbol{e}'' \\ \boldsymbol{H}(\boldsymbol{r},t) &= \mathbf{G}^{HJ}(\boldsymbol{r},t;\boldsymbol{r}',t')\cdot\boldsymbol{e}' \; ; \quad \hat{\boldsymbol{H}}(\boldsymbol{r},t) = \hat{\mathbf{G}}^{HJ}(\boldsymbol{r},t;\boldsymbol{r}'',t'')\cdot\boldsymbol{e}'' \end{aligned} \tag{B.9}$$

Substitution of the above sources and fields in reciprocity relation (B.7) leads to

$$\boldsymbol{e}''\cdot\mathbf{G}^{EJ}(\boldsymbol{r}'',t'';\boldsymbol{r}',t')\cdot\boldsymbol{e}' = \boldsymbol{e}'\cdot\hat{\mathbf{G}}^{EJ}(\boldsymbol{r}',t';\boldsymbol{r}'',t'')\cdot\boldsymbol{e}'' \tag{B.10}$$

or

$$\hat{\mathbf{G}}^{EJ}(\boldsymbol{r}',t';\boldsymbol{r}'',t'') = \mathbf{G}^{EJ^T}(\boldsymbol{r}'',t'';\boldsymbol{r}',t') \tag{B.11}$$

In a similar manner, from the point excitations

$$\begin{aligned} \boldsymbol{J} &= \boldsymbol{0} \qquad\qquad\qquad\quad ; \quad \hat{\boldsymbol{J}} = \boldsymbol{0} \\ \boldsymbol{M} &= \boldsymbol{e}'\delta(\boldsymbol{r}-\boldsymbol{r}')\delta(t-t') \; ; \quad \hat{\boldsymbol{M}} = \boldsymbol{e}''\delta(\boldsymbol{r}-\boldsymbol{r}'')\delta(t-t'') \end{aligned} \tag{B.12}$$

and the following corresponding fields

$$\begin{aligned} \boldsymbol{E}(\boldsymbol{r},t) &= \mathbf{G}^{EM}(\boldsymbol{r},t;\boldsymbol{r}',t')\cdot\boldsymbol{e}' \; ; \quad \hat{\boldsymbol{E}}(\boldsymbol{r},t) = \hat{\mathbf{G}}^{EM}(\boldsymbol{r},t;\boldsymbol{r}'',t'')\cdot\boldsymbol{e}'' \\ \boldsymbol{H}(\boldsymbol{r},t) &= \mathbf{G}^{HM}(\boldsymbol{r},t;\boldsymbol{r}',t')\cdot\boldsymbol{e}' \; ; \quad \hat{\boldsymbol{H}}(\boldsymbol{r},t) = \hat{\mathbf{G}}^{HM}(\boldsymbol{r},t;\boldsymbol{r}'',t'')\cdot\boldsymbol{e}'' \end{aligned} \tag{B.13}$$

One infers

$$\hat{\mathbf{G}}^{HM}(\boldsymbol{r}',t';\boldsymbol{r}'',t'') = \mathbf{G}^{HM^T}(\boldsymbol{r}'',t'';\boldsymbol{r}',t') \tag{B.14}$$

From the excitations

$$\begin{aligned} \boldsymbol{J} &= \boldsymbol{e}'\delta(\boldsymbol{r}-\boldsymbol{r}')\delta(t-t') \; ; \quad \hat{\boldsymbol{J}} = \boldsymbol{0} \\ \boldsymbol{M} &= \boldsymbol{0} \qquad\qquad\qquad\quad ; \quad \hat{\boldsymbol{M}} = \boldsymbol{e}''\delta(\boldsymbol{r}-\boldsymbol{r}'')\delta(t-t'') \end{aligned} \tag{B.15}$$

and the following corresponding fields

$$\begin{aligned} \boldsymbol{E}(\boldsymbol{r},t) &= \mathbf{G}^{EJ}(\boldsymbol{r},t;\boldsymbol{r}',t')\cdot\boldsymbol{e}' ; \quad \hat{\boldsymbol{E}}(\boldsymbol{r},t) = \hat{\mathbf{G}}^{EM}(\boldsymbol{r},t;\boldsymbol{r}'',t'')\cdot\boldsymbol{e}'' \\ \boldsymbol{H}(\boldsymbol{r},t) &= \mathbf{G}^{HJ}(\boldsymbol{r},t;\boldsymbol{r}',t')\cdot\boldsymbol{e}' ; \quad \hat{\boldsymbol{H}}(\boldsymbol{r},t) = \hat{\mathbf{G}}^{HM}(\boldsymbol{r},t;\boldsymbol{r}'',t'')\cdot\boldsymbol{e}'' \end{aligned} \tag{B.16}$$

One infers

$$\hat{\mathbf{G}}^{EM}(\boldsymbol{r}',t';\boldsymbol{r}'',t'') = \mathbf{G}^{HJ^T}(\boldsymbol{r}'',t'';\boldsymbol{r}',t') \tag{B.17}$$

And from the excitations

$$\begin{aligned} \boldsymbol{J} &= \mathbf{0} \quad ; \quad \hat{\boldsymbol{J}} = \boldsymbol{e}''\delta(\boldsymbol{r}-\boldsymbol{r}'')\delta(t-t'') \\ \boldsymbol{M} &= \boldsymbol{e}'\delta(\boldsymbol{r}-\boldsymbol{r}')\delta(t-t') \; ; \quad \hat{\boldsymbol{M}} = \mathbf{0} \end{aligned} \tag{B.18}$$

and the following corresponding fields

$$\begin{aligned} \boldsymbol{E}(\boldsymbol{r},t) &= \mathbf{G}^{EM}(\boldsymbol{r},t;\boldsymbol{r}',t')\cdot\boldsymbol{e}' ; \quad \hat{\boldsymbol{E}}(\boldsymbol{r},t) = \hat{\mathbf{G}}^{EJ}(\boldsymbol{r},t;\boldsymbol{r}'',t'')\cdot\boldsymbol{e}'' \\ \boldsymbol{H}(\boldsymbol{r},t) &= \mathbf{G}^{HM}(\boldsymbol{r},t;\boldsymbol{r}',t')\cdot\boldsymbol{e}' ; \quad \hat{\boldsymbol{H}}(\boldsymbol{r},t) = \hat{\mathbf{G}}^{HJ}(\boldsymbol{r},t;\boldsymbol{r}'',t'')\cdot\boldsymbol{e}'' \end{aligned} \tag{B.19}$$

One infers

$$\hat{\mathbf{G}}^{HJ}(\boldsymbol{r}',t';\boldsymbol{r}'',t'') = \mathbf{G}^{EM^T}(\boldsymbol{r}'',t'';\boldsymbol{r}',t') \tag{B.20}$$

Appendix C

The Fourier Transform Properties

The Fourier transform, in essence, decomposes or separates a waveform or function into sinusoids of different frequency which sum to the original waveform. It identifies or distinguishes the different frequency sinusoids and their respective amplitudes. The Fourier transform of $f(t)$ is defined as

$$f(\omega) = \int_{-\infty}^{+\infty} f(t) e^{j\omega t} dt \qquad ; f(\omega) = \Im\left[f(t)\right] \tag{C.1}$$

Then, the inverse Fourier transform will be

$$f(t) = \frac{1}{2\pi} \int_{-\infty}^{+\infty} f(\omega) e^{-j\omega t} d\omega \qquad ; f(t) = \Im^{-1}\left[f(\omega)\right] \tag{C.2}$$

where, the same notation for the function and its transform has been used for simplicity. The variable in parentheses is sufficient to distinguish between the function and its transform.

Some of the Fourier transform properties used in this study are:

Time Derivative Property:

$$\Im\left[\frac{df(t)}{dt}\right] = -j\omega f(\omega) \tag{C.3}$$

Shifting Property: If t' is a real constant, then

$$\Im\left[f(t-t')\right] = e^{j\omega t'} f(\omega) \tag{C.4}$$

Conjugate Property: If $f(t)$ is a real-valued function, then

$$\Im\left[f(-t)\right] = f^{*}(\omega) \tag{C.5}$$

where * indicates complex conjugate.

Convolution Theorem: The convolution of the two functions $f(t)$ and $g(t)$ is defined as

$$f(t) * g(t) = \int_{-\infty}^{+\infty} f(\lambda)\, g(t-\lambda) d\lambda = \int_{-\infty}^{+\infty} f(t-\lambda)\, g(\lambda) d\lambda = g(t) * f(t) \tag{C.6}$$

Then, the Fourier transform of this convolution assumes the following form:

$$\Im\ [f(t) * g(t)] = f(\omega)\, g(\omega) \tag{C.7}$$

and

$$\Im^{-1}[f(\omega)\, g(\omega)] = \frac{1}{2\pi}\int_{-\infty}^{+\infty} f(\omega)\, g(\omega)\, e^{-j\omega t}\, d\omega = f(t) * g(t) \tag{C.8}$$

Correlation Theorem: The cross correlation of the two functions $f(t)$ and $g(t)$ is defined as

$$f(t) \otimes g(t) = \int_{-\infty}^{+\infty} f(\lambda - t)\, g(\lambda) d\lambda = \int_{-\infty}^{+\infty} f(\lambda)\, g(\lambda + t) d\lambda \tag{C.9}$$

Then, the Fourier transform of this correlation is:

$$\Im\ [f(t) \otimes g(t)] = f^*(\omega)\, g(\omega) \tag{C.10}$$

and

$$\Im^{-1}[f^*(\omega)\, g(\omega)] = \frac{1}{2\pi}\int_{-\infty}^{+\infty} f^*(\omega)\, g(\omega)\, e^{-j\omega t}\, d\omega = f(t) \otimes g(t) \tag{C.11}$$

then,

$$f(t) \otimes g(t)\,|_{t=0} = \frac{1}{2\pi}\int_{-\infty}^{+\infty} f^*(\omega)\, g(\omega)\, d\omega \tag{C.12}$$

It is worth noting that the Fourier transform of the Dirac delta function is unity; i.e.,

$$\Im\,[\delta(t)] = 1 \tag{C.13}$$